University of Southampton

Faculty of Physical Sciences and Engineering

PRECISION DICING AND MICROMILLING OF SILICA FOR PHOTONICS

By

LEWIS GLYNN CARPENTER

Thesis for the degree of Doctor of Philosophy

October 2013

UNIVERSITY OF SOUTHAMPTON

ABSTRACT

Optoelectronics Research Centre

DOCTOR OF PHILOSOPHY

PRECISION DICING AND MICROMILLING OF SILICA FOR PHOTONICS

By Lewis Glynn Carpenter

This thesis focuses on the development of precision dicing and micromilling machining techniques for silica photonic applications. Comparison is given between the studied and conventional techniques for machining silica, such as photolithography and etching, laser machining, *etc.*.

Precision dicing was used to create low loss input/output facets in the silica-on-silicon platform. It was demonstrated that ductile type dicing can produce facets in a silica-on-silicon substrate with a smooth, mirror like finish. The facet had a surface roughness (Sa) of 4.9 nm, a factor of ~7.5 improvement on previously reported roughnesses. An individual silica/air average interface loss, caused by surface roughness scatter, was calculated to be -0.63 dB and -0.76 dB for the TE and TM polarisations, respectively.

Utilising dicing, glass photonic microcantilever devices are produced with integrated Bragg gratings and waveguides. Two cantilever interrogations methods have been shown; one utilising a single Bragg grating and the other using a pair of spectrally matched Bragg gratings to form a Fabry-Pérot interferometer. These cantilever devices were subjected to physical stimulus of external pressure change and profilometer actuation.

A precision micromill was built by the author. Precision micromilling was used to remove the cladding material from the silica-on-silicon platform, for evanescent field access. By accessing the ductile milling regime, the mill enabled three-dimensional machining of flat, smooth, chip free grooves in silica. A groove with an average surface roughness (Sa) of 3.0 nm was measured, with a depth of cut of 17 μm. This micromilling method produces grooves that are seven times smoother and cut depths forty times deeper, than previously reported in the literature.

Table of Contents

Declaration of Authorship

I, Lewis Glynn Carpenter, declare that the thesis entitled “Precision Dicing and Micromilling of Silica for Photonics” and the work presented in the thesis are both my own, and have been generated by me as the result of my own original research.

I confirm that:

- this work was done wholly or mainly while in candidature for a research degree at this University;
- where any part of this thesis has previously been submitted for a degree or any other qualification at this University or any other institution, this has been clearly stated;
- where I have consulted the published work of others, this is always clearly attributed;
- where I have quoted from the work of others, the source is always given. With the exception of such quotations, this thesis is entirely my own work;
- I have acknowledged all main sources of help;
- where the thesis is based on work done by myself jointly with others, I have made clear exactly what was done by others and what I have contributed myself;

Parts of this work have been published in the following publications (as indicated in the relevant chapters):

- L. G. Carpenter, C. Holmes, H. L. Rogers, P. G. R. Smith, and J. C. Gates, "Integrated optic glass microcantilevers with Bragg grating interrogation," Optics Express **18**, 23296–23301 (2010).
- L. G. Carpenter, C. Holmes, B. D. Snow, J. C. Gates, and P. G. R. Smith, "Photonic Microcantilevers With Interferometric Bragg Grating Interrogation," IEEE Photonics Journal **4**, 1387–1395 (2012).

- L. G. Carpenter, H. L. Rogers, Peter A. Cooper, C. Holmes, J. C. Gates and P. G. R. Smith, “Low optical-loss facet preparation for silica-on-silicon photonics using the ductile dicing regime,” Journal of Physics D: Applied Physics, awaiting type setting.

In addition this work has been presented at conferences, a full bibliography is found in Appendix A.

Signed: ……..

Date: **18th October 2013**

Acknowledgements

There are many people to whom thanks are due for their help throughout the course of my Ph.D.

Firstly, I would like to thank my supervisors, Dr. James Gates and Prof. Peter Smith, for their combined guidance and support. Especially, with the written word, spelling and grammar! I would also like to thank them for allowing me to chase my dreams even if they thought ill of it. Also, for being great people to work with and some of the best teachers I have ever had.

I am extremely grateful to all the members of my research group, past and present. I would particularly like to mention the physical micromachining boys, Dr. Chris Holmes and Peter Cooper both of which helped with the common road blockages you have to pass, when building a machine from scratch. I would also like to mention Helen Rogers, for all her help with optics, her continued patience and baking. Notable members of old to thank are Ben Snow and Richard Parker, both for their general advice and bountiful amounts of sarcasm. Finally I would like to thank Sumi Ambran, Dominic Wales, Chaotan Sima, Paolo Mennea and Stephen Lynch for their kindness and conversation.

I would like to thank all the support staff at the Optoelectronics Research Centre, who maintain its world-class facilities. A particular thanks must be made to Edwin Weatherby for the construction of the precision micromills safety enclosure and Trevor Austin's support with the machines interlock electronics. Thanks must also be given to Mark Lessey and Paul Allwood, who both supported me in the workshop.

I would also like to thank my parents, family and friends for their continued support and encouragement. Finally, I would like to thank my gorgeous and intelligent girlfriend, Katrina Morgan, for taking the brunt of my sulking and grumpiness; and for agreeing to the epic task of reading the first draft of this work with all its dyslexic oddities.

THANK YOU ALL!

Notation

AFM	Atomic Force Microscopy
AOM	Acousto-Optic Modulator
ASE	Amplified Spontaneous Emission
AWG	Arrayed Waveguide Grating
CAM	Computer-Aided Manufacturing
CCD	Charge-Coupled Device
CNC	Computer Numerical Control
CMT	Coupled Mode Theory
DNA	Deoxyribonucleic acid
EM	Electromagnetic
FDM	Finite Difference Method
FEM	Finite Element Method
FHD	Flame Hydrolysis Deposition
GGG	Gadolinium Gallium Garnet
GPIB	General Purpose Interface Bus
HF	Hydrofluoric Acid
IC	Integrated Circuits
IR	Infrared

KOH	Potassium Hydroxide
MEMS	Micro Electromechanical Systems
MOMS	Micro Optomechanical Systems
Nd:YAG	Neodymium: Yttrium Aluminium Garnet
NPL	National Physics Laboratory
OSA	Optical Spectrum Analyser
PCD	Polycrystalline Diamond
PECVD	Plasma Enhanced Chemical Vapour Deposition
PLC	Planar Lightwave Circuits
PM	Polarisation Maintaining
PMMA	Polymethylmethacrylate
PTFE	Polytetrafluoroethylene
RIE	Reactive Ion Etching
RIN	Relative Intensity Noise
SME	Small and Medium Enterprises
SMF	Single Mode Fibre
SLED	Superluminescent Diode
TE	Transverse Electric
TiAlN	Titanium Aluminium Nitride
TIR	Total Internal Reflection
TM	Transverse Magnetic
UV	Ultraviolet
WDM	Wavelength Division Multiplexing

"Oh let the sun beat down upon my face, stars to fill my dream.

I am a traveller of both time and space, to be where I have been.

To sit with elders of the gentle race, this world has seldom seen.

They talk of days for which they sit and wait and all will be revealed."

Led Zeppelin, Kashmir, 1975

1 Introduction

1.1 Motivation and aims

Silica (SiO_2) is one of the world's most ubiquitous optical materials. Silica is important in the production of fibre optics, integrated optics and bulk optics. This thesis is concerned with the machining of planar silica integrated optics. However, the precision machining techniques described here could also be utilised in the manufacture of both fibre and bulk optics.

Silica is widely used by researchers and by companies chosen for its low visible and near infrared absorptions, low thermal conductivity, high chemical resilience, good mechanical properties and low cost. In integrated optics silica is used in the fabrication of passive Planar Lightwave Circuits (PLC) [1], a notable commercial application is the Arrayed Waveguide Gratings (AWG) [2]. Silica is also used in many other areas such as rare earth doped lasers [3], optofluidics [4] [5], delay lines [6] and quantum information processing devices [7] [8].

PLC fabrication has borrowed much of the fabrication process from silicon based foundries for electronic Integrated Circuits (IC) [1]. These cleanroom techniques have the ability of making low loss waveguides for AWG production. To create low loss silica waveguides at 1550 nm they typically operate in the weakly guiding regime thus core thickness are ~5-6 μm. Also important to low loss operation, is the sidewall verticality and surface roughness, both of which interact with the mode and effect its propagation. The limit of these cleanroom IC fabrication techniques is reached when etching more than 5-6 μm, the typical core thickness of AWGs. When silica is etched on the tens of micron scale [1], these etching processes break down resulting in poor form and high surface roughness [9]. Cleanrooms are also

expensive to run financially and environmentally, making it difficult for small to medium sized enterprises (SME) to gain access and is especially expensive when producing devices in volumes of hundreds to thousands. From this discussion it can be seen that a gap exists in the fabrication technology for silica photonics, where features are on the tens of microns scale, demand accurate form and low surface roughness and ideally without the use of cleanroom facilities. This thesis proposes the use of physical micromachining via precision dicing and milling to overcome this technological gap.

When fabricating integrated optics, a set of machining requirements must be met to achieve a low loss interaction with light. The general requirements for machining integrated optic structures are centred on two concepts, form and surface roughness. Generally, form is the discrepancy in shape from the machined product to the designed product. Roughness can be thought of as the small-scale deviations that exist on top of the larger scale form deviations.

Physical micromachining refers to the removal of a material through an action that occurs between the material and a tool or particle. Physical micromachining, via grinding and polishing, has been used commercially for decades, in the planarization of wafers for the semiconductor industry (as carried out, for example, by using the products from Disco Corp.) and telescope mirrors (Zeeko Ltd.). Moreover, physical micromachining has also been used in the production of aspheric lenses by diamond turning (Moore Nanotechnology Systems). In this thesis it has been shown that these physical micromachining techniques can remove tens of microns of silica in an accurate and smooth fashion. A smooth, optical finish is achieved by working in the ductile machining regime resulting in chips of brittle material being removed via plastic deformation [10]. Within this thesis, precision dicing and milling are the physical micromachining techniques used in the creation of silica integrated optic features capable of low loss interaction with light.

1.1.1 Precision dicing

The dicing process can be likened to a precision circular saw and has primarily been developed in the semiconductor industry. Dicing as a process has been gathering more interest for the development of integrated optical devices in the past few years [11] [12]. One of the first examples of dicing being used in the production of

an integrated optic component, was by NGK Insulators Ltd., where precision dicing was used to machine periodically poled lithium niobate into a ridge waveguide [13] [14]. This type of structure was used to enhance nonlinear interaction by confining light in two dimensions. Similar ridge waveguides have also been diced in lithium niobate but with higher aspect ratios of 500:1 [11]. Very recently, Neodymium: Yttrium Aluminium Garnet (Nd:YAG) crystal waveguide lasers have been fabricated via dicing [12]. This is a considerable challenge as YAG is far harder than lithium niobate or silica, being 8 on the Mohs scale compared to 5 and 7, respectively. A silica based AWG has also been diced to create a spectrometer [15]. The diced groove was used as a microfluidic channel in conjunction with an AWG, to create a compact spectrometer to analyse the transmittance of liquids. All of these publications referenced above only provide qualitative description of the surfaces generated after dicing. SEM or microscope images are typically included. However, in order to understand the effects of dicing and to interpret the machining results in a comparable manner, quantitative analysis is needed. Within this thesis quantitative surface metrology is conducted, enabling the optimisation of the dicing procedure used to create low optical loss structures in silica. There is little in the literature on dicing silica for integrated optics thus it was pursued as a useful direction of research.

The precision dicing machine, used in this work, is a system that was originally designed to dice chips from wafers. It is shown in this thesis, in a similar way to grinding and diamond turning, that if the dicing parameters are set appropriately, the ductile cutting regime [10] can be accessed. By accessing this regime it was hoped that the creation of silica features, that were close to desired form and had nanoscale roughness, would be fulfilled. These smooth silica features would allow the creation of low loss input/output facets for free space coupling. This process would be based on dicing alone and would require no further polishing steps. This makes this process particularly interesting for the commercial sector where time and cost saving would be yielded by the removal of the labour intensive lapping and polishing steps, typically used in integrated optics. A secondary dicing aim was to calculate the optical loss caused by surface roughness as a result of dicing. Thus, experiments involving diced surfaces, waveguides and Bragg gratings were conducting, allowing an accurate loss to be experimentally measured. Examples of integrated devices that

benefitted from this research and that were produced within the research group are as follows: refractometer devices [16], single photon resolving detectors, corner mirrors [17], laser diode coupling and flat fibre multimode interference devices [18]. A tertiary aim of this study into dicing was to explore how dicing could be used to create microcantilever structures. By pairing the diced cantilever structures with embedded waveguide and Bragg grating structures, mechanical sensor fabrication was enabled. Bragg grating based interrogation, using single and interferometric systems, allowed monitoring of cantilever deflection in these structures.

1.1.2 Precision micromilling

The second physical micromachining technique studied in this thesis is precision micromilling. Precision micromilling, in our terminology, is a mill with high positional accuracy, repeatability and the ability to use micron scale bits. By accessing the ductile cutting regime for milling, silica and silicon have been slot milled on the micron scale with a smooth interface [19] [20] [21]. However, few photonic applications are presented in literature. A noteworthy structure was milled in Polymethylmethacrylate (PMMA) for optofluidic integration [22], however PMMA is far softer than silica and is thus easier to machine. An example of a milled silica device is a microfluidic system for DNA analysis [23]. This reference shows that precision micromilling, as a technique, could be useful in the production of features in silica for integrated optic applications. Therefore, precision micromilling for silica photonic applications is seen as an unexplored area and thus was researched within this thesis.

The dicing saw used for these experiments was a commercially available machine (Loadpoint MicroAce Series 3). To investigate precision micromilling, it was decided to construct a machine in-house, where the finished mill is shown in Figure 1.

Figure 1 in-house produced precision micromill.

The primary milling aim was simply to build a machine allowing three-dimensional machining in the ductile cutting regime of silica. Similarly to dicing, the secondary milling aim was to access the smooth features produced by the ductile cutting regime, through optimising the milling machining parameters. By optimising these milling parameters, the technique would enable the machining of silica features with nanoscale roughness and accurate form, with three-dimensional freedom. The tertiary milling aim was to investigate the reproducibility of the technique, where the process is repeated and the silica features are monitored allowing the degradation in form and surface quality to be monitored.

To summarise, the primary research aims of this thesis were to explore the suitability of precision dicing and milling to make low loss optical structures for silica integrated optics. These advances in the structuring of silica would be added to the Optoelectronics Research Centre's toolbox for processing silica and other optical materials.

As discussed earlier, it has been shown that there is a gap in the literature concerning the machining of silica on the tens of micron scale for integrated optic applications.

Physical micromachining via precision dicing and milling will fill this gap in the fabrication toolbox.

1.2 Synopsis

Chapter 2 begins by giving the specifications for machining silica for free space input/output couplers and waveguide components. This is followed by definitions of surface roughness and ways of measuring it. The state of the art, in silica machining is discussed, techniques include: wet/dry etching, laser machining, focused ion beam milling, grinding, dicing, diamond turning and micromilling. The background theory of waveguides and Bragg gratings is covered in chapter 3. Chapter 3 also describes the fabrication of the silica-on-silicon substrate and the creation of waveguides and Bragg gratings via direct UV writing. In chapter 4, the precision dicing machining is discussed; the optimisation of machining to create smooth silica surfaces is also covered. The optimised dicing parameters are used to create a groove intersecting a waveguide and Bragg gratings, thus allowing the loss contributed by surface roughness to be calculated. Dicing is then utilised in chapter 5 to produce microcantilever structures. These mechanical structures are combined with waveguides and Bragg gratings to produce miniature physical sensors. Single Bragg gratings detection is used to measure air pressure. A Bragg grating based interferometric interrogation is also used to measure cantilever deflection. Chapter 5 ends with a comparison between the two interrogations methods, with comments made on spectral sharpness, minimum resolvable force and sensitivity. In chapter 6 the construction of the precision milling machine is detailed. The optimisation of the milling procedure is also included whereby machining parameters are tailored to obtain smooth, ductile machined surfaces. Utilising the optimised milling procedure, the surface quality is investigated and the effect of mill wear on it is commented on.

References

1. M. R. Poulsen, P. I. Borel, J. Fage-Pedersen, J. Hübner, M. Kristensen, J. H. Povlsen, K. Rottwitt, M. Svalgaard, and W. Svendsen, "Advances in silica-based integrated optics," Optical Engineering **42**, 2821–2834 (2003).

2. C. R. Doerr and K. Okamoto, "Advances in Silica Planar Lightwave Circuits," Journal of Lightwave Technology **24**, 4763–4789 (2006).

3. D. A. Guilhot, G. D. Emmerson, C. B. Gawith, S. P. Watts, D. P. Shepherd, R. B. Williams, and P. G. Smith, "Single-mode direct-ultraviolet-written channel waveguide laser in neodymium-doped silica on silicon.," Optics Letters **29**, 947–949 (2004).

4. H. Schmidt and A. R. Hawkins, "The photonic integration of non-solid media using optofluidics," Nature Photonics **5**, 598–604 (2011).

5. R. M. Parker, J. C. Gates, D. J. Wales, P. G. R. Smith, and M. C. Grossel, "An investigation into dispersion upon switching between solvents within a microfluidic system using a chemically resistant integrated optical refractive index sensor.," Lab on a Chip **13**, 377–385 (2013).

6. H. Lee, T. Chen, J. Li, O. Painter, and K. J. Vahala, "Ultra-low-loss optical delay line on a silicon chip," Nature Communications **3**, 867 (2012).

7. A. Politi, M. J. Cryan, J. G. Rarity, S. Yu, and J. L. O'Brien, "Silica-on-Silicon Waveguide Quantum Circuits," Science (New York, N.Y.) **320**, 646–649 (2008).

8. J. B. Spring, B. J. Metcalf, P. C. Humphreys, W. S. Kolthammer, X.-M. Jin, M. Barbieri, A. Datta, N. Thomas-Peter, N. K. Langford, D. Kundys, J. C. Gates, B. J. Smith, P. G. R. Smith, and I. A. Walmsley, "Boson Sampling on a Photonic Chip.," Science (New York, N.Y.) **339**, 798–801 (2013).

9. Z. Sheng, B. Yang, L. Yang, J. Hu, D. Dai, and S. He, "Experimental Demonstration of Deeply-Etched SiO2 Ridge Optical Waveguides and Devices," IEEE Journal of Quantum Electronics **46**, 28–34 (2010).

10. T. G. Bifano, T. Dow, and R. O. Scattergood, "Ductile-regime grinding: a new technology for machining brittle materials," Journal of Engineering for Industry (Transactions of the ASME) **113**, 184–189 (1991).

11. N. Courjal, B. Guichardaz, G. Ulliac, J.-Y. Rauch, B. Sadani, H.-H. Lu, and M.-P. Bernal, "High aspect ratio lithium niobate ridge waveguides fabricated

by optical grade dicing," Journal of Physics D: Applied Physics **44**, 305101 (2011).

12. Y. Jia, C. E. Rüter, S. Akhmadaliev, S. Zhou, F. Chen, and D. Kip, "Ridge waveguide lasers in Nd:YAG crystals produced by combining swift heavy ion irradiation and precise diamond blade dicing," Optical Materials Express **3**, 433–438 (2013).

13. K. Mizuuchi, T. Sugita, K. Yamamoto, T. Kawaguchi, T. Yoshino, and M. Imaeda, "Efficient 340-nm light generation by a ridge-type waveguide in a first-order periodically poled MgO:LiNbO3," Optics Letters **28**, 1344–1346 (2003).

14. S. Kurimura, Y. Kato, M. Maruyama, Y. Usui, and H. Nakajima, "Quasi-phase-matched adhered ridge waveguide in LiNbO3," Applied Physics Letters **89**, 191123 (2006).

15. G. W. Fynn and W. J. A. Powell, *Cutting and Polishing Optical and Electronic Materials*, 2nd ed. (Institute of Physics Publishing Inc., 1988), pp. 2–3.

16. C. Holmes, L. G. Carpenter, H. L. Rogers, I. J. G. Sparrow, J. C. Gates, and P. G. R. Smith, "Planar waveguide tilted Bragg grating refractometer fabricated through physical micromachining and direct UV writing.," Optics Express **19**, 12462–8 (2011).

17. L. G. Carpenter, P. L. Mennea, H. L. Rogers, C. Holmes, J. C. Gates, and P. G. R. Smith, "Integrated corner mirrors as a platform for miniaturized planar strain sensing," European Conference on Integrated Optics (ECIO) Sitges Barcelona 18-20 April 2012 1–2 (2012).

18. S. Ambran, C. Holmes, J. C. Gates, A. S. Webb, L. G. Carpenter, F. R. M. Adikan, P. G. R. Smith, and J. K. Sahu, "Fabrication of a Multimode Interference Device in a Low-Loss Flat-Fiber Platform Using Physical Micromachining Technique," Journal of Lightwave Technology **30**, 2870–2875 (2012).

19. M. Arif, M. Rahman, and W. Y. San, "Ultraprecision ductile mode machining of glass by micromilling process," Journal of Manufacturing Processes **13**, 50–59 (2011).

20. K. Foy, Z. Wei, T. Matsumura, and Y. Huang, "Effect of tilt angle on cutting regime transition in glass micromilling," International Journal of Machine Tools and Manufacture **49**, 315–324 (2009).

21. T. J. Ko and H. S. Kim, "Micro-end-milling of single-crystal silicon," International Journal of Machine Tools and Manufacture **47**, 2111–2119 (2007).

22. D. Snakenborg, G. Perozziello, H. Klank, O. Geschke, and J. P. Kutter, "Direct milling and casting of polymer-based optical waveguides for improved transparency in the visible range," Journal of Micromechanics and Microengineering **16**, 375–381 (2006).

23. R. J. Townsend, N. R. Harris, D. Wenn, D. Brennan, and N. J. Grabham, "Design and construction of a micromilled fluidic device as part of a DNA biosensor," Proceedings of the Institution of Mechanical Engineers, Part C: Journal of Mechanical Engineering Science **222**, 847–853 (2008).

2 Machining Silica for Photonics

2.1 Introduction

This chapter introduces the general requirements for machining input/output facets and for fabricating waveguide components for silica integrated optics. These general requirements include features being created in the tens of micron scale, that are flat, smooth and chip free. Surface smoothness can be measured quantitatively through the metric of surface roughness. The chapter therefore explains what surface roughness is and the way in which it is quantified. This is followed by how surface topography as a whole, including surface roughness, can be collected by the following techniques: white light interferometry, profilometry and atomic force microscopy. These are explained and their resolutions compared.

Fabrication techniques that are capable of achieving some or all of the requirements for silica input/output coupling and waveguide components are discussed. These include photolithography, wet and dry etching, laser machining and focused ion beam milling. Further fabrication techniques, which physically machine substrates with tools or particles, such as lapping, chemical mechanical polishing, grinding, diamond turning, dicing and milling are also discussed. This is followed by elaborating on the process of ductile cutting, used in physical machining to create flat, smooth and chip free features.

2.2 Machining requirements for integrated optics

In this section the general requirements for machining photonic components will be introduced, starting with the machining for free space input/output facets for waveguides, followed by the machining for waveguide components.

2.2.1 Requirements for machining input/output facets

The general requirements for free space input/output facets in integrated optics are high verticality, nanoscale roughness and low surface chipping. The importance of these three requirements is highlighted below in Figure 1, where an example of deviation from the specification for facets is shown.

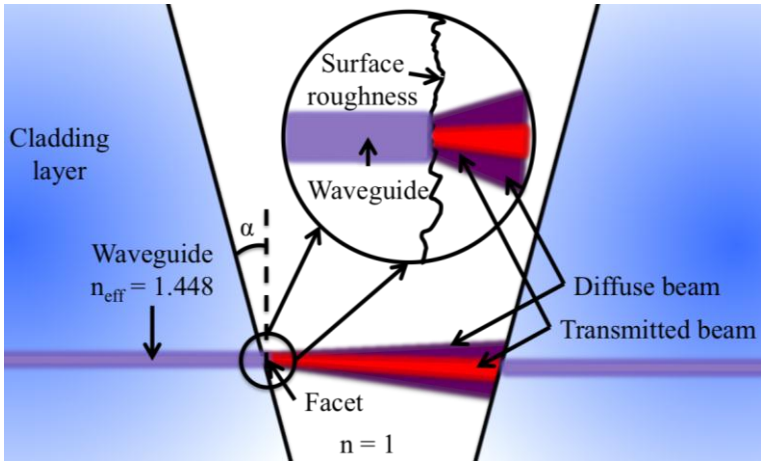

Figure 2 side view of facet for free space input/output coupling with loss mechanisms, showing an angular deviation from vertical (α) and facet surface roughness and chipping, all of which contribute to free space coupling loss.

High verticality is an important form requirement of an input/output facet. If a facet strays from being parallel to the waveguide then light propagates in the wrong direction, making coupling less efficient and bonding potentially more challenging. Chapter 4 shows that angular deviation from vertical can be related to Snell's law and a transverse misalignment. A strong relationship can be seen to exist between the angular deviation from vertical and the incurred loss, thus showing the importance and desirability of verticality [1]. For an angular deviation of ~4.5° from vertical and the light propagating over a 15 μm gap, a loss of ~0.1 dB is seen. The second

requirement mentioned previously for free space input/output facets in integrated optics is nanoscale roughness. To understand how surface roughness affects the coupling loss of facets the scalar scattering theory can be consulted. Scalar scattering theory tells us that the amount of light scattered at a facet, with surface roughness, can be related to RMS surface roughness (Sq). The scattered beam reflects in random directions and is thus seen as loss within a system. The scalar scattering theory shows that a reduction in surface roughness greatly reduces scattered light and thus smooth surfaces are desired [2] [3]. Gharbia *et al.* also shows that a reduction in facet surface roughness increases coupling efficiency, in ground facets of silica single mode fibres [4]. Elaborating on this work, it is shown in chapter 4, that for 633 nm light a surface roughness (Ra) of ~2.3 nm causes a coupling loss of ~1 dB. The third requirement is low surface chipping. Chipping, depending on how and where it forms on the facet, can act as a combination of both form error and surface roughness and thus must be avoided.

The important factors in terms of vertically, surface roughness and chipping for machining interfaces with low optical losses have been introduced. This subject is elaborated on in chapter 4, where precision dicing is used to create vertical, smooth, chip free facets for silica waveguide free space input/output coupling. The requirements for machining components, which interact with waveguides for low loss operation, is introduced next.

2.2.2 Requirements for machining waveguide components

Waveguide components, such as grooves, interact directly with the waveguide and typically with the evanescent field. These grooves can be utilised to create integrated devices such as polarisers, plasmon devices and chemical/biological sensors. The general requirements for grooves that interact with waveguides, for evanescent field access, are high controlled form (cladding offset), nanoscale roughness and low surface chipping, each affecting loss mechanisms of the waveguide structure. The importance of these three requirements is highlighted in Figure 3, where an example of deviation from the specification for waveguide components is shown.

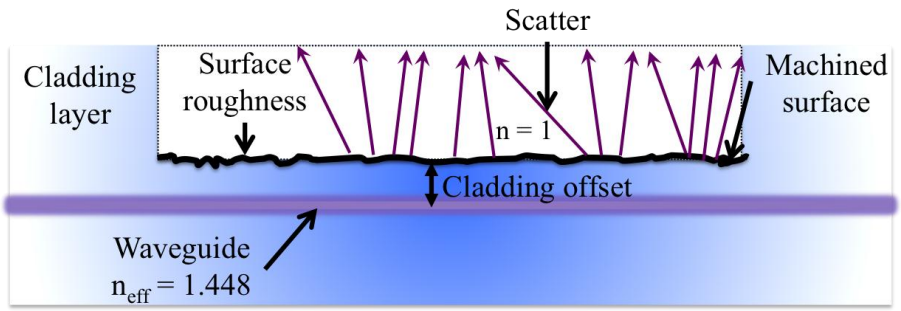

Figure 3 side view of a groove interacting with a waveguide where loss mechanisms are present, including variations of cladding offset with respect to the waveguide, surface roughness and chipping,

The operation of devices using evanescent field interactions can be severely effected if the machined grooves of the device have a cladding offset (see Figure 3). The cladding offset is defined here as the distance, typically on the micron scale, of the machined surface with respect to the waveguide. As shown with metal polarisers [5] [6], the dependence of the interaction distance between the metal and waveguide is crucial to its operation. Even hundreds of nanometres change in thickness between the metal and waveguide, changes polarisation attenuation by hundreds of dB/cm. Thus, groove form and flatness variations are critical to the performance of evanescent field devices.

Another loss mechanism that must be taken into consideration, along with flatness, is surface roughness. Surface roughness affects waveguides and structures machined in them, by causing propagation loss via scattering. The Payne and Lacey model [7] explains propagation loss as a consequence of surface roughness. The model includes factors such as the statistics of the roughness by including a function related to the correlation length of the surface roughness. Here the correlation length is defined as similar but not equal to the average surface wavelength [8]. The Payne and Lacey model also includes key parameters of the waveguide, such as dimensions and refractive indices. The model indicates that by reducing surface roughness, the amount of scatter is also reduced and thus lowers the propagation loss; hence smooth bottom grooves or sidewalls are desired. This model is discussed in more detail in chapter 6.

The third loss mechanism is surface chipping. Chipping, again, depending on how and where it forms on the groove, can act as a combination of form error, effecting

flatness, and surface roughness. These both contribute to propagation loss and thus chipping is undesirable.

These loss mechanisms are further elaborated on in chapter 6, where precision milling is used to create grooves in silica, which have a consistent depth, are flat, smooth and chip free. The requirements for machining components, which interact with waveguides for low loss operation have been introduced. As can be seen in this and the previous section, surface roughness is a requirement for both low loss coupling and waveguide interaction. Techniques used to quantify and measure surface roughness are commented on in the next section.

2.3 Metrology

2.3.1 Surface roughness definitions

Characterising the surface roughness of samples can be achieved in a variety of ways for example: interferometry, profilometry, scattering and atomic force microscopy. Popular statistics in literature used to quantify surface roughness are Ra, which is the average roughness and Rq, the root mean squared roughness, which are both 2D amplitude parameters. Ra is often used when describing machined surfaces and is by far the most popular parameter used in the literate. Rq is useful because it is the quantity used in both the scalar scattering theory and in the Payne-Lacey model, relating surface roughness to optical loss as introduced in section 2.2. All of the surface roughness parameters shown in this section are shown in their practical discrete forms.

Both Ra and Rq are defined from the mean surface level. For a surface, the mean will have equal areas above and below it, with the height being measured perpendicularly from the surface, see Figure 4. The mean will equal [8],

$$\bar{z} = \frac{1}{N}\sum_{i=1}^{N} z_i \qquad \textbf{Equation 1}$$

where N is discrete equal spaced points measured along a line (L, see Figure 4) at which the deviation from the mean is z_i. The Ra is the mean average of the absolute values of the surface heights z_i and is given by [8],

$$\mathrm{Ra} = \frac{1}{\mathrm{N}}\sum_{\mathrm{i}=1}^{\mathrm{N}} |\mathrm{z_i} - \bar{\mathrm{z}}|. \qquad \textbf{Equation 2}$$

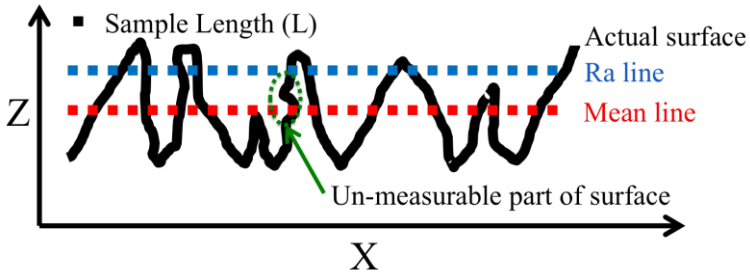

Figure 4 a schematic example of a real surface, with a mean line and 2D average surface roughness (Ra) approximately calculated. Notice the mean line has as the same quantity of area below it and above. Like any real surface there are features here that surface profilers will be unable to resolve, *i.e.* the overhung part.

Figure 4 depicts the diagrammatic calculation of Ra. Rq, the rms surface roughness, is given by [8],

$$\mathrm{Rq} = \sqrt{\frac{1}{N}\sum_{i=1}^{N} (\mathrm{z_i} - \bar{\mathrm{z}})^2} \qquad \textbf{Equation 3}$$

When calculating both Ra and Rq, the length of the surface data collected limits the largest possible spatial wavelength of the surface. Consequently, the convolution of the sampling length (L), from Figure 4, and the spatial resolution of the measurement tool, discussed in section 2.3.5, will affect the minimum and maximum resolvable spatial wavelength. If a surface does not have any large deviations, Ra and Rq will be numerically close. If a surface has a large number of holes and bumps Rq will be numerically larger than Ra.

Both Ra and Rq are 2D surface parameters whereas surface scanning techniques, such as white light interferometry, profilometer and atomic force microscopy, typically give data in 3D. These 3D parameters are termed ‘Areal’ and are denoted by a ‘S’ rather than ‘R’ [8]. Thus the 3D average surface roughness, Sa, is given by the following equation [9],

$$\mathrm{Sa} = \frac{1}{MN}\sum_{j=1}^{N}\sum_{i=1}^{M}\left|z_{i,j}\right| \qquad \textbf{Equation 4}$$

where M and N are discrete equal spaced points measured along a perpendicular line (*i.e.* the sampling length, L) at which the deviation from the mean is $z_{i,j}$. The Sa is the mean average of the absolute values of the surface heights $z_{i,j}$. Equation 4 is an international standard and has been given the following designation ISO/DIS 25178-2. Notice the subtraction of the mean is not present as software surface levelling takes this into account.

Surface levelling has to be applied before any of the amplitude surface roughness parameters are taken. The commercially available software Image Metrology, SPIP, was used extensively throughout this thesis, and advised using polynomial levelling before taken surface roughness parameters [9]. Polynomial levelling was used throughout, to correct for slope from sample mounting and aberrations from the surface scanning techniques. The polynomial levelling was based on the optimisation of the least mean square of the heights for the entire image, where the coefficients are found by minimising the square sum error. The corrected image is found by subtracting the plane. It must be noted that by using levelling, the minimum resolvable spatial wavelength is changed, as the levelling process typically removes larger wavelengths. After this, the surface roughness was taken. In the next section the white light interferometer, the most utilised surface scanning technique in the thesis, is elaborated on.

2.3.2 White light interferometer

White light interferometry sometimes called coherence scanning interferometry, is an optical non-contact surface profiling technique. This surface profiling technique was used extensively throughout the thesis, where the machine used was a Zemetrics, ZeScope. The basic operational principles are explained below and follows the National Physics Laboratory (NPL) guide [10]. The operational principles, shown in Figure 5, of a white light interferometer starts with a white light source (in the case of the ZeScope this is blue light from a light emitting diode), reflecting off the upper beam splitter. The light is collected by the objective lens and focused. The light is then split by the secondary beam splitter in the objective, and sent to a reference mirror, in the objective and to the surface. The light from the

sample surface and reference mirror recombines by the objectives beam splitter and is focused onto charge-coupled device (CCD).

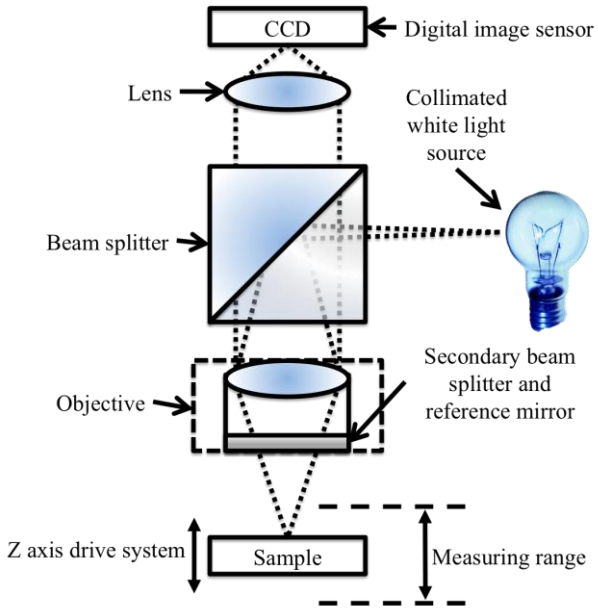

Figure 5 a typical white light interferometer, which utilises a short coherence light source and a z axis scan to obtain interference between the sample surface and reference mirror within the objective. Multipixel interferogram fitting is then used to extract the sample surface data.

The white light source has a short coherence length, unlike a laser, thus the path length between the sample surface and reference mirror must be near identical to yield interference. The coherence length (l_c) of a light source can be found by, $l_c = \lambda^2/\Delta\lambda$ [1]. If the light emitting diode operates at a wavelength (λ) 445 nm, with a full width half max spectral bandwidth ($\Delta\lambda$) of ~24 nm [11], the coherence length (l_c) would be ~8 µm. The temporal coherence is related to the coherence length, and is a measure of how well the light will interfere with itself, from one instance to the next. The types of interferometric objectives present on the ZeScope are Michelson and Mirau interferometer lenses. The 5x objective is a Michelson type lens and the 10x and 50x objectives are Mirau type lenses, see Figure 6 and Figure 7.

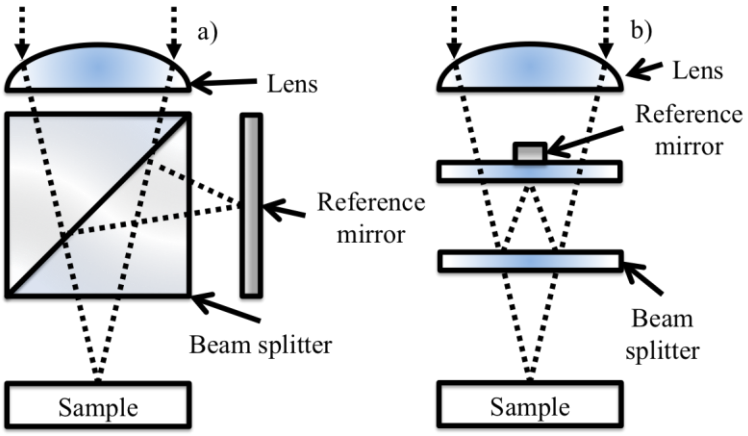

Figure 6 a) Michelson interferometer objective arrangement, b) Mirau interferometer objective arrangement. The size and positioning of the reference mirror within the Mirau is the reason for its stability and larger price when compared to the Michelson objective.

Both Michelson and Mirau interferometers use Michelson type interference but Mirau interferometers are mechanically more stable but are more expensive to produce and purchase. The ZeScope also has two extra lens in the optical path which can be used with each of the objectives to increase or decrease magnification. The objectives can achieve the following magnifications: 3.125x and 10x using the 5x objective, 6.25x and 20x using the 10x objective and 31.25x and 100x using the 50x objective. Figure 7 shows an image of the Zemetrics, ZeScope along with the three objectives.

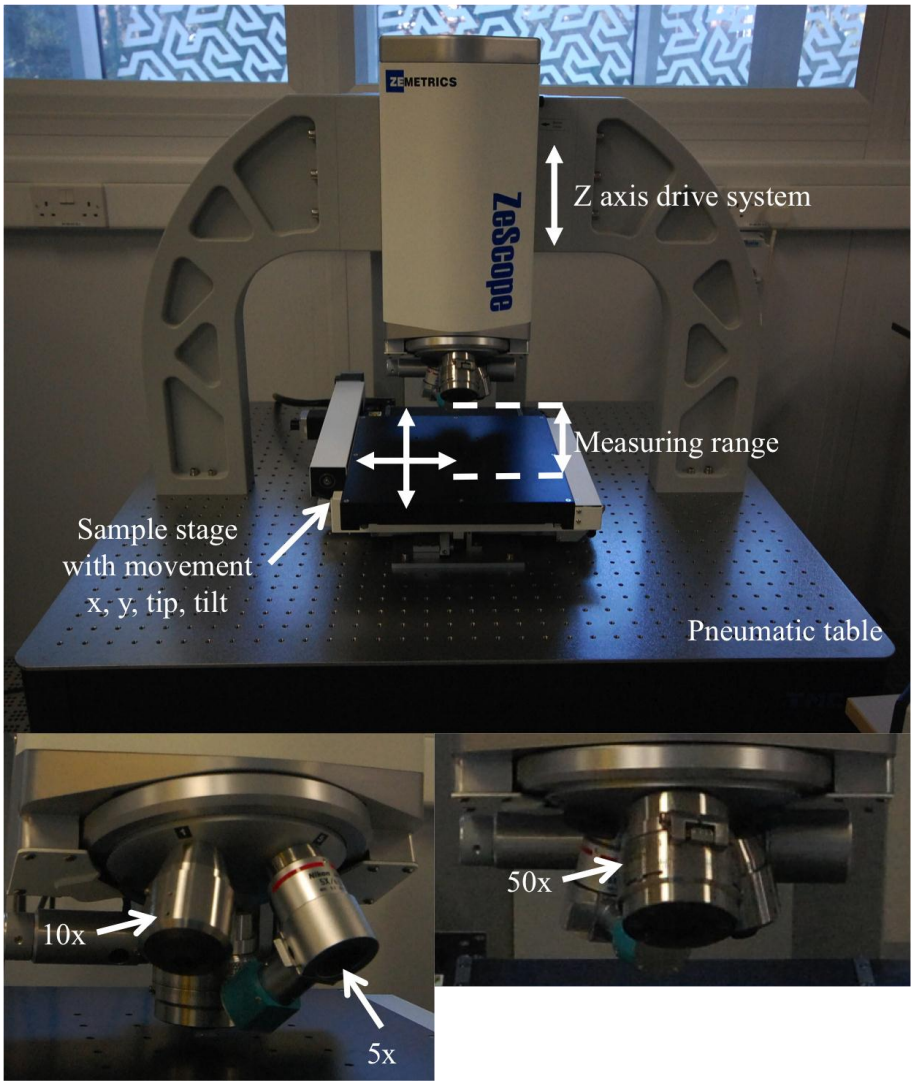

Figure 7 the Zemetrics, ZeScope, white light interferometer used through this thesis. Notice the large sample bed and long scanning range of the z axis making it particularly useful for a wide range of sample sizes. The three objectives with 5x, 10x and 50x magnifications are also shown.

The Zemetrics, ZeScope sample stage can also be seen in Figure 7. The sample stage has a large range of movement and can move 200 mm in both x and y axis and 180 mm in z axis [12]. Once the light reaches the CCD (1.3 mega pixels [12]), the intensity at each pixel is recorded relative to the z position of the objective. This creates an intensity profile *versus* the z axis position, for each pixel, thus making an image of the surface. A line of pixels in the x axis is shown with an intensity variation and sample profile, in Figure 8.

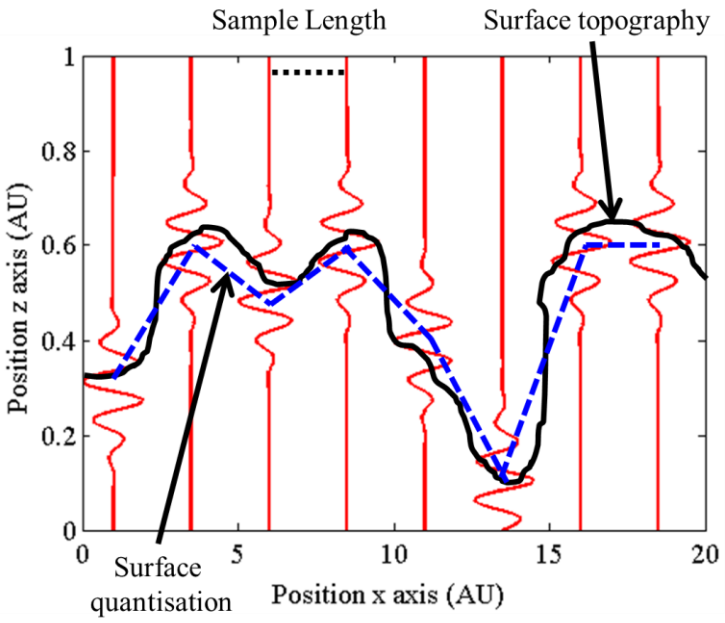

Figure 8 a schematic of the operational principle of white light interferometer, intensity modulation of light (red) when interference occurs between the surface (black) and reference mirror. The quantisation of the surface (blue) caused by the lens's diffraction limit, is also shown.

Figure 8 shows instances of interference for specific z axis positions in light intensity (red) when the optical path lengths are similar between the sample surface (black) and reference mirror in the objective (see Figure 5 and Figure 6). A Gaussian envelope function is fitted to each instances of interference, where the position of the Gaussian peak gives the position of the sample height, allowing a 3D surface height map to be constructed, using the pixel array. The white light source has a short coherence length compared to that of a laser giving two advantages as the light source. Firstly, fitting the envelope function becomes simpler because there are fewer fringes to fit over. Secondly, the z axis has to move a smaller distance, microns compared to meters, to create a full interference comb, thus positional uncertainty from the mechanical movement is reduced. The quantisation of the surface (blue) stems from the diffraction limit of the lens. The ZeScope has a RMS resolution 0.1 nm and a RMS repeatability of 0.01 nm for z axis (height) measurements [12], the lateral resolution is discussed in section 2.3.5. The physical principles and operation of a white light interferometer have been explained. Profilometry is another metrology tool and is discussed in the next section.

2.3.3 Profilometer

The profilometer, sometimes called a surface profiler or stylus profiler, was used to actuate microcantilevers in chapter 5. The profilometer used within this work is KLA-Tencor, P-16 with a Microhead 5 SR probe head. The stylus profilometer is a contact method, a diagram is shown in Figure 9 [13].

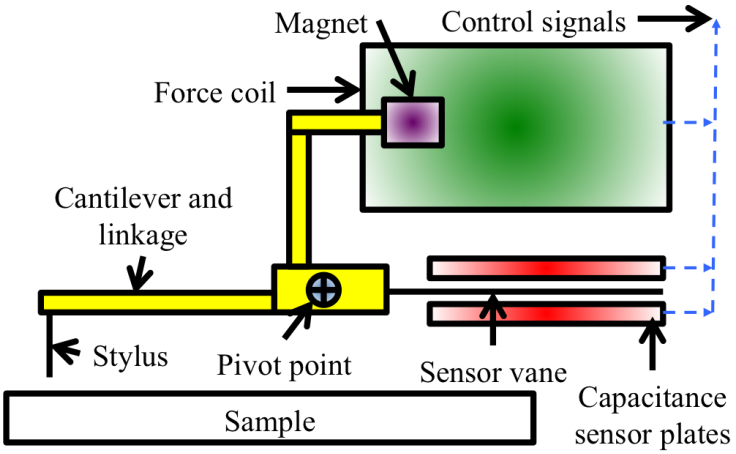

Figure 9 KLA-Tencor, P-16 profilometer, which scans a diamond point across the sample surface with a constant force, in a similar fashion to a record player, obtaining the sample's surface metrology.

Figure 9 shows a KLA-Tencor, P-16 profilometer. As it can be seen this profiler is based on electrostatics to detect deflection, but there are other types based on the piezoelectric effect, magnetostatics and optical methods. This profilometer uses a diamond stylus to traverse samples, where it is kept in contact with the sample surface by electromagnetic force compensation via a magnet and induction coil. A capacitive sensor gives feedback signals to the force coil and profile data. The stylus, sensor vane and magnet are all mechanically connected together via a cantilever arrangement. The diamond stylus has a radius of 2 µm and the sample is moved on an x, y, z and rotation axes. The sample stage can move 200 mm in both the x and y axes, whereas it has a very short z axis scan range of 327 µm when compared to the ZeScope. The P-16 has a RMS resolution 0.02 nm and a RMS repeatability of 0.6 nm for z axis (height) measurements [13], where the lateral resolution is discussed in section 2.3.5. It must be noted these are the manufacture's values for resolution and repeatability and have never been achieved in practice (by the author) and noise of 3-5 nm is typically seen on height data. This noise is likely caused by the

profilometer's location, which is in the cleanroom where noise from pumps and air currents, cause unwanted vibration.

The operation of a profilometer has been explained. Continuing with contact surface profiling techniques, atomic force microscopy is discussed next.

2.3.4 Atomic force microscope

The Atomic Force Microscope (AFM) was used to verify surface metrology results of a precision milled groove in chapter 6. The AFM used in this work is a Veeco Caliber in a tapping mode. The AFM is another contact profiling method but is far more sensitive to surface variation than the previously discussed profilometer. A diagram of an AFM shown in Figure 10 [14].

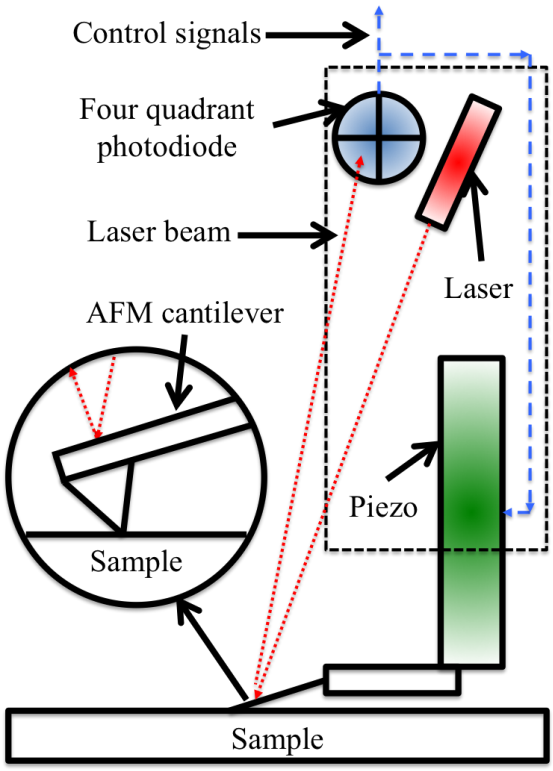

Figure 10 a typical atomic force microscope. A tip, which is sharp on the nanometre scale, is scanned across the surface. The tip floats fractions of nanometre away from the surface because of van der Waals surface interactions. The deflection of the cantilever is detected by reflecting a laser and steering it into a four quadrant photodiode. The tip is kept at a constant height from the surface by feedback sent from the photodiode to the piezo.

Atomic force microscopy works because of the forces developed between a sharp point (tip on the cantilever) and a surface. In tapping mode AFM, or 'AC' AFM, the

tip is oscillated and comes in and out of contact with the surface. The contact force of this technique is far lower than that of the profilometer so much so that van der Waals forces are detected and used as height feedback. These forces can allow the AFM tip to hover just fractions of a nanometre away from the sample surface. By collecting the deflection information of the cantilever, and scanning the sample in the x and y axes, a force map of the sample surface can be created and thus the surface profile can be extracted.

The operation of an AFM is based on the detection of deflection of the AFM cantilever caused by the forces from the surface. AFM cantilever deflection is detected by reflecting a laser off the cantilever tip to a four quadrant photodiode set a distance away, so the minute deflections of the tip cause larger movements in the reflected laser beam. The piezo stack oscillates the cantilever vertically and also scans the cantilever in x and y axes, where the vertical oscillation frequency is used in the phase sensitive detection. A lock-in detection method is used to extract the phase and amplitude of a modulated laser signal and is used as feedback to the piezoelectric transducer to maintain constant height above the sample. This height information produces a height map of the surface. The standard cantilever tip size used within this thesis was ~8 nm, with a maximum size of 12 nm. The Veeco, Caliber scanning range is 90 μm in the x and y axis and has a z axis scan range of 10 μm, which is the smallest scanning range of all of the techniques mentioned in this section. The Caliber has a resolution 0.15 nm (1kHz bandwidth) in tapping mode for z axis (height) measurements [15]. The lateral resolution is discussed in section 2.3.5.

The principles of operation of an AFM have been explained, along with white light interferometry and profilometry. The spatial resolution of each surface profiling technique is again discussed in the next section.

2.3.5 Lateral spatial resolution

The z axis (height) resolution of each profiling technique has been discussed in the subsequent sections however lateral spatial resolution has been overlooked for a more complete discussion in this section. The lateral spatial resolution indicates the resolution in the plane of scanning, the x and y axes. The better the vertical and lateral resolution a profiling tool has, the more accurate determination of surface

roughness can be made. A schematic is given in Figure 11 of the spatial frequencies that each scanning technique is sensitive to.

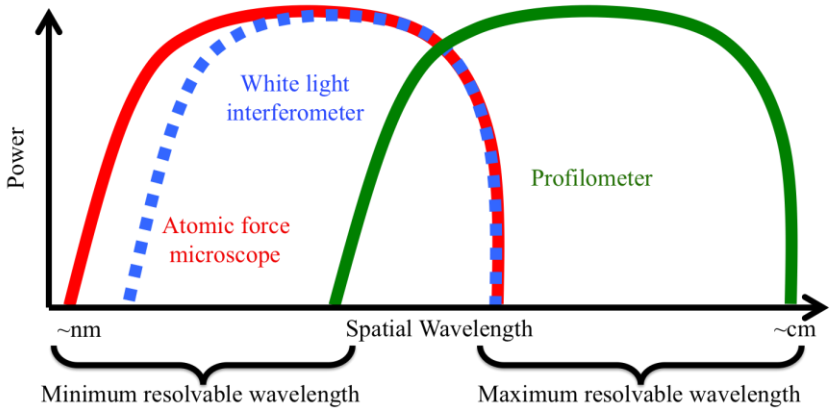

Figure 11 schematic showing the spatial resolution of each surface profiling technique.

The sketched power spectral density curves in Figure 11 shows the maximum and minimum resolvable spatial frequency in the plane of scan (x and y axes) for the three tools described in this section; white light interferometry, stylus profilometry and AFM. The largest resolvable spatial frequencies each system can detect, is dictated by the scan length. The scan length of each technique is limited to the length of the sample it can traverse over. The P-16, profilometer can scan over 200 mm so can see the largest spatial wavelengths, while the ZeScope, white light interferometer at 100x magnification has a 90 µm by 70 µm scan area, which is similar to the Calibre AFM, which has a scan area of 90 µm by 90 µm. Although the ZeScope's magnification can be reduced to increase the field of view, the increase in the acquisition of longer spatial wavelengths also means a reduction in the numerical aperture of the objective occurs, causing a reduction in lateral resolution. Thus the P-16 is limited to spatial wavelength of ~100 mm, while the ZeScope and Calibre is limited to spatial wavelength of ~45 µm.

The smallest resolvable spatial wavelength of each surface scanning technique is limited by the process used to interact with the surface. For the stylus methods, the profilometer and the AFM, the smallest resolvable spatial wavelength is limited by the radii of the tips. While for the white light interferometer, the spatial wavelength is limited by the diffraction limit of the objective. These limiting factors act to spatially filter the surface, thus there is always a convolution between the topography of the surface and the instrument being used to measure that surface, *i.e.* an etched

ridge and a surface profiler tip. The tip radius of the diamond used on the P-16 profilometer stylus was 2 µm thus a diameter of 4 µm. The Calibre AFM used a silicon cantilever with a tip of ~8 nm. The ZeScope has lateral resolution of 500 nm determined by the diffraction limit of 50x objective used, in 100x mode. The large spatial filtering of the profilometer (4 µm) made it unsuitable to measure surface roughness however the white light interferometer (500 nm) and AFM (8 nm) have relatively small amounts of filtering. The majority of surface metrology data collected in chapters 4 and 6 used the ZeScope, white light interferometer. This method was used; primarily because of the speed of acquisition compared to that of an AFM for the 90 µm by 90 µm scan areas. The ZeScope would generally take less than a minute to perform such a scan, while the Calibre would take approximately an hour. Studies have shown that white light interferometers typically overestimated surface roughness, which is attributed to multiple scattering [16], when compared to profiling techniques, which has also been confirmed by the author. However, the ZeScope was used to conduct a comparative study of surface roughnesses and was primarily used throughout the thesis for machining parameter optimisation.

Within this section surface roughness parameters have been defined and discussed along with three of the surface metrology techniques used throughout the thesis. Using the defined terms throughout this section, other silica fabrication routes can now be discussed. The next section contains a literature review of other fabrication routes for silica photonics, which can produce silica features on the tens of micron scale with high verticality, nanoscale roughness and minimum chipping. These state of the art fabrication routes are the main competitors to precision dicing and milling, which are studied in chapters 4 and 6.

2.4 Other silica fabrication routes

Silica is an important material in a whole host of photonic and optical applications. Silica, however, suffers a lack of machining techniques specifically suited to producing tens of micron features with high verticality, nanoscale roughness and minimum chipping for photonic applications. The next section provides an overview

of currently available fabrication methods used to machine silica. Comments have been made on the depth of machining, form, surface roughness and amounts of chipping and pitting; as was set as requirements, in section 2.2, for machining facets and waveguide components. As silica is one of photonics materials of choice there are a plethora of fabrication techniques, each with its particular advantages and disadvantages. The techniques discussed here are photolithography and etching, laser machining and focused ion beam milling. The first to be covered is photolithography and etching.

2.4.1 Photolithography and etching

The use of a masks and etching for the creation of integrated electronic circuits was pioneered by Robert Norton Noyce and Jack Kilby in 1959 [17]. These photolithographic techniques have become the fabrication backbone of electronics and MEMS, to create the mass produced consumer products which we all enjoy today. Integrated optics has borrowed heavily from photolithographic electronic fabrication and is the standard technique for making Planar Lightwave Circuits (PLC) in silica. It also should be mentioned that laser diodes and photonic chips using materials such as InP and GaAs both heavily rely on these techniques.

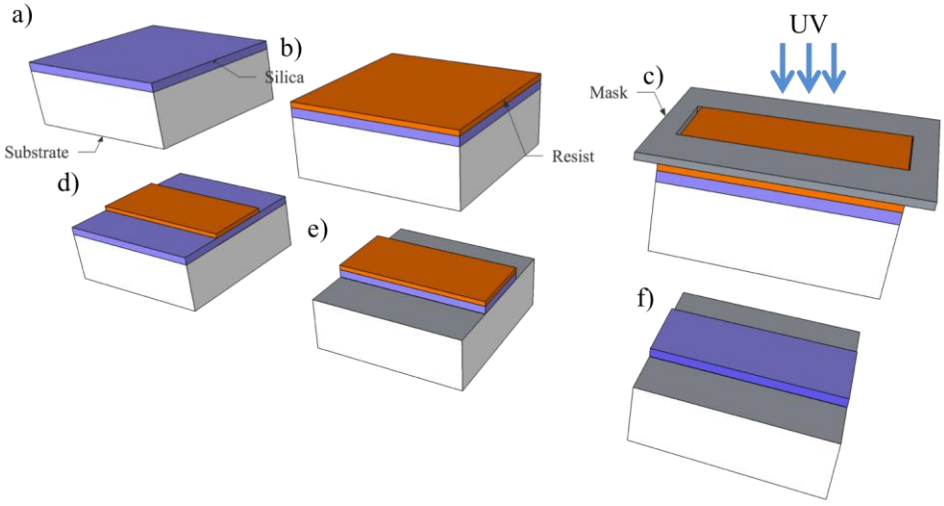

Figure 12 the general route of photolithography, a) bare substrate with silica layer to be shaped, b) resist deposited (normally by spinning) c) patterning of resist by mask (typically by UV exposure) d) unpatterned resist is removed by a chemical wash e) etching of silica f) finished silica structure.

Figure 12 shows an example of the photolithography steps used to produce a rib in silica, where the bare substrate is shown in a). Photoresist is deposited on the

surface, normally via spinning, shown in b). A mask is aligned to the substrate and the photoresist is exposed typically with UV light, but other techniques using x-rays or ions can be utilized, as shown in c). This radiation changes the photoresist, chemically. The unwanted photoresist is washed away with a chemical developer, as shown in d). The unprotected silica is etched via wet chemicals, ions, plasma or a combination and reacts in both a physical and/or chemical way to remove material, producing a rib, as shown in e). The photoresist will then be removed leaving the rib [18], shown in f). Photolithographic masks give the designer 2D freedom, whilst etching provides vertical definition. However, grading step heights is very difficult and this is why photolithography is referred to having 2½D control. Photolithographic micromachining can use both wet or dry etching as explained in the next sections.

Wet etching of silica using Hydrofluoric Acid (HF) has been widely used. It relies on a chemical reaction and has typically the fastest etch rates of most etching processes [19]. Nagarah *et al.* has shown deep etching of fused silica creating a 600 μm groove with HF. In this work special HF resistant photoresist was utilised to improve sidewall verticality and a 10 nm Ra surface roughness was achieved on the groove bottom [20]. Wet etching can produce smooth features with care, but due to the speed of the process, form is difficult to control to the hundreds of nanometre scale required for waveguide devices, as discussed in section 2.2.2.

Dry etching of silica is typically achieved with fluoroform (CHF_3) and oxygen plasma [19], which is achieved by creating the chemically reactive plasma and accelerating it towards the silica sample with an electric or magnetic field in a vacuum. This type of dry etching is referred to as Reactive Ion Etching (RIE). RIE relies on the interplay between two processes to etch the material; a chemical reaction and physical bombardment of ions. However, chemically neutral ions, such as argon, can also be used and this is simply called plasma etching. Plasma etching relies solely on the physical interaction of the ion bombardment to remove sample material. Dry etching has been performed by Li *et al.* to produce silica waveguide structures in combination with an aluminium oxide mask. The lift off technique together with reactive ion etching using carbon tetrafluoride plasma (CF_4) was used to machine though 5 μm of silica with near vertical side walls and a side wall surface roughness of ~10 nm [21]. An example of dry etching of silica on the tens of micron

scale is demonstrated by Sheng *et al.*, to produce waveguide structures. 16 µm of silica was machined using inductively coupled plasma, with CHF_3 and CF_4 as reactive ions and took 105 minutes to preform. The etched sidewall surface roughness was measured to be ~100-200 nm, the side wall verticality was measured from a micrograph to be 3.8° off vertical without signs of pitting [22]. Thus, it has been shown dry etching can create smooth, vertical, chip free features in silica for micron scale features but when pushed into machining tens of microns, both surface roughness and verticality suffer. Photolithography along with wet and dry etching of silica has been commented on. In the next section laser machining of silica will be discussed.

2.4.2 Laser machining

Laser machining of silica has had mixed success. The process relies on adding thermal energy to the silica and removing material either by evaporation or ablation. A notable mode used to create micron scale features, with super smooth surfaces, no chipping and a highly controlled lens form, uses CO_2 laser irradiation. Hunger *et al.* have shown micro lenses can be produced with a pulsed 10.6 µm laser light, with 4-120 ms pulse widths. These lenses typically have a surface roughness (Sq) of 0.2 nm with depths of cut ranging from 0.01-4 µm [23]. Evaporation of the silica is the main mechanism of material removal, while a low viscosity melt layer creates the low surface roughnesses. However, it is difficult for laser machining to create surfaces without a Gaussian shape and the resultant surface is difficult to predict because of the complicated and nonlinear nature of the machining process [23]. Picosecond laser radiation at 1053 nm from a Ti:Sapphire laser has been used to machine silica in the ablation mode by Perry *et al.*. However, surface metrology was not given and a poor surface quality and form were achieved. This is not surprising though, as the surface produced was caused by expulsion caused by the ablation as a result of the high laser powers used [24]. This section focused on the laser machining of silica with different wavelengths and pulse widths. Another technique used to machine silica is focused ion beam milling, which is discussed in the next section.

2.4.3 Focused ion beam machining

Focused ion beam milling can create smooth, chip free surfaces in three dimensions in silica. The basic focused ion beam mill works by a plasma source generating ions in a vacuum, where these are extracted and focused into a beam which is accelerated

to the substrate [25]. Work by Li *et al*. demonstrated 1.08 µm deep grooves in fused silica using focused ion beam milling. These grooves were chip free and had a surface roughness of 2.5 nm (Sq). A limitation of this technique is illustrated by the sidewalls produced which display a 10° off vertical [26]. In focused ion beam milling vertical sidewalls are affected by substrate re-deposition. The process is related to the re-deposition of material released from the substrate by the ions in previously machined areas. This process is always present in focused ion beam milling and can be minimised by slower machining rates [27]. Typical machining rates in silica with a focused ion beam mill are 2 µm/hr over a square centimetre [25], making it a lengthy process for tens of micron removal of material. Thus, focused ion beam milling can create smooth, chip free features in silica however verticality and speed are issues.

Three techniques for machining silica have been discussed in this section. In the next section, physical removal of silica via ductile machining is discussed, which is the process both precision dicing and milling use to form silica features tens of microns in scale with high verticality, nanoscale roughness and minimum chipping.

2.5 Ductile removal of material

Silica can be machined using physical removal of the material in the ductile regime, which is used in both precision dicing and milling, to create silica features on the tens of micron scale, with high verticality, nanoscale roughness and minimum chipping. Ductile regime cutting removes material via plastic deformation of chips, which is achieved by certain machining parameters (*i.e.* correct choice of the tool's translation speed, rotational speed, depth of cut, grit size, *etc.*) as stated by Bifano *et al.* [28]. If the material is machined with the incorrect machining parameters, brittle type machining occurs. This brittle type machining is caused by applying a shear stress that exceeds the material's plastic limit thus creating cracks that propagate and chip, resulting in an unsmooth, pitted and cracked surface [28].

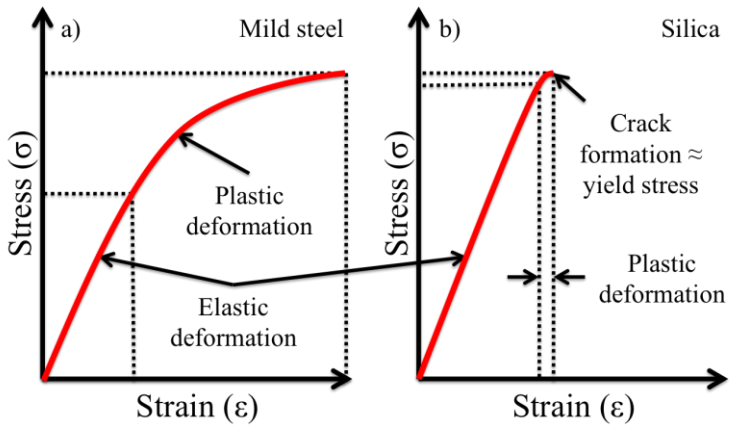

Figure 13 stress/strain diagrams of a) mild steel and b) fused silica. As the sample is subjected to strain, by elongation for example, it will elastically deform but the material will still return to its original shape after the strain is removed. Once the material has reached plastic deformation the sample will not return to its original shape. After this the yield stress is reached, the material fails, *i.e.* snaps, cracks, necks, *etc.*.

Figure 13 compares the stress/strain graphs of mild steel, a ductile material, and fused silica, a brittle material [29]. The material's strength and its failure characteristics can be inferred from the stress-strain graph. The stress-strain graph is an important representation of how a material reacts with a structural change. The salient point to take from stress-strain graph Figure 13 (b) [29], is that fused silica is a brittle material and plastic removal of the material will only happen if the strain applied is between the two arrows (see plastic deformation). This will allow microplasticity to occur and thus ductile removal of material. When ductile material removal occurs, the surface left will be very smooth however this is dependent on the size of chips removed. By keeping chip sizes between 0.6-0.8 µm, ductile removal of the majority of hard materials will be experienced [30]. Ductile material removal is not needed for mild steel because even beyond its yield stress it does not form deeply penetrating cracks that occur in brittle materials [31].

Cheung *et al.* states 'our current understanding of the physical mechanisms underlying the 'ductile-regime' machining of brittle materials is far from perfect' [32]. This makes cutting in the ductile-regime challenging to model resulting in few mathematical models. So, experimentation must be used to find the machining parameters at which ductile cutting occurs, as achieved in chapters 4 and 6. The machining techniques used to shape silica using this ductile cutting regime are discussed next.

2.6 Physical machining techniques for silica

Physical machining techniques are important in the planarization, polishing and contouring of silica in the production of free space bulk optics and mirrors. Techniques termed as 'physical' are ones in which there is an action on the substrate from a tool or particle to remove substrate material. The silica machining techniques including: lapping, chemical mechanical polishing, grinding, single point diamond turning, dicing and milling are discussed. Dicing and milling are also discussed at length in chapter 4 and 6 respectively. Unlike the silica machining techniques discussed earlier in section 2.4, such as laser machining, focused beam milling, *etc.*, the physical techniques discussed here are restricted in the dimensions they can machine in. Even though this is the case, lapping, chemical mechanical polishing, grinding, single point diamond turning, dicing and milling can still all remove more material than the other techniques (tens to hundreds of microns). Lapping and chemical mechanical polishing are discussed first.

2.6.1 Lapping and chemical mechanical polishing

Lapping and chemical mechanical polishing, shown in Figure 14, are well established in the field of wafer planarization and mirror, laser rod and beam cube production.

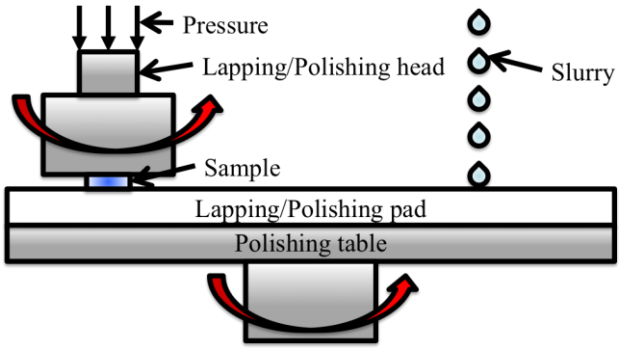

Figure 14 lapping and chemical mechanical polishing. The planarization of samples by lapping is achieved by the mechanical rotation of both the head and the pad, along with a slurry that contains abrasives. Polishing typically introduces a slurry that acts both mechanically and chemically to smooth the surface.

The basic operational principles of lapping and chemical mechanical polishing are shown in Figure 14. The sample is smoothed by the rotational movement of the head/pad and the action of abrasives. Lapping and polishing removes surface high points because the high points see an increased pressure applied to them by the head, thus being removed [33]. The difference between lapping and polishing is the material removal rate and the surface roughness achieved. Lapping is typically used to remove chips from a surface and is likely to achieve a surface roughness of 50-400 nm (Ra) [33]. Typically, chemical mechanical polishing is used to achieve a surface roughness of 3-12 nm (Ra) [33] with minimal material removal. Lapping usually utilises cast iron lapping pads and silicone carbide or aluminium oxide abrasives [34]. Polishing uses a polyurethane pad along with chemical slurry, where often colloidal silica is the chemical of choice. Chemical mechanical polishing can be liked to cleaning teeth, with a brush and toothpaste, the polyurethane pad acting as the brush and the colloidal silica as toothpaste. The chemical slurry actually acts as a wet etchant and removes high points from the surface because of the increased surface area [33].

Lapping and chemical mechanical polishing are well established in silica and can produce flat, chip free, smooth surfaces, with roughnesses as small as 0.2 nm (Rq) [33]. In terms of form, ±2 µm flatness has been measured over a 50 mm wafer in silicon carbide, sapphire and gallium nitride [35] using chemical mechanical polishing. The process, however, is time consuming and laborious because of the sample setting for each polished face required, pad preparation and cleaning for each stage of abrasive size change. The technique is also restricted to 1D machining. Both lapping and chemical mechanical polishing have been explained, with details given on its application to silica. Another type of physical machining is grinding and this will be discussed in the next section.

2.6.2 Grinding

Grinding generally removes material with a rotating cutting disc, which contains either a diamond or another abrasive material in a resin or nickel bond, allowing 1D machining. This is similar description to that of dicing but dicing can be thought as a specific type of grinding and is commented on, at length in chapter 4. Surface grinding is a well established in mirror production, where two examples of grinding are shown in Figure 15.

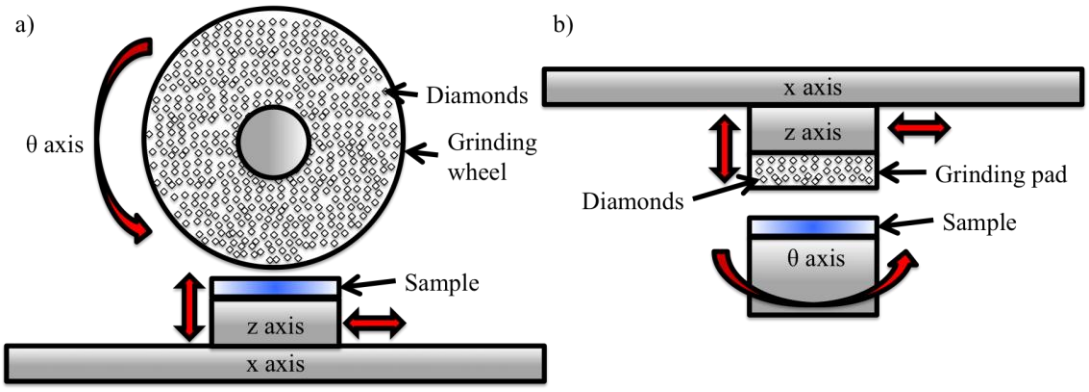

Figure 15 a) typical grinding machine b) Cranfield BoX grinding machine. Grinding machines usually consist of a set of translation stages and an abrasive that machines the sample. They typically use large abrasive cutting tools on the order of tens of centimetres, where a binder holds the abrasive grit together.

Figure 15 a) shows a diagram of a conventional grinding machine, which works in a surface plunge mode, where the sample is moved up into the rotating grinding wheel [31]. Figure 15 b) is a schematic of the Cranfield BoX grinding machine [36], where the sample rotates rather than the grinding wheel.

The Cranfield BoX has been used to planarize mirrors for the recently commissioned European Extremely Large Telescope (ELT) program. Mirror bases were made from the glass ceramics ULE and Zerodur, which both contain large portions of silica. A three stage grinding process was used with a resin bonded grinding wheel and diamond grit sizes of 76 μm, 46 μm and 25 μm, respectively. A surface roughness (Ra) was measured to be between 100-200 nm, with an impressive form accuracy of ±1 μm peak to valley, over a metre [36]. Thus grinding can be used to machine silica in a chip free way with very high form accuracy however, it does result in high surface roughness.

Lapping, chemical polishing and grinding of silica have now all been covered. The next section discusses dicing, which is the chosen fabrication technique in this thesis for creating input/output facets in silica and creating microcantilever structures.

2.6.3 Precision dicing

At its simplest level a dicing machine is a precision circular saw. The technique was originally developed for the semiconductor industry to allow dies to be sawn from a wafer after photolithographic processing. Dicing machines typically include a

spindle with a smooth rotational action and a sample bed with high positional accuracy, allowing 2D structures to be machined but is limited to straight geometries just as a circular saw would be. In a similar manner to grinding, blades used contain diamonds, which are either bonded or sintered into resin or nickel, respectively. Figure 16 shows an example of a dicing machine.

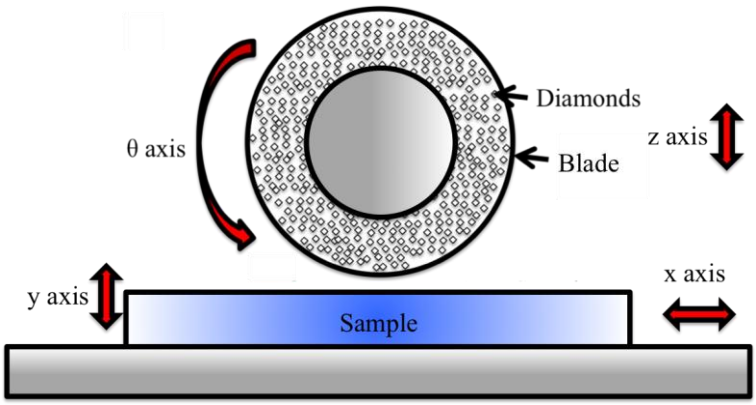

Figure 16 a typical dicing machine. Dicing is a specific type of grinding and machines by translating samples into a high speed, rotating disk of abrasives. The size of the blades are also typically smaller, 50-75 mm in diameter and 10 µm to millimetres in thickness.

Within the research group the dicing machine was used in a similar manner to that used to separate dies in electronics. The verticality and amounts of chipping achieved were good. However, the surface roughness of diced silica was high, Sa of ~200-300 nm (measured with ZeScope). Plaza *et al.* [37], reported 'practically vertical' and minimal chipping for the production of high aspect ratio, square towers in Pyrex. It was thought, after a literature review by the author, that it was possible to reduce machining parameters, such as rotational and translation speeds, to enable ductile type cutting. Ductile type machining would enable nanoscale surface roughness to be achieved simultaneously with high sidewall verticality and low amounts of chipping. This added to the recent progress in lithium niobate and YAG waveguides, as discussed in chapter 1, where diced waveguides produced were smooth and chip free in harder optical materials than silica. Precision dicing seemed an attractive avenue of research for machining silica with optical quality surfaces. After machine parameter optimisation, detailed in chapter 4, high quality sidewalls in silica were achieved with nanoscale roughness, high verticality and low amounts of chipping. From this, it can be seen that precision dicing is a good technique to be used in the fabrication of input/output facets in silica. Lapping, chemical polishing,

grinding and dicing all are 1D or 2D machining techniques. The next section, discusses diamond turning, a 3D physical machining technique.

2.6.4 Diamond turning

Single crystal diamond turning is commonly used in the production of aspheric bulk optics. Based on lathes, these machines are built with similar design ideas as the precision mill created in chapter 6. These lathes often have high precision stages and motion control along with Computer Numerical Control (CNC) and on board metrology systems. Figure 17 shows a schematic of one [38].

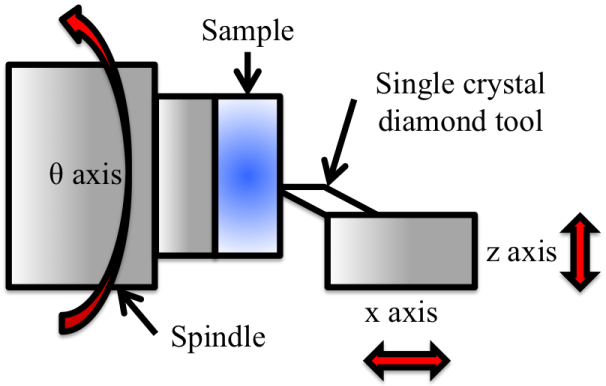

Figure 17 single crystal diamond turning lathe. This technique is typically used in the production of aspheric optics. It machines brittle materials by rotating and positioning the sample with high precision into a single crystal diamond cutting tool.

Figure 17 shows a diagram of a single crystal diamond turning lathe, in which this type of lathe can produce lenses, close to form, smooth and chip free. Silica has been machined by Ravindra *et al.* [38] in a ductile regime of cutting. Using the ductile cutting regime, accurate form is achieved in silica, which is free of chips and with surface roughnesses of 40 nm (Ra) [38]. Form control is kept by staying in the ductile cutting regime where depths of cut must be kept in the hundreds of nanometre range, thus multiple cuts are undertaken to achieve a lens. Diamond turning can be used to machine silica in a chip free way with very high form accuracy and a relatively low surface roughness. Although it machines in 3D, a limitation of turning is the features produced must have an annular shape, which is typically not suitable to integrated optics. Diamond turning lathes are one of the many physical machining techniques discussed available for ductile silica machining. Precision milling is another physical machining technique that relies on high precision stages, which is covered in the next section.

2.6.5 Precision milling

Precision milling has been used in the machining of silica before but typically is not a commercial process. In general there are two distinct machining modes a mill can operate in; side milling and slot milling (end milling). Side milling removes material parallel to the plane of the substrate, with movement within this plane only but allows no vertical cut movements. Slot milling allows more freedom than side milling and can enter and exit the substrate vertically, see Figure 18. Slot milling allows the user true 3D freedom in feature production, when compared to other techniques discussed in previous sections. To achieve ductile regime machining of silica, like the diamond turning lathe, the mill must have high positional accuracy and good decoupling from environmental effects, to achieve the small chip size necessary.

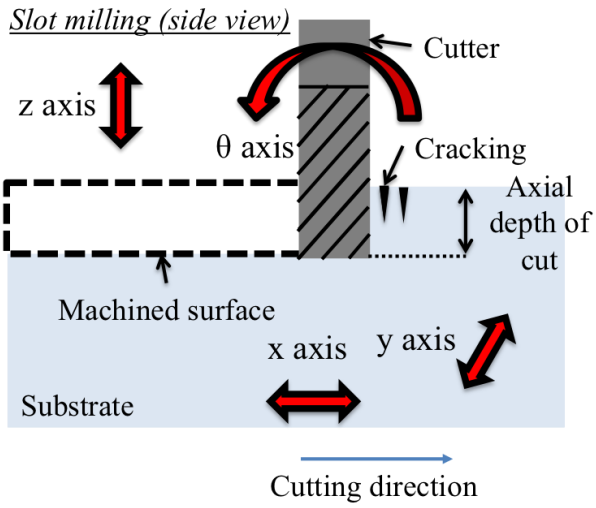

Figure 18 a typical milling machine. A precision micromill using a rotating tool along with high accuracy stages to define grooves within a sample surface.

Figure 18 shows a typical milling machine and shows a side view of slot milling. Grooves have been machined into silica with high verticality and smooth, chip free groove bottoms, typically utilising ductile type machining. Arif *et al.* demonstrated, with a precision slot milling technique, grooves that were smooth and chip free. A surface roughness (Sa) of 23.8 nm was obtained on the groove bottoms and had a depth of 400 nm [39]. Silica has also been machined in a slot milling mode with ball nosed cutters at 45° to the substrate by Foy *et al.*. The silica grooves had bottoms that were smooth and chip free albeit with a rounded bottom. A surface roughness (Sa) of <60 nm was measured, with a groove depth of 16 µm [40]. Thus, by utilising

the ductile slot milling regime, this enables nanoscale surface roughness to be achieved simultaneously with high flatness and low amounts of chipping, on the tens of micron scale. Chapter 6 extends this work and discusses machine parameter optimisation, which allowed the creation of high quality waveguide components in silica. From this, it can be seen that precision milling is a good technique to be used in the fabrication of waveguide components in silica. This section has covered the ductile mode milling of silica. The chapter is now concluded.

2.7 Conclusions

In this chapter the general requirements for machining free space input/output facets and grooves that interact with waveguides for silica integrated optics on the tens of micron scale are given. These include high verticality/flatness, nanoscale roughness and low surface chipping; all of which reduce loss mechanism. Both 2D and 3D roughness parameters have been shown and the way in which they are calculated along with levelling have been explained. The surface metrology techniques of white light interferometry, profilometry and atomic force microscopy are explained and discusses the validity of using a white light interferometry for surface roughness measurement.

Fabrication techniques that are capable of achieving some or all of the requirements set out for silica input/output coupling and waveguide components have been discussed. It was shown that wet etching of silica gave form errors even though material removal rate was quick. Dry etching to tens of micron depths gave results which were rough (100-200 nm) and had poor verticality. Laser machining using 10.6 μm laser radiation gave particularly smooth, chip free results but form was difficult to control unless a Gaussian shape was required. Focused ion beam milling again could produce smooth, chip free results but re-deposition caused form errors and the process had lengthy material removal times.

Physical machining techniques of silica were reviewed in contrast to the earlier mentioned techniques and ductile machining, which is central to these physical techniques, was discussed. The ductile cutting regime showed that machining in the

plastic region of deformation, for a brittle material, would create smooth and chip free features with no cracks. Other physical machining techniques, which are regularly used to machine silica, were explained. Lapping and chemical mechanical polishing can give flat, smooth and chip free machining but are restricted to machining of a single dimension and is time consuming. Grinding has been shown as a good planarization tool but again limited to a single dimension of machining and in terms of surface roughness it can produce. Diamond turning is commonly used to produce aspheric lenses and can produce devices with tight form requirements, which are smooth and chipless but can only do so with annular shapes. Precision dicing is typically used in the separating of dies from wafers. It was chosen to machine input/output facets in this thesis because it has been shown that it can produce vertical grooves with minimal chipping, in the tens of micron scale. However, it was theorised that nanoscale roughness could be achieved by accessing the ductile cutting regime. Precision milling has had success in literature for producing grooves in silica with nanoscale roughness, without chipping and in the tens of micron scale. From these results, milling was chosen to produce components that interact with waveguides whilst dicing was use for making input/output facets.

From this chapter, the requirements for input/output facets and waveguide components for silica photonics have been set out. The chapter has also given the reason for using dicing and milling as the choices for 2D and 3D machining techniques for these silica features. The next chapter covers the theory of waveguides and Bragg gratings and their fabrication in the silica-on-silicon substrate. This silica-on-silicon substrate is subsequently machined by dicing and milling in the chapters thereafter.

References

1. A. Ghatak and K. Thyagarajan, *Introduction to Fiber Optics* (Cambridge University Press, 1998), pp. 16–157.

2. H. E. Bennett and J. O. Porteus, "Relation Between Surface Roughness and Specular Reflectance at Normal Incidence," Journal of Optical Society of America **51**, 123–130 (1961).

3. M. Zeman, R. A. C. M. M. van Swaaij, J. W. Metselaar, and R. E. I. Schropp, "Optical modeling of a-Si:H solar cells with rough interfaces: Effect of back contact and interface roughness," Journal of Applied Physics **88**, 6436–6443 (2000).

4. Y. A. Gharbia, G. Milton, and J. Katupitiya, "The effect of optical fiber endface surface roughness on light coupling," in *Optical Fabrication, Testing, and Metrology*, R. Geyl, D. Rimmer, and L. Wang, eds. (2004), Vol. 5252, pp. 201–208.

5. K. Thyagarajan, Y. Bourbin, A. Enard, S. Vatoux, and M. Papuchon, "Experimental demonstration of TM mode-attenuation resonance in planar metal-clad optical waveguides," Optics Letters **10**, 288–290 (1985).

6. D. Kumar, V. K. Sharma, and K. N. Tripathi, "Design and fabrication of multilayer metal-clad dielectric surface plasmon waveguide polarizers," Optical Engineering **45**, 054601 (2006).

7. F. P. Payne and J. P. R. Lacey, "A theoretical analysis of scattering loss from planar optical waveguides," Optical and Quantum Electronics **26**, 977–986 (1994).

8. J. C. Stover, *Optical Scattering: Measurement and Analysis*, 2nd ed. (SPIE Press, 1995), pp. 20–53.

9. Image Metrology A/S, *The Scanning Probe Image Processor SPIP User's and Reference Guide Version 5.1* (2010).

10. R. Leach, L. Brown, X. Jiang, R. Blunt, M. Conroy, and D. Mauger, *A NATIONAL MEASUREMENT GOOD PRACTICE GUIDE No.108 Guide for the Measurement of Smooth Surface Topography Using Coherence Scanning Interferometry* (2008).

11. "http://zeiss-campus.magnet.fsu.edu/articles/lightsources/leds.html," .

12. Zemetrics, *ZeScope Specification* (2010).

13. KLA-Tencor, "P-16 Specification," (2007).

14. I. Chasiotis, "Atomic Force Microscopy in Solid Mechanics," in *Springer Handbook of Experimental Solid Mechanics*, W. Sharpe Jr., ed. (2008), pp. 409–414.

15. Vecco, *Caliber Specification* (2006).

16. F. Gao, R. K. Leach, J. Petzing, and J. M. Coupland, "Surface measurement errors using commercial scanning white light interferometers," Measurement Science and Technology **19**, 015303 (2008).

17. R. Noyce, "SEMICONDUCTOR DEVICE-AND-LEAD STRUCTURE," US Patent 2,981,877 (1961).

18. R. G. Hunsperger, *Integrated Optics Theory and Technology*, 6th ed. (Springer, 2009), pp. 75–77.

19. W. C. Crone, "A Brief Introduction to MEMS and NEMS," in *Springer Handbook of Experimental Solid Mechanics*, W. N. Sharpe Jr., ed. (Springer, 2008), pp. 212–213.

20. J. M. Nagarah and D. A. Wagenaar, "Ultradeep fused silica glass etching with an HF-resistant photosensitive resist for optical imaging applications," Journal of Micromechanics and Microengineering **22**, 035011 (2012).

21. W. T. Li, D. A. P. Bulla, J. Love, B. Luther-Davies, C. Charles, and R. Boswell, "Deep dry-etch of silica in a helicon plasma etcher for optical waveguide fabrication," Journal of Vacuum Science & Technology A: Vacuum, Surfaces, and Films **23**, 146–150 (2005).

22. Z. Sheng, B. Yang, L. Yang, J. Hu, D. Dai, and S. He, "Experimental Demonstration of Deeply-Etched SiO2 Ridge Optical Waveguides and Devices," IEEE Journal of Quantum Electronics **46**, 28–34 (2010).

23. D. Hunger, C. Deutsch, R. J. Barbour, R. J. Warburton, and J. Reichel, "Laser micro-fabrication of concave, low-roughness features in silica," AIP Advances **2**, 012119 (2012).

24. B. C. Stuart, M. D. Feit, S. Herman, A. M. Rubenchik, B. W. Shore, and M. D. Perry, "Nanosecond-to-femtosecond laser-induced breakdown in dielectrics.," Physical Review. B, Condensed Matter **53**, 1749–1761 (1996).

25. J. McGeough, "Ion Beam Machining," in *Micromachining of Engineering Materials*, J. McGeough, ed. (Marcel Dekker Inc, 2002), pp. 277–289.

26. W. Li, S. Dimov, and G. Lalev, "Focused-ion-beam direct structuring of fused silica for fabrication of nano-imprinting templates," Microelectronic Engineering **84**, 829–832 (2007).

27. J. Orloff, M. Utlaut, and L. Swanson, "Interaction of Ions and Solids," in *High Resolution Focused Ion Beam FIB and Its Applications* (Kluwer Academic, 2003), p. 144.

28. T. G. Bifano, T. Dow, and R. O. Scattergood, "Ductile-regime grinding: a new technology for machining brittle materials," Journal of Engineering for Industry (Transactions of the ASME) **113**, 184–189 (1991).

29. H. Eda, "Ductile Grinding of Ceramics: Machine Tool and Process," in *Handbook of Advanced Ceramic Machining*, I. Marinescu, ed. (CRC Press, Taylor & Francis Group, 2007), pp. 1–4.

30. B. K. A. Ngoi and P. S. Sreejith, "Ductile Regime Finish Machining – A Review," Advanced Manufacturing Technology **16**, 547–550 (2000).

31. H. Yasui, "Ductile-Mode Ultra-Smoothness Grinding of Fine Ceramics with Coarse-Grain-Size Diamond Wheels," in *Handbook of Advanced Ceramic Machining*, I. D. Marinescu, ed. (CRC Press, Taylor & Francis Group, 2007), pp. 29–32.

32. C. Cheung and W. B. Lee, *Surface Generation in Ultra-precision Diamond Turning: Modelling and Practices* (Professional Engineering Publishing, 2003), p. 4.

33. C. Gui, M. Elwenspoek, J. G. E. Gardeniers, and P. V. Lambeck, "Present and Future Role of Chemical Mechanical Polishing in Wafer Bonding," Journal of The Electrochemical Society **145**, 2198–2204 (1998).

34. G. W. Fynn and W. J. A. Powell, *Cutting and Polishing Optical and Electronic Materials*, 2nd ed. (Institute of Physics Publishing Inc., 1988), p. 40.

35. Logitech, *Silicon Carbide, Sapphire & Gallium Nitride Substrate Preparation* (2012).

36. X. Tonnellier, P. Morantz, P. Shore, and P. Comley, "Precision grinding for rapid fabrication of segments for extremely large telescopes using the Cranfield BoX," Proceedings of SPIE Modern Technologies in Space- and Ground-based Telescopes and Instrumentation. **7739**, (2010).

37. J. Plaza, M. J. Lopez, A. Moreno, M. Duch, and C. Cane, "Definition of high aspect ratio glass columns," Sensors and Actuators A: Physical **105**, 305–310 (2003).

38. D. Ravindra and J. Patten, "Ductile Regime Single Point Diamond Turning of Quartz Resulting in an Improved and Damage-Free Surface," Machining Science and Technology **15**, 357–375 (2011).

39. M. Arif, M. Rahman, and W. Y. San, "Ultraprecision ductile mode machining of glass by micromilling process," Journal of Manufacturing Processes **13**, 50–59 (2011).

40. K. Foy, Z. Wei, T. Matsumura, and Y. Huang, "Effect of tilt angle on cutting regime transition in glass micromilling," International Journal of Machine Tools and Manufacture **49**, 315–324 (2009).

3 Photonic Platform

3.1 Introduction

This chapter covers the background theory and fabrication techniques for buried channel waveguides and Bragg gratings, which were used in conjunction with diced features in chapters 4 and 5. The fabrication of the silica-on-silicon substrate is explained, and the use of this substrate is discussed in the dicing and milling optimisation tests reported in chapters 4 and 6. The treatment of waveguides and Bragg grating are based on the approach set out in texts by Ghatak [1] and Griffiths [2].

The chapter starts with Snell's law to begin the explanation of slab planar waveguides. Moving on from a ray description to a modal description of planar waveguides, Maxwell's equations are used and simplified to produce the wave equation. Boundary conditions are used to solve the wave equations for the Transverse Electric (TE) mode. The solutions are plotted showing the number of modes that can exist for a given waveguide and the resulting field distributions. A summary of the analytic solution is given for solving a buried channel waveguide, with mention of numerical techniques. The basics of Bragg gratings are also covered and the Bragg equation is derived using a wavevector approach. Coupled mode equations give further insight into Bragg gratings and were used in a piece of software written by the author, to fit spectra in chapter 5. Bragg grating apodisation and chirp is also covered.

The second part of the chapter covers fabrication techniques used in the production of buried channel waveguides and Bragg gratings. This starts with an explanation of the silica-on-silicon substrate used within this thesis. The method used in the

production of the silica layers, flame hydrolysis deposition, is also covered with mention to the dopants added and their effect on the resultant silica glass layer. Also included, is the fabrication of the buried channel waveguides and Bragg gratings in the silica-on-silicon platform via direct UV writing. The topics of index matching and the practical implementation of Bragg grating apodisation are discussed. The chapter ends with waveguide and Bragg grating characterisation, the equipment used and practical issues addressed.

3.2 Waveguide theory

Waveguides are designed to guide light from place to place and come in a variety of geometries. These include slab, rib, channel, graded, *etc.*. Within this section the analytical solution of a planar slab waveguides and its application to solving buried channel waveguide problems is discussed. This is of interest as buried channel waveguides are used throughout this thesis in the form of direct UV written waveguides, chapters 4 and 5. The planar slab waveguide is first described in terms of light rays, using Snell's law.

3.2.1 Snell's law

When light passes through a boundary of two dissimilar refractive indices the light under goes reflection and refraction. Snell's law can describe the angle, at which the light will be refracted [1],

$$n_1 \sin\theta_i = n_2 \sin\theta_r \qquad \textbf{Equation 5}$$

where θ_i and θ_r are the angles of incidence and refraction respectively, and where n_1 and n_2 are the refractive indices of the two media either side of the planar interface as shown in Figure 19.

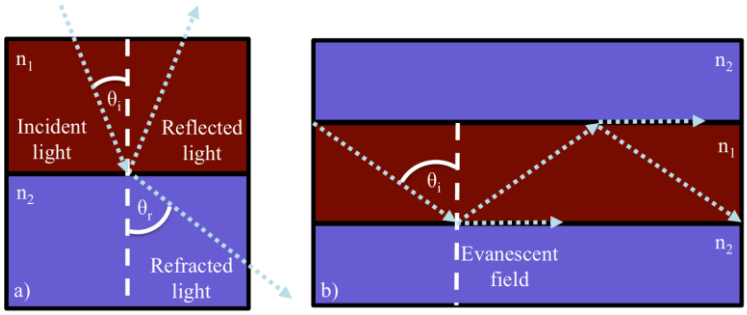

Figure 19 a) diagram depicting Snell's law, b) a light beam under going total internal reflection (TIR) in a waveguide structure, core shown in red cladding in blue.

Figure 19 a) shows both reflected and refracted light, while Figure 19 b) shows Total Internal Reflection (TIR) in a waveguiding core structure (red). For TIR to occur, $n_1 > n_2$ and the angle of incidence (θ_i) must be greater than $\theta_c = \sin^{-1}(n_2/n_1)$ for (θ_r = 90°). At this angle of incidence the light will propagate along the boundary, this angle is called the critical angle (θ_c), and for any angles greater than this, all the light will reflect as shown in Figure 19 b). At the critical angle light stops being refracted and TIR holds the light within the core and waveguiding occurs. However some light does exist outside core. This is called the evanescent field but ray optics does not accurately describe this phenomenon and waveguide propagation is better described in terms of optical modes.

3.2.2 Planar slab waveguide

Figure 19 b) shows an example of a slab waveguide. Even though simple slab structures were not used within this thesis, light guidance can be solved analytically for this case, thus giving a general insight into the propagation characteristics of channel waveguides. In Figure 19 b) light guidance is introduced by a ray-optic description. Modal analysis of light guidance within waveguides, starting with Maxwell's equations, gives a more mathematically rigorous result. Planar slab waveguides have been described before and the analysis shown in this chapter is based on work by Ghatak and Thyagarajan [1]. The analysis starts with Maxwell's equations for an isotropic, linear material,

$$\nabla \cdot \boldsymbol{\mathcal{D}} = \rho_f \qquad \textbf{Equation 6}$$

$$\nabla \times \boldsymbol{\mathcal{E}} = -\frac{\partial \boldsymbol{\mathcal{B}}}{\partial t} \qquad \textbf{Equation 7}$$

$$\nabla \cdot \boldsymbol{\mathcal{B}} = 0 \qquad \textbf{Equation 8}$$

$$\nabla \times \boldsymbol{\mathcal{H}} = \boldsymbol{J_f} + \frac{\partial \boldsymbol{\mathcal{D}}}{\partial t} \qquad \textbf{Equation 9}$$

where $\boldsymbol{\mathcal{D}}$ is the electric flux density (bold type set denoting a vector), ρ_f is the total charge density, $\boldsymbol{\mathcal{E}}$ is the electric field strength, $\boldsymbol{\mathcal{B}}$ is the magnetic flux density, t is time, $\boldsymbol{\mathcal{H}}$ is the magnetic field strength and $\boldsymbol{J_f}$ is the total current density. The slab waveguide analysed here is a dielectric thus is non-conducting and non-magnetic, thus $\boldsymbol{J_f}$ goes to zero. By using the following assumptions,

$$\mu = \mu_r \mu_o \because \ \mu_r = 1 \ \therefore \mu = \mu_o \qquad \textbf{Equation 10}$$

$$\varepsilon = \varepsilon_r \varepsilon_o \because \ \varepsilon_r = n^2 \therefore \varepsilon = n^2(x)\varepsilon_o \qquad \textbf{Equation 11}$$

$$\boldsymbol{\mathcal{D}} = n^2 \varepsilon_o \boldsymbol{\mathcal{E}} \qquad \textbf{Equation 12}$$

$$\boldsymbol{\mathcal{B}} = \mu_o \boldsymbol{\mathcal{H}} \qquad \textbf{Equation 13}$$

where μ_o is the permeability of free space, μ_r is the permeability of the material, ε_o the permittivity of free space, ε_r the permittivity of the material and n the refractive index of the guiding medium. Maxwell's equations with rearrangement, can be expressed in terms of $\boldsymbol{\mathcal{E}}$ and $\boldsymbol{\mathcal{H}}$ fields,

$$\varepsilon_o \nabla \cdot (n^2 \, \boldsymbol{\mathcal{E}}) = 0 \qquad \textbf{Equation 14}$$

$$\nabla \times \boldsymbol{\mathcal{E}} = -\mu_o \frac{\partial \boldsymbol{\mathcal{H}}}{\partial t} \qquad \textbf{Equation 15}$$

$$\nabla \cdot \boldsymbol{\mathcal{H}} = 0 \qquad \textbf{Equation 16}$$

$$\nabla \times \boldsymbol{\mathcal{H}} = n^2 \varepsilon_o \frac{\partial \boldsymbol{\mathcal{E}}}{\partial t}. \qquad \textbf{Equation 17}$$

To obtain the vectorial wave equation for the propagation of light in an optical medium in terms of electric and magnetic fields, the curl of both Equation 15 and Equation 17 must be taken,

$$\nabla \times (\nabla \times \boldsymbol{\mathcal{E}}) = -\mu_o \frac{\partial (\nabla \times \boldsymbol{\mathcal{H}})}{\partial t} = -\varepsilon_o \mu_o n^2 \frac{\partial^2 \boldsymbol{\mathcal{E}}}{\partial t^2}. \qquad \textbf{Equation 18}$$

Now using the vector identity $\nabla \times (\nabla \times \boldsymbol{V}) = \nabla(\nabla \cdot \boldsymbol{V}) - \nabla^2 \boldsymbol{V}$ with Equation 18 yields,

$$\nabla(\nabla \cdot \boldsymbol{\mathcal{E}}) - \nabla^2 \boldsymbol{\mathcal{E}} = -\varepsilon_o \mu_o n^2 \frac{\partial^2 \boldsymbol{\mathcal{E}}}{\partial t^2}. \qquad \textbf{Equation 19}$$

Equation 14 can be rewritten in the following form,

$$\varepsilon_o \nabla \cdot (n^2 \boldsymbol{\mathcal{E}}) = \varepsilon_o (\nabla n^2 \cdot \boldsymbol{\mathcal{E}} + n^2 \nabla \cdot \boldsymbol{\mathcal{E}}) \quad \textbf{Equation 20}$$

thus,

$$\nabla \cdot \boldsymbol{\mathcal{E}} = -\frac{1}{n^2} \nabla n^2 \cdot \boldsymbol{\mathcal{E}}. \quad \textbf{Equation 21}$$

Equation 21 can be substituted into Equation 19 to give,

$$\nabla^2 \boldsymbol{\mathcal{E}} + \nabla \left(\frac{1}{n^2} \nabla n^2 \cdot \boldsymbol{\mathcal{E}} \right) - \varepsilon_o \mu_o n^2 \frac{\partial^2 \boldsymbol{\mathcal{E}}}{\partial t^2} = 0. \quad \textbf{Equation 22}$$

Equation 22 describes the electric fields for an arbitrary or inhomogeneous refractive index. Planar slab waveguides are made of distinct homogenous layers of refractive index thus the second term vanishes leaving the scalar wave equation to hold in each region,

$$\nabla^2 \boldsymbol{\mathcal{E}} - \varepsilon_o \mu_o n^2 \frac{\partial^2 \boldsymbol{\mathcal{E}}}{\partial t^2} = 0. \quad \textbf{Equation 23}$$

The scalar wave equation can also be found for the magnetic field by similar analysis, by applying the curl to Equation 17 and by using Equation 15 and Equation 16 yielding,

$$\nabla^2 \boldsymbol{\mathcal{H}} - \varepsilon_o \mu_o n^2 \frac{\partial^2 \boldsymbol{\mathcal{H}}}{\partial t^2} = 0. \quad \textbf{Equation 24}$$

If the direction of propagation of the light is parallel to the z axis, see Figure 20, and the refractive index is constant in two directions, both y and z, and only varies in x, thus $n^2 = n^2(x)$, the solutions of the wave equations are therefore,

$$\mathcal{E}_j = E_j(x) e^{j(\omega t - \beta z)}, j = x, y, z \quad \textbf{Equation 25}$$

$$\mathcal{H}_j = H_j(x) e^{j(\omega t - \beta z)}, j = x, y, z \quad \textbf{Equation 26}$$

where β is the propagation constant of the mode and ω is the angular frequency. The propagation constant is related to the effective refractive index (n_{eff}) by $\beta = k_o n_{eff}$, where k_o is the free space wavenumber and $k_o = 2\pi/\lambda = \omega/c$. Equation 25 and Equation 26 describe the optical modes, where their electromagnetic fields depend only on time and the z coordinate, and represent travelling waves.

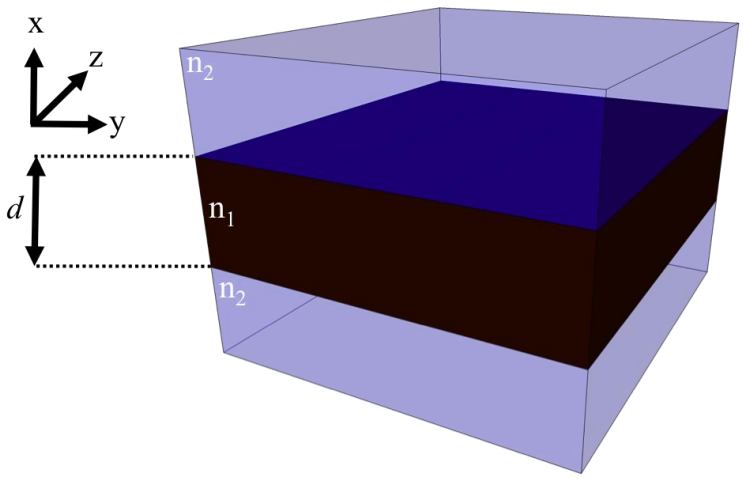

Figure 20 planar slab waveguide. Here $n_1 > n_2$, where n_1 provides the guiding layer for the launched light.

To discover a physical interpretation of these equations, they are substituted back into Maxwell's equations, Equation 15 and Equation 17. This analysis shows that for a planar slab waveguide, Maxwell's equations reduce to two components; the transverse electric mode or TE mode, which has its electric field oscillating in the y axis (see Figure 20) and the transverse magnetic mode or TM mode, which has its magnetic field oscillating in the y axis (see Figure 20). For a more rigorous analysis of the equations discussed here see Appendix B. Both the TE and the TM modes can be described by ordinary second order differential equations obtained from the solution to the wave equations. The electric field of the TE mode can be expressed by,

$$\frac{d^2\mathrm{E}_y}{dx^2} + (k_o^2 n_1^2 - \beta^2)\mathrm{E}_y = 0, |x| < {}^{d}/_{2} \qquad \textbf{Equation 27}$$

$$\frac{d^2\mathrm{E}_y}{dx^2} + (k_o^2 n_2^2 - \beta^2)\mathrm{E}_y = 0, |x| > {}^{d}/_{2} \qquad \textbf{Equation 28}$$

where a core layer centred around x = 0, with a thickness d, with a refractive index n_1 and cladding layer refractive index of n_2 (see Figure 20). The electric field within the core layer is described by Equation 27 and the cladding by Equation 28. Simplification is made by substituting $\kappa = \sqrt{k_o^2 n_1^2(x) - \beta^2}$ and $\gamma = \sqrt{\beta^2 - k_o^2 n_2^2(x)}$,

$$\frac{d^2\mathrm{E}_y}{dx^2} + \kappa^2\mathrm{E}_y = 0, |x| < {}^{d}/_{2} \qquad \textbf{Equation 29}$$

$$\frac{d^2\mathrm{E}_y}{dx^2} - \gamma^2\mathrm{E}_y = 0, |x| > {}^{d}/_{2} \quad \textbf{Equation 30}$$

The solution of Equation 29 represents the amplitude of electric field in the core and can be written in the following form,

$$\mathrm{E}_y(x) = A\cos\kappa x + B\sin\kappa x\,, |x| < {}^{d}/_{2} \quad \textbf{Equation 31}$$

while the solution of Equation 30 represents the amplitude of electric field in the cladding and can be written in the following form,

$$\mathrm{E}_y(x) = \begin{cases} Ce^{-\gamma x}, x < -{}^{d}/_{2} \\ \dfrac{x}{|x|}De^{-\gamma|x|}, x > {}^{d}/_{2} \end{cases} \quad \textbf{Equation 32}$$

where A, B, C and D are constants. Further boundary conditions are added to these equations to solve them. Firstly the solution must be continuous at the core/cladding interface (*i.e.* continuity of $\mathrm{E}_y(x)$ and $d\mathrm{E}_y/dx$ at $x = \pm d/2$) and symmetric or antisymmetric around the centre of the core (at x = 0) because the refractive index is symmetric about this point. Thus,

$$\mathrm{E}_y(x) = \begin{cases} A\cos\kappa x\,, |x| < -{}^{d}/_{2} \\ Ce^{-\gamma x}, |x| > {}^{d}/_{2} \end{cases} \quad \textbf{Equation 33}$$

the core and cladding solution for the symmetric mode, respectively and,

$$\mathrm{E}_y(x) = \begin{cases} B\sin\kappa x\,, |x| < -{}^{d}/_{2} \\ \dfrac{x}{|x|}De^{-\gamma|x|}, |x| > {}^{d}/_{2} \end{cases} \quad \textbf{Equation 34}$$

the core and cladding solution for the antisymmetric mode, respectively. Therefore,

$$A\cos\frac{\kappa d}{2} = Ce^{\frac{-\gamma d}{2}} \quad \textbf{Equation 35}$$

$$-\kappa A\sin\frac{\kappa d}{2} = -\gamma Ce^{\frac{-\gamma d}{2}}. \quad \textbf{Equation 36}$$

By dividing Equation 36 by Equation 35, symmetric modes can be found,

$$\xi\tan\xi = \frac{\gamma d}{2} \quad \textbf{Equation 37}$$

where $\xi = \frac{\kappa d}{2}$. By applying the same boundary condition, the antisymmetric modes can be found,

$$-\xi \cot \xi = \frac{\gamma d}{2} \quad \textbf{Equation 38}$$

Equation 37 and Equation 38 both describe the symmetric or antisymmetric optical modes of the TE polarisation. Now,

$$\frac{\gamma d}{2} = \sqrt{\frac{V^2}{4} - \xi^2} \quad \textbf{Equation 39}$$

where,

$$V = k_o d \sqrt{n_1^2 - n_2^2} \quad \textbf{Equation 40}$$

where V is known as the dimensionless waveguide parameter or 'V number'. Thus substituting Equation 39 into Equation 37 and Equation 38 yields,

$$\xi \tan \xi = \sqrt{\frac{V^2}{4} - \xi^2}, symmetric\ modes \quad \textbf{Equation 41}$$

and

$$-\xi \cot \xi = \sqrt{\frac{V^2}{4} - \xi^2}, antisymmetric\ modes. \quad \textbf{Equation 42}$$

By plotting Equation 41 and Equation 42, see Figure 21, these transcendental equations can be solved to discover which waveguide properties such as: core layer thickness d, core refractive index n_1 and cladding layer with refractive index n_2, can guide light for a given wavelength of operation λ.

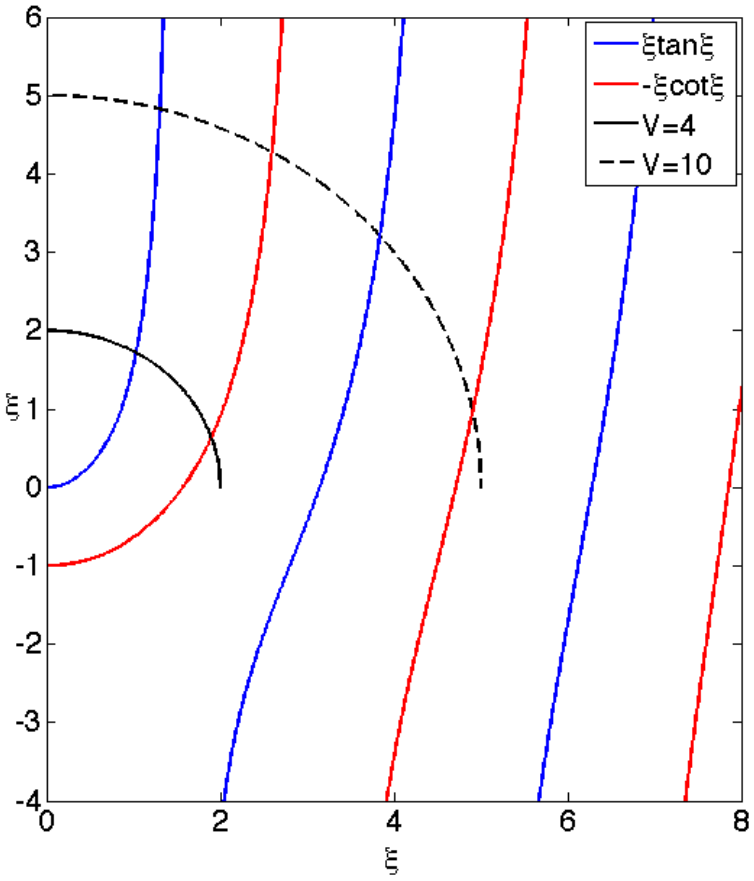

Figure 21 graphical solution for the guided modes of a planar slab waveguide. Shown are the symmetric (blue) or antisymmetric (red) optical modes and waveguides with V numbers of 4 (solid black) and 10 (dashed black).

Figure 21 shows a graphical solution for the number of guided modes of a planar slab waveguide. Where the radii and curves meet show the number of modes that will be present in a waveguide of a given V number. The circles have a radius of $V/2$, the solid black circle that has a V number of 4 supports 2 modes, while the dashed black circle with a V number of 10 supports 4 modes. By plotting Equation 33 and Equation 34 the modal electric field distribution within the core and cladding can be shown in Figure 22.

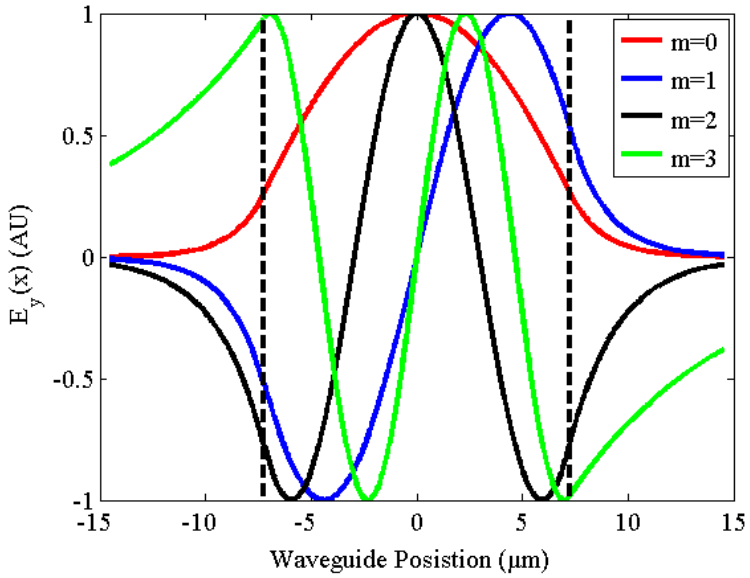

Figure 22 scaled electric field distribution for a planar slab waveguide with a V number = 10. m=0 shows the fundamental mode and m=1 to m=3 shows a portion of the higher order modes that exist within this waveguide.

Figure 22 shows the scaled electric field distribution of the four spatial modes. Where m=0 and m=2 are symmetric, or even modes, and m=1 and m=3 are antisymmetric, or odd modes. It can be seen that for higher order modes, a greater proportion of the field and thus optical power exists in the cladding region.

To plot Figure 22, a core layer thickness (d) of 14.5 μm was used, with a core refractive index (n_1) of 1.45, a cladding layer refractive index (n_2) of 1.44 and a wavelength of operation (λ) 1550 nm, which achieved a V number of ~10. Generally as the V number increases, the more optical modes the waveguide can support. A larger V number can be obtained by using a thicker core layer, a larger refractive index difference ($n_1 - n_2$) or shorter wavelength of operation. However, for single mode operation, which all of the waveguides are in this thesis, the V number must between zero and π.

The analytical solution of a planar slab waveguide has been described; in the next section channel waveguides, which are used throughout the thesis, are covered.

3.2.3 Channel waveguides

Up to now only planar slab waveguides have been considered because of their simple analytical solution. However, planar slab waveguides only confine the light in one direction so to do so in two, channel waveguides must be used. Channel

waveguides need special consideration when solving them to discover the propagation characteristics. In Figure 23 a variety of channel waveguides are shown.

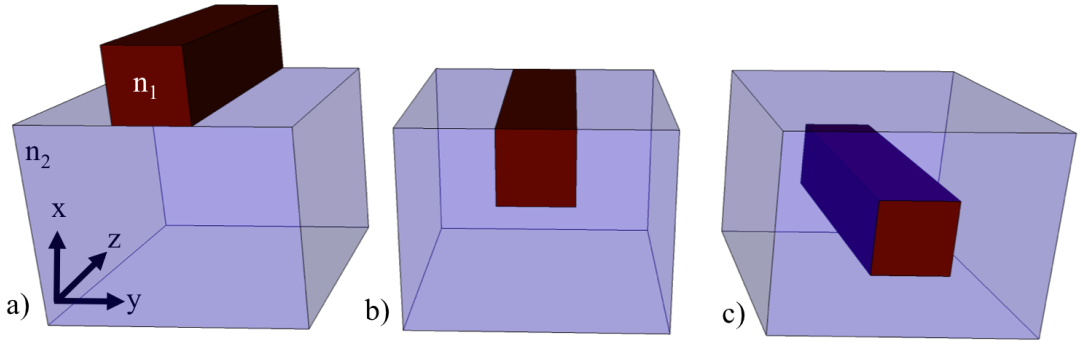

Figure 23 a variety of channel waveguides. a) rib, b) diffused and c) buried.

Figure 23 shows three different types of channel waveguides, as before n_1 is the refractive index of the core and n_2 is the refractive index of the cladding. The buried channel waveguide, Figure 23 c), best represents the waveguides used throughout this thesis. An effective way of solving a buried channel is by using the effective index method as described in work by Okamoto [3]. The effective index method works by splitting the channel waveguide into a series of slab waveguides, solving each slab and then combining the results, as shown in Figure 24.

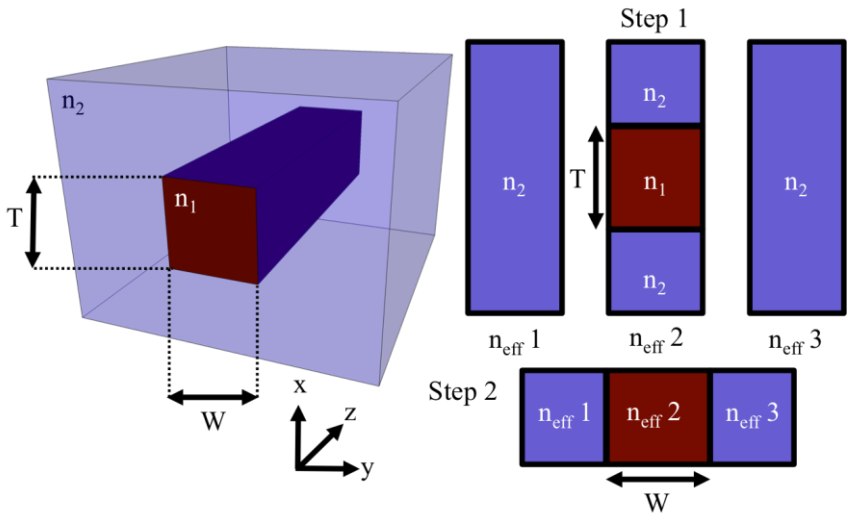

Figure 24 effective index method used to solve buried channel waveguide, which uses the mathematical process detailed in section 3.2.2 twice, as shown by steps 1 and 2.

Step 1 from Figure 24, shows how the channel waveguide is split into three slab waveguides along the y axis and the effective refractive index (n_{eff}) being

calculated for each. Step 2 consists of making a slab waveguide from x direction using the refractive indices calculated in step 1. Thus, from steps 1 and 2 an effective refractive index for the optical mode can be calculated, using the same mathematics used to solve the simple planar slab waveguide in section 3.2.2.

For more complicated wave guiding structures and refractive index profiles, an analytical solution may be difficult to derive. Numerical solutions can be used to solve these more complicated waveguide geometries. Commercial waveguide solvers are numerous and are usually based on techniques such as: finite difference method, finite element method and beam propagation method. A brief overview of channel waveguide solving has been given. The next section introduces Bragg grating operation and modelling.

3.3 Bragg gratings

Bragg gratings consist of a distributed periodic refractive index change of the effective refractive index of a waveguide. This can be achieved by a change in the local refractive index or waveguide dimension. At a location of one of these effective refractive index perturbations, a fraction of that light will be reflected, as described by Fresnel's equations. For multiple perturbations the incoming light will experience multiple reflections from each refractive index interface. Each reflected ray's phase will be dependent on its wavelength and the period of refractive index modulation. For a given wavelength within the bandwidth centred around the Bragg central wavelength, the reflected rays will add constructively creating a backward propagating wave. All other wavelengths outside a specific bandwidth of the Bragg wavelength will add up destructively and be transmitted through the filter, see Figure 25. Bragg gratings take their name from the Bragg law of X-ray diffraction by a crystal lattice, but manifest themselves here in a simpler one dimension problem due to of the confinement of the waveguide.

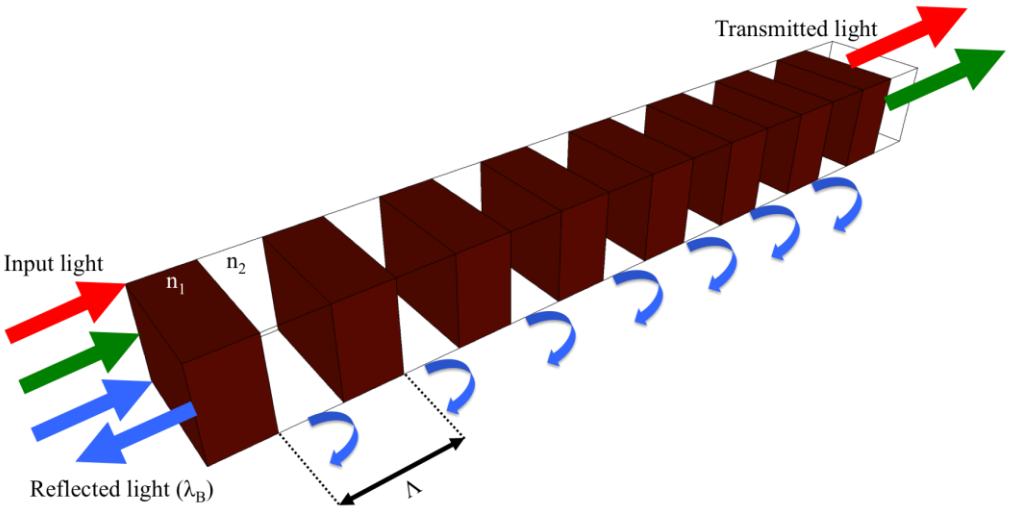

Figure 25 planar Bragg grating operation. Broadband light represented by the red, green and blue arrows is launched into the Bragg gratings core mode. The blue light couples resonantly with the periodic variation (Λ) of refractive indices (n_1 and n_2) and is launched into a counter propagating core mode. The red and green light is transmitted through the structure, as they do not resonantly interact with the refractive index structure.

Gratings based in waveguides can be categorised in to two groups; long period gratings (or transmission gratings) and short period (Bragg gratings). Long period gratings are characterised by selecting certain wavelengths to be converted from a core mode to a forward propagating cladding mode. Typically Bragg gratings couple light from a core mode to a counter propagating core mode. However, in some structures the light can couple into counter propagating cladding modes, these gratings are usually called tilted or blazed gratings. Long period gratings are not used in this thesis and the following section discusses Bragg gratings.

Bragg gratings have a number of properties that can be modified for a desired spectral response. These include their length, refractive index modulation, apodisation and chirp. These are the parameters that are required to fit the complex Fabry–Pérot spectra created by a pair of spectrally matched Bragg gratings used to interrogate cantilever deflection in chapter 5. Much of the work in the literature has been based on fibre Bragg gratings but in this thesis planar Bragg gratings are used. However, fibre Bragg gratings and planar Bragg gratings are similar in their performance despite the differences in geometry. Direct UV writing is used to inscribe the planar Bragg gratings and this fabrication process is covered in

section 3.5. The theory behind the transformation of forward propagating wave to a backward propagating wave in a Bragg grating for specific wavelengths of light, is described through the Bragg condition, discussed in the next section.

3.3.1 Bragg condition

The Bragg condition is the set of circumstances under which a forward propagating optical mode in a waveguide interacts with a grating structure and is converted into a backward propagating mode. To describe the Bragg condition, the laws of energy and momentum conservation are used. Thus, the total energy and the sum of the incident, transmitted and reflected light must be equal, assuming a lossless waveguide. Moreover, from Planck's relation the frequency and thus wavelength of the incident and reflected light must be constant. Knowing that momentum is conserved, the wavevectors of the incident light and Bragg grating must equal the reflected wavevector [1]. Thus,

$$k_r = k_i + K \qquad \textbf{Equation 43}$$

where k_r is the wavevector of the reflected light, k_i is the wavevector of the incident light, K is the wavevector of Bragg grating, $K = 2\pi/\Lambda$ and Λ is the Bragg grating period, see Figure 25. The wavevectors of this system are shown in Figure 26 [1].

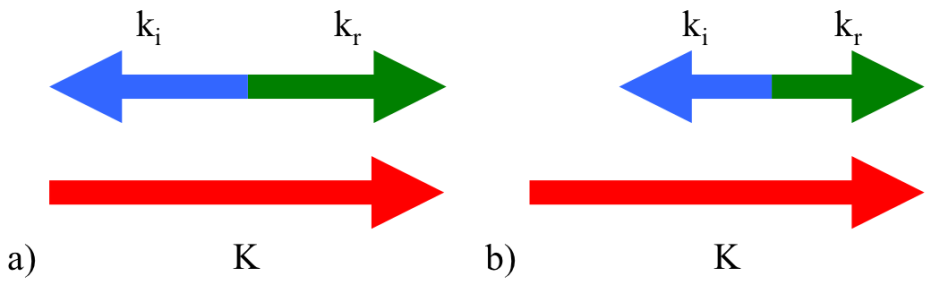

Figure 26 wavevectors of a Bragg grating, a) light satisfying the Bragg condition with a strong back reflection. b) the light does not satisfy the Bragg condition and thus minimal power is reflected.

Figure 26 a) shows the sum of the lengths of k_r and k_i are equal to the length of K, resulting in the system now being at resonance and hence light is coupled into a backward propagating mode. Figure 26 b) shows the sum of the wavevectors is not equal to the length of K, thus the system launches little or no power into the backward propagating mode. This situation relates to the condition where the

wavelength of the light is larger than that of the Bragg condition. As can be seen in Figure 26 a), the Bragg condition is met when $k_r = -k_i$. Hence Equation 43 becomes [1],

$$\frac{2\pi}{\lambda} n_{eff} + \frac{2\pi}{\Lambda} = -\frac{2\pi}{\lambda} n_{eff} \qquad \textbf{Equation 44}$$

where n_{eff} is the effective refractive index of the optical mode. Simplifying to,

$$\lambda_B = 2n_{eff}\Lambda \qquad \textbf{Equation 45}$$

where λ_B is the Bragg central wavelength of reflection.

3.3.2 Coupled mode theory

To further understand Bragg gratings, Coupled Mode Theory (CMT) can be a useful tool by allowing the spectral response to be modelled for a given Bragg grating structure. To begin the analysis an expression is defined which describes the refractive index profile encountered by the mode when travelling in the z direction [1]. The refractive index change the optical mode will interact with, when propagating along the grating, travelling in the z direction, is given by the following [1],

$$\delta n_{eff}(\mathrm{z}) = \overline{\delta n_{eff}}(\mathrm{z})\left(1 + \gamma \cos\left(\frac{2\pi}{\lambda} z + \phi(z)\right)\right) \qquad \textbf{Equation 46}$$

where $\overline{\delta n_{eff}}$ is the constant offset or 'DC' effective refractive index perturbation averaged over a single period (Λ), γ is the fringe visibility of the index change, and $\phi(z)$ describes the grating chirp. Following the analysis for codirectional coupling by Ghatak and Thyagarajan [1], the coupling between forward and backward propagating modes is described by,

$$\mathcal{E}(x,z,t) = \left(A(z)E_1(x)e^{-j\beta_1 z} + B(z)E_2(x)e^{j\beta_2 z}\right)e^{j\omega t} \qquad \textbf{Equation 47}$$

where $E_1(x)$ and $E_2(x)$ are the transverse mode patterns, β_1 and β_2 are the propagation constant for the forward and backward propagating modes and $A(z)$ and $B(z)$ are z dependent amplitudes. Consideration of perturbation and coupling terms for a weak grating [1] leads to the following coupled equations,

$$\frac{dA}{dz} = \kappa B e^{j\Gamma z} \qquad \textbf{Equation 48}$$

$$\frac{dB}{dz} = \kappa A e^{-j\Gamma z} \qquad \textbf{Equation 49}$$

where Γ is the core power confinement factor for the mode of interest, $\Gamma = \beta_1 + \beta_2 - K$, κ is the coupling coefficient and is defined as,

$$\kappa = \frac{\pi \overline{\delta n_{eff}}}{\lambda_B} \qquad \textbf{Equation 50}$$

In this case, the coupling is between two identical optical modes, just moving in opposite directions thus $|\beta_1| = |\beta_2| = (2\pi/\lambda_o)n_{eff}$, where $K = 2\pi/\Lambda$. The phase-matched condition of $\Gamma = 0$ (see Figure 26 a)) is used to solve Equation 48 and Equation 49.

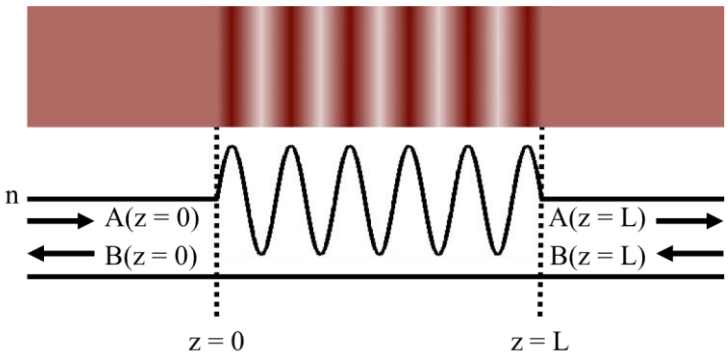

Figure 27 a periodic variation in core refractive index, with the directions of modal propagation shown.

Figure 27 is used to deduce appropriate initial conditions. It shows a Bragg grating of length L and it is assumed at $A(\mathrm{z} = 0)$ the power will be one and at $B(\mathrm{z} = \mathrm{L})$ there is no grating thus no backward propagating wave, so the power will be zero. By using these initial conditions, the ordinary differential equations in Equation 48 and Equation 49 can be solved using the adaptive step-size, 4th order Runge-Kutta numerical integration tool in Matlab [4]. The code used in this thesis has been adapted from a previous version written by Benjamin Snow [5].

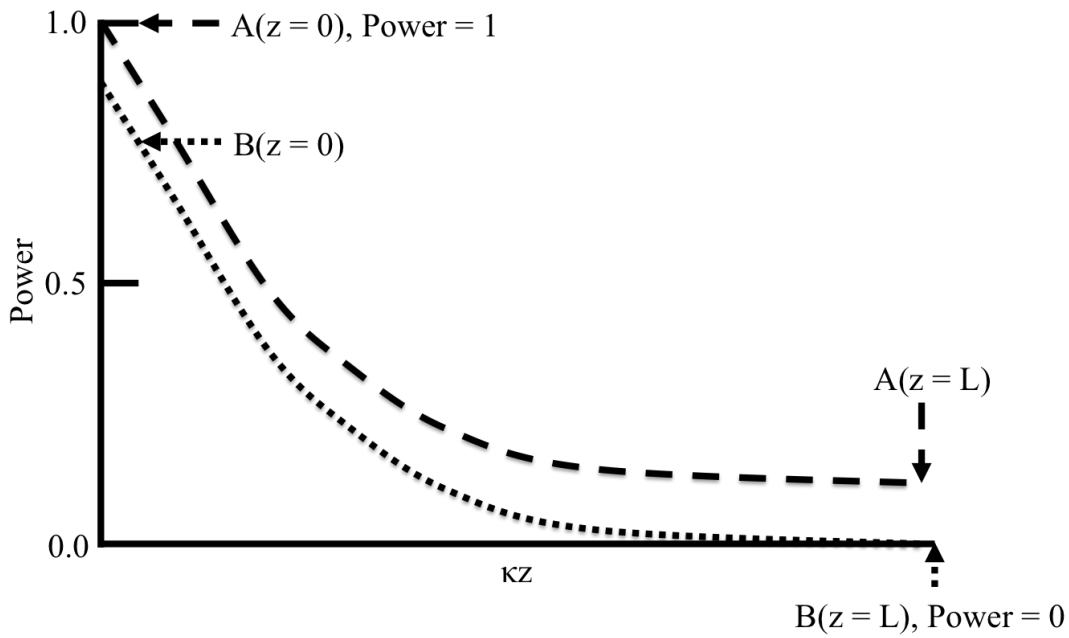

Figure 28 the exponential solutions to the coupled mode equations for a Bragg grating these are divided, the modulus taken and squared to find the reflectivity at a single wavelength, the process is repeated to find the whole spectra.

The code calculates the values of $B(\mathrm{z}=0)$ and $A(\mathrm{z}=\mathrm{L})$ by interpolating the exponential power drop along the grating (in the z direction) for each wavelength of interest, as shown Figure 28. Then to find the reflectivity of the grating the B and A exponents are divided, and the modulus is then taken and squared.

An analytical expression for a uniform Bragg grating's reflectivity is given by Erdogan [6],

$$r = \frac{sinh^2\left(\sqrt{\kappa^2 - \hat{\sigma}^2}L\right)}{cosh^2\left(\sqrt{\kappa^2 - \hat{\sigma}^2}L\right) - \frac{\hat{\sigma}^2}{\kappa^2}} \qquad \textbf{Equation 51}$$

where κ is the 'AC' coupling coefficient and $\hat{\sigma}$ is the 'DC' coupling coefficients, $\hat{\sigma} = \delta + \sigma$ where,

$$\sigma = \frac{2\pi\overline{\delta n_{eff}}}{\lambda} \qquad \textbf{Equation 52}$$

$$\delta = 2\pi n_{eff}\left(\frac{1}{\lambda} - \frac{1}{\lambda_B}\right) \qquad \textbf{Equation 53}$$

where δ is simply the difference in the k vector between the designed wavelength of operation (λ_B the central Bragg wavelength) and the other propagating wavelengths (λ). Hence the maximum reflectivity (r_{max}) is when $\hat{\sigma} = 0$,

$$r_{max} = tanh^2(\kappa L) \qquad \textbf{Equation 54}$$

and the maximum reflectivity occurs at a wavelength (λ_{max}) of,

$$\lambda_{max} = \left(1 + \frac{\overline{\delta n_{eff}}}{n_{eff}}\right)\lambda_B. \qquad \textbf{Equation 55}$$

As can be seen from Equation 51, a uniform Bragg gratings spectral response will be a sinc-squared type. By increasing grating parameters such as the 'AC' coupling coefficient (κ) and/or by increasing the grating length (L), the overall strength of the grating will increase, as shown by Equation 54. As κL is increased, saturation is reached and the Bragg grating begins to flat-top as shown in Figure 29 for $\kappa L = 8$.

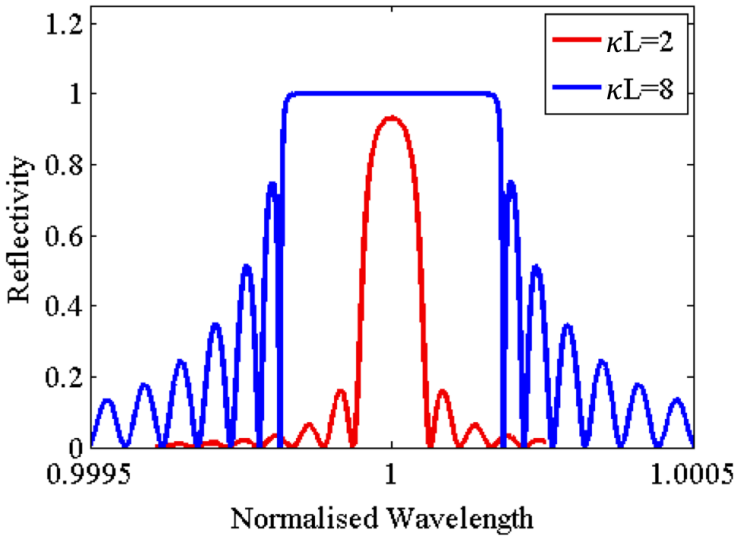

Figure 29 uniform Bragg gratings with different values of grating strength (κL).

Figure 29 shows two Bragg gratings of different strengths, the red line has a $\kappa L = 2$ and the blue line has a $\kappa L = 8$, where the blue line shows classic signs of saturation with it's flat topped central lobe.

The bandwidth of a uniform Bragg grating can be defined as the spectral width between the first zeros either side of the central reflection peak, which is described by [6],

$$\frac{\Delta\lambda_o}{\lambda} = \frac{\overline{\delta n_{eff}}}{n_{eff}} \sqrt{1 + \left(\frac{\lambda_B}{\overline{\delta n_{eff}} L}\right)^2} \qquad \textbf{Equation 56}$$

where $\Delta\lambda_o$ is the bandwidth. The bandwidth of a Bragg grating is dependent of the length of the grating (L) and the 'DC' effective refractive index modulation ($\overline{\delta n_{eff}}$). Within Equation 56 it depends if grating length or 'DC' effective refractive index modulation is the dominant term. In the case of the *weak grating limit* where $\overline{\delta n_{eff}} \ll \lambda_B/L$, the Bragg gratings length (L) becomes dominant and Equation 56 simplifies to,

$$\frac{\Delta\lambda_o}{\lambda} \approx \frac{\lambda_B}{n_{eff} L}. \qquad \textbf{Equation 57}$$

Conversely, in the case of the *strong grating limit* where $\overline{\delta n_{eff}} \gg \lambda_B/L$, the Bragg grating's 'DC' effective refractive index modulation ($\overline{\delta n_{eff}}$) becomes dominant and Equation 56 simplifies to,

$$\frac{\Delta\lambda_o}{\lambda} \approx \frac{\overline{\delta n_{eff}}}{n_{eff}}. \qquad \textbf{Equation 58}$$

Moreover, for the *strong grating limit*, light at the Bragg central wavelength (λ_B) may not propagate the full length of the Bragg grating because the first part of the grating will reflect all of the light. This is significant as it moves the average point of reflection from the spatial centre of the Bragg grating to closer to the end at which the light enters the structure. Furthermore, this adds complexity for calculating the strain sensed by a Bragg grating and is further discussed in chapter 5. Within this section CMT have been shown to be an effective way to calculate the spectra for a given Bragg grating structure. The strength of reflectivity and bandwidth have also been covered. In the next section Bragg grating apodisation is described.

3.3.3 Apodisation

The Bragg gratings shown in spectra up to now have had a uniform profile to their refractive index modulation. This is the reason for the presence of large side lobes around the central peak. These side lobes make the spectra more difficult to analyse and more difficult to fit using automated fitting algorithms, limiting their usefulness in sensing, filtering and dispersion compensation applications. To remove these side lobe oscillations, apodisation can be used and is done so by controlling the refractive

index modulation of the grating. When Fourier theory is applied to gratings, it can be used to infer spatial and refractive index profiles from spectral information and *vice versa*. The uniform grating's spectral response is a result of the Fourier transform of a sine wave, windowed by a rectangle function, which calculates a sinc and when squared to gain the intensity becomes a sinc-squared function, as depicted in Figure 29 and Figure 30. The side lobes are present because of the steep nature of the rectangle function, similar to the Fourier transform of a Dirac or Heaviside function. The steepness causes many different frequency sine waves to be included. Thus by windowing the sine wave of the grating with a smoother function, this smooths the resultant spectra. If a Gaussian windowing function is used it reduces the side lobes and in the case of a Gaussian function, it is also the Fourier transform of itself. All of the Bragg gratings produced for this thesis uses a Gaussian windowing function, where as Figure 30 shows a uniform and Gaussian apodised Bragg grating.

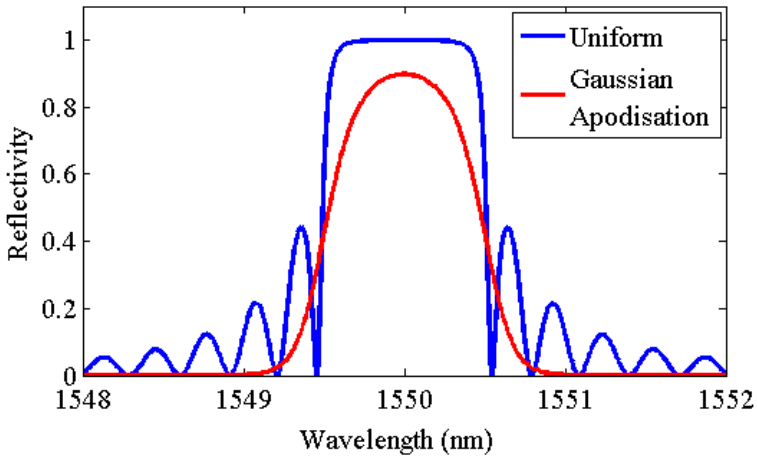

Figure 30 Unapodised (blue) and Gaussian apodised (red) Bragg grating spectra calculated using the coupled mode solver.

Figure 30 shows a uniform or unapodised Bragg grating (blue) and a Gaussian apodised Bragg grating (red). These were plotted using the coupled mode solver, which was discussed in section 3.3.2. Bragg grating apodisation has been covered, the next section discusses chirp, which is another grating parameter.

3.3.4 Chirp

Chirp is described as an increase/decrease in a signal's frequency with time. With sound it would be an increase/decrease in pitch (*i.e.* frequency) with time. For gratings, chirp can be described as an increase/decrease in grating period (Λ) with

position (z). Linear chirp has been used within this thesis as one of the fitting variables used in chapter 5. Linear chirp increases/decreases the grating period (Λ) in a linear manner with respect to the position along the grating, as shown by the modified central Bragg wavelength equation (Equation 45),

$$\lambda_B = 2n_{eff}\Lambda(z) \qquad \textbf{Equation 59}$$

and,

$$\Lambda(\mathrm{z}) = \Lambda_o + \Lambda_1(z) \qquad \textbf{Equation 60}$$

where Λ_o is the starting grating period and $\Lambda_1(z)$ is the grating period which varies in position. Within this thesis chirp is reported in nm/cm, which describes the spectral shift of the Bragg central wavelength (nm) for the position along the grating (cm).

This section has covered the theory of Bragg gratings and explained the concepts of coupled mode theory, apodisation and chirp. The next section summarises the manufacture of silica-on-silicon substrates using flame hydrolysis deposition, which allows definition of both buried channel waveguides and Bragg gratings. Silica-on-silicon is the doped form of silica used throughout this thesis for machining in chapters 4 and 6 and cantilever device production in chapter 5.

3.4 Silica-on-silicon fabrication

Silica-on-silicon is the predominant form of silica machined and experimented on, within this thesis. However, more detailed studies into the theory and manufacture have been undertaken within other theses [7] [8]. The key motivation behind using silica-on-silicon is that direct UV writing can be used to define single mode waveguides and Bragg gratings within it. Combining precision diced or milled structures with direct UV written integrated optic elements, provides a route to fabricate novel devices but also to interrogate optical properties of the machined interfaces. An example of a typical silica-on-silicon structure used throughout the thesis is shown in Figure 31.

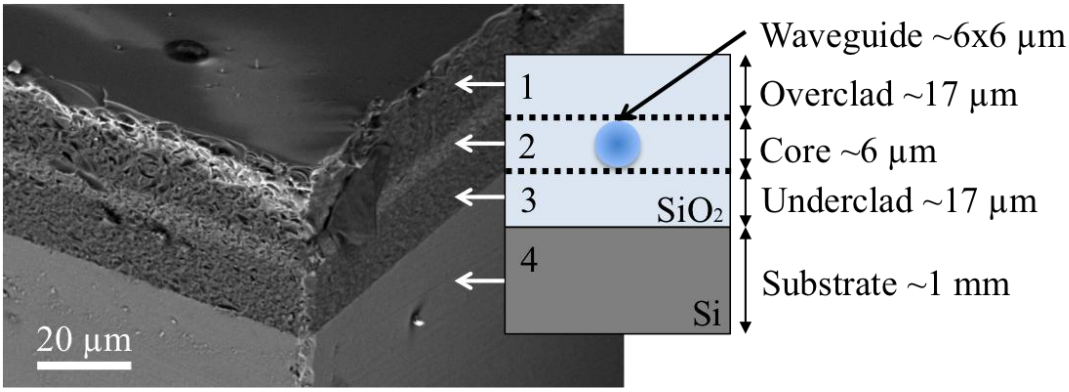

Figure 31 an SEM image and diagram of the typical silica-on-silicon structure used within this thesis. Note the thin light guiding silica layers upon the thick silicon substrate. SEM image courtesy of James Gates and Neil Sessions.

Within Figure 31 notice the relatively thin light guiding layers of the silica compared to the thick silicon substrate, where the typical thicknesses of the silica-on-silicon sample is given. The glass composition variation, defined by differences in doping concentration, is illustrated by the different shades of the overclad, core and underclad in the SEM image. This effect occurs because the SEM's backscatter detector was used and the difference in atomic weight of the layers, caused by the various atomic weights of the dopants, causes different scattering characteristics of the electrons from the sample's surface.

Fabrication of the silica-on-silicon substrate begins with the creation of the underclad, by wet oxidisation of a silicon substrate. Single side polished silicon wafers are oxidised in a wet furnace (H_2O), at 1100 °C for several weeks until a ~17 µm, of thermally grown silica has formed. 17 µm of thermally grown oxide is needed as the evanescent tail (see section 3.2.2), which exists in the cladding and can extends for ~15 µm. Thus, a thick oxide must be present to stop the light interacting with the silicon, which has a high relative refractive index (~3.5 at 1550 nm) and would couple and absorb the mode. The thermal oxide also acts as a stress relieving layer as the thermal process grows the layer on both sides of the wafer, helping to reduce the thermal mismatch between silicon and silica. These wafers are typically purchased from CIP (Centre for Integrated Photonics) Technologies and Gemfire Corp.. After this the guiding layer and the overclad are deposited typically using Flame Hydrolysis Deposition (FHD), Plasma Enhanced Chemical Vapour Deposition (PECVD) or sputtering. All of the samples used throughout this thesis

use FHD silica layers produced by CIP or at the University of Southampton's own FHD facilities. The typical dimensions and thermal oxide growth for the silica-on-silicon substrate have been covered. The FHD process used to produce the cores and clads of wafers is explained in the next section.

3.4.1 Flame hydrolysis deposition

Flame Hydrolysis Deposition (FHD), shown in Figure 32, can deposit glass films that are low loss and with low stresses. It is a popular glass deposition tool in the production of PLC because of its fast deposition rate compared to PECVD or sputtering.

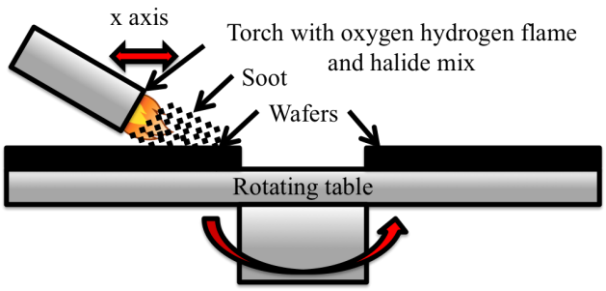

Figure 32 typical flame hydrolysis deposition system. This system has the ability to deposit large quantities (tens of microns per hour) of high purity, optical grade silica. It rotates samples on a table, while a torch passes over depositing a soot of silica and dopants. Deposition results from hydrolysis and oxidation reactions from halide precursors, which are bubbled through to the oxygen hydrogen flame.

As shown in Figure 32, an oxygen hydrogen flame produces a soot made from the halide precursors, which is deposited on the surface of the silica underclad. Reaction of the halides occurs from two distinct reactions; oxidisation (see Equation 61) and hydrolysis (see Equation 62). This forms a silica powder or soot, as seen below for silicon tetrachloride [9],

$$SiCl_4 + O_2 \rightarrow SiO_2 + 2Cl_2 \qquad \textbf{Equation 61}$$

$$SiCl_4 + 2H_2O \rightarrow SiO_2 + 4HCl\,. \qquad \textbf{Equation 62}$$

The prominence of which reaction, either hydrolysis or oxidation, is dictated by the flame temperature, where oxidation dominates above 1200 °C [9]. A flame temperature of 2000 °C [10] is the typically achieved for an oxygen hydrogen flame, thus oxidation dominates.

Dopants are commonly added to control the silica layers physical properties, such as refractive index, photosensitivity and melting point. The dopants used in this thesis were germanium, phosphorous and boron in halide forms. In a similar way to the silicon tetrachloride, soot is formed by either hydrolysation or oxidation. After the soot layer is deposited to form the core or overclad glass layer, the soot must be consolidated. Layer consolidation is achieved by annealing within a furnace at ~1360 °C for the core and ~1200 °C for the overclad, the process takes several hours. A layer-by-layer approach is used within silica-on-silicon production to stop diffusion of dopants from one layer to the next. Table 1 indicates what physical effect the dopants have on the glass layer [11] [12] [13].

Table 1 dopant effects on silica FHD layer (*partially increase but must be codoped with germanium, **promotes photosensitivity but only partially [13]**).**

Dopant	Refractive index	Photosensitivity	Melting point	Thermal expansion
Germanium	Increases	Increases	Decreases	Increases
Boron	Decreases	*	Decreases	Increases
Phosphorus	Increases	**	Decreases	Increases

The dopants germanium, phosphorous and boron each have various physical effects on silica layers, as shown in Table 1. The refractive index and photosensitivity of the layers is important when creating buried channel waveguides and Bragg gratings within the core layer using direct UV writing (see section 3.5). The refractive index profile will determine the guidance conditions and the mode profiles that are achievable. Typically the core layer of the wafers used within this thesis are doped with germanium and boron to increase the photosensitivity of the core layer, thus allowing direct UV writing, with germanium being the dominant dopant for increased photosensitivity. The overclad is doped with boron and phosphorous so it is *not* photosensitive to UV irradiation. Although, changes of ~10^{-5} in refractive index have been observed [13]. Phosphorous and boron are added to the overclad predominately to lower the consolidation temperature of the layer but also to control refractive index. Typical nitrogen flow rates and dopant pressures are given for different core and overclad recipes in Table 2 and Table 3, respectively.

Table 2 typical values for nitrogen bubbler flow and precursor pressures for FHD core layer fabrication.

Precursor	Nitrogen flow rate (l/min)	Pressure (kPa)
$SiCl_4$	114-142	25.9
$GeCl_4$	43-51	10.1
BCl_4	26-61	-

Table 3 typical values for nitrogen bubbler flow and precursor pressures for FHD overclad layer fabrication.

Precursor	Nitrogen flow rate (l/min)	Pressure (kPa)
$SiCl_4$	137-139	25.9
PCl_4	31	13.3
BCl_4	69-70	-

Photosensitivity can be described as a material property change for absorbed radiation. Within this thesis the desired material property change is in the core layer's refractive index with exposure to UV irradiation (244 nm), supplied from the direct UV writing system. This has been a well-known phenomena in germanium doped optical fibres and is the physical process used in the manufacture of fibre Bragg gratings [1]. Even though this phenomenon is heavily used in the production of Bragg gratings the underlying physical mechanisms are still unclear. It is thought that refractive index changes of germanosilicates is caused by UV bleaching and the breaking of $Ge-Si$ bands [11]. The relief of stresses frozen into the glass matrix during fabrication is also believed to be related [11].

Hydrogen loading can be used to further increase UV photosensitivity, without increasing germanium doping. Increased germanium doping is an unwanted route to increase photosensitivity as it can cause difficulty in glass consolidation and increases optical loss. Hydrogen loading uses high pressure hydrogen to ingress hydrogen into the glass samples. Throughout the work carried out within this thesis, samples were held at pressures of ~120 bar for at least one week. Hydrogen loading

is thought to increase photosensitivity by reacting at $Si-O-Ge$ sites to form $Si-OH$ and thus form oxygen deficient Ge. These oxygen deficient germanium sites have strong absorptions at ~240 nm thus aiding in UV photosensitivity [11]. Due to the limited dimensions of the hydrogen loading cell, it is unpractical to hydrogen load and direct UV write a whole 150 mm (6 inch) wafers. Thus, wafers are diced using the precision dicing machine into typically 20 by 10 mm chips. A resin bonded blade is used at a rotational speed of 20 krpm and a translational speed of 0.5 mm/s.

The process of using flame hydrolysis deposition to create silica-on-silicon substrates, that are suitable for direct UV writing, has been explained. In the following section the process of waveguide and Bragg grating definition in silica-on-silicon substrates using direct UV writing is discussed.

3.5 Direct UV writing

Direct UV writing and direct grating writing has been developed and even commercialised in the University of Southampton and at Stratophase Ltd. (a related spin out company) for over a decade. The motivation for the work drew on Svalgaard's original, late 1990's, research [14]. Thus, there are whole theses devoted to this subject, and some state of the arts texts have been written by Ian Sparrow [8] and Christopher Holmes [10]. In this section an overview will be given of the direct UV writing technique used throughout this thesis.

Direct UV writing is the name given to the definition of buried channel waveguides within the core layers of the silica-on-silicon samples described in section 3.4. Generally the process gives two dimensional confinement; the underclad and overclad giving the first dimension, and the refractive index change caused by the UV laser spot giving the second. To begin the process the UV laser spot is focused into the plane. To ensure the beam is focused across the whole chip, back reflection patterns are used and pitch and roll are corrected until the pattern is constant across the whole chip. The chip is then translated under the UV laser beam by CNC (Computer Numerical Control) to form the buried channel waveguides. The direct UV writing approach used within the thesis is the two beam direct grating writing

method and has the added advantage of creating simultaneous buried channel waveguide and Bragg grating definition.

3.5.1 Direct grating writing

Direct grating writing uses interfered beams from a UV laser to form an interference pattern, which enables Bragg gratings to be formed; see Figure 33.

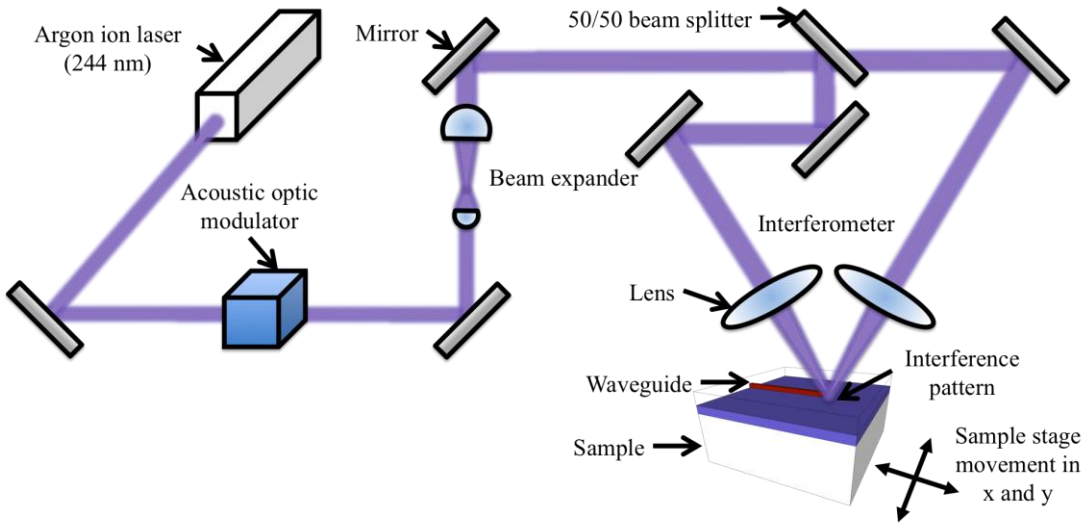

Figure 33 direct grating writing setup. The system has the ability to define single mode channel waveguides and Bragg gratings simultaneously with different central Bragg wavelengths and apodisations. This is achieved with UV laser radiation, which is amplitude modulated, passed through a free space interferometer and focused on a sample, which is translated by high precision high bearing stages.

Figure 33 depicts the direct grating writing system. As can be seen from Figure 33, an interference pattern is produced in the chip's core by interfering two light paths, which are split by a beam splitter. To control the position of the Bragg gratings, amplitude modulation is used by the means of an acoustic optic modulator. Effectively the acoustic optic modulator is used to modulate the laser power, on and off, allowing the pattern to be stamped into the core, thus forming a Bragg grating. Moreover, if the laser power is left on, the interference pattern is smeared out, forming a buried channel waveguide.

The UV laser source used in the setup depicted in Figure 33, is a frequency doubled argon-ion laser operating at 244 nm (Lexel, 95-SHG). The 488 nm line is excited within the argon-ion laser and this line is doubled by an intra-cavity beta-barium-borate, BaB_2O_4 (BBO) crystal. To excite the nonlinear process, phase matching is

achieved by angle tuning the crystal. The 244 nm laser ligth produced, excites both the photosensitivity of the germanosilicate and the oxygen deficient Ge sites caused by hydrogen loading to alter the refractive index (see section 3.4.1). Moreover, the good spatial coherence of the laser allows inference with its self, as the coherence length is greater than the interferometer path imbalance length.

The direct grating writing technique typically achieves 'DC' effective refractive index modulation or contrast ($\overline{\delta n_{eff}}$), *i.e.* the difference between the UV exposed refractive index and the initial refractive index, of $5\text{x}10^{-3}$ [10]. The refractive index contrast is dependent on the UV exposure and a succinct way of expressing this is via fluence. Fluence (F) is measured in kJ/cm^2 and is expressed in terms of intensity, laser spot diameter, exposure time and takes the form [10],

$$F = \frac{I_{UV} a}{v_{tran}} \qquad \textbf{Equation 63}$$

where I_{UV} is the average power density of the focused laser spot (kWcm^{-2}), a is the laser spot diameter (cm) and v_{tran} is the sample translation speed (cms^{-1}). To create Bragg gratings that reflect at wavelengths centred around the telecommunication C-band (1525-1565 nm), *e.g.* 1550 nm, the interference pattern must be tailored to produce fringe periods (Λ) (see Equation 45) of the order of 530 nm. Thus, for a spot size of ~6 μm, fewer than twelve fringes will occur. The fringe period in the interferometer shown in Figure 33, is dictated by the half angle (θ) at which the beams cross. Thus [10],

$$\theta = \sin^{-1} \frac{\lambda_{UV}}{2\Lambda} \qquad \textbf{Equation 64}$$

where λ_{UV} is the laser writing wavelength (244 nm). Thus the interferometer should be set to an angle at which the beams cross (2θ) at ~26.6° to achieve gratings at 1550 nm in silica.

To access other Bragg central wavelengths (λ_B) without changing the angle at which the beams cross, the period (Λ) or the effective refractive (n_{eff}) from Equation 45 can be altered to obtain the desired Bragg central wavelength. The way in which this direct grating writing technique obtains different Bragg central wavelengths is through detuning the period (Λ), where a small displacement is added or subtracted to the exposures of the interference pattern effectively smearing the set period (Λ).

This technique can be used to reach a Bragg central wavelength from 1400 nm to 1700 nm. However, because the interference pattern is smeared, the reflection strength of the Bragg grating is reduced as this detuning is increased, limiting the detuning range. In order to achieve these small detunings, high precision air bearing stages (Aerotech, ABL9000) were used, which have position resolution of 1 nm and repeatability of 100 nm.

In a similar manner to that of reflections seen in a transmission line system for mismatches in impedances, a similar effect is seen with Bragg gratings in waveguides. To achieve simple Bragg grating spectra without unwanted reflections, the average refractive index of the buried channel waveguide and Bragg grating must be matched. If this is not achieved, Fresnel reflections will occur at the interfaces *i.e.* where the Bragg grating meets the waveguide. The average refractive index can be controlled by modifying the laser's duty cycle, see Figure 34.

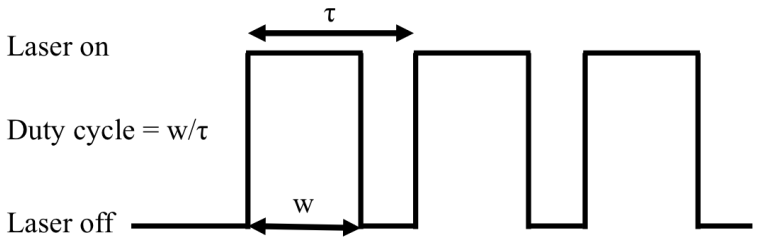

Figure 34 duty cycle definition for Bragg grating inscription.

Figure 34 shows the concept of duty cycle with respect to laser power. For a duty cycle of one, a channel waveguide is created, while conversely a duty cycle of zero creates no index change and a void is made between the waveguides. The larger the duty cycle the higher the average refractive index will be. However, to index match the channel waveguide and Bragg grating, the channel will have to be fabricated at a slower speed (v_{tran}) to achieve the correct fluence. Moreover, it has been found experimentally that a duty cycle of ~0.4 [10] must be used to achieve the maximum Bragg reflection strength. This is due to constraints on experimental considerations, such as the drift in laser power, the stability of the free space interferometer and sample stage. All of these contribute to the maximum achievable 'DC' effective refractive index modulation ($\overline{\delta n_{eff}}$), that a particular sample of germanosilicate

experiences. Figure 35 shows the duty cycle and speed profile needed to index match a uniform Bragg grating.

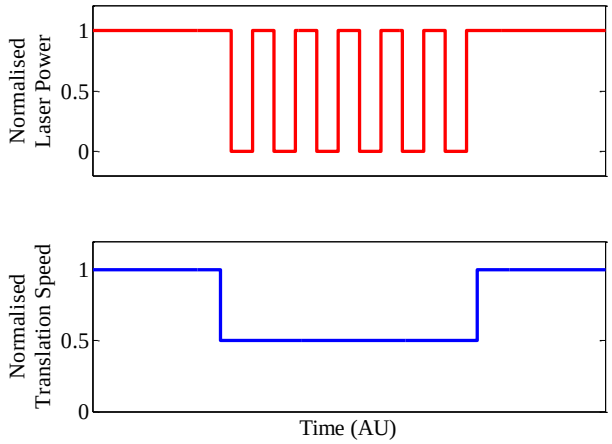

Figure 35 duty cycle and speed profile to create an index matched uniform Bragg grating within a waveguide.

To achieve Bragg gratings other than uniform gratings, apodisation of the refractive index profile is used. The apodisation of Bragg grating to achieve more desirable spectra, as discussed in section 3.3.3, is achieved by adjusting the duty cycle and translation speed along the length of the grating to effect the effective refractive index modulation. To achieve a Gaussian spectral response, using Fourier theory, the spatial profile must be Gaussian. To do this the duty cycle and translation speed have Gaussian profiles over the grating length, as shown in Figure 36.

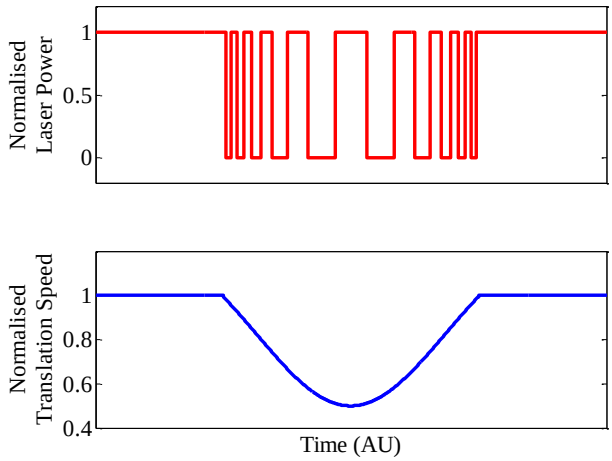

Figure 36 duty cycle and speed profile to create an index matched Gaussian apodised Bragg grating within a waveguide.

Figure 36 shows the duty cycle and translation speed change with a function of position over the grating length. To achieve a Gaussian grating response, the strength of the modulation changes in a Gaussian fashion, over the length of the Bragg grating by altering the duty cycle. This is similar to a technique called pulse width modulation, utilised in power electronics, which represents sine waves as a sequence of digital pulses with varying widths [15]. By changing the duty cycle over the grating, this changes the average refractive index across the grating too. To stop unwanted Fresnel reflections, the translation speed profile is also Gaussian to obtain the required fluence to ensure index matching. Figure 37 shows experimental implementation of the Gaussian apodisation technique compared with a uniform Bragg grating.

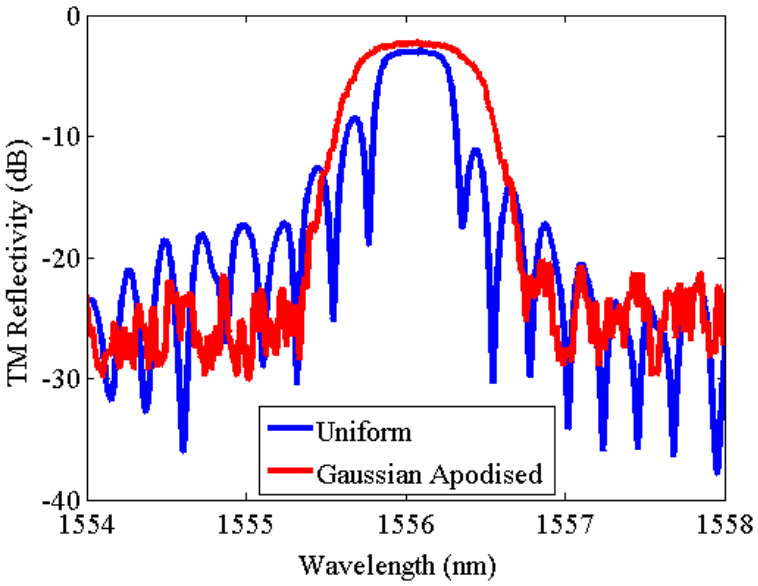

Figure 37 two Bragg gratings, 3 mm in length, both written with a fluence of 14 kJ/cm^2 and a duty cycle 0.4. These spectra should be similar to the simulation shown in Figure 30, where the Gaussian apodised peak sits below the uniform apodised peak. However, here because of different launch efficiency for each waveguide interrogated, which is not taken into account when normalising, there is this discrepancy.

Figure 37 shows the reflectivity of both a uniform (blue) and Gaussian (red) apodised Bragg grating, both being 3 mm in length and written with a fluence of 14 kJ/cm^2 and a duty cycle 0.4. Notice that the reflection strength is similar for both of the gratings but the Gaussian Bragg gratings has a larger bandwidth. The Gaussian apodised Bragg grating has $\gtrsim$20 dB of side lobe suppression, making it spectrally simpler to fit to. Typically, uniform apodised Bragg gratings should have a greater

amplitude than Gaussian apodised Bragg gratings, for a similar lengths and writing conditions. Figure 37 shows the opposite of this, which is most likely due to different coupling efficiency achieved when coupling from one waveguide to the next. This assumption can be made because both the uniform and Gaussian apodised Bragg gratings show flat-tops, which is the classic sign of saturation. The normalisation described in the next section does not take the coupling efficiency from the interrogation equipment to the waveguide into account.

The production of silica-on-silicon with the process of defining waveguides and Bragg gratings using direct grating writing has been covered in the previous sections. The standard method for optical characterisation of these waveguides and gratings is explained in the following section.

3.6 Waveguide and Bragg grating characterisation

To optically characterise waveguides and Bragg gratings after direct UV writing, a spectrally broadband interrogation routine is used, as shown in Figure 38 and schematically in Figure 40.

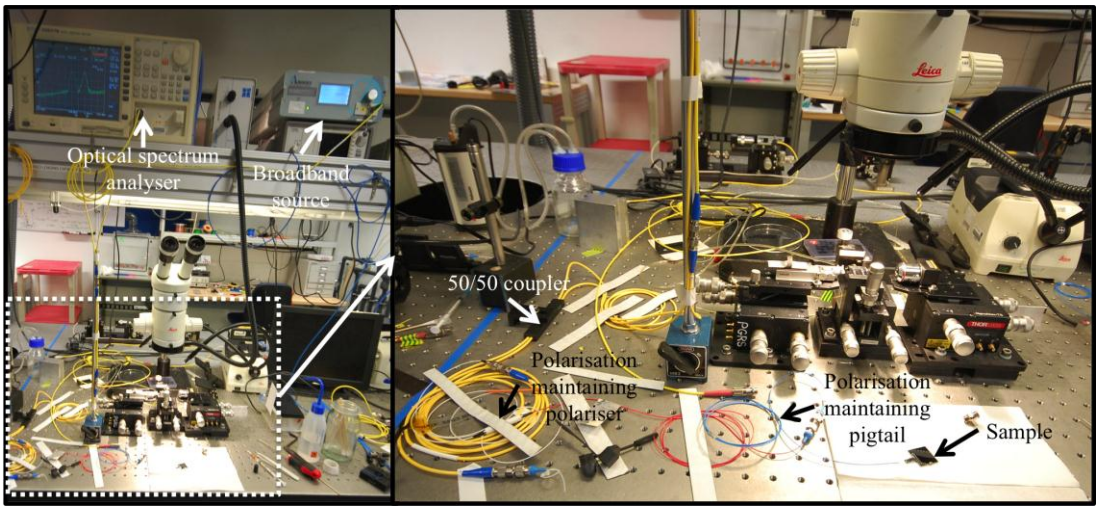

Figure 38 waveguide and Bragg grating broadband characterisation setup.

Broadband infrared light is supplied to the waveguide structure by either an Amplified Spontaneous Emission (ASE) source or a Superluminescent Diode (SLED). An AFC, BBS 1550 A TS erbium fibre ASE and Amonics, ASLD-CWDW-

5-B-FA were used for the ASE and SLED sources, respectively. The difference in these sources is the spectral broadness, where the SLED has a far broader spectrum than the ASE source as shown by Figure 39.

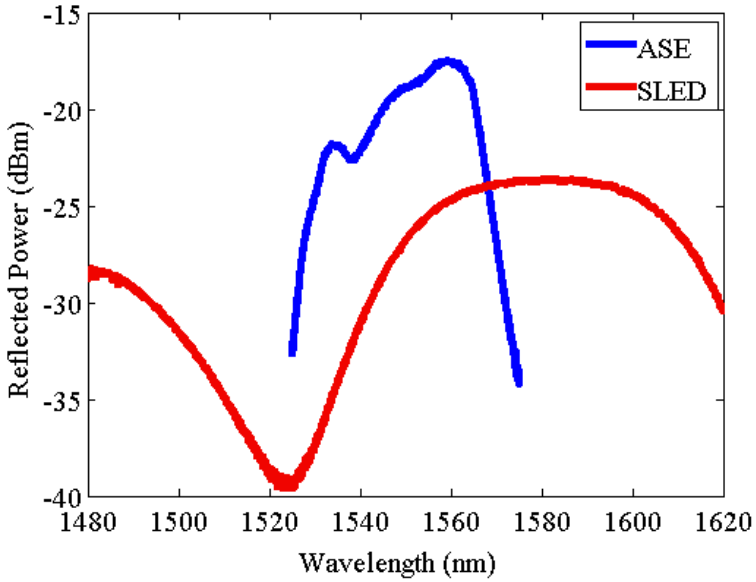

Figure 39 background spectrum from the broadband emission from the Amplified Spontaneous Emission (ASE) and Superluminescent Diode (SLED) used throughout thesis.

As shown schematically in Figure 40, infrared light is coupled into a 50/50 splitter and then into a Polarising Maintaining (PM) polariser, which polarises the inserted light and its output is aligned to the ferrule keyway of the PM output fibre. This PM polariser is then connected to a PM pigtail, which is aligned to the waveguide using a stage system, pictured in Figure 38. Temporary and permanent coupling was achieved by using either refractive index matching gel (ThorLabs G608N3) or UV-curable glue (Dymax OP-4-20641), respectively.

Within this thesis PM fibre optic pigtails have been used throughout to characterise waveguides and Bragg gratings. PM pigtails were purchased from OZ Optics Ltd.. The PM pigtails construction involved a PM fibre being glued into a silicon v-groove and capped with a silica block. The polarisation was set by rotating the PM fibre in the v-groove until the magnetic field of the TM polarisation was parallel to the top and bottom faces of silicon and silica blocks or the plane of the chip's core layer. Thus, to access the TM polarisation of the sample a ferrule with its keyways aligned to each other was used to connect the PM polariser and the pigtail. Moreover, to

access the TE polarisation of the sample a ferrule with its keyways aligned 90° to each other was used to connect the PM polariser and the pigtail.

The unused fibre of the 50/50 splitter is terminated to prevent back reflections. One of the fibres of the 50/50 splitter is sent to an Optical Spectrum Analyser (OSA) (Ando, AQ6317B). The OSA is connected via General Purpose Interface Bus (GPIB) to a computer operating Labview allowing spectra to be collected. Intensity/wavelength data is acquired from the OSA via a GPIB connection and Labview is used to manipulate and save it. The Labview software is also used to fit Gaussian envelopes to Gaussian apodised Bragg gratings. The software allows parameters such as Gaussian width, centre wavelength, peak intensity and intensity offset to be extracted on the fly.

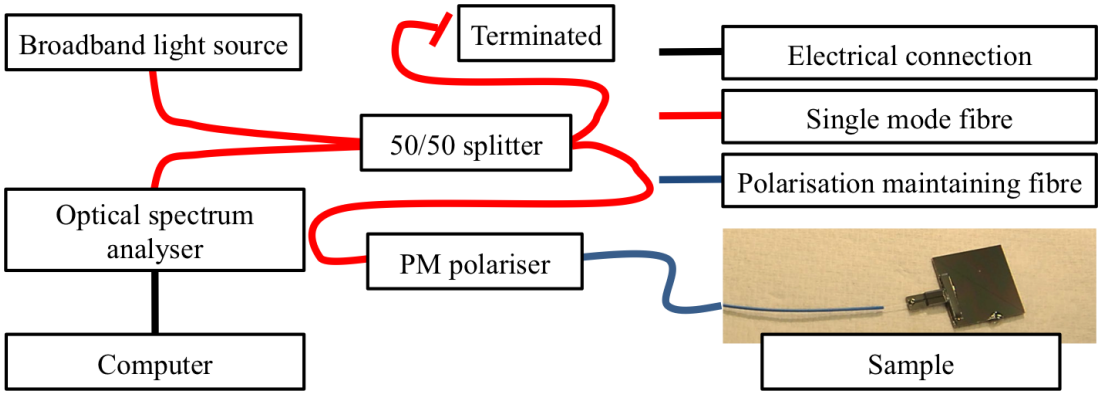

Figure 40 schematic of characterisation setup.

Both the broadband light sources shown in Figure 39 have intensity variation along their spectra. To normalise to these intensity variations, the intensity must be taken at a known reflectivity. This is achieved by disconnecting the sample and recording the ~4% of light reflected from the silica/air interface of the fibre. This background spectrum is taken with the OSA and then divided by the spectra collected from the sample, the logarithm is then taken giving the reflectivity in decibels. The background spectra is also used as a check to identify broken or contaminated equipment, as the spectra should not change significantly between setups. Optical characterisation of these direct UV written waveguides and gratings have been explained, with details on the equipment used, methods for temporary and permanent optical coupling and spectral normalisation.

This chapter has included theory and techniques used throughout this thesis. Some of the concepts in waveguide theory are used to in chapter 6 when the effect of surface roughness on waveguides is summarised. Coupled mode theory is used in the fitting of spectra in chapter 5. FHD silica-on-silicon is used throughout the thesis as the main substrate for machining testing. Examples of direct UV written waveguides and Bragg gratings are presented in chapters 4 and 5.

References

1. A. Ghatak and K. Thyagarajan, *Introduction to Fiber Optics* (Cambridge University Press, 1998), pp. 16–477.

2. D. J. Griffiths, *Introduction to Electrodynamics*, 3rd ed. (Pearson Education inc, 2008), pp. 408–410.

3. K. Okamoto, *Fundamentals of Optical Waveguides*, 2nd ed. (Elsevier Inc, 2006), pp. 27–41.

4. P. Bogacki and L. F. Shampine, "A 3(2) Pair of Runge - Kutta Formulas," Applied Mathematics Letters **2**, 321–325 (1989).

5. B. D. Snow, "Thesis: Liquid Crystal Adaptive Planar Optical Devices," University of Southampton (2010).

6. T. Erdogan, "Fiber grating spectra," Journal of Lightwave Technology **15**, 1277–1294 (1997).

7. S. P. Watts, "Thesis: Flame Hydrolysis Deposition of Photosensitive Silicate Layers Suitable for the Definition of Waveguiding Structures through Direct Ultraviolet Writing," University of Southampton (2002).

8. I. J. G. Sparrow, "Thesis: Development and Applications of UV Written Waveguides," University of Southampton (2005).

9. J. R. Bautista and R. M. Atkins, "The formation and deposition of SiO2 aerosols in optical fiber manufacturing torches," Journal of Aerosol Science **22**, 667–675 (1991).

10. C. Holmes, "Thesis: Direct UV Written Planar Devices for Sensing and Telecommunication Applications," University of Southampton (2009).

11. M. G. Sceats, G. R. Atkins, and S. B. Poole, "Photolytic Index Changes in Optical Fibers," Annual Review of Materials Science **23**, 381–410 (1993).

12. D. Shin, "Effect of boron concentration on the UV photosensitivity of silica glass film for planar lightwave circuit," Applied Surface Science **253**, 8003–8007 (2007).

13. B. Malo, J. Albert, F. Bilodeau, T. Kitagawa, D. C. Johnson, K. O. Hill, K. Hattori, Y. Hibino, and S. Gujrathi, "Photosensitivity in phosphorus-doped silica glass and optical waveguides," Applied Physics Letters **65**, 394–396 (1994).

14. M. Svalgaard, C. V. Poulsen, A. Bjarklev, and O. Poulsen, "Direct UV writing of buried singlemode channel waveguides in Ge-doped silica films," Electronics Letters **30**, 1401–1403 (1994).

15. S. J. Chapman, *Electric Machinery Fundamentals*, 4th ed. (McGraw-Hill, 2005), p. 202.

4 Precision Dicing of Silica

4.1 Introduction

This chapter focuses on the optimisation of the dicing process to create low loss input/output facets in the silica-on-silicon platform. A loss measurement for free space launching is carried out and the loss caused by the dicing process is calculated. The motivation for the optimisation of free space input/output facets in the silica-on-silicon platform is to create lower loss coupling. Smooth facets are particularly useful for free space launching, as index matching oils or epoxies cannot be used, which typically reduce the tolerances on facet form and surface roughness. This research has benefitted many applications in the research group including: refractometer devices [1], single photon resolving detectors (Paolo Mennea), corner mirrors [2], laser diode coupling (James Gates and Steven Lynch) and flat fibre, multimode interference devices [3].

A dicing machine, used in the dicing process, can be likened to a circular saw. The technique was originally developed for the semiconductor industry to allow dies to be sawn from a wafer after photolithographic processing. Surprisingly dicing techniques, other than die separation have seen very little application to optics. Areas where the precision dicing has been employed includes lithium niobate waveguides for nonlinear processes [4], Neodymium: Yttrium Aluminium Garnet (Nd:YAG) crystal waveguide lasers [5] and Arrayed Waveguide Gratings (AWG) spectrometers [6]. Dicing has also been used to create microcantilevers which is discussed in chapter 5.

This chapter includes an overview of dominant machining factors affecting dicing quality in silica-on-silicon. By monitoring facet surface roughness the dicing procedure is optimised, with the blade rotational speed and sample translational speed being the parameters that are varied. Comments are made on the facet surface roughness, texture and chipping and is compared to a lapped and polished silica facet. After finding the optimised machining parameters by monitoring facet surface roughness, these parameters are used to create a groove through a waveguide containing Bragg gratings. The grooved waveguide is used to determine the average interface loss per facet, caused by scattering as a consequence of facet surface roughness. The facet quality of diced in house fabricated silica-on-silicon wafers is discussed. The fabrication of GGG ($Gd_3Ga_5O_{12}$, Gadolinium Gallium Garnet) channel waveguide lasers using diced trenches to form the ridge waveguide, is commented on.

4.2 Dicing principles

At its simplest level the precision dicing machine is a circular saw. At the machine's heart is an aerostatic spindle, which has an inherently smooth rotational action. This is in addition to the high positional accuracy of the sample bed, which allows micron scale features to be cut into substrates, see Figure 41. Samples can be diced, cut all of the way through, or grooved to make a small channel. The blades used contain diamonds, which are either bonded or sintered into resin or nickel, respectively. The surface roughness and amount of chipping for cutting brittle materials (*e.g.* silicon, silica, lithium niobate *etc.),* is highly reliant on machine setup.

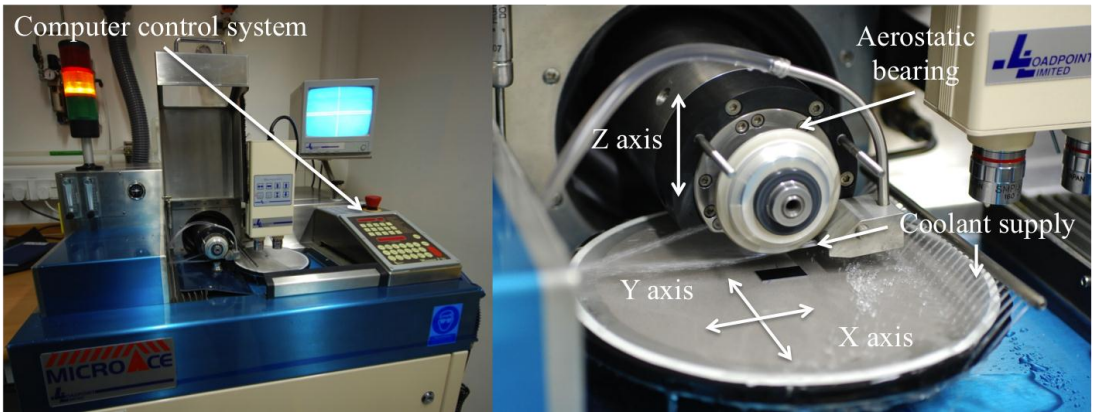

Figure 41 the Loadpoint MicroAce Series 3 (*Daisy the Dicer*). This system uses a high precision aerostatic bearing spindle to obtain a smooth rotational motion where sample movement is achieved by a precision bed.

The machine setup depends upon the following parameters: Blade rotational speed, sample translational speed, depth of cut, sample cooling, blade bond material, diamond size and dressing. These are all dominant parameters needed to obtain good quality grooves in brittle materials (*i.e.* groove with high sidewall verticality, nanoscale roughness and low surface chipping) [7]. The basics of precision dicing have been covered, the next section defines the requirements of free space input/output facets in silica-on-silicon waveguides.

4.3 Requirements for dicing input/output facets

The general requirements for free space input/output facets in silica integrated optics are high verticality, nanoscale roughness and low surface chipping, which yields low loss coupling. The large scale, one dimensional, form error for an interface for input/output coupling, is how vertical it is with respect to the waveguide. Thus, it is measured as an angle (α) as shown below in Figure 42.

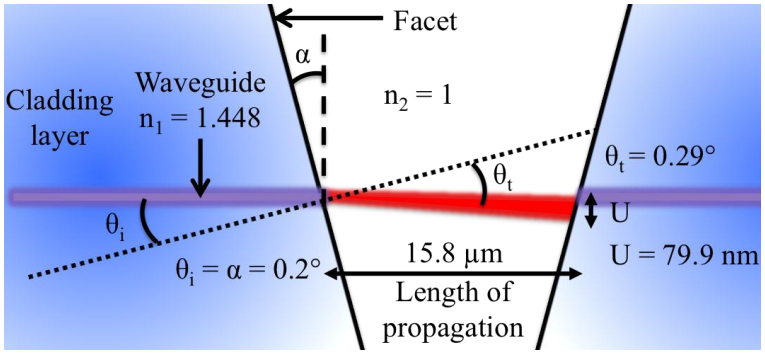

Figure 42 schematic showing the angle at which the facet deviates from vertical with respect to the waveguide. Using Snell's law the angle (θ_t) at which the light refracts can be calculated.

To find the angle at which the light refracts at (θ_t), Snell's law can be used in the following form [8],

$$\theta_t = \sin^{-1}\frac{n_1 \sin\theta_i}{n_2} \qquad \textbf{Equation 65}$$

where the various refractive indices and angles are shown in Figure 42. By knowing the angle of refraction and the length of propagation of the light and by using trigonometry, the transverse misalignment (U) from an opposing waveguide can be calculated. Thus, the free space coupling loss due to modal mismatch from transverse misalignment can be calculated [8],

$$\alpha_T = 1 - exp\left(\frac{-U^2}{\omega^2}\right) \qquad \textbf{Equation 66}$$

where α_T is the fractional loss from transverse misalignment, U is the transverse mismatch and ω is the modal field diameter. ω is ~10 µm for the single mode, silica-on-silicon, channel waveguides at 1550 nm. Figure 43 shows the loss expected for facets with different angles (α), for different lengths of propagation.

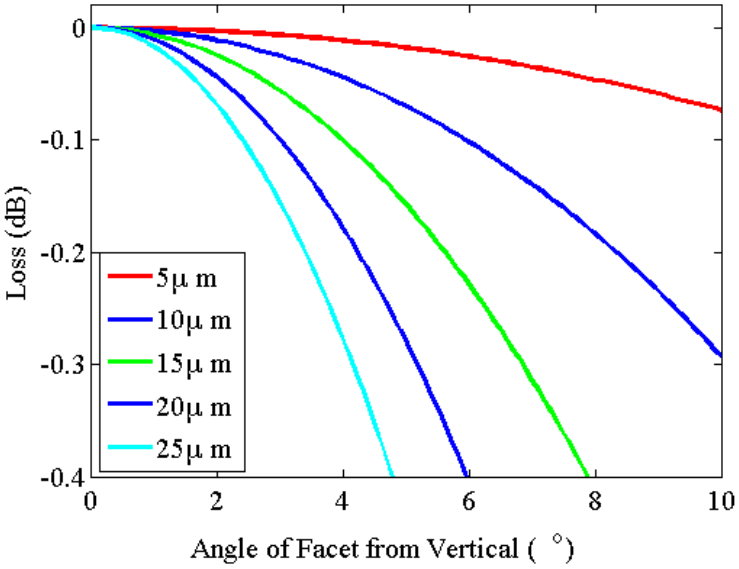

Figure 43 loss from facets that deviate from vertical, *i.e.* are not perpendicular to the waveguide, for different lengths of propagation. 15.8 μm is the length of propagation used in the experiment detailed in section 4.6.

From Figure 43, a loss of -0.5 dB is expected for a propagation of length of 15 μm for 8.5 ° from vertical. From previously diced grooves the verticality of diced sidewalls has been measured to be <0.2° from vertical, by SEM inspection. Thus for an angle of 0.2° and a length of propagation of 15.8 μm, which is used in section 4.6, a loss of -2.8 $x10^{-4}$ dB is calculated. Thus, facet verticality is negligible for diced grooves.

The surface roughness, along with verticality, is another one of the general requirements for free space input/output facets in silica integrated optics, as shown below in Figure 44.

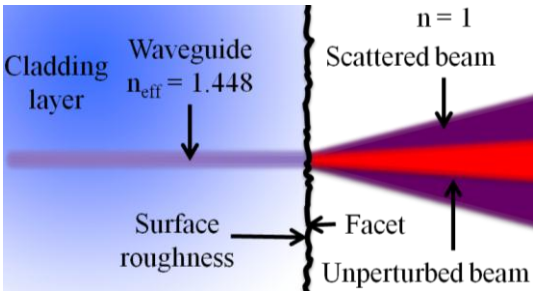

Figure 44 facet surface roughness causing beam perturbation, which acts as a loss mechanism and scatters in a broad range of angles.

The nanoscale surface roughness, shown in Figure 44, is small when compared to the wavelength of light of operation (λ). Thus, scattering caused by facet surface roughness is said to be in the Rayleigh regime, where light scatter is proportional to λ^{-4} [8]. Scalar scattering theory tells us that, in the case of normal incidence light, the scattered part of the beam can be related to RMS surface roughness (Rq), by the following equation [9] [10],

$$R_d = R_o\left(1 - exp\left(-\left[\frac{4\pi R_{\mathrm{q}} n_{eff}}{\lambda}\right]^2\right)\right) \qquad \textbf{Equation 67}$$

where R_d is the scattered beam, R_o is the unperturbed beam, R_q is the RMS surface roughness, n_{eff} is the effective index of the waveguide and λ is the wavelength of operation. Thus by reducing surface roughness the amount of scatter is also reduced and thus lowers the achievable interface loss. R_d acts as a loss mechanism and scatters in a broad range of angles, unlike the specular beam which is still estenitally Gaussian. Using Equation 67 cannot produce an estimate of loss from scattering, as R_d and R_o are values that typically are gained from performing a total integrated scatter experiment. These experiments typically use integrating spheres to determine both R_d and R_o, for free space optic components.

An experimental approach has been used by Gharbia *et al.* to find the coupling efficiency of ground silica Single Mode Fibre (SMF) facets, with different surface roughnesses [11]. Each fibre facet was ground [12] using various grit sizes ranging from 3-0.5 µm to produce different surfaces roughnesses; a cleaved fibre was also included. To collect coupling loss data from the SMF, 633 nm laser light was coupled into a cleaved end of the fibre and light was then launched from the ground facet into free space and collected on a photodiode. Atomic force microscopy was used to collect the surface roughness from each fibre optic facet. To fit the data to a logarithmic scale, linear fitting was used to obtain the intercept for normalisation, which is shown in Figure 45.

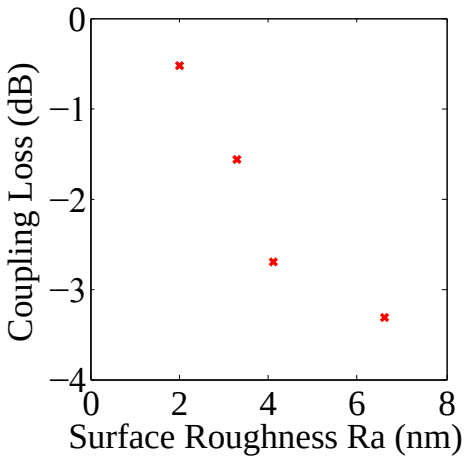

Figure 45 fibre optic facet surface roughness against the coupling loss, notice the reduction in loss for a reduction in roughness [11].

Figure 45 shows that reduction in coupling loss from a SMF facet can be achieved by reducing facet surface roughness. Notice, for a surface roughness of 4.0 nm a coupling loss of ~2 dB is achieved. If the surface roughness is approximately halved to 2.3 nm, the loss is halved to ~1 dB. The wavelength of light of operation in the work (λ) presented in [11], is 633 nm (fibre optic single mode at 633 nm). However, within this thesis, λ = 1550 nm. Thus, by working at a longer λ less coupling loss will be seen because of the λ^{-4} dependence of Rayleigh scattering.

If the input/output facet has both high verticality and nanoscale roughness, the last requirement would be to have low surface chipping. Chipping can be classified as a combination of misalignments (transverse and/or angular), with surface roughness, depending how the chip has formed. The effects from surface chipping can be reduced by the employment of a thick overclad. However, in many waveguide geometries this is not possible, highlighting the need to reduce the probability of a chipping event.

In this chapter, facet surface roughness is used to optimise the dicing procedure. The reasoning for optimising surface roughness rather than sidewall verticality or chipping, is that high sidewall verticality is typically obtained because of the mechanical interaction of the blade and substrate [7]. Moreover, if the material is removed in a ductile machining regime (see chapter 2), to obtain the low surface roughnesses needed, no chipping should occur. Surface roughness is also quantitative and easily obtained through surface profiling. The dependence on

angular misalignment in terms vertically, surface roughness and chipping for a machining interfaces with low optical losses have been discussed. The following section discusses the experimental procedure, where surface roughness is used to optimise dicing parameters.

4.4 Dicing procedure

Literature was consulted to obtain a starting point for grooving facets in silica-on-silicon. In the papers, comments on sidewall surface roughness were usually qualitative and not quantitative. For example, machining parameters were found for diced Nd:YAG crystal waveguide lasers, where 'smooth' results were achieved [5]. The dicing parameters used were as follows: depths of cut of 4.5-9 μm, a rotational speed of 20 krpm and a translational speed of 0.1 mms^{-1} [5]. In the fabrication of lithium niobate waveguides, no quantitative roughness measurement is given either but again 'smooth' results were achieved [4]. Dicing parameters included a depth of cut of 526 μm, a rotational speed of 10 krpm and translational speed of 0.2 mms^{-1} [4]. The machining of Pyrex #7740 has been reported by Plaza *et al.* [6]. To create 800 μm high square pillars, a depth of cut of 800 μm, a translational speed of 0.3 mms^{-1} and a rotational speed of 28 krpm with a resin bonded blade was used [7]. However, surface metrology was not given but the images of the Pyrex structures look particularly rough.

Information on the fundamentals of dicing is lacking in academic literature, whereas a large body of work can be found on the subject of grinding (see chapter 2). Where grinding has been written about, there is an emphasis on free space optics and ceramics [13]. The principle ideas of high quality grinding however can be applied to the dicing technique as they both use abrasives held in a binder. Generally, it can be said that to obtain good quality dicing in brittle materials, blades with the smallest diamond size (largest grit size) and in the lowest concentration, with the softest wearing bond should be used [5] [14] [15]. The diamond size is crucial if nanoscale roughnesses is to be achieved. However, there is a point where the diamonds become too small, causing the blade to wear too quickly, affecting the overall form of the

groove (*i.e.* the grooves depth will decrease as the blade wears). Moreover, if the diamonds are too large, the scratches made while dicing are too deep to obtain the surface roughness required. Choosing a soft wearing blade bond allows the blade to lose dull cutting diamonds by the increased friction they see at the cutting interface. These dull diamonds are torn from the blade matrix and fresh cutting diamonds are exposed [16], thus maintaining the surface quality while dicing. Extremely thin grinding-tool studies performed on 'optical glass' by Chen *et al.* [15] suggested that slow translational speeds and shallow depths of cut can initiate ductile type machining. Ductile type machining being a route to silica grooves with nanoscale roughness and low surface chipping.

To discover the dicing machine parameters that machine silica-on-silicon in a ductile regime, a machine parameter test is undertaken by varying the blade rotational speed and translation speed. The dicing parameters used in the machining of Pyrex, Nd:YAG and lithium niobate, discussed in section 4.4, were taken into consideration. The parameters kept constant consisted of the dicing machine used, blade dressing and sample cooling which are covered in the next section.

4.4.1 The machine, dressing and coolant

For the dicing experiments carried out within this thesis, a Loadpoint MicroAce Series 3 was used, shown in Figure 41. The MicroAce has a positional accuracy of 2 μm in the x and y axes and 1 μm in the z axis. The dicing procedures of blade dressing and sample cooling were both suggested by the dicing machine and blade manufactures. Blade dressing entails the machining of a sacrificial material, typically at speeds greater than those used for machining of the final substrate. The reason for blade dressing is twofold. Firstly, it trues the blade to the rotational centre of the spindle and removes any offset from clamping or blade manufacture [17]. Secondly, it aids in the removal of old dull diamonds from the blade bond, leaving fresh cutting diamonds in its place [17]. In order to ensure the blade temperature is stabilised, coolant is used. This also stabilises the sample temperature, whilst providing lubrication at the cutting interface and removes cutting debris [17]. However, it is difficult to say if lubrication in the macro sense, is happening at the micro scale as suggested by the equipment manufacturer. A discussion on blade type, grit size and bond material is covered in the next section.

4.4.2 Blade selection

As detailed in the previous section 4.4.1, grit size and concentration are important for reducing surface roughness. Typically nickel bonded blades, when compared to resin bonded blades, have a greater range of smaller thickness blades. The thinnest blade available at the time was selected, to reduce diffraction losses caused by light propagating across the groove, see section 4.6. Thus, a Disco ZH05-SD5000-N1-50 BA blade was used. The nickel bonded blade had a diameter of ~54.5 mm, a width of 15-20 µm, grit size of #5000 (~0.5-3 µm in size) and the lowest grit concentration for this blade. However, recently a resin bonded blade (Disco P1A8-53-SD5000-R-10-MB01), has been used in the production of Nd:YAG waveguide lasers [5]. Notice, the same grit size of #5000 is used, a low grit concentration (10) and a weak bond strength (B01). The weak bond strength allows for more efficient in-machining dressing. Figure 46 shows an SEM micrograph of a Disco MBT-6476 SD4000-L-50-MT38 blade, which has a similar diamond size to that of the Disco ZH05 blade used.

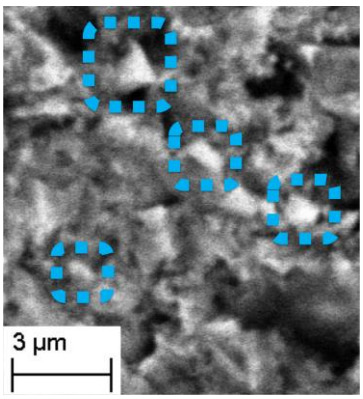

Figure 46 SEM micrograph of dicing blade, blue dashed lines shows diamond size and locations. Diamond grit size range from ~0.5-3 µm in size.

Figure 46 shows that for a dicing blade of SD4000 grit, the diamonds are typically a ~0.5-3 µm in size. In this section initial dicing parameters from literature and key parameters such as the dicing machine, blade dressing, coolant and blade type have been discussed. In the following sections the dicing parameter test is expanded upon and sidewall metrology is included.

4.5 Optimum dicing parameters for silica-on-silicon

A dicing parameter test was used to find the parameters needed to obtain the smoothest groove sidewall in the silica waveguiding layer of the silica-on-silicon substrate, see chapter 3. This work has been the subject of a conference paper [18]. The experimental procedure starts with the blade being dressed in a 100 mm wafer of silicon. The depth of cut is 100 µm, with a rotational speed of 20 krpm, with a translation speed of 1 mms^{-1} for five passes and 3 mms^{-1} for a further five passes, and was the process advised by the blade producer. Cleaned FHD samples were then fixed to UV sensitive tape, as shown in Figure 47. This tape was chosen due to its loss of adhesion when exposed to UV light. The depth of cut was set to 100 µm, which corresponds to an actual depth of cut of ~60-80 µm due to an offset and uncertainty in the height sensing system of the dicing machine. The 100 µm depth of cut was set to ensure the silica layer is completely cut through, see Figure 48. The silica-on-silicon samples were grooved with the following machining parameters: rotational speeds of 15k, 20k and 25k rpm with translational speeds of 0.1, 0.3, 0.5, 0.7 and 0.9 mms^{-1}. The pairing of rotational and translational speeds creates fifteen grooved samples. One litre per minute of deionised water was used as cooling throughout the experiments, as recommended by Loadpoint. Each time a groove was made, an automated height sensing routine was utilised to compensate for blade wear.

Figure 47 mounting of four silica-on-silicon chips with 100mm silicon wafer for blade dressing on the UV sensitive tape.

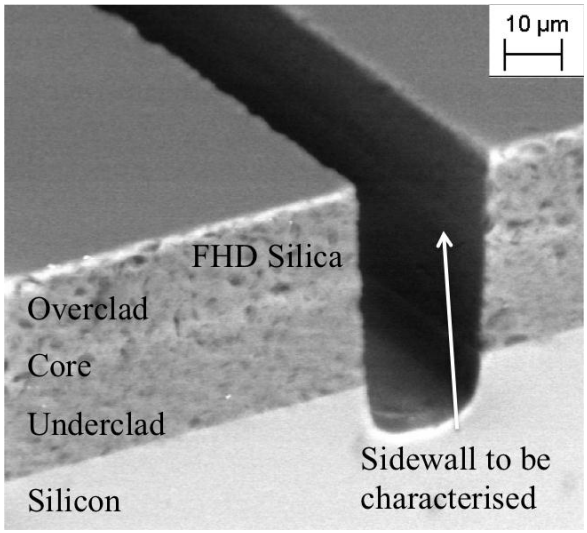

Figure 48 SEM micrograph of a facet grooved into the silica through to the silicon layer of a silica-on-silicon sample. Notice the high sidewall verticality and the rounding at the bottom of the groove, which is characteristic of all diced grooves.

After the groove has been diced, inspection of the sidewall of the groove is almost impossible, see Figure 48. Thus to gain access to the facets, the chip is diced again, this time from the reverse side of the chip.

4.5.1 Sidewall inspection

A '*Groove Flip Dice*' technique was used to inspect the grooved chips sidewalls, see Figure 49. The reasoning for not cutting through the whole substrate at once is because of the limited blade exposure of the nickel blade (ZH05), which was restricted to a depth of cut of ~100 µm. The depth of cut also affects the regime of material removal and as the depth of cut increases so does the chance of, unwanted, brittle machining. The first stage of the '*Groove Flip Dice*' technique is to *groove* the chips (sidewall of interest) and then *flip* these. These are then placed on new UV tape and *diced* to remove the silicon but leaving the silica untouched, see Figure 49.

The silicon dicing uses a resin bonded blade (Disco RO8100848202 SM SD800 R13B01 0.1), with a diameter of 76.2 mm, a width of 100 µm and a #800 grit size. Dressing of this blade was carried out using 75 mm square of silicon carbide, with a depth of cut of 100 µm, at 20 krpm, with a translation speed of 50 mms^{-1} for forty passes, again on advice of Loadpoint. The chips were then split and mounted on a fresh UV tape with the facet facing parallel to the plain of surface characterisation. A white light interferometer (see chapter 2) was used to obtain surface metrology on

silica facets and to calculate the facets average areal surface roughness (Sa) [19], as indicated by the red line in Figure 49.

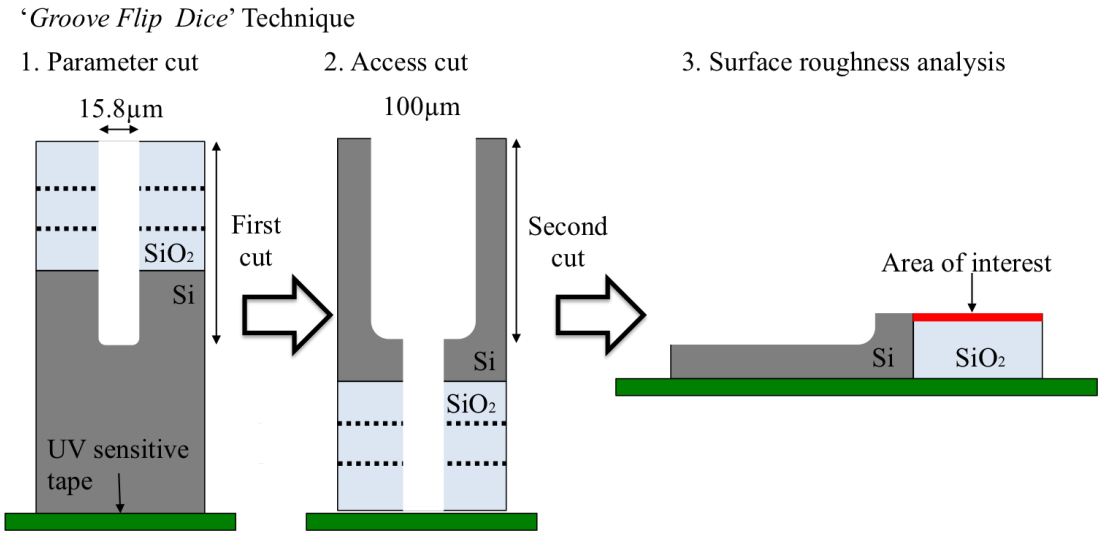

Figure 49 cutting order to investigate the surface roughness of grooved facets made (not to scale).

Other viewing techniques were attempted but were unsuccessful. These include viewing the groove from the top at an angle, as this would be the simplest and fastest approach to viewing the facets. However, because the sidewalls were at 45° to the objective, too much light was scattered for the white light interferometer to reconstruct an accurate scan. To improve the amount of light collected a thin layer of gold was deposited (hundreds of nanometres thick) to increase reflectivity, but still too much light was scattered.

4.5.2 Facet metrology

Each groove, machined at the varying dicing parameters was imaged, using a white light interferometer (Zemetrics, ZeScope) at 100x magnification, to obtain 3D surface metrology data. Figure 50 is a levelled image showing the variation in height of the groove diced with the parameters of 20 krpm and 0.1 mms^{-1}.

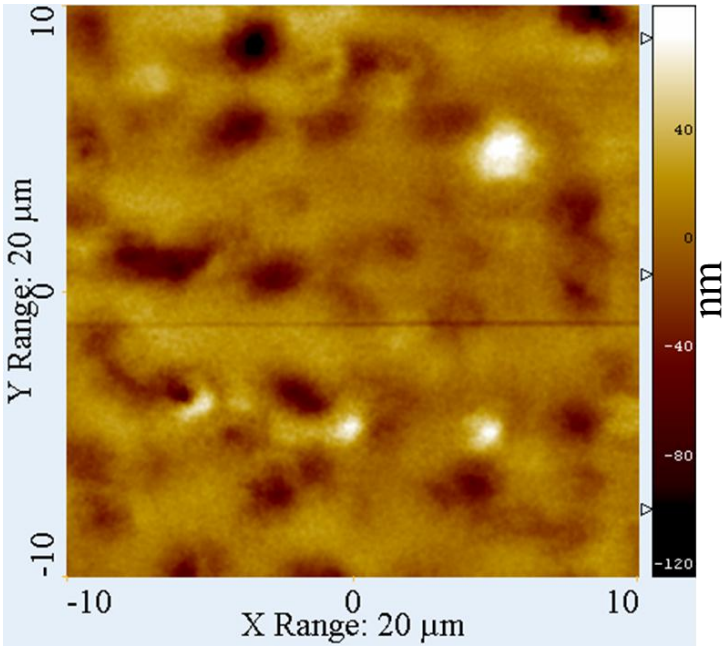

Figure 50 white light intereferometer surface profile of facet diced at 20 krpm and 0.1 mms^{-1}, colour bar shows variations in height (nm). A smooth surface has been generated but still has some micron level pitting, making this machined in the partially ductile regime. This facet had a surface roughness (Sa) of 14.8 nm with a standard error of 1.4 nm.

Figure 50 shows that partial ductile machining has occurred on the facet because of the presence of pitting (~1-2 µm). Figure 51 shows the feed rate against average surface roughness (Sa). The feed rate is defined as the distance travelled by the blade in one revolution. Each Sa value was calculated by selecting ten, 10 µm by 10 µm square samples on each 90 µm by 20 µm ZeScope scans in five columns and two rows. Square samples are used to stop the bias of surface texture, from the difference in lengths of the scan areas rectangular shape, effecting average surface roughness calculated. Also the raw rectangular scans from each ZeScope scan vary in actual size from sample misalignment. Thus, by taking samples with predefined sizes allows for a more fair comparison, from sample to sample. Polynomial levelling is then used before the average surface roughness (Sa) is taken; both of these are applied using the commercially available software Image Metrology, SPIP. Polynomial levelling is used to remove any arbitrary offset added by sample setting and long period waviness, thus leaving the nanoscale roughness in the height data. A mean was then taken over the ten samples and the Sa plotted, along with the standard error used to create the error bars in Figure 51.

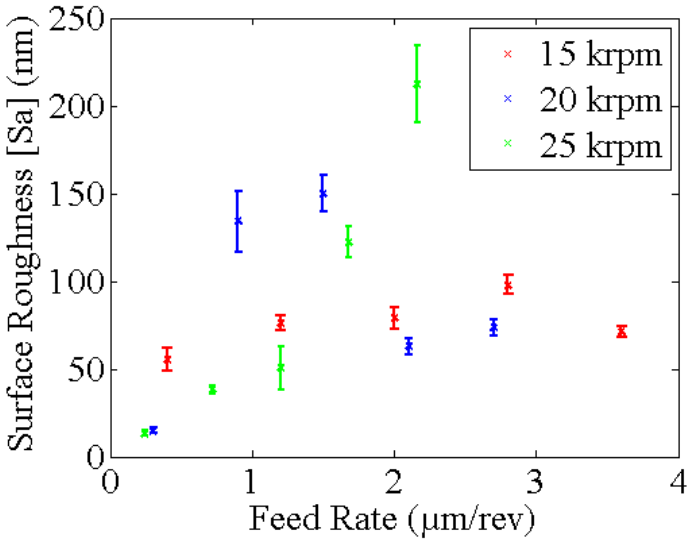

Figure 51 relationship between areal average surface roughness and feed rate with the standard error used for error bars. The smoothest machining results occur at feed rates < 0.4 µm/rev, which correspond to rotational speed of 20 krpm or 25 krpm at a translation speed of 0.1 mms^{-1}.

Figure 51 shows, that for feed rates < 0.4 µm/rev, the surface roughness (Sa) becomes <15 nm and with a small standard error, and a good consistency in surface roughness over the facet is shown. Feed rates > 0.4 µm/rev seem to give a generally rough (i.e. > 15 nm Sa) finish to the facet, with large variations in Sa over the facet, indicated by large standard errors. Moreover, there is a large spread in both Sa and standard error for the facets machined with a feed rate > 0.4 µm/rev. This can be attributed to chipping and cracking being randomly distributed over the surface. To obtain the smallest surface roughness, a rotational speed of 20 krpm or 25 krpm at a translation speed of 0.1 mms^{-1} must be used. These results also match with the ones used in the production of Nd:YAG waveguides [5], albeit with a smaller depth of cut.

Throughout the parameter tests, the condition of the blade was being altered. This lead to varying blade conditions for each groove diced. Both of the grooves with the lower surface roughness (<15 nm) were made after previous grooves were already machined. The grooves machined with a rotational speed of 15 krpm were machined first, with translational speeds starting at 0.1 mms^{-1} increasing to 0.9 mms^{-1}. This process was then repeated for 20 krpm and 25 krpm, respectively. The two smoothest results, at rotational speeds of 20 krpm and 25 krpm at 0.1 mms^{-1}, were machined at different stages in the experiment but still created smooth facets despite

the decreasing blade condition. In order to achieve the smoothest groove, a groove was diced at the optimum parameters with freshly dressed blade.

To look at the effect of dressing on the surface quality, a nickel bonded blade (Disco ZH05-SD4000-N1-50 HG, width of 50-60µm and a 4000 grit) was dressed (using the same technique as explained in section 4.4) and a groove was made in the a new silica-on-silicon chip from the same wafer as before. The groove was made using the parameters of a rotational speed of 20 krpm and a translational speed of 0.1 mms^{-1}. Figure 52 shows the surface profile of the facet.

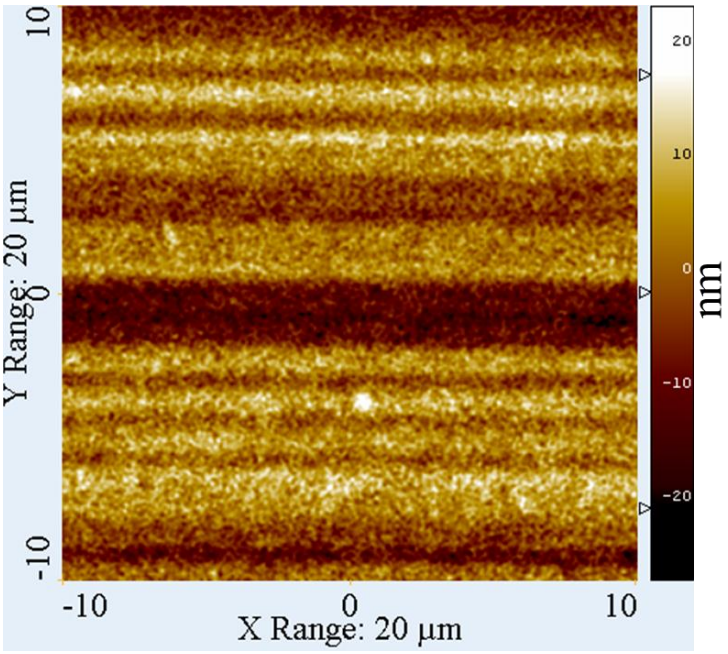

Figure 52 white light intereferometer surface profile of facet diced at 20 krpm and 0.1 mms^{-1}, with silicon dressing before dice. Colour bar shows variations in height (nm). A particularly smooth surface has been generated. This facet had a surface roughness (Sa) of 4.9 nm with a standard error of 87 pm. Notice dirt adhering to the surface by the presence of high points.

The primary difference between Figure 52 and Figure 50, where Figure 52 is machined with a freshly dressed blade, is the surface texture and the height range in which both of these profiles are over. The mean surface roughness (Sa) for Figure 52 is 4.9 nm (Sa) with a standard error of 87 pm whereas Figure 50 had a Sa of 14.8 nm and a standard of 1.4 nm. This makes the surface roughness of Figure 52 ~3 times smaller than Figure 50. Figure 52 also shows the classic signs of a ductile machined surface shown by the characteristic streaks left by the diamonds within the blade. The smoother facet shown in Figure 52 can be attributed to the newly dressed blade

uncovering more fresh diamond from the bond, compared to the worn state of blade used in Figure 50. The high points present on Figure 52 is dirt adhered to the surface and not chipping, another characteristic of ductile mode machining. The result of 4.9 nm Sa, is a seven and half times improvement on a previously reported surface roughness of 58 nm achieved by Chen *et al.*; where optical glass was grooved with an 8 µm depth of cut, utilising diamond impregnated nickel bonded blades [15].

Surface metrology has been discussed and the optimum dicing parameters giving the smoothest sidewall have been found. In the next section a lapped and chemical mechanical polished silica-on-silicon sample is examined and compared to grooved facets.

4.5.3 Polishing

Other facet fabrication techniques for silica-on-silicon can be used for free space coupling, such as lapping and polishing, see chapter 2. In order for a comparison to be made with the diced groove technique, as discussed previously, a polished chip was also measured using the white light interferometer. This chip was lapped and polished by James Gates, where the sample was first lapped using a cast iron plate with aluminium oxide grit. The grit size was sequentially reduced from 9 µm, to 3 µm and 1 µm, where each grit was used for approximately ten minutes. Following this, chemical mechanical polishing was carried out where a polyurethane plate using colloidal silica was employed, again for ten minutes. Figure 53 shows a surface profile of the lapped and polished facet.

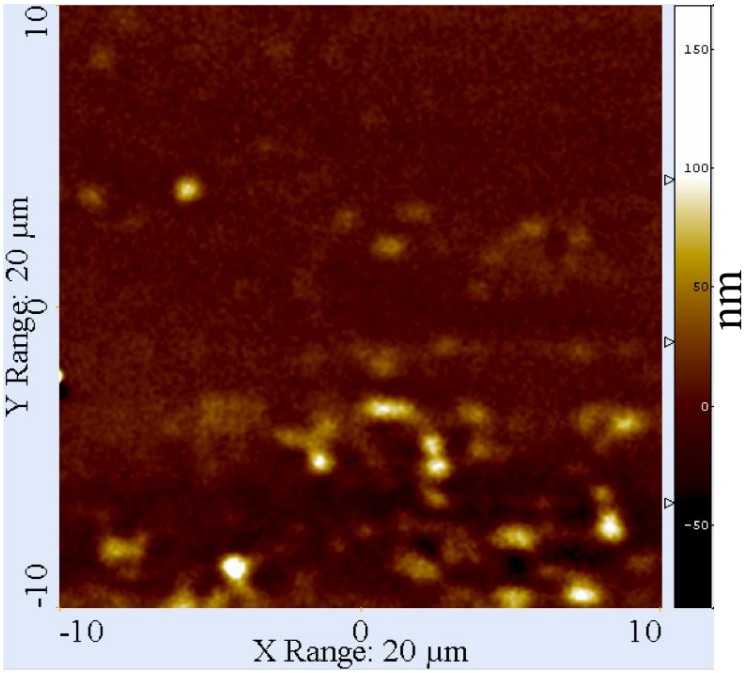

Figure 53 white light intereferometer surface profile of facet of a lapped and polished sample. Colour bar shows variations in height (nm). A poor facet has been generated but not in terms of surface roughness but in overall form, see Figure 54. This facet had a surface roughness (Sa) of 8.5 nm with a standard error of 96 pm.

The polished chip, seen in Figure 53, compared to the diced facet, seen in Figure 50 and Figure 52, has a less ordered surface texture, with a Sa of 8.5 nm and a standard error of 96 pm. Figure 53 Sa is ~1.7 times larger than the roughness measured on the diced facet's (Figure 52). The higher roughness of the polished sample is surprising, as it has been shown that lapping and polishing can achieve surface roughnesses (Sq) in silica as small as 0.2 nm [6]. However, the polished sample here is a silica-on-silicon composite, which has been polished with large area form error, across the facet, as shown in Figure 54.

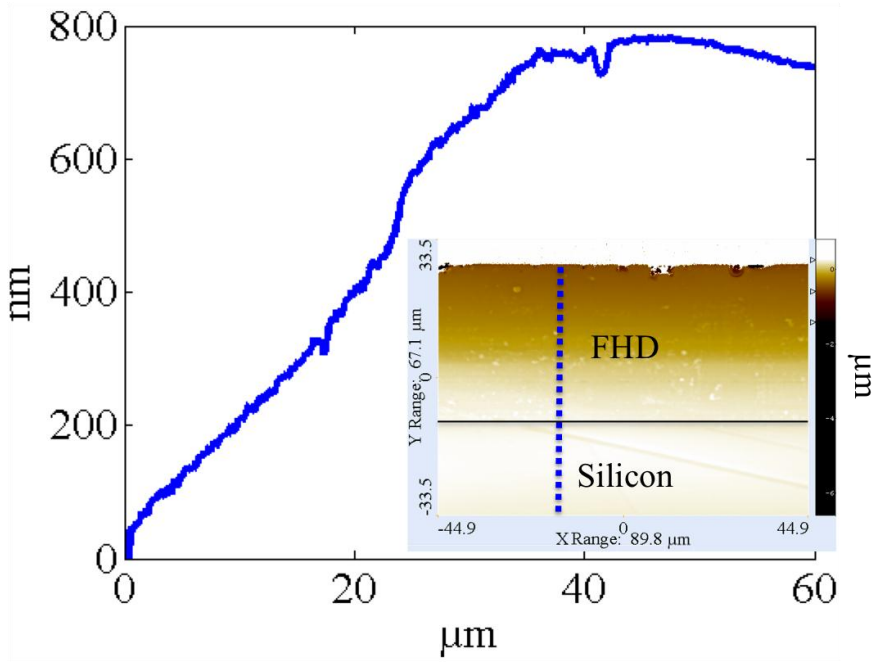

Figure 54 surface profile of a single line scan of the entire facet (both silica and silicon) of a lapped and polished sample, the blue dotted line on the insert shows the location on the surface profile. The colour bar in the insert shows variations in height (µm).

Figure 54 shows a surface profile of the silica-on-silicon sample where the surface has been removed and shows that the silica has been preferentially polished. The silica layer has been polished by ~780 nm more than the silicon, as shown by the profile and colour plot. The reasoning for this uneven polish is that the FHD is more aggressively attacked by the colloidal silica because of its chemical composition and thus is removed at a quicker rate. Uneven polishing has been shown before in the case of laser rod production when silica washers are used as means of mounting and protecting laser crystal rods [20].

Surface metrology and profilometer results have been used to allow a comparison between polished silica-on-silicon facets and diced facets, to be made. These results show diced facets have lower surface roughness and better overall form, in terms of facet flatness, when compared to lapped and polished facets.

In the following section explores the optical loss caused by scattering from free space input/output coupling.

4.6 Optical characterisation of diced facets

To investigate the optical loss caused by scattering, from free space coupling into a facet, a Bragg grating based loss technique was utilised. For this, a groove was diced through a channel waveguide and a series of Bragg gratings, as shown schematically in Figure 55. This allows a ratiometric loss technique to be implemented by utilising the Bragg gratings on either side of the groove [21]. Device fabrication was conducted in conjunction with Helen Rogers [22] and has been the subject of a conference paper [23].

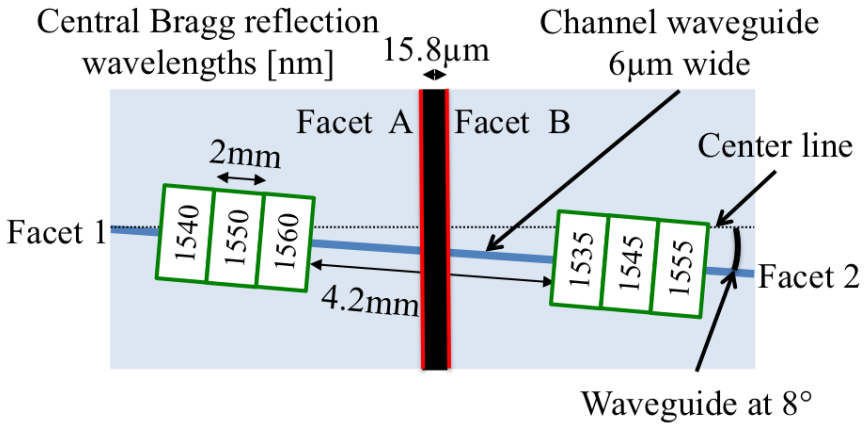

Figure 55 chip configuration of waveguides (blue lines), groove (thick black line) and facets (red lines). Green boxes denote Bragg gratings position with the central Bragg wavelength given inside (not to scale).

The integrated optic structure illustrated in Figure 55 was fabricated via direct UV writing [24], see chapter 3. The Bragg gratings on either side of the groove structure, allows the transmission loss through the groove to be ascertained. Channel waveguides are inscribed at an 8° angle from the perpendicular line drawn from input facets 1 and 2, to reduce return loss. The Bragg gratings central wavelengths are also shown in the green boxes of Figure 55. The groove that emulates free space launch was diced using a similar nickel bonded blade (Disco ZH05-SD5000-N1-50 BA) to the one used in the machine parameter test but was thinner, thus reducing loss from diffraction. The same dressing conditions were used as in section 4.4 and the machining parameters used were a rotational speed of 20 krpm at a translational

speed of 0.1 mms^{-1}. The loss technique was implemented by collecting the reflection strength of each grating, from each facet 1 and 2, see Figure 55. The reflection spectra was collected through pigtails, by utilising a broadband source, 50/50 coupler, polariser and optical spectrum analyser, see chapter 3. The reflection spectra for both the TE (Transverse Electric) and TM (Transverse Magnetic) polarisations are shown in Figure 56, the TE having its electric field component parallel to the planar core layer of the device.

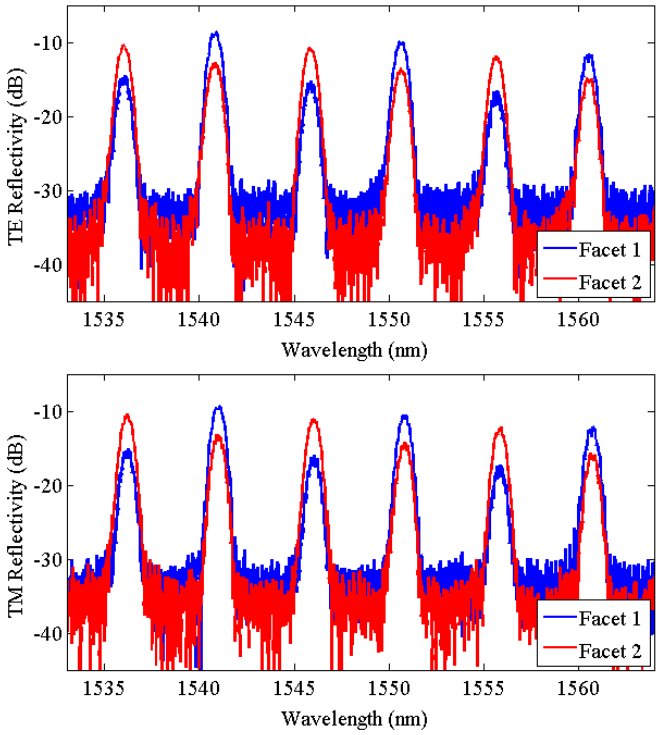

Figure 56 reflection spectra collected from facets 1 and 2. Notice the change in amplitudes of the Bragg gratings, depending if they are before or after the groove.

As can be seen from Figure 56 there is a difference in amplitudes when comparing light launched into facet 1, compared to facet 2. The difference in reflected amplitudes is because of the loss caused by diffraction, refractive index mismatch, and scattering when the light propagates the groove between facets A and B; and launch efficiency into the waveguide and waveguide propagation loss, see Figure 55. The facet losses have been calculated using the technique described by Rogers *et al.* [21], where the total resultant loss from the groove for both polarisations is shown in Figure 57.

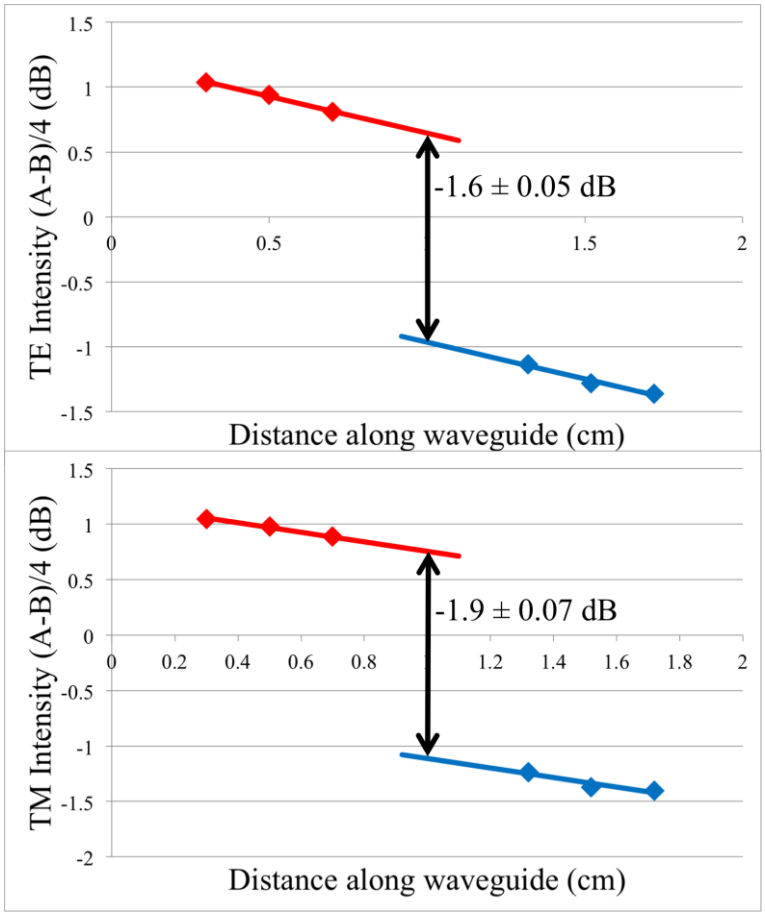

Figure 57 ratiometric loss technique applied to calculate total optical loss of propagating the groove. A linear line fit was then performed on all six data points to calculate the intensity offset.

The data plotted in Figure 57, derives from the Bragg grating peak heights shown in Figure 56. The peaks were calculated using the Gaussian fitting code described in chapter 3. The logarithm of the peak intensity is taken from each grating and the difference is taken for light launched in facet 1 and facet 2 (see Figure 55). These ratios were then plotted versus spatial position on the chip. Linear line fitting was then performed on all six data points and the intensity offset calculated, this was used as the total groove loss. The confidence limits were calculated by taking the standard error on all six points.

The total loss for both facets A and B (see Figure 55) from scattering can be calculated if Fresnel losses and losses due to modal mismatch from diffraction are deducted.

To calculate the polarisation dependent Fresnel losses, the angle at which the light refracts at, as it traverses the groove, must be found. To find this angle, Snell's law is used again, see Equation 65, where the various refractive indices and angles are shown in Figure 58 a) and b).

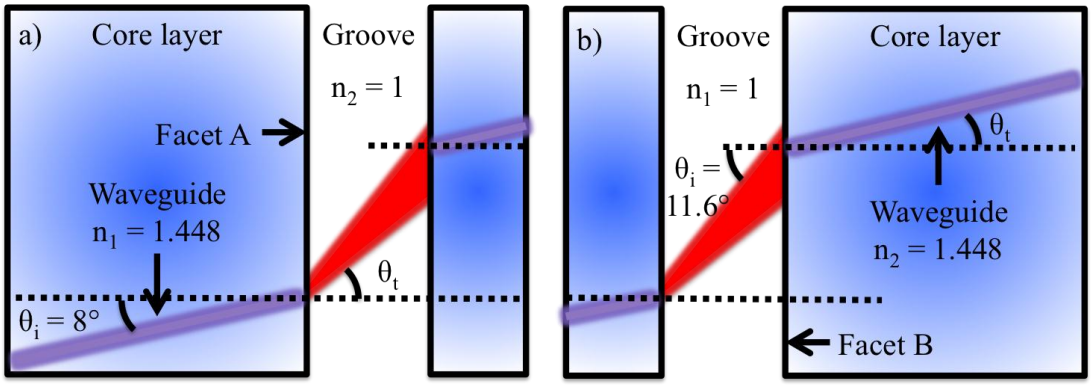

Figure 58 ray diagram for a) light leaving Facet A and b) light entering Facet B.

The complete ray diagram, combining Figure 58 a) and b) for the groove, is shown in Figure 59.

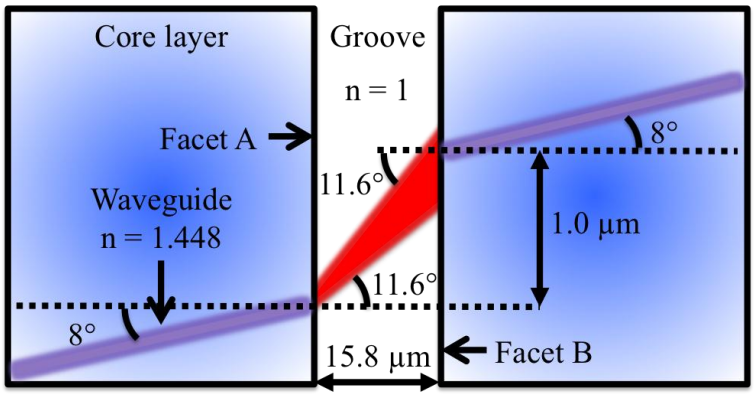

Figure 59 the ray diagram for the groove showing the solutions to Snell's law, diffraction of the beam as it crosses the groove and the transverse mismatch.

From the ray diagram description of light crossing the groove, as shown in Figure 59, the polarisation dependent Fresnel losses can be calculated. For the TE polarisation [25],

$$R_{in/out} = \left(\frac{n_1 \cos\theta_i - n_2 \cos\theta_t}{n_1 \cos\theta_i + n_2 \cos\theta_t}\right)^2 \qquad \textbf{Equation 68}$$

where R_{out} uses the values in Figure 58 a) and R_{in} uses the values in Figure 58 b). The Fresnel losses for TM polarisation [25],

$$R_{in/out} = \left(\frac{n_1 \cos\theta_t - n_2 \cos\theta_i}{n_1 \cos\theta_t + n_2 \cos\theta_i}\right)^2 \quad \textbf{Equation 69}$$

where for R_{out} uses the values in Figure 58 a) and R_{in} uses the values in Figure 58 b).

The free space coupling loss due to modal mismatch from transverse misalignment is shown in Equation 66 and from longitudinal mismatch is [8],

$$\alpha_L = \left[\frac{D\lambda}{2\pi n_{eff}\omega^2}\right]^2 \quad \textbf{Equation 70}$$

where α_L is the fractional loss from modal mismatch caused by diffraction *i.e.* longitudinal misalignment, D is the longitudinal mismatch, λ is the wavelength of operation, n_{eff} is the effective refractive index and ω is the modal field diameter. In the device described previously longitudinal mismatch (D) is the groove width at 15.8 µm, λ is 1550 nm, n_{eff} is 1.448, ω is ~10 µm and U is 1.0 µm from Figure 59.

The free space insertion loss for each facet was calculated by using the following equation,

$$L_f = \left(10log_{10}\left(\frac{10^{(L_t/10)}}{(1-R_{out})(1-R_{in})(1-\alpha_L)(1-\alpha_T)}\right)\right)\Big/2 \quad \textbf{Equation 71}$$

where L_f is the loss in decibels for each facet, L_t is the loss in decibels for the total groove loss taken from Figure 57 and R_{out} and R_{in} is the Fresnel loss for TE and TM polarisations respectively. From Figure 57, L_t is -1.6 dB and -1.9 dB for TE and TM polarisations respectively, R_{out} and R_{in} is 0.034 and 0.032 respectively for TE, R_{out} and R_{in} is 0.033 and 0.036 respectively for TM, α_L is 0.73x10^{-3} and α_T is 0.011. Using these figures an individual average interface loss of -0.63 dB and -0.76 dB for the TE and TM polarisation is calculated, respectively. The dominant factor effecting the calculation of L_f is the Fresnel losses; these are three times larger than those given by longitudinal mismatch and approximately forty times larger than modal mismatch. These results are similar to those reported by Choi *et al.* [18], where they etch waveguides and grooves in a silica-on-silicon substrate using plasma enhanced etching and measured a scattering loss of ~0.6 dB for their etched facets. Other similar results reported by Ou *et al.* [27] measured a loss of ~0.94 dB of excess loss per facet for a 24 µm groove created by reactive ion etching. The

difference in the loss values calculated for each polarisation can be attributed to the physical difference in size between the larger TM mode compared to the smaller TE mode. One assumption made in the loss calculation is to neglect the fractional loss from modal mismatch caused by diffraction from angular misalignment. This assumption is made due to the measurement of the facet verticality being <0.2°, as seen by SEM inspection of a previously machined groove. Analysis of the coupling loss in free space input/output coupling caused by surface roughness has been shown. This optical loss technique, along with surface metrology, allowed the verification of the optimised dicing process to produce ultra-smooth facets in silica-on-silicon. The dicing of grooved facets has been conducted on FHD silica-on-silicon wafers that were fabricated at the University of Southampton itself. This is discussed further in the following section.

4.7 Dicing of in-house produced FHD silica-on-silicon wafers

Towards the end of the Ph.D., the group's FHD machine was commissioned and a wafer was produced. After direct UV writing both waveguides and Bragg gratings, the ratiometric loss technique was implemented, as described in section 4.6. Losses of ~0.24 $dBcm^{-1}$ were measured by group member, Paolo Mennea, which are similar to those reported here [21] by Helen Rogers. The in-house made low loss FHD wafer was grooved using the same blade and procedure as used in Figure 52 of section 4.5.2, which previously achieved 4.9 nm of roughness. The wafer used previously to obtain the optimised parameters, was bought and produced by CIP Technologies. The surface profile of dicing facets within the in-house fabricated FHD wafer are shown in Figure 60.

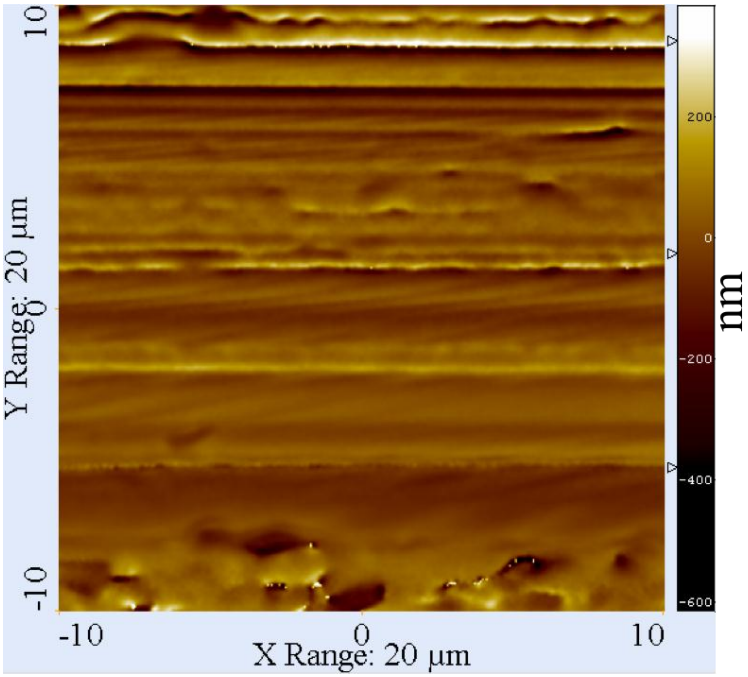

Figure 60 white light intereferometer surface profile of facet machined at 20 krpm and 0.1 mms^{-1}, with silicon dressing before dicing. Colour bar shows variations in height (nm). A poor facet has been machined in terms of surface roughness and chipping. This facet had a surface roughness (Sa) of 49.3 nm with a standard error of 15.6 nm.

The in-house FHD wafer, see Figure 60, shows large amounts of surface texture over a larger height range, when compared to commercial FHD wafer, see Figure 52. Figure 60 has a Sa of 49.3 nm and a standard error of 15.6 nm, which is ~10 times larger than the roughness measured on the Figure 52. The unexpected result may be due to the differences in the furnace conditions, heating ramp rates or amounts of dopants used between the commercially and in-house wafers. These differences in the consolidation and composition of the FHD glass may have caused differences in hardness compared with the commercial FHD. Also more dopants, *i.e.* germanium and boron, were added to increase photosensitivity. These extra dopants may have caused crystallinity within the amorphous structure of the FHD glass, which would also result in variations in hardness throughout the glass. Commercial FHD silica-on-silicon wafers, fabricated by CIP Technologies, where therefore used throughout this thesis.

4.8 Dicing of gadolinium gallium garnet for waveguide lasers

The fabrication of GGG ($Gd_3Ga_5O_{12}$, Gadolinium Gallium Garnet) channel waveguide lasers, in collaboration with Katherine A. Sloyan (during her Ph.D.) under the guidance of Timothy C. May-Smith and Robert W. Eason, was conducted. Layers of pulse laser deposited undoped GGG underclad, neodymium doped GGG and undoped GGG overclad, were sawn using similar feed rates to the optimised condition in silica, to form ridge waveguides [28] [29]. The results of the grooving are shown in Figure 61.

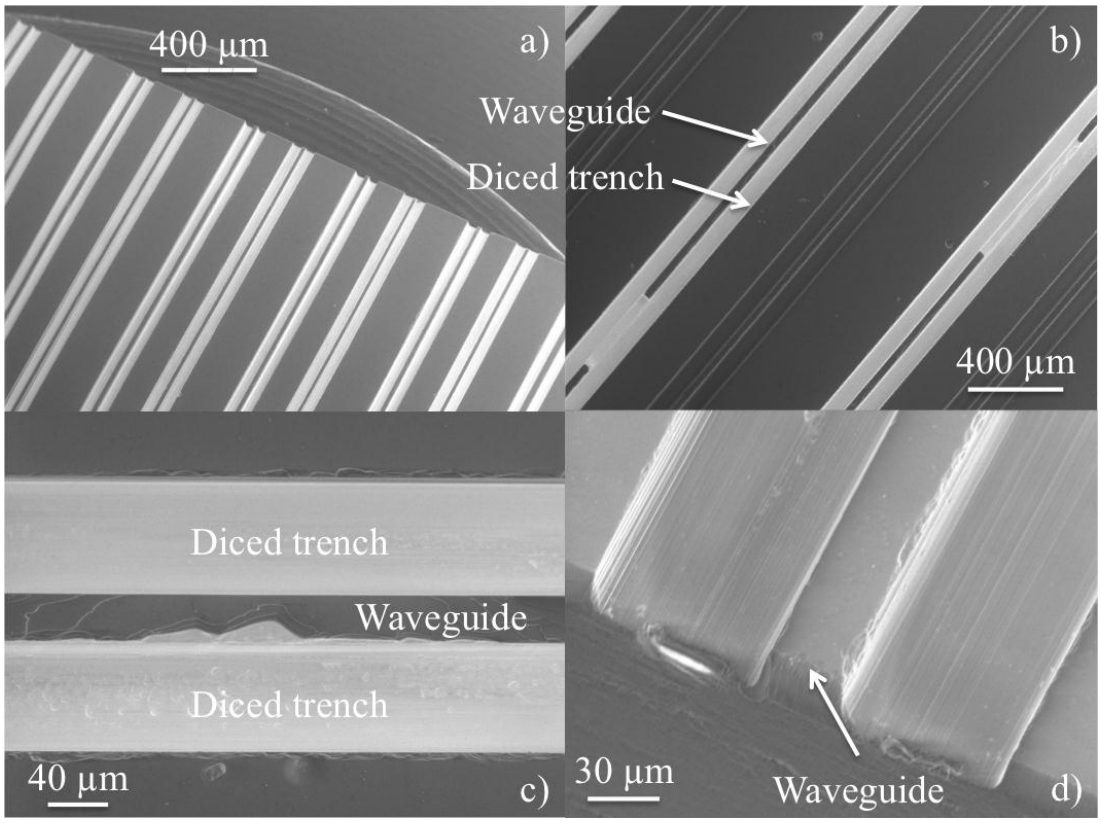

Figure 61 SEM micrographs of grooved GGG samples. SEM micrographs courtesy of Katherine Sloyan [29]**. Notice the chipping on the waveguides was a limiting factor in the production of working lasers.**

Figure 61 show top down views of diced GGG waveguides at different magnifications. Notice in Figure 61 b), c) and d) that there is significant chipping and delamination of the GGG layers. The poor quality of the grooves is due to the

hardness of GGG, which has similar mechanical properties to the commonly known garnet, YAG (Yttrium Aluminium Garnet), with a Mohs hardness of 8.5 [30]. Due to the poor quality of the grooves produced, lasing was not seen as the pump could not overcome the losses of the waveguide.

4.9 Conclusions

In this chapter it has been demonstrated that dicing can produce facets in silica-on-silicon substrate with a smooth, mirror like finish. The dicing machining parameters were optimised by monitoring average surface roughness, by means of a white light interferometer. It was found that by pre-dressing and using a rotational speed of 20 krpm and a translational speed of 0.1 mms^{-1} gave the smoothest finish. Once machined, the facets areal average surface roughness (Sa) was measured and found to be 4.9 nm, a factor ~7.5 times improvement on previously seen roughnesses in optical grade silica. Using the optimised dicing parameters a groove was sawn into a waveguide with Bragg gratings and a ratiometric loss technique was used to determine the total loss of the groove. By subtracting losses from diffraction, modal mismatch and Fresnel losses caused by the light traversing the groove, an individual average interface loss of -0.63 dB for the TE polarisation and -0.76 dB for the TM polarisation was then found.

References

1. C. Holmes, L. G. Carpenter, H. L. Rogers, I. J. G. Sparrow, J. C. Gates, and P. G. R. Smith, "Planar waveguide tilted Bragg grating refractometer fabricated through physical micromachining and direct UV writing.," Optics Express **19**, 12462–8 (2011).

2. L. G. Carpenter, P. L. Mennea, H. L. Rogers, C. Holmes, J. C. Gates, and P. G. R. Smith, "Integrated corner mirrors as a platform for miniaturized planar strain sensing," European Conference on Integrated Optics (ECIO) Sitges Barcelona 18-20 April 2012 1–2 (2012).

3. S. Ambran, C. Holmes, J. C. Gates, A. S. Webb, L. G. Carpenter, F. R. M. Adikan, P. G. R. Smith, and J. K. Sahu, "Fabrication of a Multimode Interference Device in a Low-Loss Flat-Fiber Platform Using Physical Micromachining Technique," Journal of Lightwave Technology **30**, 2870–2875 (2012).

4. N. Courjal, B. Guichardaz, G. Ulliac, J.-Y. Rauch, B. Sadani, H.-H. Lu, and M.-P. Bernal, "High aspect ratio lithium niobate ridge waveguides fabricated by optical grade dicing," Journal of Physics D: Applied Physics **44**, 305101 (2011).

5. Y. Jia, C. E. Rüter, S. Akhmadaliev, S. Zhou, F. Chen, and D. Kip, "Ridge waveguide lasers in Nd:YAG crystals produced by combining swift heavy ion irradiation and precise diamond blade dicing," Optical Materials Express **3**, 433–438 (2013).

6. K. Kodate and Y. Komai, "Compact spectroscopic sensor using an arrayed waveguide grating," Journal of Optics A: Pure and Applied Optics **10**, 044011 (2008).

7. J. Plaza, M. J. Lopez, A. Moreno, M. Duch, and C. Cane, "Definition of high aspect ratio glass columns," Sensors and Actuators A: Physical **105**, 305–310 (2003).

8. A. Ghatak and K. Thyagarajan, *Introduction to Fiber Optics* (Cambridge University Press, 1998), pp. 16–157.

9. H. E. Bennett and J. O. Porteus, "Relation Between Surface Roughness and Specular Reflectance at Normal Incidence," Journal of Optical Society of America **51**, 123–130 (1961).

10. M. Zeman, R. A. C. M. M. van Swaaij, J. W. Metselaar, and R. E. I. Schropp, "Optical modeling of a-Si:H solar cells with rough interfaces: Effect of back contact and interface roughness," Journal of Applied Physics **88**, 6436–6443 (2000).

11. Y. A. Gharbia, G. Milton, and J. Katupitiya, "The effect of optical fiber endface surface roughness on light coupling," in *Optical Fabrication, Testing, and Metrology*, R. Geyl, D. Rimmer, and L. Wang, eds. (2004), Vol. 5252, pp. 201–208.

12. Y. A. Gharbia, G. Milton, and J. Katupitiya, "Nano-grinding of micro profiles and microlenses on optical fibers endfaces for use in optical-fiber sensors," in *Third European Workshop on Optical Fibre Sensors*, A. Cutolo, B. Culshaw, and J. M. López-Higuera, eds. (2007), Vol. 6619, p. 66192R–66192R–4.

13. H. Eda, "Ductile Grinding of Ceramics: Machine Tool and Process," in *Handbook of Advanced Ceramic Machining*, I. Marinescu, ed. (CRC Press, Taylor & Francis Group, 2007), pp. 1–28.

14. H. Yasui, "Ductile-Mode Ultra-Smoothness Grinding of Fine Ceramics with Coarse-Grain-Size Diamond Wheels," in *Handbook of Advanced Ceramic Machining*, I. D. Marinescu, ed. (CRC Press, Taylor & Francis Group, 2007), pp. 29–32.

15. S.-T. Chen and S.-J. Lin, "Development of an extremely thin grinding-tool for grinding microgrooves in optical glass," Journal of Materials Processing Technology **211**, 1581–1589 (2011).

16. K. Cheng, "Abrasive Micromachining and Microgrinding," in *Micromachining of Engineering Materials*, J. McGeough, ed. (Marcel Dekker Inc, 2002), pp. 98–101.

17. LoadPoint Ltd., *MicroAce Manual Series 3* (2002).

18. L. G. Carpenter, H. L. Rogers, C. Holmes, J. C. Gates, and P. G. R. Smith, "Polish-like facet preparation via dicing for silica integrated optics," SPIE Photonics West, 2013 (2013).

19. D. J. Whitehouse, *Handbook of Surface and Nanometrology*, 2nd ed. (CRC Press, Taylor & Francis Group, 2011), p. 188.

20. G. W. Fynn and W. J. A. Powell, *Cutting and Polishing Optical and Electronic Materials*, 2nd ed. (Institute of Physics Publishing Inc., 1988), pp. 170–181.

21. H. L. Rogers, S. Ambran, C. Holmes, P. G. R. Smith, and J. C. Gates, "In situ loss measurement of direct UV-written waveguides using integrated Bragg gratings," Optics Letters **35**, 2849–2851 (2010).

22. H. L. Rogers, "Thesis: Direct UV-written Bragg gratings for waveguide characterisation and advanced applications," University of Southampton (2013).

23. L. G. Carpenter, H. L. Rogers, C. Holmes, J. C. Gates, and P. G. R. Smith, "Facet Machining of Silica Waveguides with Nanoscale Roughness without Polishing or Lapping," CLEO-Europe/IQEC 2013 Munich 12-16 May 2013 (2013).

24. G. D. Emmerson, C. B. E. Gawith, S. P. Watts, R. B. Williams, P. G. R. Smith, S. G. Mcmeekin, J. R. Bonar, and R. I. Laming, "All-UV-written integrated planar Bragg gratings and channel waveguides through single-step direct grating writing," IEE Proceedings Optoelectronics **151**, 119–122 (2004).

25. A. Ghatak and K. Thyagarajan, *Introduction to Fiber Optics* (Cambridge University Press, 1998), pp. 16–17.

26. D. Choi, J. Lee, D. Kim, and S. Jung, "Modification of sidewall roughness in silica deep etching and their influences on coupling loss in hybrid integration," Proceedings of SPIE **4944**, 337–345 (2003).

27. H. Ou, "Trenches for Building Blocks of Advanced Planar Components," IEEE Photonics Technology Letters **16**, 1334–1336 (2004).

28. K. A. Sloyan, L. G. Carpenter, T. C. May-smith, C. Holmes, J. C. Gates, P. G. R. Smith, and R. W. Eason, "Fabrication of Multilayer Crystalline Rib Waveguides by a Combined Multi-Step Pulsed Laser Deposition/Precision Machining Technique," CLEO/Europe and IQEC 2011 Conference Submission (2011).

29. K. Sloyan, "Thesis: Multi-beam pulsed laser deposition for engineered crystal films," University of Southampton (2012).

30. V. Peters, "Thesis: Growth and Spectroscopy of Ytterbium Doped Sesquioxides," University of Hamburg (2001).

5 Photonic Microcantilevers

5.1 Introduction

Microcantilevers are ubiquitous ultra sensitive structures that prove useful for a plethora of miniaturized sensing applications ranging from the detection of chemical and biological analytes, to Atomic Force Microscopy (AFM) [1] and force detection [2]. Electronic or optical mechanisms are typically used to sense cantilever deflection. Cost effective and well established electronic deflection detection is prevalent in consumer electronics in the form of MEMS (Micro Electromechanical Systems), and are present in everyday appliances such as laptops, smart phones and cars. However, MEMS type devices typically cannot be used in areas of strong EM fields or in hazardous environments where there are ignition risks. On the contrary, optical deflection detection does not face these problems.

Optical deflection detection is widely used in both free-space optics and waveguide-based approaches [3] [4] [5]. Particularly waveguide interrogation, utilising fibre optic interrogation, has the ability to work in some of the worlds most extreme environments such as in oil/geothermal wells where both high temperatures/pressures exist [6] [7]. Moreover, by taking advantage of telecommunication techniques, fibre optics can be networked into large area sensor grids and used as undersea hydrophone systems [8]. Waveguide-based interrogation devices offer high sensitivity of free-space optics but without the regular need for realignment and the associated mechanical instabilities [9].

Fibre Bragg gratings also allow deflection detection, but the sizes of these cantilevers are typically on the scale of centimetres [10]. Other fibre-based designs

utilise interference to measure deflection. Fibre top cantilevers are fabricated from the facets of fibres and are on the micron scale, typically 125 microns in length. These fibre top cantilevers have been shown to achieve sensitivities comparable to those of commercially available instruments [11].

While fibre optics offer an attractive route for creating devices with single cantilevers, multiple cantilevers integrated on a single fibre would be challenging to fabricate. However, integrated optics offers a way to realize multiple cantilevers on a single device. Moreover, cantilevers coupled with Bragg gratings give a simple way to address multiple cantilevers spectrally, *i.e.* at different wavelengths, through a single connection.

In this chapter two cantilever interrogations methods utilising single Bragg gratings and pairs of spectrally matched gratings forming Fabry-Pérot interferometers are discussed. Both types of cantilever have been the subject of journal papers published by the author [12] [13]. The first cantilever interrogation method that will be discussed is the single Bragg grating structure. A general overview of glass microcantilever fabrication, used for this single Bragg grating case, is given, including comments on direct UV writing, precision dicing, wet etching and the minimisation of return loss. A cantilever deflection theory is then developed for this single Bragg grating interrogation, which relates strain to central Bragg wavelength shift. This cantilever device with single Bragg grating interrogation is then used with a phase sensitive technique to explore the change in its mechanical resonance characteristics with changing external pressure. The second cantilever interrogation method, using pairs of spectrally matched gratings to form a Fabry-Pérot interferometer, is discussed next. Specific fabrication techniques for the Fabry-Pérot interferometer are also explained, with comments on other unsuccessful fabrication routes. This chapter also includes cantilever deflection theory relating strain to the optical phase change that occurs in the Fabry-Pérot device. A profilometer was used to deflect the Fabry-Pérot cantilever while reflection spectra are collected and coupled mode theory was used to extract the optical phase. These results are all compared to theory for both the single Bragg grating and Fabry-Pérot design. Comments are made on the single Bragg grating and Fabry-Pérot cantilever's minimum resolvable force, spectral sharpness and sensitivity. The machining of cantilevers without using wet etching is also covered. The basic operation of how a

Bragg grating inside a cantilever can enable strain to be sensed is discussed in the next section.

5.1.1 Basic operation

The basic photonic microcantilever device discussed throughout this chapter takes advantage of Bragg gratings within the cantilever to sense strain from induced deflection. An induced deflection of the cantilever will result in a linear strain along its length, thus by fabricating a waveguide and Bragg gratings within the cantilever, the Bragg grating's spectral response changes with the induced strain can be monitored. This is illustrated schematically in Figure 62 a), the Bragg grating resides in the cantilever, integrated into a waveguide structure.

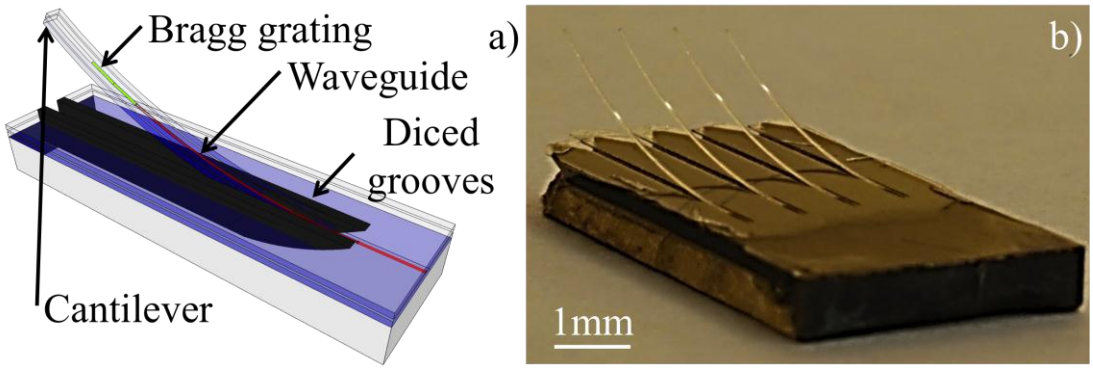

Figure 62 a) schematic of cantilever utilising Bragg grating deflection sensing and b) actual device. Cantilever deflection is sensed by the actuation causing strain to be applied to the Bragg grating and thus shifts the Bragg central wavelength.

Figure 62 b) shows a micrograph of a typical device with four cantilevers, with a length to width aspect ratio of ~83:1. From Figure 62 b), the four microcantilevers visible are ~5 mm in length, ~60 μm wide and ~40 μm in height. The cantilever fabrication process used to create these devices will now be discussed in the next section.

5.2 Microcantilever fabrication

The typical fabrication process used to create microcantilevers involves three distinct steps. Firstly, grooves that define the mechanical structure of the cantilever are

diced. Following this waveguides and Bragg gratings are then inscribed into a silica-on-silicon substrate. The cantilever device is then released from the substrate via a wet etching process. All the steps of this process will now be discussed in further detail, starting with the dicing of the cantilever structure.

5.2.1 Dicing the mechanical structure

The base material used to create cantilever structures is a silica-on-silicon substrate made by depositing the silica layers using Flame Hydrolysis Deposition (FHD), as described in detail in chapter 3. Definition of the cantilever's structure is achieved by the physical micromachining of grooves through the silica layer into the silicon with a precision dicing saw, as discussed in chapter 4. The dicing parameters used to cut the grooves were a translation speed 0.5 mms^{-1} and a rotational spindle speed of 20 krpm. The grooves were cut through the silica layer, where the layer was ~40 μm, into the silicon substrate thus a depth of cut of ~100 μm was used. A nickel bonded blade was used (Disco ZH05-SD5000-N1-50 BC) with a diameter of ~54.5 mm, a width of 25-30 μm, grit size of #5000 (~0.5-3 μm in size) and the lowest grit concentration for this blade. Using the dicing saw allows the length and width of the cantilever to be predefined, as shown below in Figure 63.

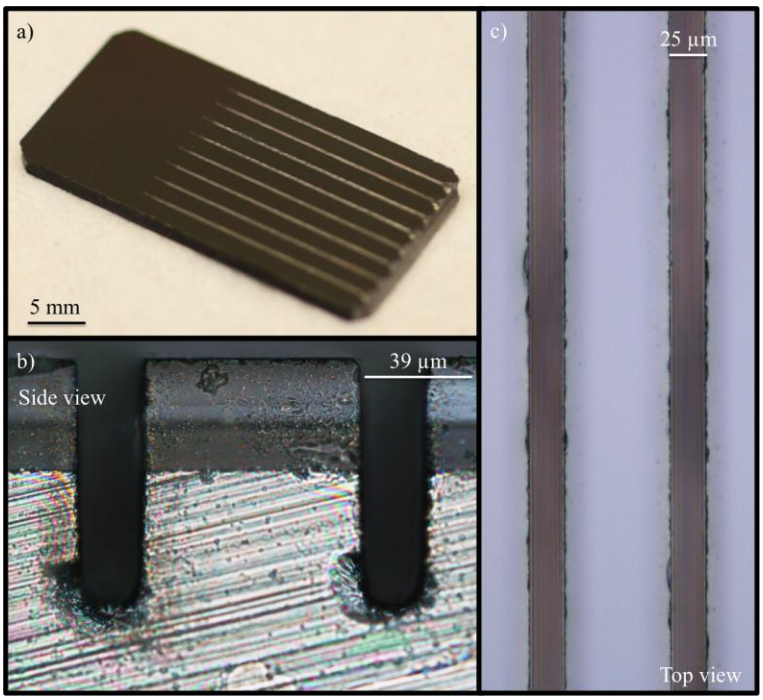

Figure 63 micrographs of diced cantilever structures.

Figure 63 shows micrographs of grooves diced into the silica-on-silicon substrates prior to waveguide and grating fabrication. Figure 63 a) shows an entire chip with eight cantilever structures present, the chip having a total of sixteen grooves present. Figure 63 b) shows a side view looking down a pair of grooves. Notice the access made to the silicon (white coloured with diagonal scratches present) for the wet etchant. Figure 63 c) shows a top view of a pair of grooves. It must be noted that these grooves, unlike one discussed in chapter 4, did not need a high quality finish because there was no light interacting with the sidewalls. Figure 63 c) shows an example of topside chipping at the groove edges. This was the dominant effect needing to be reduced when optimising (with microscope inspection) the dicing procedure. Dicing was used to define the mechanical structure of the cantilever. The next step in the fabrication process is the definition of optical waveguides and Bragg gratings. These are mentioned next.

5.2.2 Waveguide and Bragg grating definition

Waveguides and Bragg reflectors were direct UV written into the photosensitive layer, aligning to the centre of the un-etched cantilever, which was made by the grooves, diced previously. The single mode channel waveguides at 1550 nm, have a n_{eff} of ~1.448, a width of ~6 µm, as defined by the UV laser spot size, and a height of ~6 µm, as defined by the planar core layer [14] [15]. Gaussian apodisation was implemented with amplitude modulation to suppresses the side lobes of a uniform Bragg grating, making the Bragg grating spectrally simpler. For a more detailed explanation of FHD silica-on-silicon and direct UV writing see chapter 3. Simultaneous inscription of single mode channel waveguides and Bragg gratings, to create cantilever deflection interrogation, have been explained. The next section explains the last step of the fabrication process, explaining how the silica structure is released from the silicon substrate via wet etching.

5.2.3 Wet etching

After the dicing and UV writing, the silicon substrate was etched with heated Potassium Hydroxide (KOH) [16] to free the silica cantilever from the substrate as shown in Figure 64. A 5mol concentration of KOH was used. It was heated to ~100 °C and etched for approximately 24 hours.

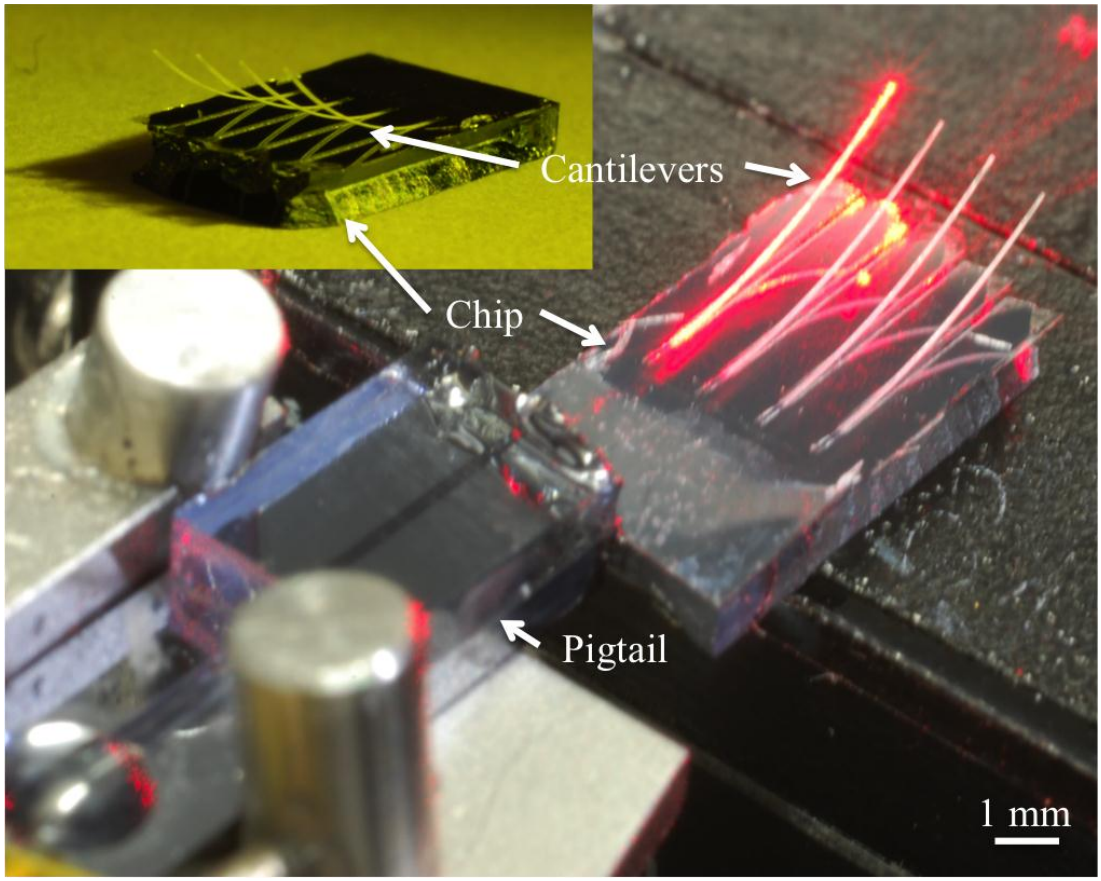

Figure 64 micrographs of typical cantilever devices after wet etching. The main image shows a fibre pigtail launching 633 nm light into the waveguide structure integrated within the cantilever device. The insert shows the device before optical characterisation.

Figure 64 shows typical devices produced using the aforementioned fabrication process. Figure 64 shows a pigtailed device where the fibre pigtail allows access to the UV written structures; the inset shows an un-pigtailed device.

Approximately forty of these glass microcantilevers devices have been fabricated and approximately a third were been rendered inoperable after the etching stage. The main route of failure was from KOH weakening the optical input facet of the device (*i.e.* where the pigtail joins the chip in Figure 64). The lack of silicon beneath the input facet provided little support and regularly resulted in damage to the silica waveguide. There were a number of methods employed to prevent degradation to the input facets during the etching stage. The first method used to protect the facet, was to wrap it in Polytetrafluoroethylene (PTFE) tape. However failure ensued from the KOH wicking underneath the tape. The second method tried was to cover the input facet in SU8 photoresist, but although literature suggests SU8 is resistant to KOH, it

failed to protect the facet. Another method was to create a PTFE holder, which held only the cantilever part of the device in the KOH whilst the input facet was kept out of it. The KOH still managed to wick up the device and damaged the input facet. The latter iteration of this method was to include a PTFE grease around the gaps of the PTFE holder. This method proved to work with no signs of input facet degradation and has been used thereafter.

5.2.4 Minimising return loss

Another notable improvement to the performance on early microcantilever design is the inclusion of an 8° input and output facet. The 8° input and output facet improved return loss by reducing Fresnel reflections at the interface in a similar geometry used in angle polished fibre optic connectors. Output facets were also cut at an 8° angle to stop back reflection interfering with the Bragg reflection. However, this changed the length of each microcantilever and thus altered the etch time for each. This problem was removed by leaving 1.5 mm of microcantilever after the end of the waveguide to allow light to diffuse into the planar layer. This provided sufficient suppression of the back reflected light and was as effective as the 8° cut facet. An overview of cantilever fabrication has been given. Single Bragg grating interrogation is now introduced and the device design is included.

5.3 Single Bragg grating microcantilever interrogation

To investigate microcantilevers with single Bragg grating interrogation of cantilever deflection, a device was created with a number of Bragg gratings distributed along the length of the waveguide. The waveguide was integrated into the cantilever and chip. Cantilever fabrication was conducted with Helen Rogers and Christopher Holmes. Figure 65 shows a diagram, schematic and micrograph of the microcantilever device.

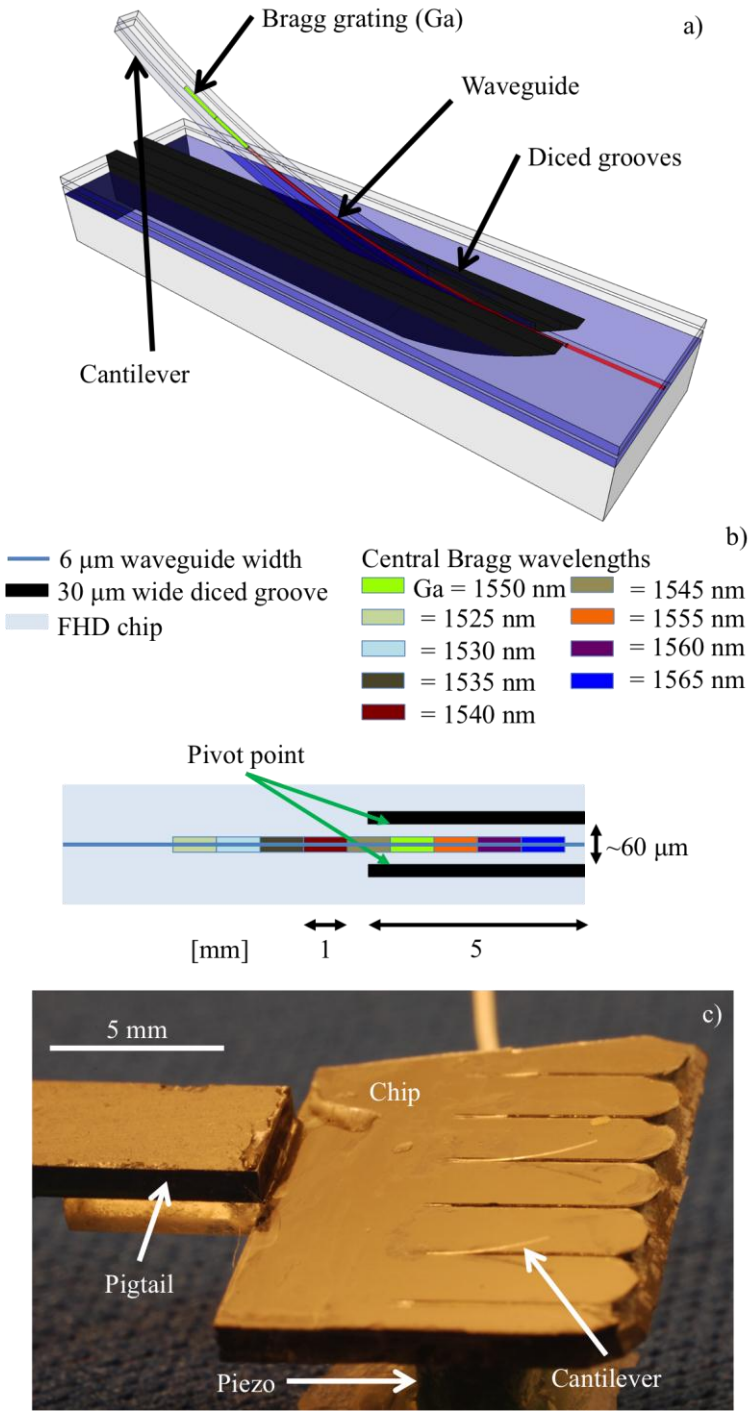

Figure 65 microcantilevers with a single Bragg grating interrogation. a) diagram (not to scale), b) top view schematic (not to scale) and c) micrograph.

Figure 65 a) shows a diagram of the microcantilever with single Bragg grating interrogation, deflection being measured by grating Ga (shown as green). Figure 65 b) shows a schematic of the device with the locations and central Bragg wavelengths indicated. Figure 65 c) is a micrograph of the actual cantilever device used within this section. The optical connection was via a Polarisation Maintaining (PM) fibre

pigtail is shown along with the piezo used for mechanical excitation. The device originally contained nine cantilevers each being ~5 mm in length, ~60 µm wide and ~50 µm in height. As shown in Figure 65 b) the waveguide contained nine 1mm Bragg gratings equally distributed along 6 µm wide channel waveguides; five located within the substrate and five within the cantilever. However, the device was damaged and several cantilevers were lost and also resulted in the cantilever interrogated within this section losing ~1 mm of its length. Thus, as it can be seen from the reflection spectra in Figure 66, the Bragg grating at 1565 nm was lost.

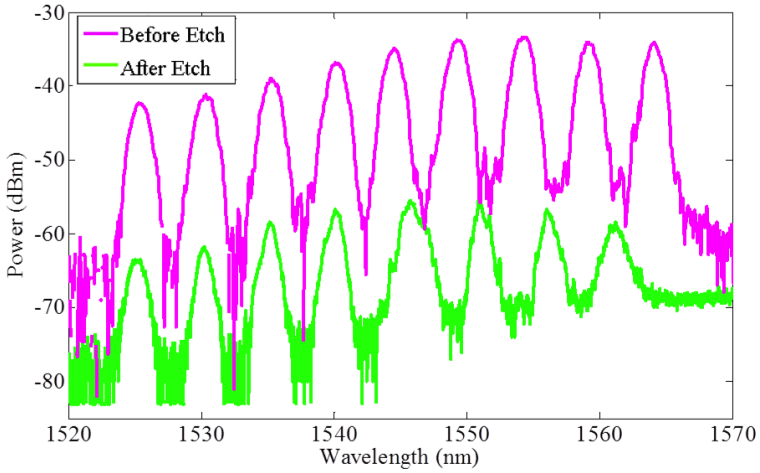

Figure 66 reflection spectra were collected before (pink) and after (green) wet etching with KOH for the device shown in Figure 65. Counting from left-hand side (green), the first four Bragg gratings reside within the chip and a further four reside within the cantilever.

The reflection data shown in Figure 66 is taken from the device shown in Figure 65. The reflection spectra were collected before and after wet etching with KOH, with a broadband source, 50/50 coupler, PM polarizer and an Optical Spectrum Analyser (OSA). The central Bragg wavelengths of the gratings along the cantilever device ranged from 1525-1560 nm with an equal spectral spacing of 5 nm. Differences in amplitude of the Bragg gratings in Figure 66 were caused by a change in the coupling efficiency, which can be attributed to the damage caused to the input facet by the wet etching process before the protocol with the PTFE holder was implemented. Also notice a shift in the central Bragg wavelengths of the four Bragg gratings residing in the cantilever, which were originally written at 1545, 1550, 1555 and 1560 nm (pink line). This shift is further explained in section 5.7, which relates to the release of stresses contained in the glass layers as a result of the FHD

fabrication. To predict Bragg grating response in the cantilever structures fabricated, an analytical expression is developed in the following section.

5.4 Single Bragg grating deflection theory

Bragg gratings residing within the waveguides allows monitoring of the local strain field in 1 mm intervals along the length of the cantilever. The single Gaussian apodised Bragg gratings within the microcantilever can be described by this equation and relates the spectral shift in the Bragg grating's central wavelength to strain [17],

$$\frac{\Delta\lambda_B}{\lambda_B} = \varepsilon - \frac{\varepsilon n_{eff}^2}{2}(p_{12} - \upsilon(p_{11} + p_{12})) \qquad \textbf{Equation 72}$$

where $\Delta\lambda_B$ is the change in central wavelength of the Bragg reflection, λ_B is the central Bragg wavelength, ε is the induced strain, n_{eff} is the effective refractive index for a given wavelength, p_{ij} is the strain-optic tensor and υ is Poisson's ratio. This formula includes both the pitch change of the grating and the refractive index change from induced strain. Primarily the central Bragg wavelength change results from the change in the grating pitch. Equation 72 also shows that the central Bragg wavelength is affected by the material's strain-optic properties, which affects its density and thus refractive index.

For direct UV written waveguides, the effective refractive index (at 1550 nm) is n_{eff} ~1.448. Assuming FHD silica has similar strain-optic coefficients and similar Poisson's ratio to plasma enhanced chemical vapour deposition silica, the values are as follows; p_{11} = 0.121, p_{12} = 0.270, and υ = 0.2 [18]. Thus, Equation 72 can be simplified to,

$$\Delta\lambda_B \approx 0.8\varepsilon\lambda_B. \qquad \textbf{Equation 73}$$

Equation 72 shows the central Bragg wavelength shift is proportional to strain where the dominant mechanism is Bragg grating elongation.

5.5 Pressure sensing

To investigate the glass microcantilever response as a physical sensor, air pressure changes were measured. To make the device sensitive to changes in air pressure it was operated akin to an Atomic Force Microscope (AFM) in a 'tapping mode' [1]. One of the microcantilever's resonant mechanical flexure modes was excited with a piezo, as shown in Figure 65 c). The Bragg grating with the greatest response to strain had a laser source spectrally tuned to a part of the grating's spectra, that created a signal whose amplitude is proportional to $\Delta\lambda_B$ (change in central wavelength) and consequently strain. From Figure 66, green line, counting from the left hand side, the sixth Bragg grating was interrogated in this experiment, which has a peak at ~1550.9 nm. This Bragg grating, being the most sensitive to strain, fits with standard cantilever theory as it is known that strain increases linearly towards the pivot point (Figure 65 b)), see section 5.4 [19]. A lock-in detection method was used to read the reflected intensity and phase of the signal at the mechanical oscillation frequency, a schematic of the experimental setup is shown in Figure 67.

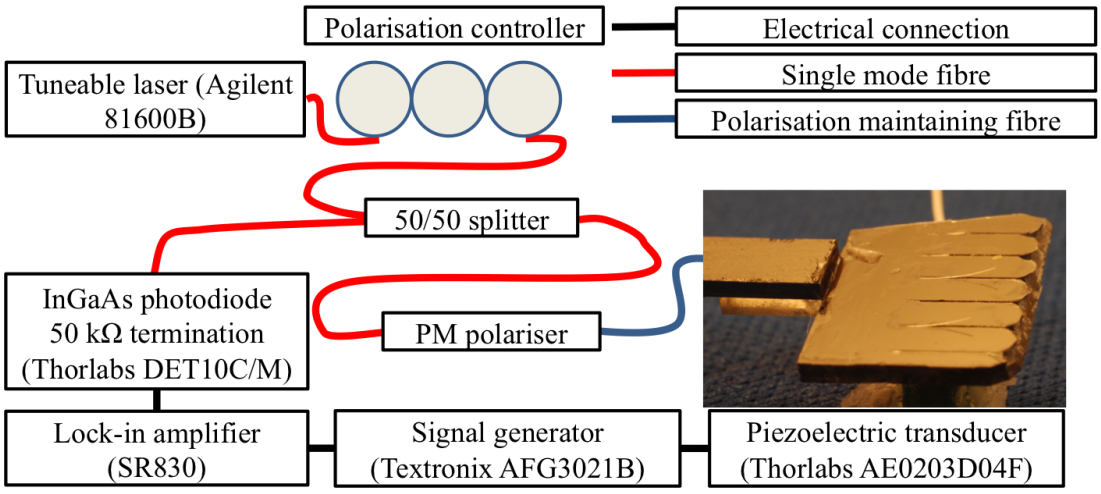

Figure 67 phase sensitive interrogation of cantilever mechanical resonances, with electrical and optical connections.

To match the point of the highest gradient on the sixth Bragg grating, a tuneable laser (Agilent, 81689A) was tuned to a wavelength of 1550.7 nm. The piezoelectric transducer, shown in Figure 65 c), was driven through a frequency of 10-100 kHz.

The reflected optical signal, from the Bragg grating, was measured with a terminated photodiode (InGaAs photodiode, Thorlabs, DET10C/M with 50 kΩ termination). The photodiode signal was sent to a lock-in amplifier (Stanford Research Systems, SRS830) and the piezo transducer was driven from the internal sinusoidal output of the lock-in amplifier, with the signal generator (Textronix, AFG3012B) used for impedance matching. There was significant Relative Intensity Noise (RIN) from the tuneable laser, below 10 kHz thus frequencies below this were avoided. A mechanical resonance with a large amplitude was found to be at ~25.7 kHz and was used because of the absence of relative intensity noise. To investigate how pressure affects the mechanical resonance of the microcantilever, the microcantilever was placed in a vacuum chamber using a fibre feed through. The air was then evacuated from the vacuum chamber down to 16 μbar and the piezo transducer was swept from 25 to 27.5 kHz. The pressure inside the vessel was then brought back to atmosphere and was held at set pressures using a needle valve. At each pressure, the piezo was swept in frequency and the photo diode signal collected. A vacuum pump (Trivac E2) was used in conjunction with an integrated pressure sensor (Leybold TTR 91) throughout this experiment. The amplitude and phase of the cantilever are shown for varying pressures in Figure 68 and Figure 69, respectively.

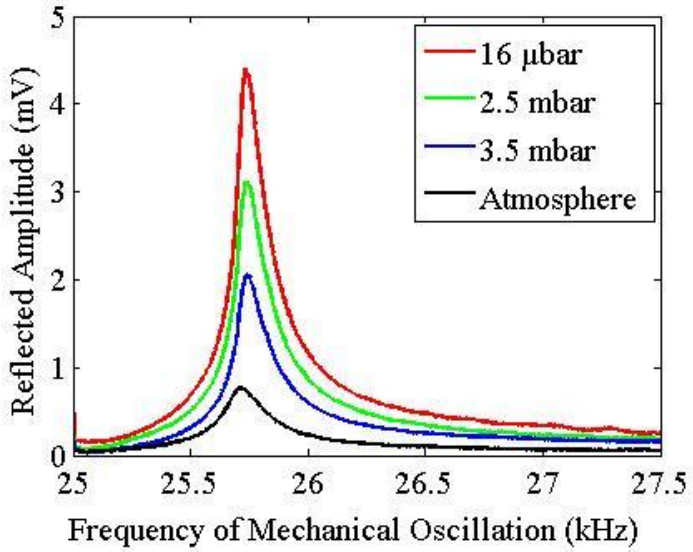

Figure 68 change in reflected amplitude from the cantilever with mechanical driving oscillation.

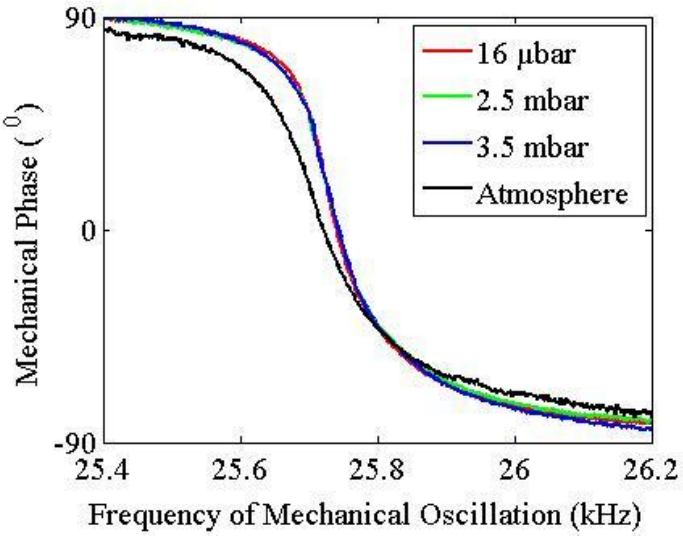

Figure 69 change in reflected phase from the cantilever with mechanical driving oscillation.

Figure 68 and Figure 69 shows the amplitude and phase response of a selection of mechanical resonances taken over a pressure range from 16 µbar to atmosphere. Figure 69 shows the characteristic 180° phase change of mechanical resonance. For each pressure the amplitude response of every mechanical resonance was fitted, by applying a damped driven oscillator model [20],

$$A(\omega) = \frac{{F_o}/{m}}{\sqrt{[(\omega_o^2 - \omega^2)^2 + 4\gamma^2\omega^2]}} \qquad \textbf{Equation 74}$$

where $A(\omega)$ is the amplitude, F_o is the maximum applied force, m is the mass, ω is the angular frequency of the piezo, ω_o is the resonant angular frequency of the cantilever and γ is the damping coefficient. Optimisation of all of the damped driven oscillator parameters was achieved using the Nelder-Mead simplex search method [21], which was implemented by using the 'fminsearch' function within Matlab. The damping coefficient of the cantilever's mechanical resonance at 25.7 kHz is plotted against vacuum chamber pressure and is shown in Figure 70.

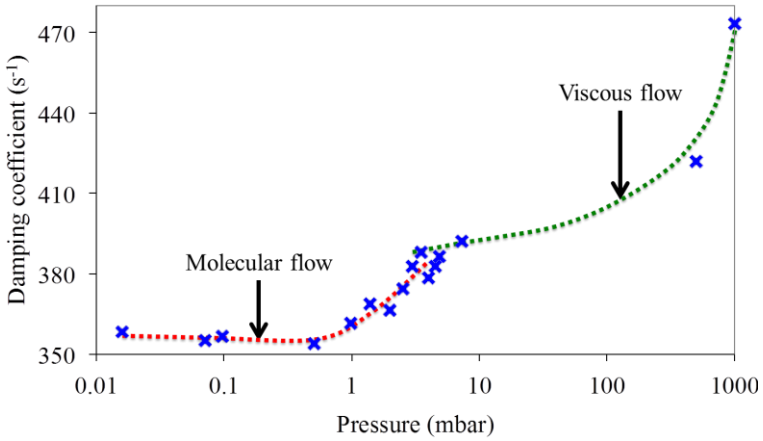

Figure 70 cantilever's mechanical resonance damping coefficient against vacuum chamber pressure. Notice the change in flow regime of the gas, from molecular to viscous, at around 1 mbar.

Figure 70 shows two distinct regimes, see red and green guide lines. There is a characteristic transition from molecular flow to viscous flow of the air at around 1 mbar. Figure 70 agrees with the similar regime reported by Kumazaki *et al.* [22], who investigated changes in mechanical resonance for different air pressures for an optical fibre based cantilever. The increase in damping coefficient, shown in Figure 70, is related to a decrease in mean free path of the air particles, as the pressure within the vacuum chamber is increased. In the molecular flow regime, few gas molecules are present because of the lower pressure, thus fewer collisions occur between the gas molecules and the cantilever, resulting in the mean free path dominating. At high pressures the behaviour tends towards a classical viscous fluid. In the molecular regime this allows the cantilever to oscillate with a greater amplitude, as shown by the 4.5 mV peak amplitude at 16 μbar, seen in Figure 68, when compared to the 0.7 mV peak amplitude at atmospheric pressure. This change in peak amplitude is directly affected by the reduced dampening coefficient that occurs when pressure alters between 16 μbar and atmosphere. This can be seen in Figure 70, where the dampening coefficient changes by ~110 s^{-1}. As the pressure within the vacuum chamber increases, the air system moves into the viscous flow regime, where more gas molecule/cantilever collisions occur. This reduces cantilever deflection (Figure 68) and increases the cantilever dampening coefficient (Figure 70). There are few points measured within the viscous flow regime owing to limited control of the needle valve at the higher pressure.

After the pressures experiments were conducted, the device's performance was quantified by Christopher Holmes [23]. This was achieved by using a profilometer to actuate the cantilever while simultaneously collecting broadband spectra to measure the Bragg central wavelength shift for each Bragg grating within the cantilever. Thus Christopher's experiment allowed device performance metrics, such as minimum resolvable force and sensitivity, to be measured; these are discussed and compared to a Fabry-Pérot configuration in section 5.9.

The cantilever's change in dampening coefficient has showed regime change in air molecule/cantilever interactions, using single Bragg grating interrogation. In the next section the fabrication of Fabry-Pérot cantilever interrogation is covered, along with the successful and unsuccessful fabrication methods used.

5.6 Fabry-Pérot interferometer microcantilever fabrication

In the previous sections, a cantilever with single Bragg gratings interrogation was investigated and the change in its mechanical resonance was measured in response to a change in ambient pressure [12]. This section investigates increasing the cantilevers sensitivity to displacement by implementing a Fabry-Pérot configuration. This cavity system presents a route to increase the spectral sharpness of the spectral response.

As discussed earlier, an induced deflection of the cantilever will result in a linear strain along its length, when a point force is applied. An optical phase change occurs upon induced strain within the waveguide in the cantilever. This phase change can be sensed interferometrically between either a pair of Bragg gratings or a Bragg grating and mirror (see Figure 71). Monitoring of this interference allows the displacement of the cantilever to be sensed. The author attempted three methods to create a Fabry-Pérot interferometer within the microcantilever structure. These were:

- Adding gold to the end facet creating a broadband mirror (see Figure 71 a)).
- Pairing a Gaussian apodised and chirped Gaussian apodised Bragg grating (see Figure 71 b)).

- Using a pair of spectrally matched gratings and counteracting changes in the Bragg central wavelength during cantilever fabrication, by adding a predetermined shift (see Figure 71 c)).

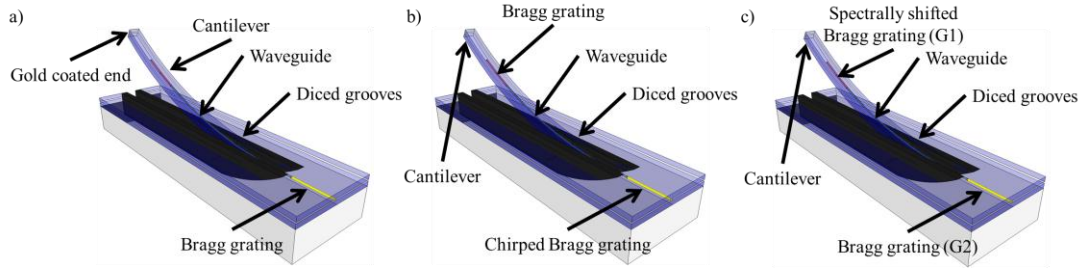

Figure 71 two unsuccessful designs for Fabry-Pérot interferometers. a) used a gold coated cantilever facet, b) used a Bragg grating in the cantilever and a chirped grating within the chip and c) shows the successful design utilising a pair of spectrally matched Bragg gratings.

The first method, shown in Figure 71 a) produced very poor cavities due to the low reflectivity of the gold end mirror. This is thought to be primarily due to the quality of the cantilever facet, which was damaged by the KOH (Potassium Hydroxide) wet etching, as discussed in section 5.2.3. Microscope inspection also showed that the evaporated gold did not adhere well to the end of the cantilever. This is attributed to contamination of dust and dirt resulting from the inability to clean the microcantilevers without surface tension snapping them.

The second method shown in Figure 71 b), failed also due to the reflectivity of the chirped grating being insufficient to create Fabry-Pérot interference large enough to resolve above the background optical noise. The length of the chirped grating was already 4mm and could not be significantly increased without changing the device length. However, this method would have been an elegant solution to creating a cavity, as the large bandwidth of the chirped Bragg grating would have given a greater spectral tolerance to aligning the cavity. Moreover, it is not a broadband reflector as the first method, thus would have allowed the device still to be spectrally multiplexed.

The third method, shown in Figure 71 c), gave the best results after maximising the spectral overlap of two gratings to form a Fabry-Pérot interferometer, taking advantage of spectrally matched saturated Bragg gratings within the bulk chip and cantilever. This is illustrated schematically in Figure 71 c), where Bragg grating G1 resides in the cantilever, and Bragg grating G2, within the bulk chip. During the

fabrication of the cantilever the Bragg grating within the cantilever is spectrally shifted, compared to the one in the bulk substrate. The spectral shift results from a release of the stress from the thermal mismatch of Flame Hydrolysis Deposition (FHD) glass and silicon. The following section explains the fabrication used to produce these devices.

5.7 Fabry-Pérot interferometer fabrication with pre-shifted Bragg Gratings

It was found experimentally that G1 (see Figure 73 a)) experiences a central Bragg wavelength shift of 1.77 nm for the Transverse Electric (TE) polarization after the wet etching process. This spectral shift of the Bragg grating residing in the cantilever is associated from the release of compressive stresses locked into the sample from the high consolidation temperatures (~1200°C) used in the FHD process and are a result of the mismatch in thermal expansion coefficients between the silica and silicon. To ensure two Bragg gratings overlap spectrally, the spectral shift of a single Bragg grating residing in cantilever was empirically found. To measure the spectral shift of a single Bragg grating within a cantilever after wet etching, a device was created with three 1 mm Gaussian apodised gratings, two residing within the cantilever and one within the chip in a similar fashion to the device shown in Figure 65. Before and after wet etching the cantilever devices, the reflection spectra were collected, as shown in Figure 72.

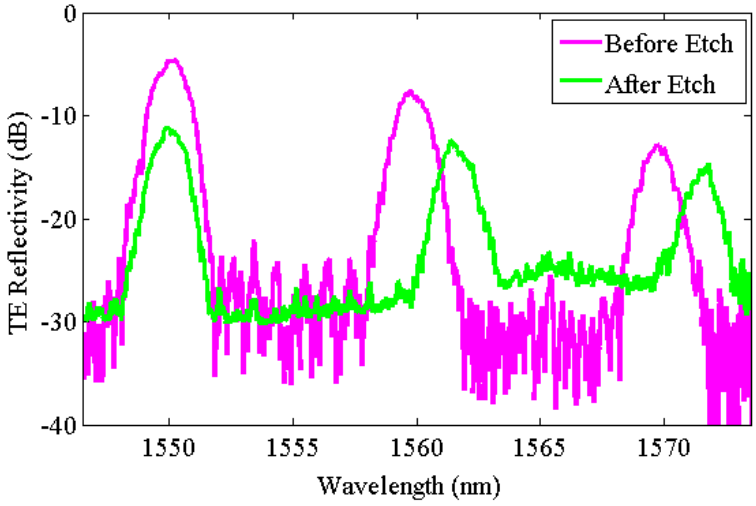

Figure 72 reflection spectra (TE polarization) of the three 1mm Gaussian apodised Bragg gratings within a microcantilever before (pink) and after (green) wet etching. The Bragg grating centred at 1550nm is in the bulk chip and the other two are located within the cantilever.

Figure 72 shows the reflection spectra of the device fabricated to determine the spectral shift of Bragg grating within a cantilever after wet etching. The reflection spectra were collected using a broadband source, 50/50 coupler, PM polarizer and an Optical Spectrum Analyser (OSA). The TE reflection spectra data shows an average spectral shift in central wavelength of 1.77 nm. With this knowledge a new device was then created to fabricate a Fabry-Pérot interferometer. To ensure spectral overlap of the two gratings after etching, the Bragg grating in the cantilever (G1) was spectrally shifted by –1.77 nm compared to that in the bulk (G2), as shown in Figure 73 a).

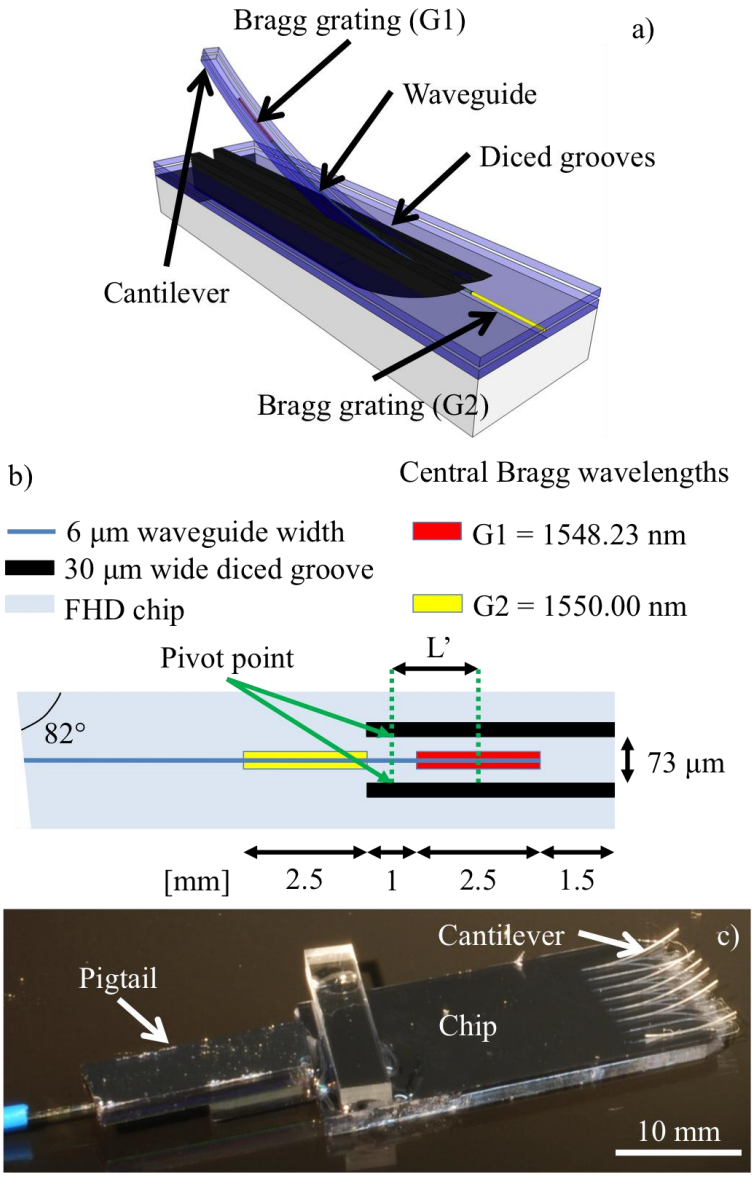

Figure 73 microcantilevers with a Fabry-Pérot interrogation, a) diagram (not a scale), b) top view schematic (not to scale) and c) micrograph.

Figure 73 a) shows a 3D diagram of a microcantilever with Fabry-Pérot interrogation, the cavity being made between G1 and G2. Figure 73 b) shows a schematic of the device with the locations and central Bragg wavelengths indicated, the G1 (red) and G2 (yellow) gratings forming the Fabry-Pérot cavity after etching. It should be noted that G1 and the space between the gratings in the cantilever will be sensitive to strain, G2 will be insensitive to strain because it is placed in the chip. The microcantilever is formed between the pair of diced grooves (black). To improve return loss as discussed in section 5.2.4, the device had an input facet diced to 8° and the waveguide in the cantilever was also terminated at 1.5 mm before the

end of the cantilever. Figure 73 c) is a micrograph of the actual cantilever device used within this section. In Figure 73 c) the optical connection is also shown via a Polarisation Maintaining (PM) fibre pigtail. Notice the glass strengthening bar which improved the longevity of the glued pigtail. The spectra were taken before and after wet etching of the device, as shown in Figure 74.

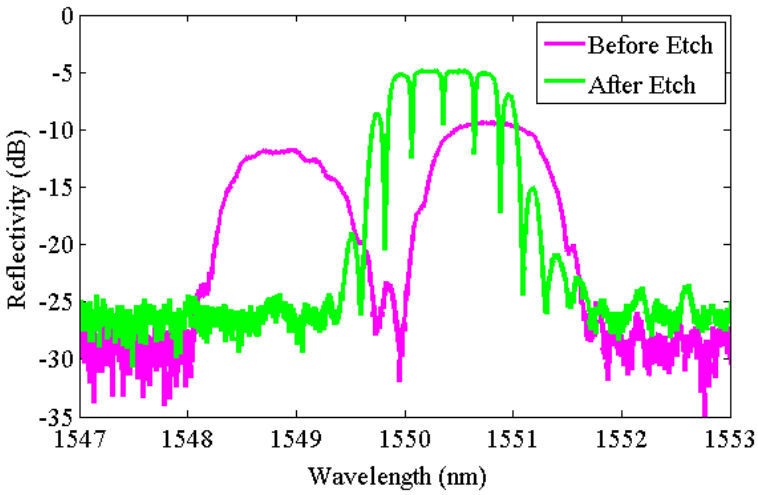

Figure 74 reflection spectra of cantilever with Fabry-Pérot interrogation, before (pink) and after (green) wet etching, TE polarization.

Figure 74 shows the predetermined spectral separation of the two cavity Bragg gratings of 1.77 nm in pink. After etching, the creation of the Fabry-Pérot cavity featuring sharp resonance fringes is depicted in green. The spectra in Figure 74 was collected in reflection using a broadband source, OSA, 50/50 coupler and PM polarizer set for TE.

The fabrication of Fabry-Pérot interferometer using the pre-shifted Bragg grating approach has been covered. In the next section an analytical function is produced relating cantilever deflection, to shifts in optical phase in the Fabry-Pérot cavity.

5.8 Fabry-Pérot interferometer deflection theory

The strain applied by a point force in a cantilever can be calculated by standard solid mechanics theory and can be applied to predict the optical phase change caused in the Fabry-Pérot interrogated cantilever. The microcantilever is assumed to be a

homogenous, isotropic, rectangular beam and its response to strain is related to its second moment of inertia. Thus [19],

$$\varepsilon = \frac{\sigma}{E} = \frac{My}{EI} \quad \textbf{Equation 75}$$

$$M = Fl \quad \textbf{Equation 76}$$

$$I = \frac{wx^3}{12} \quad \textbf{Equation 77}$$

where ε is the strain, σ is the stress, E is the Young's modulus, M is the moment of loading, y is the distance from the neutral axis, I is the second moment of inertia, F is the force on the cantilever, l is the cantilever's length, w is the cantilever's width and x is the thickness of the silica. Combining Equation 75, Equation 76 and Equation 77 from above, produces a simplified expression relating force to strain,

$$\varepsilon = \frac{12Fly}{Ewx^3}. \quad \textbf{Equation 78}$$

This equation calculates the strain at the pivot point (see Figure 65 and Figure 73), which is at the point of maximum strain. The strain along the cantilever can be calculated by linear interpolation from the pivot point, which sees a maximum strain value, to zero strain at the cantilever's free end. Thus to optimize sensitivity to strain, the grating must be as close to the pivot point as possible in a single Bragg grating interrogation system. To further increase the strain sensitivity, the length of the cantilever could be maximized and the width and thickness must be minimised. However, the thickness of the FHD silica layers are restricted in order to yield low-loss single mode waveguides and be insensitive to external factors such as moisture.

Later a surface profilometer was used to calibrate the optical response of the Fabry-Pérot interrogated cantilever, as described in section 5.9. The expected strain is calculated from the applied force provided by a profilometer (see chapter 2) and the physical constants of the wafer. The profilometer and wafer parameters are as follows: 491 µN of force (F), over a cantilever length (l) of 4.1 mm, a vertical displacement from the neutral axis (y) of 8 µm as measured from the waveguide, a Young's modulus (E) of 80 GPa [18], a cantilever width of (w) of 73 µm and a thickness (x) of 54 µm, see Figure 75. From this equation the strain at the pivot point, which is the point of maximum strain where the cantilever joins the chip, is calculated to be 219 µε (microstrains).

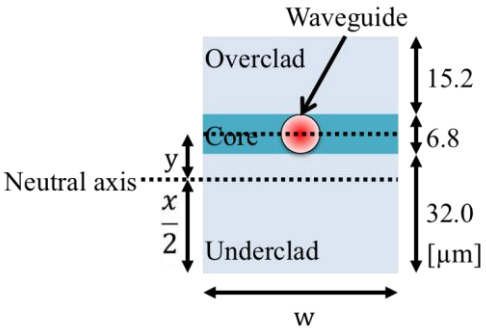

Figure 75 Fabry-Pérot interrogated cantilever dimensions side view (not to scale).

There are two physical mechanisms that induce a Fabry-Pérot fringe shift when the cantilever is deflected. A change in cavity length of the silica waveguide induces fringe shift, as does a change in refractive index of the waveguide via the strain-optic effect. This Fabry-Pérot fringe shift can be quantified by measuring its change in optical phase. Linear interpolation was used to calculate the strain along the length of the cantilever; this was calculated from the pivot point to the end of the stylus sweep (4.1 mm along the cantilever). The profilometer was only able to traverse 4.1 mm along the cantilever because of its vertical scanning limit. The length of the cavity (L') is defined as the distance measured from the pivot point (Figure 73 b)) to the centre of the Bragg grating within the cantilever (G1), corresponding to an effective reflection point (approximated to be at the midpoint of the grating [24]). The cavity length in the cantilever (L'), was measured to be 1.8 mm using a white light interferometer (Zemetrics, Zescope, see chapter 2) at 10x magnification, to find the pivot point and the end of the device.

The optical phase change within the Fabry-Pérot will be the integrated optical path change due to the strain along its length. This effectively averages the strain, which is given by the midpoint of the cavity within the cantilever. Under the linear assumption of strain, decreasing from the cantilever's pivot point, the average strain applied (ε_{ave}) to the Fabry-Pérot is 172 με. The total induced optical change in phase for a single round trip caused by this strain is given by [17],

$$\Delta\phi = \left\{\frac{2\pi n_{eff}}{\lambda_o}\right\}\left\{1 - \frac{n_{eff}^2}{2}[p_{12} - \upsilon(p_{11} + p_{12})]\right\} L'\varepsilon_{ave} \qquad \textbf{Equation 79}$$

where $\Delta\phi$ is the phase difference, n_{eff} is the effective refractive index of the waveguide, λ_o is the central wavelength of the comb, p_{ij} is the strain-optic tensor, υ

is Poisson's ratio, L' is the length of the cavity affected by strain and ε_{ave} is the average induced strain. With a n_{eff} of 1.448, λ_o is taken as ~1550.4 nm from Figure 74, taking the values for silica of p_{11} of 0.121, p_{12} of 0.270, υ of 0.2 [18], a L' of 1.8 mm and a strain $\varepsilon_{ave}$of 172 με. This predicts a phase difference ($\Delta\phi$) of 1.42 radians. The theoretical prediction is compared in section 5.9 to the experimentally measured optical data collected whilst interrogating the cantilever under strain. The Fabry-Pérot phase change is found by fitting the spectra with coupled mode theory.

An analytical function has been presented that relates applied point force, to the cantilever, to shifts in optical phase of the Fabry-Pérot interferometer. To validate the analytical model, an experiment was performed where a Fabry-Pérot cantilever is deflected by a profilometer while optical reflection spectra is recorded.

5.9 Displacement sensing

To investigate the Fabry-Pérot fringe shift, the cantilever was displaced by applying an accurate point force (see Figure 76), via a profilometer. A similar experiment was carried out by Christopher Holmes on the single Bragg grating device [23]. The profilometer (KLA-Tencor, P16, stylus profiler, see chapter 2) was used to apply a point force, scanning from before the pivot point of the cantilever, to 4.1 mm along its length. As discussed in section 5.8, the profilometer had a limited vertical scan range, thus only being able to traverse the first 4.1mm of the 5mm cantilever length. A point force of 491 μN was applied along the length of the cantilever. A raster scan was used to apply the force laterally over the waveguide in 1 μm steps, to ensure that the applied force about the pivot point had a negligible component of torsional strain. While the profilometer was scanning the length of the cantilever, reflection spectra were simultaneous collected from the device, see Figure 76.

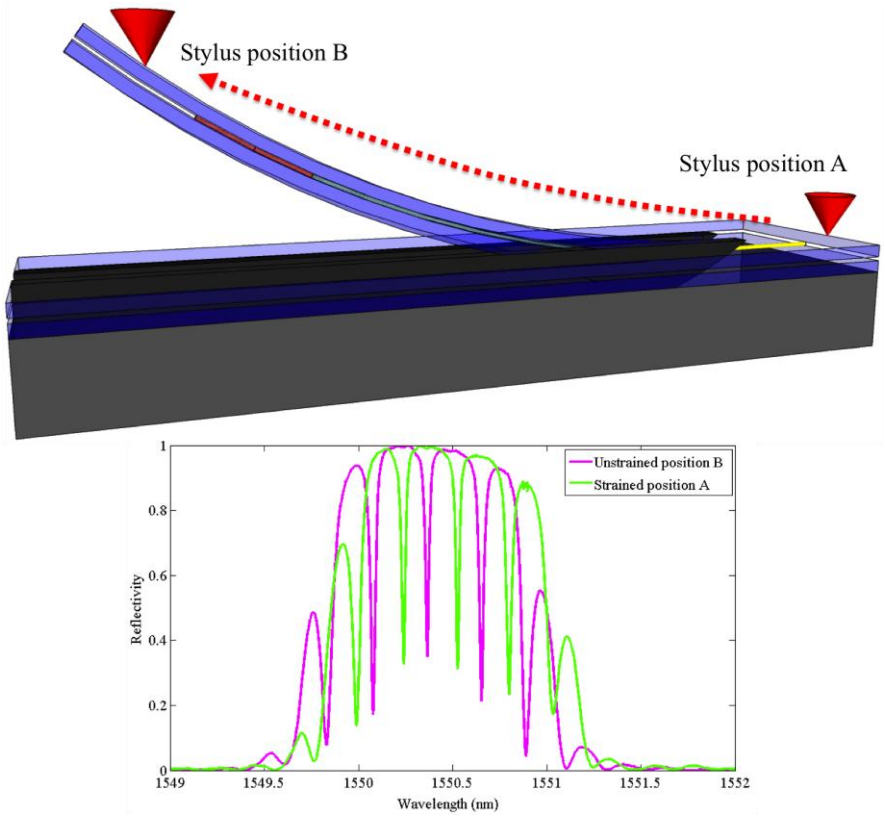

Figure 76 side view of the 3D cantilever diagram showing the progression of the profilometer, with the resultant spectra of the Fabry-Pérot cantilever for the unstrained and strained states.

Figure 76 shows a schematic of the profilometer's progression over the length of the cantilever. Figure 76 also shows the spectra of the cavity in an unstrained and strained states, *i.e.* when the stylus is in contact with the chip and with the end of the cantilever, respectively. Both spectra were collected using a broadband source, OSA, 50/50 coupler and PM (Polarising Maintaining) polarizer set for TE. The acquisition rate was such that 197 samples were taken from the unstrained, to strained states.

The experimental procedure has been explained for the accurate deflection of the cantilever. Fitting of the Fabry-Pérot comb shift using coupled mode theory to calculate the optical phase shift from the applied point force is discussed in the next section.

5.9.1 Coupled mode theory fitting

To fit the Fabry-Pérot comb, Coupled Mode Theory (CMT) [25] was utilized, see chapter 3. This allowed the cavity's optical phase change to be calculated with applied stylus force. An analytical solution of a sine modulated Gaussian was applied to the Fabry-Pérot comb, however this gave a poor fit as the function did not

fit well to the saturated Bragg gratings, used to make the comb. Thus, CMT was used to accurately fit Bragg grating features such as grating strength, chirp and Fabry-Pérot spectral overlap.

The coupled mode equations from chapter 3 have to be modified to accurately represent the Fabry-Pérot interferometer. Thus, terms describing the Gaussian apodisation of the pair of Bragg gratings have been added, with respect to their spatial positions. G1 (see Figure 73 b)), which is the Bragg grating within the cantilever has also been given a phase shift (ϕ), relative to the grating (G2) within the chip, and linear chirp (F). A schematic of the refractive index profile the coupled mode equations are based on, is shown in Figure 77.

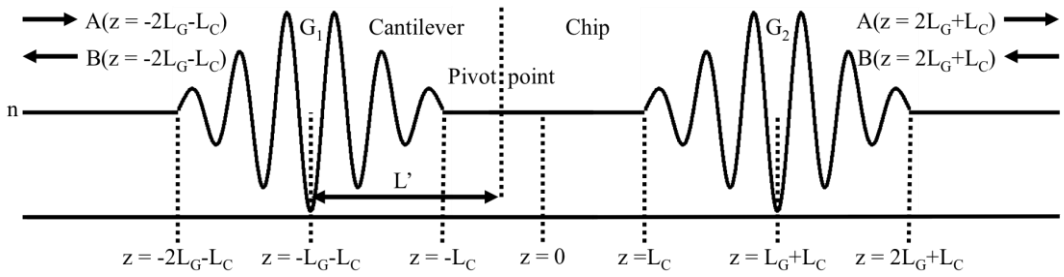

Figure 77 schematic of refractive index modulation of Fabry-Pérot interferometer z = 0 set to the middle of the cavity, with G1 and G2 within the cantilever and chip respectfully.

Figure 77 shows the refractive index profile used to represent the Fabry-Pérot interferometer. The centre point of the cavity is set to z = 0, where the Bragg gratings lengths are $2L_G$ and the space between the Bragg gratings is $2L_C$, producing coupled equations for the region $z < -L_C$,

$$\frac{dA}{dz} = a_1\kappa_1 B e^{j\Gamma_1 z+\phi+fz^2}, z < -L_C \qquad \textbf{Equation 80}$$

$$\frac{dB}{dz} = a_1\kappa_1 A e^{-j\Gamma_1 z+\phi+fz^2}, z < -L_C \qquad \textbf{Equation 81}$$

where $A(z)$ and $B(z)$ are z dependent amplitudes and $a_1$is the apodisation profile for G1. Thus,

$$a_1 = e^{-\frac{|z-L_G-L_C|^2}{L_G^2}}. \qquad \textbf{Equation 82}$$

κ_1 is the coupling coefficient for G1, taking the form,

$$\kappa_1 = \frac{\pi\overline{\delta n_{eff}}}{\lambda_{B1}} \quad \textbf{Equation 83}$$

where $\overline{\delta n_{eff}}$ is the constant offset or 'DC' effective refractive index modulation averaged over a single grating period (Λ) of the Bragg grating and λ_{B1} is the Bragg central wavelength of G1. Remembering the Bragg central wavelength equation, $\lambda_{B1} = 2n_{eff}\Lambda_1$, where n_{eff} is the effective refractive index of the mode and Λ_1 is the Bragg grating period for G1. The 'DC' refractive effective index modulation ($\overline{\delta n_{eff}}$) and G1's grating period (Λ_1) were parameters that were optimised to fit the comb.

Also, Γ_1 is the core power confinement factor for G1. $\Gamma_1 = \beta_1 + \beta_2 - K_1$, where β_1 and β_2 are the propagation constant for the forward and backward propagating modes respectfully and $K_1 = 2\pi/\Lambda_1$. The coupling is between two identical optical modes, just moving in opposite directions, thus $\beta_1 = \beta_2 = (2\pi/\lambda_0)n_{eff}$, resulting in,

$$\Gamma_1 = (4\pi/\lambda_0)n_{eff} - 2\pi/\Lambda_1 \quad \textbf{Equation 84}$$

where λ_0 is the wavelengths the coupled mode equations are solved over, the wavelength range was set to 1549-1552 nm. Furthermore, ϕ is the optical phase between the pair of gratings and f is the chirp operator which is defined as,

$$f = \frac{2\pi F n_{eff}}{\left(2n_{eff}\Lambda_1\right)^2} \quad \textbf{Equation 85}$$

where F is the linear chirp in nm/cm. Both optical phase (ϕ) and the linear chirp (F) were parameters that were optimised to fit the comb. For the region in-between G1 and G2 ($-L_C < z < L_C$) the coupled mode equations become,

$$\frac{dA}{dz} = 0, -L_C < z < L_C \quad \textbf{Equation 86}$$

$$\frac{dB}{dz} = 0, -L_C < z < L_C\,. \quad \textbf{Equation 87}$$

Both Equation 86 and Equation 87 equal zero because there is no grating present so it is assumed no power transfers between forward and backward propagating modes. The coupled mode equations for G2, in the region $z > L_C$, takes the form,

$$\frac{dA}{dz} = a_2\kappa_2 B e^{j\Gamma_2 z}, z > L_C \quad \textbf{Equation 88}$$

$$\frac{dB}{dz} = a_2\kappa_2 A e^{-j\Gamma_2 z}, z > L_C\,. \quad \textbf{Equation 89}$$

This variant of the coupled mode equations representing G2, do not posses optical phase and chirp terms. A second phase term is unneeded because the phase is a term that is relative between G1 and G2. A chirp term is also negated as G1 and G2 were both direct UV written without chirp. Chirp is only included in G1's equations because it resides within the cantilever and is subjected to the release of fabrication stresses, thus was thought might exhibit chirp. a_2 is the apodisation profile for G2 and takes the form,

$$a_2 = e^{-\frac{|z+L_G+L_C|^2}{L_G^2}} \quad \textbf{Equation 90}$$

Notice the signs have reversed in the exponent. κ_2 is the coupling coefficient for G2 and is defined as,

$$\kappa_2 = \frac{\pi\overline{\delta n_{eff}}}{\lambda_{B2}} \quad \textbf{Equation 91}$$

where λ_{B2} is the Bragg central wavelength of G2 and was experimentally measured before etching the device, see Figure 74. Γ_2 is the core power confinement factor for G2,

$$\Gamma_2 = (4\pi/\lambda_0)n_{eff} - 2\pi/\Lambda_2 \quad \textbf{Equation 92}$$

where Λ_2 is the Bragg grating period for G2.

To deduce appropriate initial conditions Figure 77 is used and uses the same assumptions as in chapter 3. Figure 77 shows the Fabry-Pérot interferometer's refractive index profile. It is assumed at $A(\mathrm{z} = -2L_C - L_G)$, the power will be one and that at $B(\mathrm{z} = 2L_C + L_G)$ there is no grating thus no backward propagating wave, so the power will be zero. By using these initial conditions, the coupled mode equations can be solved using adaptive step-size, 4th order Runge-Kutta [26], numerical integration tool in Matlab. The code calculates the values of $B(\mathrm{z} = -2L_C - L_G)$ and $A(\mathrm{z} = 2L_C + L_G)$ by interpolating the exponential power drop along the grating (in the z direction) for each wavelength of interest (λ_o). Then to

find the reflectivity of the grating the B and A, exponents are divided and the modulus is taken and then squared.

Optimisation of coupled mode equation parameters to fit the comb was achieved using the Nelder-Mead simplex search method [21]. The Nelder-Mead simplex search was implemented by using the 'fminsearch' function within the Matlab's optimisation toolbox. The fitted Bragg grating parameters included: the 'DC' effective refractive index modulation averaged over a single grating period ($\overline{\delta n_{eff}}$), the mismatch in wavelength between the Bragg gratings central wavelengths of the two gratings making up the Fabry-Pérot ($\delta\lambda_B$) where $\delta\lambda_B = \lambda_{B2} - 2n_{eff}\Lambda_1$ and G1 grating period (Λ_1) was the fitted parameter, the optical phase between the pair of gratings (ϕ), the linear chirp of the cantilever Bragg grating (F) and an amplitude offset (C). As above the waveguide had an effective refractive index (n_{eff}) of 1.448. A 535 nm grating period (Λ_2) was measured from Figure 74 for the Bragg grating in the bulk (G2). The optimised CMT fit to the Fabry-Pérot interferometer is shown in Figure 78.

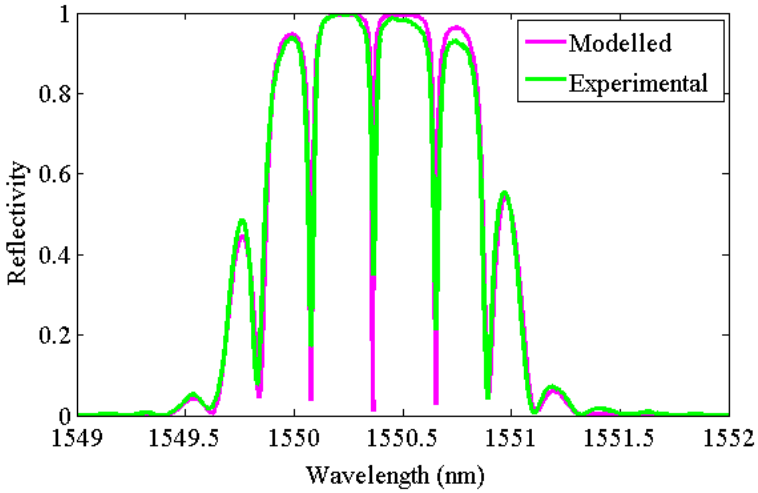

Figure 78 modelled (pink) and experimental reflectivity (green) of the Fabry-Pérot interrogation cantilever in an unstrained state.

Figure 78 showing the unstrained Fabry-Pérot spectra was fitted using coupled mode solver (pink) and the experimentally collected spectra (green). The CMT fitting calculated the following Bragg grating parameters for the unstrained condition: $\overline{\delta n_{eff}}$ = 8.06 x10^{-4}, $\delta\lambda_B$ = -24.3 pm, ϕ = 2.70 radians, F = 1.21 x10^{-6} nm/cm and C = 1.35 x10^{-3}. Using these grating parameters for the unstrained Fabry-Pérot, except

for optical phase (ϕ), the progression in optical phase (ϕ), with the movement of the profilometer along the cantilever length, was fitted. The new optical phase was found for 36 of the 197 samples, equally spaced along the length of the cantilever. The maximum optical phase was calculated to be 6.41 radians, 4.1 mm along the length of the cantilever. To convert from the theoretical parameter phase difference ($\Delta\phi$), from section 5.8, to the fitted phase parameter (ϕ), the initial phase of the of the unstrained Fabry-Pérot device (2.70), must be added to $\Delta\phi$.

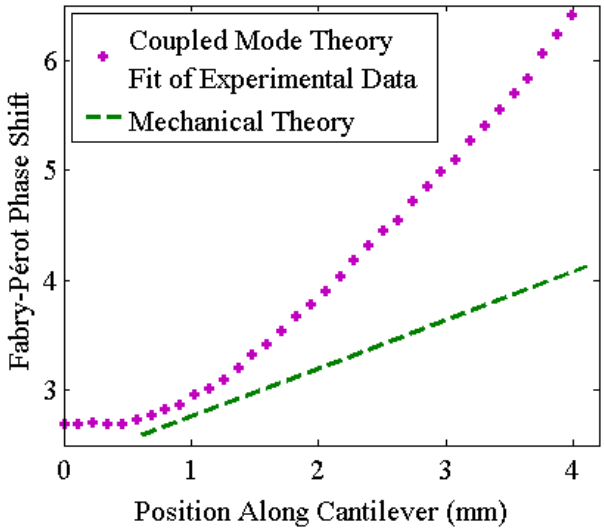

Figure 79 CMT fitted (dashed pink) and theoretical (dashed green) Fabry-Pérot phase shift with profilometer position on the cantilever. Mechanical theory plot has 2.70 radians offset accounting for initial starting phase of the cantilever.

Figure 79 shows the dependence of the Fabry-Pérot phase shift inferred from coupled mode theory (dashed pink) and the predicted phase shift from section 5.8 (dashed green), as a function of stylus position on the microcantilever. 2.70 radians has been added to the predicted phase shift as this is the initial starting phase of the Fabry-Pérot cavity in its unstrained state. The coupled mode theory had a maximum phase value of 6.41 radians, thus a phase shift (ϕ) of 3.71 radians is calculated, compared to the predicted phase shift ($\Delta\phi$) of only 1.42 radians, using the equation from section 5.8. Both trends shows a progressive increase in phase for the Fabry-Pérot, however the CMT fitted experimental phase shift (ϕ) disagree by a factor of ~2.6 with the predicted phase shift ($\Delta\phi$).

There are several factors that could explain discrepancy in the fitted experimental phase shift (ϕ) and predicted phase shift ($\Delta\phi$). The predicted phase shift ($\Delta\phi$)

assumes only small deflection, thus accurately predicts the initial behaviour when the deflection is linear, see Figure 79 (dashed green where gradients are well matched at ~1mm), as the initial gradients are very similar. Later, however, the deflection is likely to be nonlinear. The affects of both the residual stress in the glass laminate and the complex bending mechanics at the pivot point (see Figure 73) is ignored for simplicity. It should also be mentioned that mechanical constants such as Young's modulus, strain-optic tensor and Poisson's ratio, are not readily available for FHD glass and could have attributed to the errors seen.

Coupled mode theory has been used to infer optical phase change in the cavity from applied force; these results have also been compared to analytical predictions. The minimal resolvable force is an important quantity to a deflection sensor and is elaborated on in the next section.

5.9.2 Minimum resolvable force

To calculate the minimum resolvable force the Fabry-Pérot cantilever can resolve, the signal-to-noise ratio of the device and the interrogation equipment was measured. The fringe at ~1550.1 nm, shown in Figure 78, showed the greatest wavelength shift, from the spectra collected during stylus profiling, and was fitted using an inverted Gaussian function. The inverted Gaussian provided a wavelength shift for an applied force of 491 μN, thus allowing the force to be calibrated for this particular fringe. The Fabry-Pérot cantilever without loading was observed and same fringe was fitted again, utilising an inverted Gaussian function. This technique observed phase noise of an unloaded cantilever via monitoring the central wavelength jitter of the inverted Gaussian function. The standard deviation was taken over eight spectra that were collected in the cantilever's unstrained state. The detected wavelengths shifts, from random experimental noise, indicated that forces as small as 264 nN are potentially resolvable. This corresponds to a mass of 27 ng applied at the 4.1mm point on the Fabry-Pérot interrogated cantilever.

The minimum resolvable force for a cantilever with single Bragg grating interrogation was also calculated. This minimal resolvable force measurement was calculated by Christopher Holmes [23], where this single Bragg grating device is discussed in section 5.3. A similar technique, as before in the previous paragraph, was used to evaluate the experimental noise. The standard error of five consecutive

Bragg central wavelength measurements, of the sixth Bragg grating, counting from the left as shown in Figure 66, was taken. The minimum resolvable force for single Bragg grating cantilever interrogation was calculated to be 1.0 μN. Thus, the Fabry-Pérot interrogated cantilever has ~4 times better resolution than the single Bragg grating cantilever interrogation. This is most likely because the fringe is easier to fit to, due to its higher reflection strength (see Figure 66 and Figure 74) and the fringe's spectral sharpness.

Comparing the Fabry-Pérot interrogated cantilever to other Bragg grating based force sensors, shows it has a competitive minimum resolvable force value. A fibre Bragg grating was coupled to a steel cantilever to measure force and temperature simultaneously and had a minimum resolvable force of 13 mN [27]. Thus, the Fabry-Pérot interrogated cantilever can detect forces ~50 times smaller than this device. Another device optically couples a fibre Bragg grating with a highly reflectant membrane to form a Fabry-Pérot interferometer. This device can also measure force and temperature simultaneously and had a minimum resolvable force of 2.5 N [28], thus the Fabry-Pérot interrogated cantilever can resolve forces ~9000 times smaller. However, both of these fibre Bragg grating based devices are limited by the resolution of their spectral measurement system and not by experimental noise as the Fabry-Pérot cantilever is.

In the next section comments are made on the spectral sharpness of the Fabry-Pérot cavity and it is compared to the earlier device with single Bragg grating interrogation, as discussed in section 5.3.

5.9.3 Spectral sharpness

To compare the strain sensitivity between single Bragg grating and Fabry-Pérot cantilever interrogation, spectral sharpness is inspected. It is expected that Fabry-Pérot interrogation is the more sensitive because it possess greater spectral intensity/wavelength gradients. To compare spectral sharpness, the model in section 5.4 and the spectra shown in Figure 66 (sixth Bragg grating counting from left), were used to calculate intensity changes due to strain. Modelling was conducted using a 1mm Gaussian apodised Bragg grating at the point of highest strain with an identical cantilever geometry (*i.e.* same thickness, length, applied force *etc.*) as the new Fabry-Pérot device, enabling good comparison. The equations

in section 5.4 provides a Bragg central wavelength shift, thus the maximum intensity change, at a single wavelength which can be inferred using the spectra in Figure 66, thereby simulating the response of a fixed wavelength laser interrogation system. The comparison was taken for a strain of 8 με, which is equivalent to 23 μN of applied point load, 4.1 mm along the cantilever length or 1.025 mm traversed along the Fabry-Pérot device with the profilometer. Both of these result in the same applied strain. The calculated shift for an applied strain 8 με for the single Bragg grating was 11.0 pm compared to a measured shift of 10.7 pm for the Fabry-Pérot device measured from the subsequent spectra (not shown) between the unstrained and strained spectra shown in Figure 76, thus both devices shows a similar spectral change.

To simulate intensity based interrogation, *i.e.* with a tuneable laser, 50/50 splitter, polariser and photodetector, a single wavelength was monitored at a point of highest gradient for both the Fabry-Pérot comb and single Bragg grating systems and the normalised relative intensity changes were determined. As seen earlier, the relative wavelength shifts are comparable for the Fabry-Pérot and single Bragg grating device, however there was a factor of eleven times improvement in the intensity modulation for Fabry-Pérot interrogation compared to the single Bragg grating device. The eleven-fold improvement in intensity modulation can be attributed to the spectral sharpness of the Fabry-Pérot fringes compared to the single Bragg grating, even though the spectral shift of the two systems is comparable.

The spectral sharpness of the Fabry-Pérot cavity was compared to the single Bragg grating interrogation. The next section covers a calculation of the sensitivity of the Fabry-Pérot device.

5.9.4 Sensitivity

For Bragg grating based sensors, a typical metric of sensitivity is wavelength shift per unit applied force. The microcantilever with Fabry-Pérot interrogation had a recorded sensitivity of 330 nmN^{-1}. The minimum resolvable force was calculated by using the inverted Gaussian, as discussed in section 5.9.2, to determine the maximum fringe shift for the maximum force applied. For the Fabry-Pérot interrogation system a sensitivity of 330 nmN^{-1} was calculated. The Fabry-Pérot interrogation system is over twenty times more sensitive than a similar MEMS based

Bragg grating device shown in [29]. Comparing the microcantilever Fabry-Pérot interrogation to fibre Bragg grating based sensor, the device is orders of magnitude more sensitive in terms of spectral shift per applied force than a fibre Bragg grating based sensor [30].

Christopher Holmes preformed similar profiling experiments on the single Bragg grating device, discussed in section 5.9. Similar forces were applied and a sensitivity of 450 nmN^{-1} [23] was reported, thus the single Bragg grating interrogation is more sensitive in terms of wavelength shift per unit applied force, than Fabry-Pérot interrogation. The greater dynamic range is due to the positioning of the single Bragg grating, as it can be placed closer to the pivot point, thus is subjected to a higher strain field than the cavity.

5.10 All diced microcantilevers

As mentioned in section 5.2.3, the wet etching stage used in the release of the microcantilever structures from the silicon substrate can affect the optical performance of the device. The optical performance is normally diminished when the wet etching weakens the optical facets, where the fibre optic pigtail connection is made. From this it can be seen that the removal of the wet etching stage would be beneficial. A potential avenue of research exists in all diced microcantilever structures, where preliminary results are shown in Figure 80.

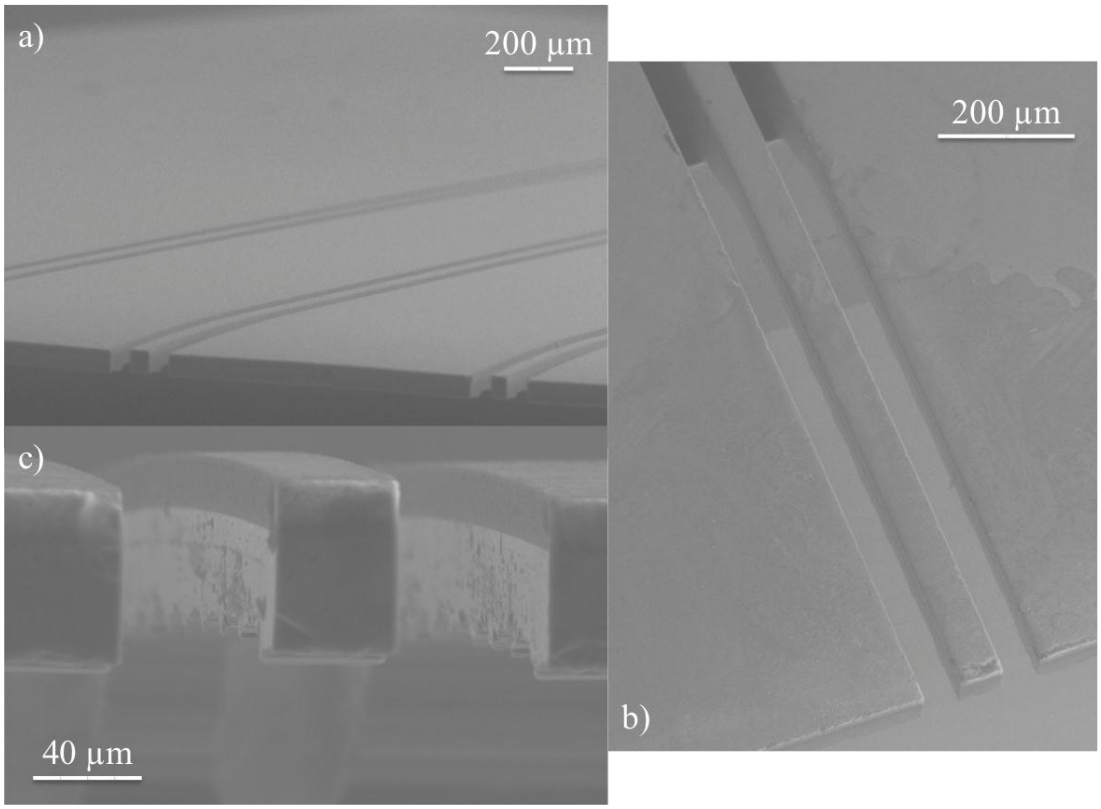

Figure 80 all diced microcantilever structures SEM micrographs.

Figure 80 a) and b) show top views of the all diced microcantilever structures at different magnifications. Figure 80 c) is a side view: notice the curvature of the cantilever from residual fabrication stresses. The fabrication process is the same as the cantilevers discussed in section 5.2, where the mechanical structure of the cantilever is diced in the region, where the waveguides and Bragg gratings were written. However, instead of wet etching, the device is flipped and, using a large resin bonded blade commonly used for wafer dicing, the silicon is sawn away to create the cantilever length and thickness desired.

5.11 Conclusions

In this chapter novel glass microcantilevers with integrated Bragg gratings and waveguides have been demonstrated. Cantilever fabrication used a combination of direct UV writing, precision dicing and wet etching. Two cantilever interrogations methods have been discussed; one utilising a single Bragg grating and the other uses

a pair of spectrally matched Bragg gratings to form a Fabry-Pérot interferometer. Deflection theories for both interrogation techniques are also presented using appropriate bending theories and allow the prediction of central Bragg wavelength or phase shift for the single Bragg grating and Fabry-Pérot interrogation systems to be measured, respectively.

The cantilever device with single Bragg grating interrogation was oscillated to a mechanical resonance with a piezo. A phase sensitive technique was used to acquire amplitude and phase data on the mechanical resonance characteristics. The cantilever device was then subjected to changing external pressure within a vacuum system and has shown changes in the damping coefficient due to the transition from molecular to viscous flow, at around 1 mbar. These changes in mechanical resonance for different air pressures agree with work carried out in optical fibre based cantilevers.

The Fabry-Pérot interrogation system was investigated with a commercially available profilometer, which could accurately deflect the cantilever while the reflected optical response was measured. Coupled mode theory was used to fit the Fabry-Pérot spectra as it changed with cantilever deflection and allowed the optical phase to be monitored. A phase shift of the Fabry-Pérot interferometer of 3.71 radians was measured for a 491 μN of applied point force, 4.1 mm along the length of the cantilever. The actual Fabry-Pérot cantilever showed a greater phase shift than the predicted results, and was attributed to nonlinear bending at larger deflections.

The smallest resolvable force of the Fabry-Pérot interrogation system was 264 nN, which is approximately a factor of four times improvement on the single Bragg grating cantilever interrogation. The spectral sharpness of the Fabry-Pérot was compared with a single Bragg grating, yielded a factor of eleven times improvement in terms of intensity/wavelength gradient. The Fabry-Pérot interrogation system had a wavelength shift force sensitivity or the dynamic range of 330 nm/N, which is a reduction of ~27% from the single Bragg grating cantilever interrogation.

References

1. I. Chasiotis, "Atomic Force Microscopy in Solid Mechanics," in *Springer Handbook of Experimental Solid Mechanics*, W. Sharpe Jr., ed. (2008), pp. 409–414.

2. K. Zinoviev, C. Dominguez, J. A. Plaza, V. Javier, C. Busto, and L. M. Lechuga, "A Novel Optical Waveguide Microcantilever Sensor for the Detection of Nanomechanical Forces," IEEE Journal of Lightwave Technology **24**, 2132–2138 (2006).

3. K. M. Goeders, J. S. Colton, and L. A. Bottomley, "Microcantilevers: sensing chemical interactions via mechanical motion.," Chemical Reviews **108**, 522–42 (2008).

4. A. Llobera, V. J. Cadarso, K. Zinoviev, C. Dominguez, S. Buttgenbach, J. Vila, and J. A. Plaza, "Poly(Dimethylsiloxane) Waveguide Cantilevers for Optomechanical Sensing," IEEE Photonics Technology Letters **21**, 79–81 (2009).

5. R. G. Hunsperger, *Integrated Optics Theory and Technology*, 6th ed. (Springer, 2009), pp. 1–413.

6. "http://www.tgs.com/reservoir/stingray-systems/our-technology.aspx," .

7. H. Nakstad and J. T. Kringlebotn, "Probing oil fields," Nature Photonics **2**, 147–149 (2008).

8. C. K. Kirkendall and A. Dandridge, "Overview of high performance fibre-optic sensing," Journal of Physics D: Applied Physics **37**, R197–R216 (2004).

9. R. G. Hunsperger, *Integrated Optics Theory and Technology*, 6th ed. (Springer, 2009), pp. 1–7.

10. K.-R. Sohn and J.-H. Shim, "Liquid-level monitoring sensor systems using fiber Bragg grating embedded in cantilever," Sensors and Actuators A: Physical **152**, 248–251 (2009).

11. D. Iannuzzi, K. Heeck, M. Slaman, S. de Man, J. H. Rector, H. Schreuders, J. W. Berenschot, V. J. Gadgil, R. G. P. Sanders, M. C. Elwenspoek, and S. Deladi, "Fibre-top cantilevers: design, fabrication and applications," Measurement Science and Technology **18**, 3247–3252 (2007).

12. L. G. Carpenter, C. Holmes, H. L. Rogers, P. G. R. Smith, and J. C. Gates, "Integrated optic glass microcantilevers with Bragg grating interrogation," Optics Express **18**, 23296–23301 (2010).

13. L. G. Carpenter, C. Holmes, B. D. Snow, J. C. Gates, and P. G. R. Smith, "Photonic Microcantilevers With Interferometric Bragg Grating Interrogation," IEEE Photonics Journal **4**, 1387–1395 (2012).

14. M. Svalgaard, C. V. Poulsen, A. Bjarklev, and O. Poulsen, "Direct UV writing of buried singlemode channel waveguides in Ge-doped silica films," Electronics Letters **30**, 1401–1403 (1994).

15. G. D. Emmerson, C. B. E. Gawith, S. P. Watts, R. B. Williams, P. G. R. Smith, S. G. Mcmeekin, J. R. Bonar, and R. I. Laming, "All-UV-written integrated planar Bragg gratings and channel waveguides through single-step direct grating writing," IEE Proceedings Optoelectronics **151**, 119–122 (2004).

16. H. Seide, L. Csepregi, A. Heuberger, and H. Baumgärtel, "Anisotropic Etching of Crystalline Silicon in Alkaline Solutions," Journal of Electrochemical Society **137**, 3612–3626 (1990).

17. C. S. Baldwin, "Optical Fiber Strain Gages," in *Springer Handbook of Experimental Solid Mechanics*, W. N. Sharpe Jr., ed. (Springer, 2008), pp. 355–364.

18. L. Grave De Peralta, A. A. Bernussi, H. Temkin, M. M. Borhani, and D. E. Doucette, "Silicon-dioxide waveguides with low birefringence," IEEE Journal of Quantum Electronics **39**, 874–879 (2003).

19. J. M. Gere and S. P. Timoshenko, *Mechanics of Materials*, Forth (Stanley Thornes, 1999), pp. 6–315.

20. G. R. Fowles and G. L. Cassiday, *Analytical Mechanics*, 5th ed. (Saunders College, 1986), pp. 98–103.

21. J. C. Lagarias, J. A. Reeds, M. H. Wright, and P. E. Wright, "Convergence properties of the Nelder-Mead simplex method in low dimensions," SIAM Journal of Optimization **9**, 112–147 (1998).

22. H. Kumazaki, S. Inaba, and K. Hane, "Pressure dependence of resonance characteristics of the microcantilever fabricated from optical fiber," Vacuum **47**, 475–477 (1996).

23. C. Holmes, L. G. Carpenter, H. L. Rogers, J. C. Gates, and P. G. R. Smith, "Quantifying the optical sensitivity of planar Bragg gratings in glass micro-cantilevers to physical deflection," Journal of Micromechanics and Microengineering **21**, 035014 (2011).

24. T. Erdogan, "Fiber grating spectra," Journal of Lightwave Technology **15**, 1277–1294 (1997).

25. A. Ghatak and K. Thyagarajan, *Introduction to Fiber Optics* (Cambridge University Press, 1998), pp. 473–477.

26. P. Bogacki and L. F. Shampine, "A 3(2) Pair of Runge - Kutta Formulas," Applied Mathematics Letters **2**, 321–325 (1989).

27. Y. Li, Y. Feng, X. Peng, and H. Zhang, "Simultaneous measurement of the temperature and force using a steel cantilever soldered with a partially nickel coated in-fibre Bragg grating," Optics Communications **285**, 4275–4279 (2012).

28. J. Y. Li, X. G. Huang, G. M. Cheng, L. X. Chen, and X. M. Jin, "Integration of a Micro Fabry-Perot Cavity and a Fiber Bragg Grating Sensor for Simultaneous Measurement Of Stress And Temperature," Microwave and Optical Technology Letters **55**, 2440–2444 (2013).

29. K. Reck, E. V. Thomsen, and O. Hansen, "MEMS Bragg grating force sensor," Optics Express **19**, 19190–19198 (2011).

30. N. Basumallick, I. Chatterjee, P. Biswas, K. Dasgupta, and S. Bandyopadhyay, "Fiber Bragg grating accelerometer with enhanced sensitivity," Sensors and Actuators A: Physical **173**, 108–115 (2012).

6 Precision Micromilling of Silica

6.1 Introduction

Milling is a complementary technique to precision dicing. However, while dicing is restricted to two-dimensions, milling allows three-dimensional machining whilst also potentially working in the ductile cutting regime. The precision milling machine has been developed in-house to mill brittle materials, such as silica. The aim was to develop a milling system capable of machining flat, smooth, chip free grooves in silica. The capability would allow access to the evanescent field by removal of cladding material, enabling the fabrication of various devices. The general requirements for grooves which interact with light are high flatness, nanoscale roughness and low surface chipping, each minimising light scatter and producing a low loss interaction. This chapter shows that precision micromilling is able to offer these requirements. The technique as demonstrated for the first time achieved, smooth, chip free milling of silica to a depth of 17 μm in a single pass. This boasts a forty two times improvement on previously reported depths of cut [1].

This chapter focuses on the optimisation of a milling process, to create smooth grooves in a silica-on-silicon platform. A basic theory of milling and in particular, ductile milling, is included along with a thorough account of equipment and procedures. This chapter also includes an overview of dominant machining factors affecting milled groove quality in silica-on-silicon. The milling procedure optimisation is also included whereby surface roughness and chipping has been monitored and reduced. Surface metrology and microscope images are presented. Utilising the optimised milling procedure, mill wear was studied. The machining of the cladding of a standard silica single mode fibre is also commented on.

6.2 Milling theory

To achieve grooves for interaction with light in integrated optics, the general requirements are high flatness, nanoscale roughness and low surface chipping; all of which provide low loss propagation through the groove area by minimising light scatter. Grooves in silica for this purpose can be created via milling in the ductile regime, which allows material to be removed from brittle substrates in a smooth, crack free process. In order to achieve the chip size necessary to instigate ductile regime machining, the profile of the mill must be controlled with high precision and with good decoupling from environmental effects. Milling principles are covered in the next section defining the conventions used in this chapter.

6.2.1 Milling principles

In general there are two distinct machining modes a mill can operate in; side milling and slot milling (end milling). Side milling removes material parallel to the plane of the substrate, with movement within this plane only (*i.e.* no vertical cut movements), see Figure 81. Slot milling allows more freedom than side milling and can enter and exit the substrate vertically, see Figure 81.

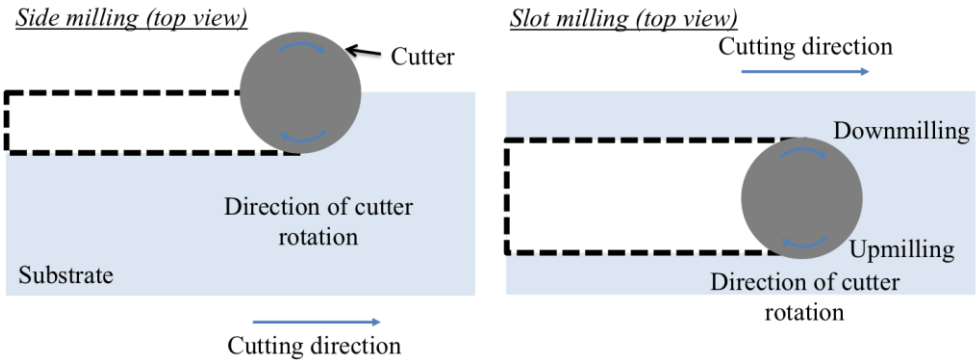

Figure 81 top view of side and slot milling, showing the removal of material by dotted black lines.

Generally the ability to side or slot mill is dictated by the mill used, where slot mills have at least one set of cutting flutes that meet at the centre point of the mill, thus allowing them to drill material. Side mills, however, can have cutting faces that do

not pass the centre point of the mill, but typically have more than 2 flutes, thus enabling greater material removal rates.

The milling conventions have been explained here. The next section is concerned with a ductile regime of material removal, which allows brittle materials to be machined in a fracture free way.

6.2.2 Ductile removal of material with a slot mill

The precision milling technique machines silica with smooth, chip free surfaces by utilizing the ductile cutting regime. Ductile regime cutting removes material via plastic deformation of chips, this is achieved by certain machining parameters (*i.e.* correct choice of tool's translation speed, rotational speed and depth of cut) [2]. Bifano *et al.* suggested that a feed rate of ~<50 nm/rev is needed to ensure ductile type machining of silica. If the material is machined with the incorrect machining parameters, brittle type machining occurs. This brittle type machining is caused by applying a shear stress that exceeds the material's plastic limit thus creating cracks that propagate and chip, producing an unsmooth, pitted and cracked surface, as discussed in chapter 2 [2].

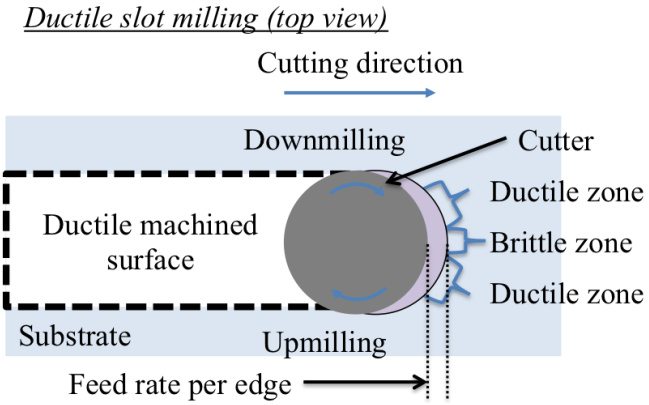

Figure 82 top view of ductile slot milling.

Figure 82 shows a schematic of ductile slot milling, where the smooth, chip free surface is left on the bottom of the groove being created. Figure 82 also denotes downmilling and upmilling in relation to mill rotation. This is important as it affects edging chipping and is discussed in section 6.5. It is suggested by Arif *et al* [1], that brittle fracture occurs if a feed rate per edge (f_c) ~> 45 nm/edge, for soda lime glass, which is calculated by [1],

$$f_c = \frac{0.15E}{H\left(\frac{K_{IC}}{H}\right)^2}$$ **Equation 93**

where f_c is the feed rate per edge (*i.e.* feed rate per number of flutes), E is Young's modulus (modulus of elasticity), H is the hardness and K_{IC} is the fracture toughness. The relevant parameters for two common silica glasses, fused silica (Corning 7940) and borosilicate (Corning 7740), are a Young's modulus of 72.5 GPa and 62.7 GPa, a hardness of 5.88 GPa and 4.94 GPa, and a fracture toughness of 0.741 $MPam^{1/2}$ and 0.76 $MPam^{1/2}$, respectively [3].

With these parameters a feed rate per edge can be calculated, using Equation 93 to machine fused silica and borosilicate, in a ductile mode: A feed rate per edge of <29 nm/edge and <45 nm/edge is required for fused silica and borosilicate, respectively. Thus because of the purity and thus hardness of fused silica compared to borosilicate, the feed rate per edge is slower. Flame hydrolysis deposition silica most likely lies between fused silica and borosilicate in terms of composition, thus the machining condition for ductile removal of material will probably be between 29-45 nm/edge. The ductile removal of materials enables smooth grooves to be made in glass and using the theory developed above, the material rates needed to achieve this are found. In order to characterise how waveguide loss is affected by surface roughness, the theory of waveguide scattering is included in the next section.

6.2.3 Requirements for milling waveguide components

The precision micromilling technique is used to access the evanescent field by removal of cladding material to access the core of a waveguide. The general requirements for grooves to access waveguides that interact with light, would to be to have nanoscale roughness, low long-range roughness, low form errors (cladding offset), high flatness and low surface chipping, shown in Figure 83. Each of these requirements will minimise light scatter, allowing low loss light propagation through the groove structure.

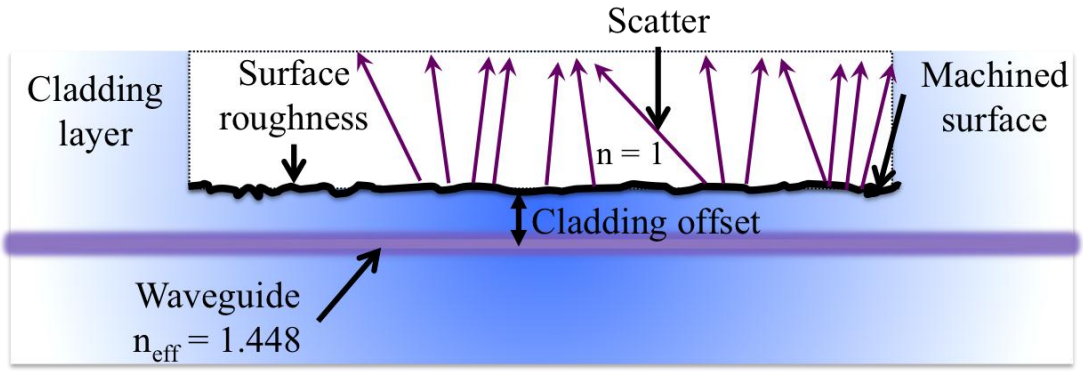

Figure 83 side view of a groove interacting with a waveguide where loss mechanisms are present. Nanoscale roughness, long-range roughness and surface chipping are represented by surface roughness. Form errors and flatness are represented by cladding offset.

Figure 83 shows how a milled groove with defects will scatter light. Nanoscale roughness, long-range roughness and surface chipping are represented by surface roughness within the diagram. Both form error and flatness are represented by cladding offset within the diagram. This section discusses these requirements in more detail and explains to what extent precision micromilling can fulfil them.

The surface roughness created at the bottom of grooves, created by the removal of the cladding material via precision micromilling, can be thought of as a waveguide with surface roughness. The Payne and Lacey theorem for loss in planar slab waveguides caused by scattering as a consequence of surface roughness (S_q), is given by the following equation [4] but can also be valid for channel waveguides [5],

$$\alpha = 4.34 \frac{S_q^2}{k_o \sqrt{2} (d/2)^4 n_1} g(V) f(x, \gamma) \qquad \textbf{Equation 94}$$

where α is the scatter loss in dB/cm, S_q RMS surface roughness, k_o is the wavenumber in vacuum ($k_o = 2\pi/\lambda$, λ is the wavelength of operation), d is the waveguide width, n_1 is the refractive index of the guiding core layer. $g(V)$ is a function dependent on the waveguide geometry and is given by,

$$g(V) = \frac{U^2 V^2}{1 + W} \qquad \textbf{Equation 95}$$

where $U = k_o \frac{d}{2} \sqrt{n_1^2 - n_{eff}^2}$, $V = k_o \frac{d}{2} \sqrt{n_1^2 - n_2^2}$ and $W = k_o \frac{d}{2} \sqrt{n_{eff}^2 - n_2^2}$. n_2 is the refractive index of the cladding layer and n_{eff} is the effective refractive index of the mode. Also, $f(x, \gamma)$ is a function depending on the correlation length (L_C) of the

surface roughness and waveguide geometry, assuming the surface roughness has exponential statistics and is given by,

$$f(x,\gamma) = \frac{x\sqrt{1 - x^2 + \sqrt{(1+x^2)^2 + 2x^2\gamma^2}}}{\sqrt{(1+x^2)^2 + 2x^2\gamma^2}} \qquad \textbf{Equation 96}$$

where $x = 2W\,L_C/d$, $\gamma = n_2 V/n_1 W\sqrt{\Delta}$ and $\Delta = n_1^2 - n_2^2/2n_1^2$. The correlation length (L_C) is defined as the 37% or $1/e$ of the roughness's spectral density, similar but not equal to the average surface wavelength [6].

The propagation loss caused by scatter, using the Payne and Lacey theorem and typical values for direct UV written waveguides (see chapter 3) is calculated, for a waveguide width (d) of 5.6 μm, an initial core refractive index (n_1) of 1.4461 with a 'DC' refractive index offset of 5x10^{-3} [7] from direct UV writing, a cladding layer refractive index (n_2) of 1.4448 and an effective refractive index (n_{eff}) of 1.446 (TE). The best overall result achieved by precision micromilling technique in silica is discussed in section 6.6.3 and is shown in Figure 84 and Figure 110.

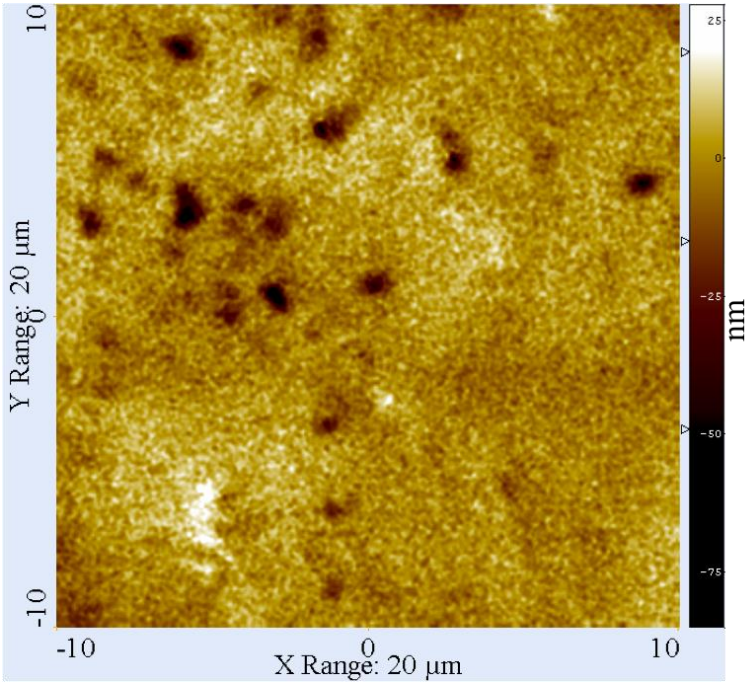

Figure 84 white light interferometer surface profile of the middle of the second groove bottom, machined at 40 krpm and 0.75 mm/min, colour bar shows variations in height (nm). The groove had a RMS roughness of ~7.1 nm (Sq) and a correlation length (L_C) of 580 nm.

Figure 84 is a white light interferometer profile. The 3D RMS surface roughness was calculated to be ~7.1 nm (Sq) and had a correlation length (L_C) of 580 nm, as measured by white light interferometer (ZeScope). By substituting these values into Equation 94, Equation 95 and Equation 96, a propagation loss caused by scatter of 0.065 dB/cm is calculated. The surface roughness here is on both sides of a the channel waveguide, in the instance of a milled groove only one side of the waveguide would interact with the roughness thus the propagation loss caused by scatter can be halved [4], equalling 0.032 dB/cm. Halving the surface roughness to 3.6 nm, reduces the loss to 0.0083 dB/cm. Figure 85 shows the propagation loss for varying surface roughnesses, as calculated by the Payne and Lacey theorem for the direct UV written waveguide parameters, and a correlation length (L_C) of 580 nm.

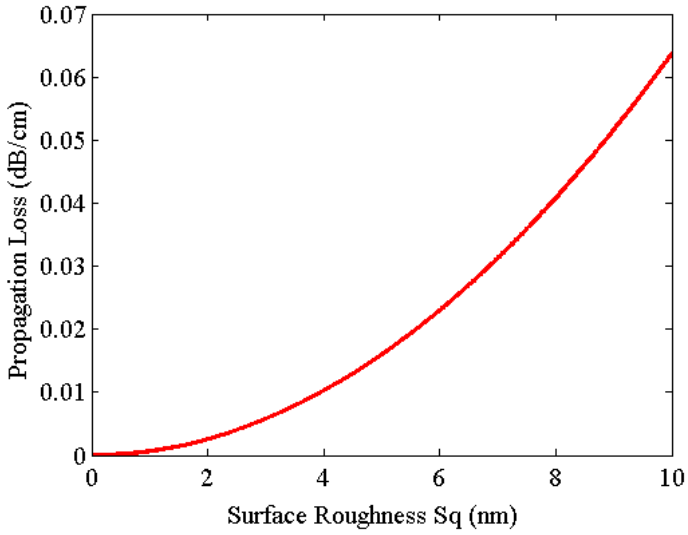

Figure 85 propagation loss with varying waveguide surfaces roughnesses, using the waveguide parameters for the direct UV written waveguide and a correlation length (L_C) of 580 nm.

Figure 85 shows the propagation loss reducing exponentially with a reduction in surface roughness for the direct UV written waveguide geometry. The direct UV written waveguides described are weakly guiding, thus $\gamma \gg 1$ [4]. The γ calculated here is ~21 and x is ~ 0.23; within this regime for γ and x, Payne *et al.* described that the way to further reduce propagation loss caused by scatter, is to reduce surface roughness (S_q) or to increase d the waveguide width [4]. This statement is only really applicable to single mode waveguides. As the waveguide width increases it allows multiple spatial modes to exist, some of these modes will interact more with the waveguide sidewalls and thus more with the surface roughness, as shown in

chapter 3. From Equation 94 other insights can be drawn for lowering the attenuation caused by scatter. Moving to longer wavelengths also reduces loss, which is now a more attractive route as 2 μm lasers and broadband amplifiers are becoming increasingly commercially available [8]. Equation 94 also tells us that scattering increases for higher index contrasts $(n_1 - n_2)$ and thus for strongly guiding waveguides ($\gamma \approx 1$). This is caused by an increase in $g(V)$, which depends on the waveguide geometry and refractive indices. This is a well-known fabrication difficulty in high index contrast waveguides such as silicon-on-insulator, where surface roughness reduction from 10 nm to 2 nm reduces propagation losses from 32 dB/cm to 0.8 dB/cm [9].

The variation in form, caused by milled removal of cladding material, can be divided into two distant sections: long-range roughness and form/flatness. Continuing with the Payne and Lacey theorem. The effect of the correlation length (L_C), which can be thought of as the average surface wavelength, has a maximum effect (L_{Cmax}) on the magnitude of the scattered light when,

$$L_{Cmax} = \frac{1}{\sqrt{3}k_o\left(n_{eff} - n_2\right)}. \qquad \textbf{Equation 97}$$

For the UV written waveguide discussed above, the correlation length (L_{Cmax}) is ~43 μm. The maximum scatter occurs when the correlation length (L_C) becomes close to the beat length between guided and radiation modes, where guided modes exist for $n_2 < n_{eff} < n_1$ and the radiation modes exists for $n_{eff} < n_2$ [10] [11]. This can be thought of as a grating type of effect, similar to long period gratings and at a length scale of tens of microns, it is considered a form error.

For grooves that deviate in form (cladding offset) and flatness, the operation of devices using evanescent field interactions can be affected. This has been observed in metal polariser devices using titanium indiffused planar lithium niobate waveguides [12] and ion-exchanged magnesium fluorine single mode waveguides [13], here the dependence of the thickness between the metal and waveguide is crucial for its operation. Both Thyagarajan *et al.* and Kumar *et al.* showed hundreds of dB/cm change in terms of loss (polarisation attenuation) for the Transverse Magnetic (TM) polarisation, for a hundred nanometre change in

separation between the waveguide and metal. The sensitivity of these devices indicates that groove flatness and form is critical to device performance.

The precision milling machine was able to machine a groove with ~200 nm (cladding/separation from the core) of error in overall form error (mean depth) and the groove bottom flatness deviated by ~19.4 nm (standard deviation). This groove is discussed in section 6.6.3 and is shown in Figure 112. Both form and flatness are in the order of hundreds and tens of nanometres range, respectfully.

Chipping formation, depending on how and where they form on the groove surface, these can act as a combination of form error, flatness error and surface roughness; all contributing to propagation loss, and are thus undesirable. Furthermore, if the material milled is removed in a ductile machining regime, no chipping and low surface roughness will occur [2].

From the analysis of nanoscale roughness, low long-range roughness, low form errors, high flatness and low surface chipping, precision milling would seem to be viable technique to access the evanescent field by removal of cladding material in silica. In this chapter groove surface roughness is used as one of the parameters to optimise the milling procedure. The reasoning for optimising surface roughness rather than form/flatness or chipping, as was done for dicing, is that flatness is typically defined by the mechanical interaction of the tool and substrate. Also low surface roughness would imply operation in the ductile regime and minimal chipping should occur. Surface roughness is also quantitative and easily obtained through surface profiling.

6.3 The micromill

At the heart of the in house built micromill, is a set of high precision air bearing stages and an aerostatic spindle, which have the ability to control movement on the scale of a few hundreds of nanometre. This gives the ability to machine micron scale features on a variety of substrates; silica is concentrated on here. Precision micromills have been created before and examples are commercially available, with

similar designs and performance as the one built for this Ph.D.. Examples include the: Moore Nanotech 350UPM, Kugler Micromaster 3/5X, Ultramill Kern micro and the Sodick AZ150 [14]. Consultation of literature shows that commercial mills have many design similarities. These design similarities are based around the machine structure having a high loop stiffness enabling mechanical stability and good isolation from environmental vibrations. The high loop stiffness results in the system having a high resonant frequency and high thermal stability. The milling machines also have high precision axes with high precision control [14]. Linking these pillars of design, with an air-bearing spindle, interchangeable milling bits and a coolant circuit, provides the building blocks for the precision milling machine.

6.3.1 Micromill design

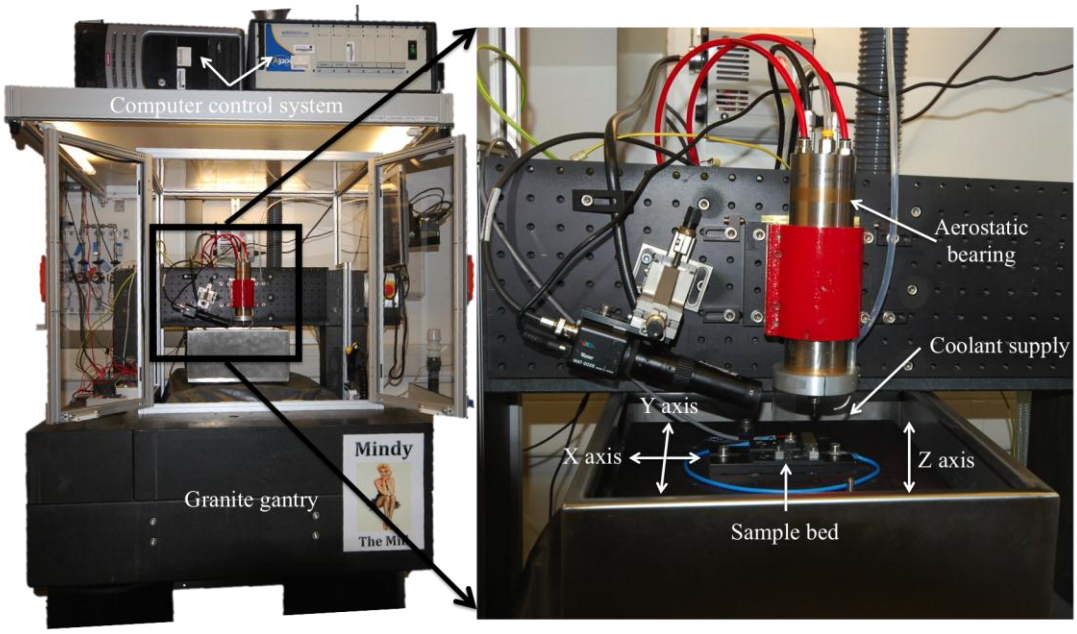

Figure 86 precision micromill (*Mindy the Mill*).

The glass machining experiments were performed on a precision micromill built by the author, as shown in Figure 86. The mill consists of air bearing slide-ways in the x and y axis (Aerotech, ABL8020), which has a resolution of 1 nm and a repeatability of 200 nm. The z lift stage consists of an air compensated stage (Aerotech, AVL125), which has a resolution of 4.5 nm and a repeatability of 300 nm. The mill uses a Loadpoint grinding spindle (B01020-dc), which uses an aerostatic bearing. The grinding spindle can run up to 60 krpm and has a dynamic runout of ~100 nm (personal correspondence with David Gilham Director of Loadpoint Bearings Ltd.

27/3/2012). The spindle is also kept at a constant temperature via a chiller unit to reduce thermal creep whilst in operation, (~20° C). The x, y, z stages and spindle are all attached to a granite frame; this gives the machine high loop stiffness between tool and work piece. The granite frame is also placed on pneumatic legs to suppress building vibrations. The definitions for the specifications shown in Figure 87 *i.e.* resolution, accuracy *etc.*, are given in the following reference [15], where accuracy is defined as the difference between the actual position in space and the position as measured by the machine. Repeatability is defined as the range of positions attained when the machine is repeatedly commanded to one location under identical conditions. Examples of accuracy and repeatability are shown in Figure 87.

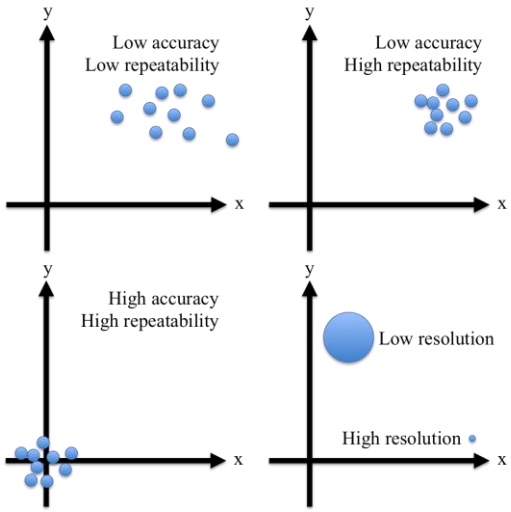

Figure 87 Aerotech's definition of accuracy, repeatability and resolution.

The key figures to note here are the repeatability and resolution rather than accuracy, as probing will be used throughout thus making a user defined position. As accuracy is the absolute measurement of the depth of cut, width of a ridge, *etc.*, post metrology can be performed to discover machine error and if the precision is sufficient, the machine error can be accounted for. The forces involved in ductile machining are typically much smaller than a Newton. In experiments involving the micromilling of silicon, forces of ~0.4-0.6 N were used to remove material in the ductile regime [16]. Arif *et al.*, showed forces of <0.4 N were present in the ductile machining micromilling of silica with a slot mill. Both of these forces are negligible compared to the maximum applied loads of the air-bearing stage (~700N) and the air-bearing spindle (~100N). The pillars of design, which the micromill followed,

have been discussed, the next section explaining and the way in which the spindle is aligned to the sample bed.

6.3.2 Spindle alignment

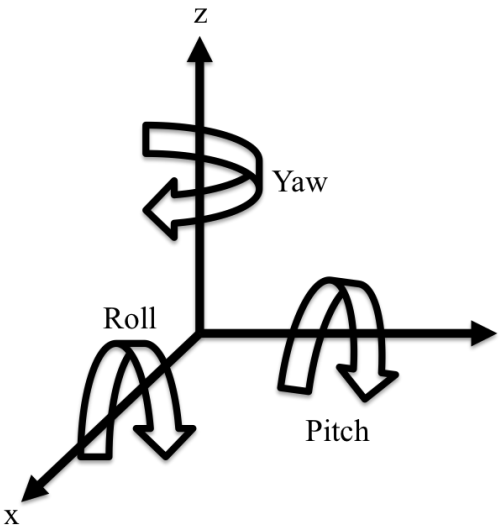

Figure 88 definition of sample pitch, roll and yaw.

To remove the static angular misalignment from the spindle to the mill bed *i.e.* pitch and roll (see Figure 88) the spindle was adjusted (see Figure 89). Spindle alignment to the work bed was achieved by attaching a dial gauge to the spindle collet via an arrangement of clamps. The spindle's roll was adjusted for, by actuating the taps either side of the spindle, see Figure 89. The spindle's pitch was adjusted by adding shim, of ~100 µm in thickness, behind the backing plate, see Figure 89. The dial gauge was engaged to the work bed and swept in an arc defined by the spindles rotational centre and the length of the clamp. The spindle's roll and pitch were corrected until the dial gauge saw no more than ~±10 µm of deviation across the sweep. An arm length of ~93 mm was used to attach the dial gauge, which gives ~6.2×10^{-3}° of angular misalignment.

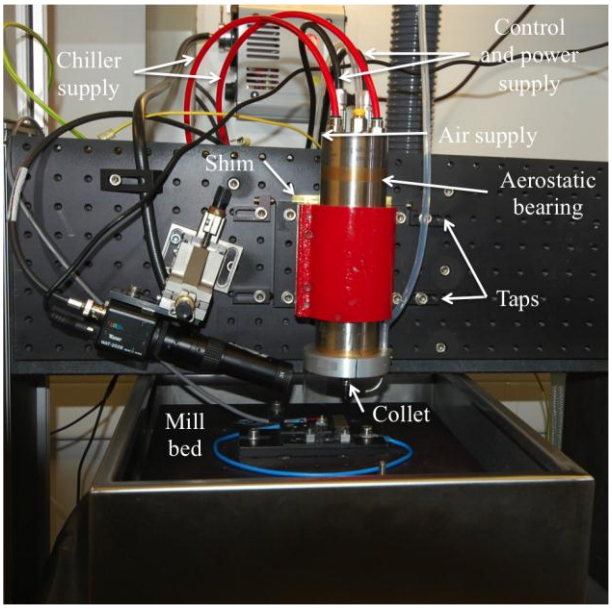

Figure 89 spindle alignment to mill bed using taps and shim, as shown.

Figure 89 also shows the various services, of compressed air, chilled water supply, control signals and electrical drive power. The spindle alignment has been covered and the next section discusses the mill selection.

6.3.3 Mill bits

As described in 6.2.1 there are two distinct types of milling, end and slot milling. To engage in milling grooves within a silica substrate, a slot mill was required. As the typical size of a silica waveguide is in the order of ~6 µm, a cutter on the tens to hundreds of micron diameter was required. An example of the slot mill used throughout is shown in Figure 90.

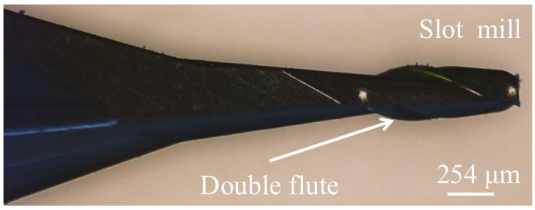

Figure 90 micrograph of a 254 µm diameter, two flute, slot mill. This type of mill is used throughout this thesis.

There are numerous types of mills with different sizes, flutes, flank angle and constituent materials. A literature review highlighted two potential types of mill materials appropriate for machining glass. Mills that have previously been used were made from Polycrystalline Diamond (PCD) [17] [18] or tungsten carbide with a

coating of Titanium Aluminium Nitride (TiAlN) [1] [19]. However, Polycrystalline diamond mills are typically machined using wire electrode discharge grinding [17], which requires a conductive spindle. The Loadpoint grinding spindle (B01020-dc), does not have a conductive path but recently plans have been implemented with Loadpoint to design and build one of the first ever aerostatic bearing spindles to be used for machining polycrystalline diamond mills. Peter Allen Cooper is currently conducting this research, within the group, to integrate this new spindle into the current micromill setup.

There were few suppliers of coated tungsten carbide mills on the tens to hundreds of micron diameter. The Harvey Tool Company was one of the few that did offer the option of titanium aluminium nitride or diamond coatings on small radii cutters. Due to the success of dicing using diamond impregnated blades (see chapters 4 and 5) and the milling conducted using polycrystalline diamond tools [17], a diamond coating was investigated. Diamond coated tungsten carbide mills were sourced from Harvey Tool Company at a cost of $30 a mill (as of 8th October 2013). There is currently no literature on diamond coated tungsten carbide mills used to mill silica but they have successfully been used to machine silicon [20]. Harvey's supplied 254 µm diameter, two flute, slot mills, see Figure 90, with an amorphous coating achieved by chemical vapour deposition.

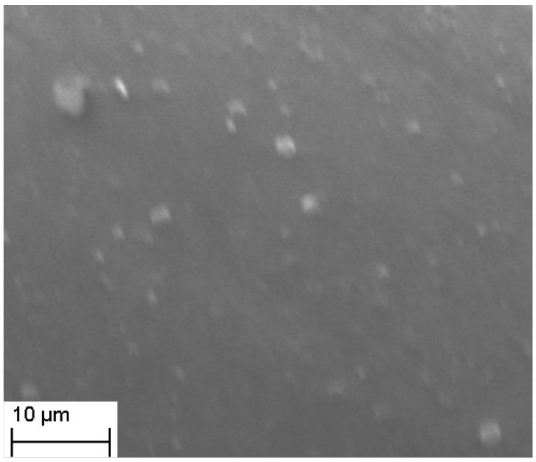

Figure 91 SEM micrograph of the diamond coating of the 254 µm diameter, two flute, slot mill shown in Figure 90.

The SEM micrograph in Figure 91, shows the amorphous diamond coating present on the slot mill. The diamond size ranged from ~0.5-3.5 µm. The diamond size is

similar to those present in the dicing blades used in the previous chapters to obtain smooth facets in silica. Mill selection and coating have now been discussed and the section will discuss the successful and unsuccessful sample setting.

6.3.4 Sample setting

The setting of samples (mounting), to machine brittle materials is not trivial. If the sample is held with too much force, cracking can occur and with too little force, it will move whilst machining is taking place. Methods investigated included a vacuum chuck, double sided adhesive copper tape, adhesive carbon tape and wax. The method needed to hold the sample securely throughout the machining process whilst subjected to a coolant jet. All these methods held under machining but once a water coolant was added, the vacuum chuck and tapes failed due to coolant ingress. The wax provided a robust bond with the key ability of being able to remove the residue without damaging the sample surface. This is not a surprising result as the wax used is specifically designed to hold optical materials for polishing and thus is subjected to both coolant and polishing forces. The disadvantage in using wax is that the sample must be heated to set and remove it from the machining bed. Wax setting was used in conjunction with optical sample mounts as shown in Figure 92. The wax used through out is a Logitech OCON-200 wax. The optical mounts allowed rigid fixing to the mill bed with ridges to provide coarse sample alignment.

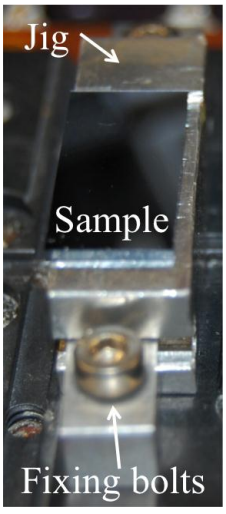

Figure 92 sample mounting, utilised standard mounts for the characterisation of planar optical samples.

Now that the sample setting technique used throughout has been explained, the next section will go on to discuss sample cooling and stage protection.

6.3.5 Cooling and environmental protection

A coolant jet of deionised water was added to the micromill as shown in Figure 86. Coolant is used to temperature stabilise both the mill and sample, at the cutting interface. Dry mode cutting was attempted, however it caused catastrophic failure of the sample via cracking. The presence of coolant within the machine meant the delicate stages had to be protected from splash back and leaks. Thus stainless steel troughs with drainage were added to remove spent coolant to drain. The stages were also protected with rubber gators and plastic sheet, see Figure 86. The subsystems of the mill have been covered. The next section describes the techniques used to probe the sample.

6.4 Sampling mapping

Humans depend on their senses to be able to interpret the world around them; it is the same for CAM (Computer-Aided Manufacturing). To be able to precisely machine a work piece, first the workpiece needs to precisely located, *i.e.* where is the mill bit in relation to the workpiece? When setting a mill, the workpiece and the position of the tool will vary each time it is set, this is why having a system to locate the unique positions of both is needed in all CAM. Commercially available CAM will often use one of three ways to locate a workpiece: piezoelectric strain detection, electrical characteristic change *i.e.* short circuit, capacitance *etc.* and laser based positioning [21]. The choice was made to use the piezoelectric strain detection for its ability to deal with the harsh working environments and the added advantage of it being easy to implement and inexpensive. To build a 3D map of the sample, both the plane of the surface must be found along with where the plane is constrained (*i.e.* where the chip sides lay). This is done by probing the sample with the end of the mill, see Figure 93.

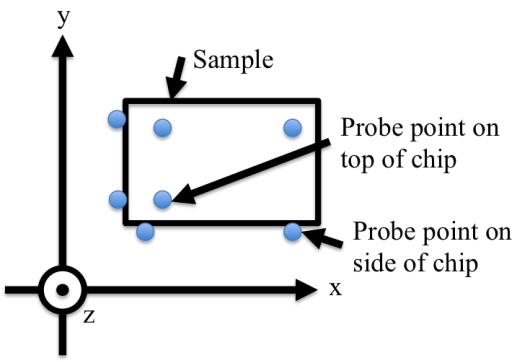

Figure 93 sample mapping using mill probing. The blue spots show the location of the probe points.

The basic concept of operation for sample mapping is:

- The workpiece is slowly moved down towards the mill bit (0.25 mm/min translation speed in z and 0.75 mm/min translation speed in the x and y axis).
- When the mill bit comes into contact with the workpiece, pressure is applied to the sample.
- The pressure is converted into an electrical signal, via the piezo transducer, which is amplified and sent to the axis controller.
- The stage then halts. The stage controller performs this task with a latency of 1 µs.
- The program reads the axis position and stores it.
- This is repeated in numerous locations on the workpiece providing information about the plane and position of the sample.
- Sample pitch, roll and yaw (Figure 88) are now eliminated by changing the z axis position as the cutter moves in x and y to keep a constant depth of cut.

Within this section the basic probing technique is explained, the next section includes information on the working of the electronics.

6.4.1 Sample probing with mill end and piezo

The operation of the height sensor's electronics will now be explained. When the mill piece comes into contact with the workpiece, the piezo transducer produces an

electrical current proportional to the mechanical impulse. The piezo used is a PI, DuraAct, Patch Transducer, P-876.A15, epoxy is used to bond the mating plate to attach it to the bed of the mill and a jig mount with various tapped holes to bolt sample holders into, as shown in Figure 94.

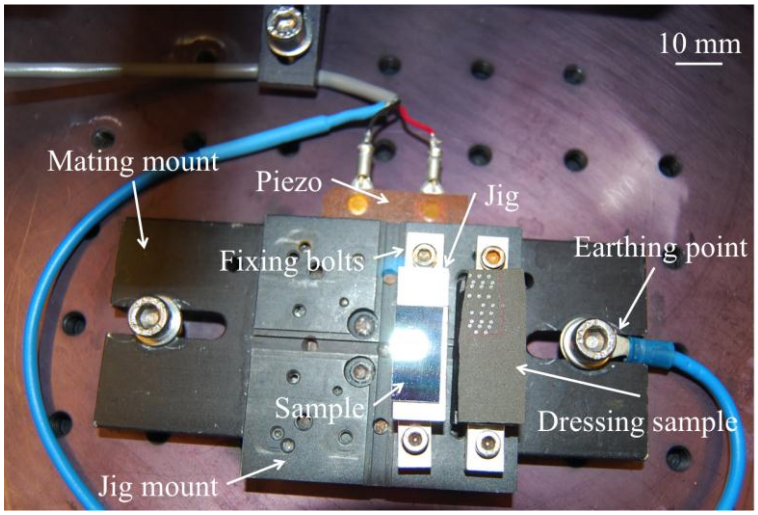

Figure 94 integrated piezo bed for sample mapping with mill.

The piezo signal is amplified by a bootstrap preamplifier [22] to boost the magnitude of the signal and enables impedance matching of the operational amplifier and the piezo transducer. The pre-amplified signal is sent to a comparator, the comparator triggers on a sufficiently large electrical impulse, causing the comparator to switch to a high state. The high-speed digital input of the Aerotech stage controller monitors the output of the comparator and once high, halts the axis. The comparator trigger level is trimmed via a potentiometer providing discrimination from background electrical noise. The various sections of the electronics are shown in Figure 95.

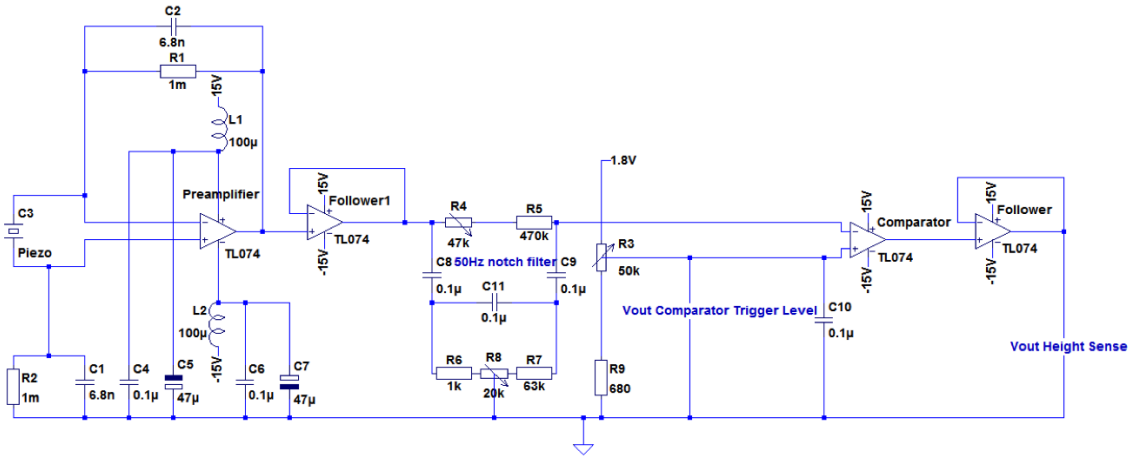

Figure 95 electronics schematic used to interrogate the piezo.

The PROBE function, within the G-code language, was used to allow continual monitoring of the piezo. PROBE continually monitors the input via the high speed digital line at 1MHz, this corresponds to a distance of 0.25 nm and 0.75 nm moved in the z and x/y axis respectively, for one cycle of high speed digital line. Once positions are taken in individual places on the workpiece, a software plane can be calculated. The sample map is then calculated and the pitch, roll and yaw of the sample on the bed can be machined out on the fly by translating the z axis to counteract sample tilt.

The piezo and the associated electronics used have been described. In the next section the verification process used to calibrate a single probe location is examined.

6.4.2 Verification of plane probing

To verify the electronics and programing used to probe the sample plane, a piece of ultra flat glass was probed and drilled to find if there was an offset between the actual depth of cut and the program depth of cut. The piece of flat glass (BK7) used was a Comar precision glass window with $\lambda/4$ (λ = 633nm) flatness, which implies it will deviate $\leq$158 nm in flat form over at least 90% of the sample. A new 254 µm in diameter, two flute, slot mill, see Figure 90, was used throughout the calibration test. The calibration was carried out while the spindle was rotating at 20 krpm, as preliminary testing showed more repeatable results for a rotating spindle compared to a static one. This is thought to be because the rotating cutter causes greater vibrational impulse to the piezo when probing the sample, thus greater signal is seen by the piezo.

To find the error of a single probing event, multiple points were used later to calculate the pitch and roll of the sample. The ultra flat glass was probed and then drilled to depths varying from 1, 2, 3, 4 and 5 µm. The distance between drilled holes was 300 µm, to minimise errors in sample flatness. This was repeated five times for each depth. The holes were drilled with a rotation speed of 20 krpm and a translation speed of 0.25 mm/min. A white light interferometer (Zemetrics, ZeScope) was used to gather depth information of the drilled holes, where a 10x objective was used to collect the profiles. Using the commercially available software Image Metrology, SPIP, appropriate levelling was applied to remove the linear plane of the sample. A histogram of the drilled hole was taken and its depth extracted by taking the value where the histogram decreases rapidly at the greatest depth of cut, see Figure 96. In Figure 96 this value is ~5.65 µm.

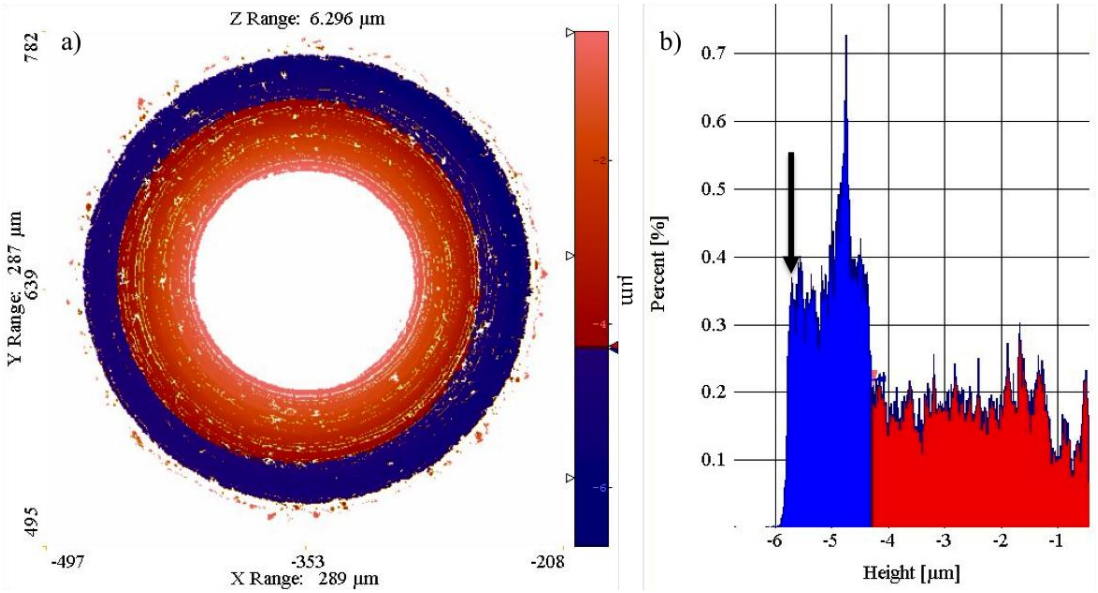

Figure 96 a) white light interferometer surface profile, at 10x magnification of a hole drilled with a programed axial depth of cut of 5 µm. b) histogram of the observed axial cut depth. Notice the deeper machined area in blue compared to red because of the location of the mill's cutting flutes. The black arrow denotes where the histogram observed axial cut depth rapidly decreases, at a value of ~5.65 µm.

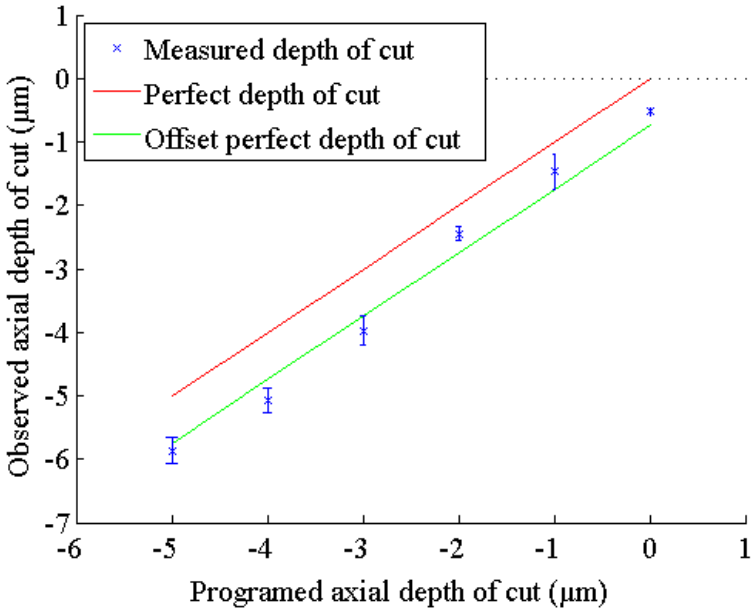

Figure 97 verification of plane by drilling and comparing the actual depth achieved to the programed value.

By finding the maximum depth of cut for each drilled hole, using the technique explained in Figure 96, the average and standard deviation of the five drilled holes at various depths was plotted in Figure 97. The red line in Figure 97 represents the ideal scenario where the programed position is the same as the observed axial cut. The Green line in Figure 97 is the regression of the means where the offset (systematic error) has been optimised, the resulting offset is -743 nm. To calculate the random error of the z axis probing, the standard deviation of the observed axial cut depths were taken and subtracted by the programed cut depths and the mean offset (-743 nm). The calculated random error in z axis probing was 277 nm. Thus an offset of -743 nm must be added when machining and the user must be aware of error in surface probing to be 277 nm.

Verification of a single probe point has been examined. The next section looks to verify the entire sample plane from a number of probe points.

6.4.3 Verification of plane definition

To calculate a virtual plane of the sample surface, three or more points on the surface are needed. Primary component analysis was used to fit a plane through multiple probing points, this was implemented using Matlab [23]. The standard deviation of the residuals is used as an error figure for the fitting of the data points. To validate

the program, a forty point plane fit, over a 2 by 1 cm sample size, was conducted three times on a piece of the ultra-flat glass. This achieved standard deviations of 382 nm, 565 nm and 407 nm of error across the plane, thus showing the repeatability of the system is approaching the limit or errors shown for single height senses of ~ 277 nm.

Plane definition verification has been explained; the next section shows how the plane is used to eliminate sample misalignment to enable precision milling.

6.4.4 Mill movement

To simplify cutter path programing, a transformation in coordinate systems had to be implemented from the simple programing plane.

The concept of program plane transformation to sample plane is as follows:

- Cutter path programed in program plane.
- Program plane unit vector calculated.
- The sample's surface and sides are probed in multiple locations, see section 6.4.
- Primary component analysis is used to fit a virtual plane through the surface probe points, Cartesian equation found for plane.
- Linear regression used to fit side probe points in both x and y directions.
- Corner of the sample plane calculated in machine encoder units.
- Unit vector calculated for the corner of sample.
- Transfer matrix calculated.
- Now possible to convert cutter path from program plane into the sample plane (*i.e.* encoder values).

This simple transformation of coordinate systems coupled with multipoint plane probing allowed simple cutter path programing with hundreds of nanometre accuracy. Mill path with compensation for sample skew has been explained, and now the experimental procedure used when micromilling glass will be discussed in the next section.

6.5 Micromilling procedure

Mill rotational speed, translational speed, depth of cut, cutter path, sample cooling, mill material, diamond size and dressing and are dominant parameters for obtaining good quality milled grooves in silica and other brittle materials. A milled groove is deemed to be good quality when it has nanoscale roughness, a constant depth profile and low amount of surface chipping. Within the following section preliminary results are discussed on the micro milling of flame hydrolysis deposited silica with diamond coated tungsten carbide micromills.

6.5.1 Cutter path and dressing

The cutter path is critical to milled grooved quality. The simplest cutter path is a vertical one, where vertical plunge milling begins the groove, followed by lateral milling and a vertical exit, as shown in Figure 98 a).

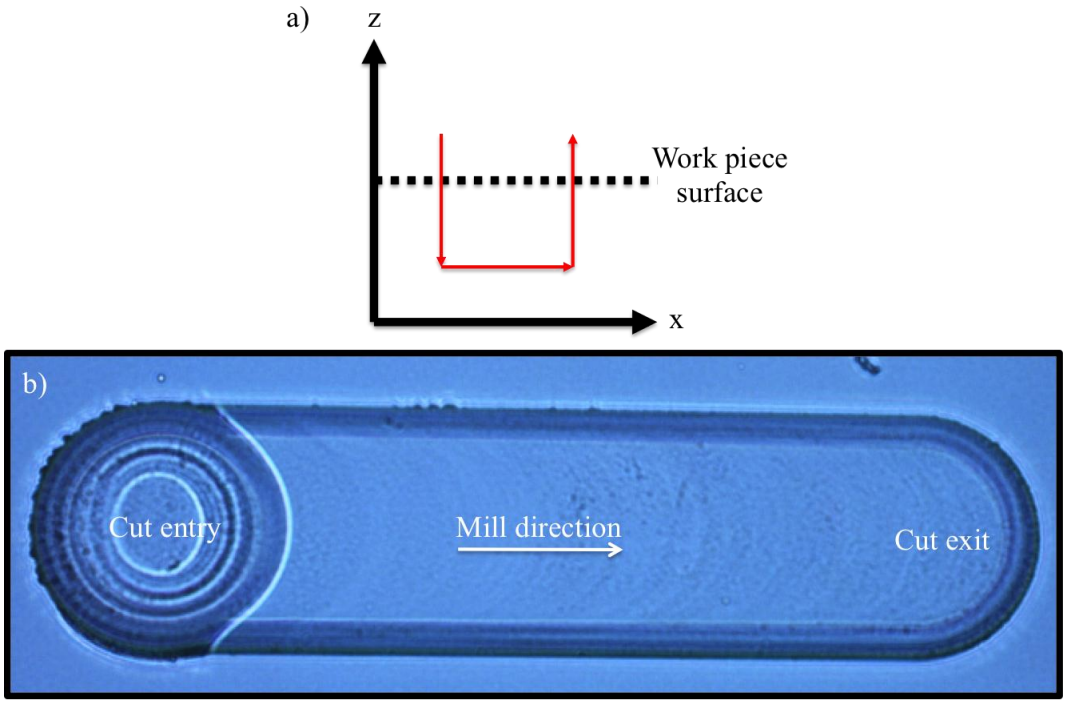

Figure 98 vertical cutter path. a) schematic of the cutter path with red arrows showing direction of travel in the x and z axis. b) shows a microscope image of the groove, notice the entry is chipped most likely due to the material being unable to escape from the drilling phase.

Figure 98 b) shows a circular indentation at the cutter entry, which is believed to be because of the drilling action. This circular indentation is thought to be caused by poor chip material removal, thus causing a build up of unwanted material. The poor material removal may also cause brittle removal of material and thus instigate chipping in this area. Another possible hypothesis for the circular indentation, is the difficulty in material removal causes the z axis to overshoot.

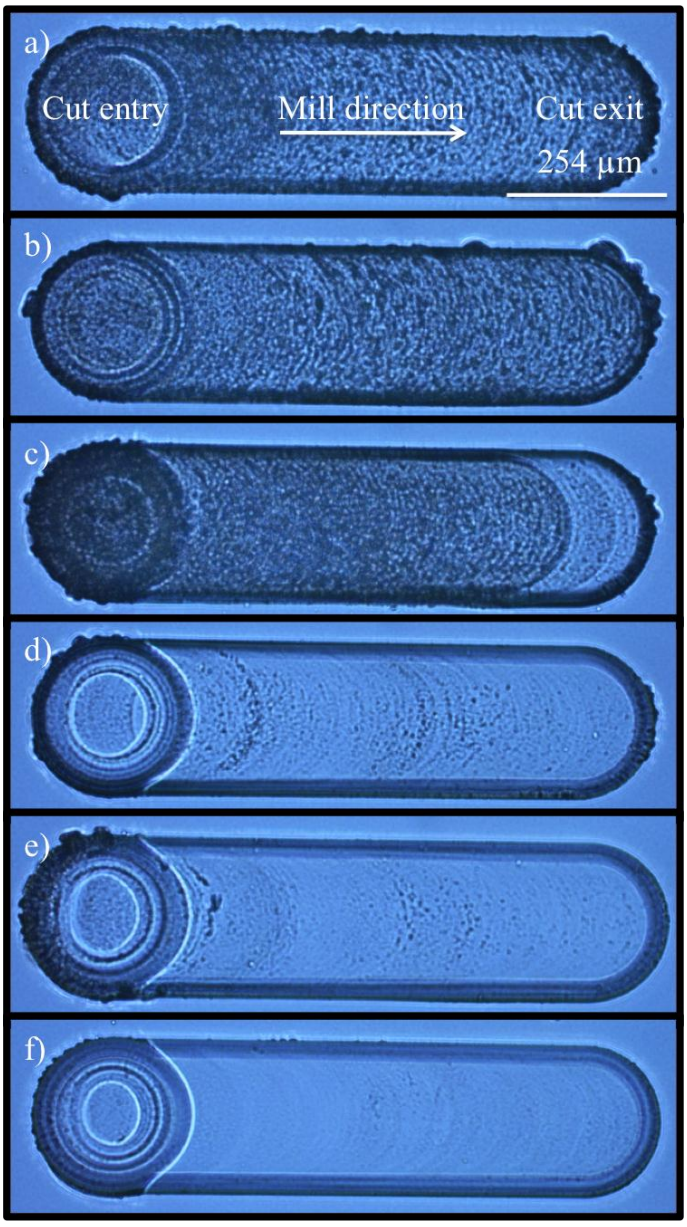

Figure 99 microscope image of groove sequentially machined from a) to f). It is evident that the surface becomes smoother and the chipping and groove width reduces from groove a) to f), which is indicative of mill dressing whilst machining the silica.

The grooves in Figure 98 b) and Figure 99 f) are the same and the grooves from Figure 99 a) to f) are machined consecutively on the same sample. Each groove was machined using a vertical cutter path, as before in Figure 98 a). The dramatic improvement in groove quality from Figure 99 a) to f) it is thought to be from mill dressing. More evidence of mill dressing is the ~4% reduction in groove width from Figure 99 a) to f). As mentioned previously, dressing in dicing can hugely effect the cut quality in silica, see chapter 4. As with dicing, the tool is trued to the rotational centre of the spindle and removes any offset from clamping or mill manufacture. As it can be seen from Figure 99 a) to f), the groove bottom quality (from microscope inspection) greatly increases as the amount of chips decrease. Thus with each new mill, the mill was dressed in silicon carbide with a peck drilling routine in order to ensure mill concentricity to the spindle. The dressing routine consisted of drilling into the silicon carbide in 10 µm steps, to a depth of ~3-5 µm deeper than that used in the machining of the work piece. Dressing used the same rotational speed as the work piece machining and a translational speed of ~2.5 mm/min in the z axis. This dressing routine was implemented five times before machining of the work piece commenced.

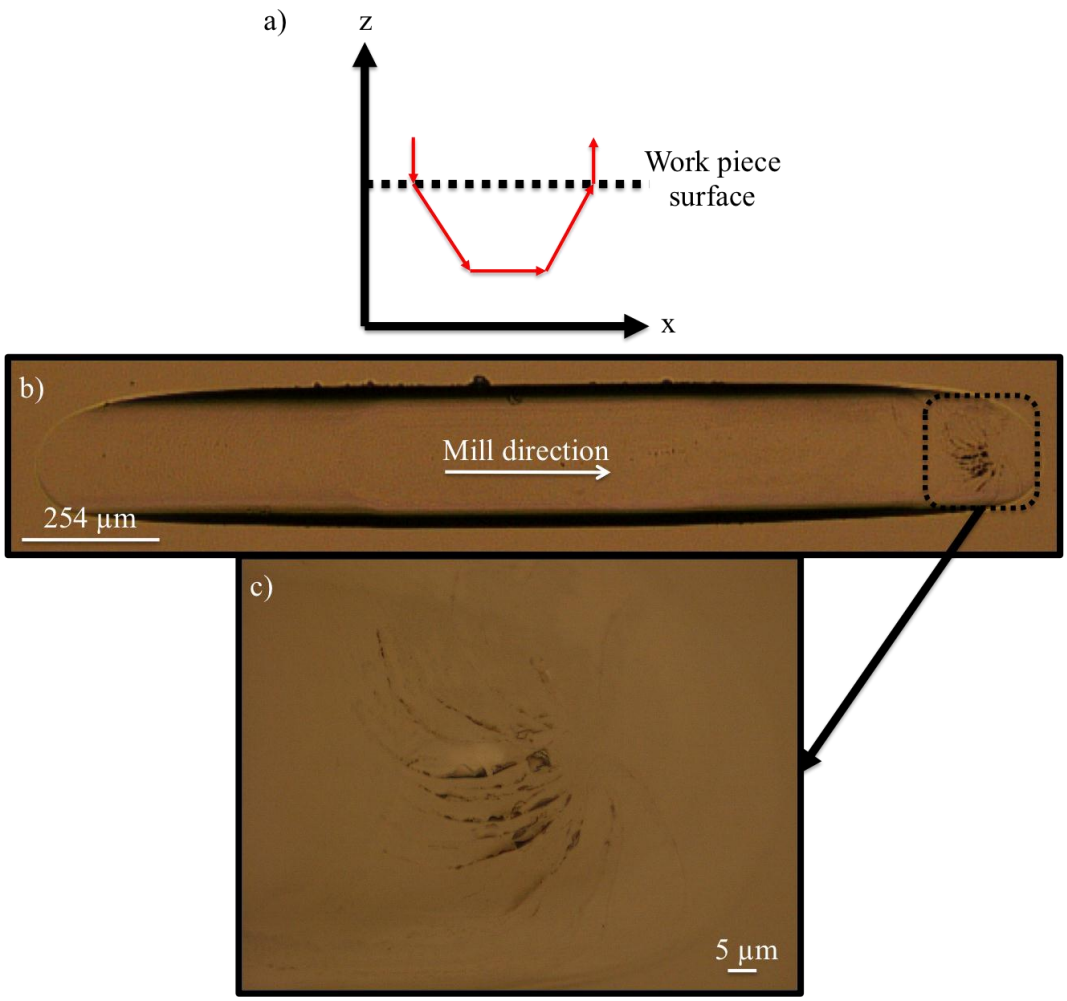

Figure 100 cutter path with linear descent, in the x and z axis, starting at the work piece surface. a) schematic of the cutter path with red arrows showing direction of travel in the x and z axis. b) shows a microscope image of the groove, notice the entry is smooth but the exit is scuffed. c) shows the scuff enlarged.

To reduce the build up of material whist machining, as seen in Figure 98 and Figure 99, a linear descent in the x and z axis was used, as shown in Figure 100 a). The linear descent provided space for the machining debris to be expelled as it moves in the x direction. However, this type of approach can cause scuff marks at the entrance and exit of the mill, as can be seen from Figure 100 b) and c). The mill engages from the surface of the work piece in an unsmooth way, causing added stress to the surface which results in chipping. Figure 100 b) shows a clear example of the effect of downmilling and upmilling (see Figure 82). There is a large difference between the side chipping, the downmilling side (top side) shows far more than the upmilling side (bottom side). This difference has been noted before by Arif *et al.* [1].

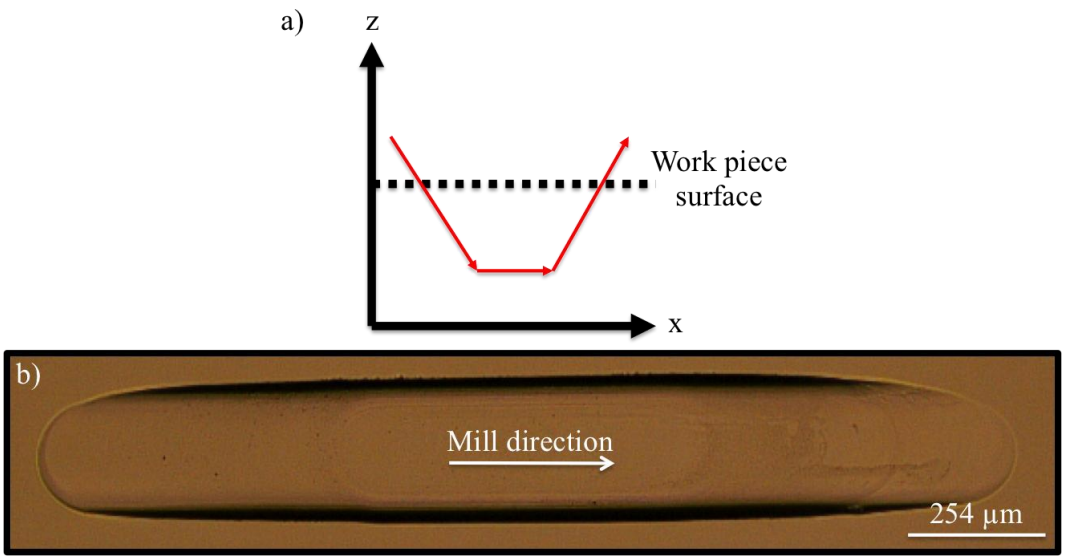

Figure 101 cutter path with linear descent starting above the work piece surface. a) schematic of the cutter path with red arrows showing direction of travel in the x and z axis. b) shows a microscope image of the groove, notice the smooth bottom and the absence of chipping because the ductile cutting regime has been maintained throughout the machining process.

The vertical approach was removed as seen in Figure 101 a) and replaced with just a linear descent. Figure 101 b) shows no signs of scuffing and a smooth chip free groove has been milled. Thus this cutter path was used throughout future milling experimentation.

The cutter path and dressing procedure to obtain favourable results in silica-on-silicon have been discussed. The optimisation of machining parameters, such as rotational and translational speeds is developed in the next section.

6.6 Optimum micromilling parameters for silica-on-silicon

To find optimum machining parameters to create high-quality grooves in Flame Hydrolysis Deposition (FHD) silica-on-silicon, a parameter test was undertaken. Parameters such as depth of cut, cutter path, sample cooling, mill material, diamond size and dressing were all kept constant. The parameters changed are the cutter's rotational and translational speed. The remaining parameters were kept constant for the following reasons. The depth of has been kept constant as this technique was envisaged to access the core structure of a waveguide by removing the cladding layer

be it a fibre or a planar waveguide. The cutter path strategy was kept constant because of reasons discussed in section 6.5.1. Jet sample coolant was kept at a constant amount and was not changed to oil based due to the drainage constraints. Mill parameters, such as mill material and diamond size were dictated by the manufacturer so were also constants in testing. The variable parameters will now be discussed in more detail.

6.6.1 Rotational and translational speed optimisation

A large machine parameter space was chosen, when varying the spindle rotational and translational speeds. The rotational speeds were varied from 10, 20, 40 and 60 krpm, while the translational speed were 0.250, 0.325, 0.750, 1.000, 1.250 and 1.500 mm/min. These parameters determined the feed rates, where feed rate is defined as the distance travelled by the mill in one revolution, which predicted ductile machining, see section 6.2.2. Fourteen individual samples were machined with different parameters, each with nineteen grooves machined in succession. Each groove was 1.5 mm in length and was machined into the top surface of the FHD silica. An example of the first eight grooves machined at a rotational speed of 40 krpm and translational speed of 0.75 mm/min can be seen in Figure 102.

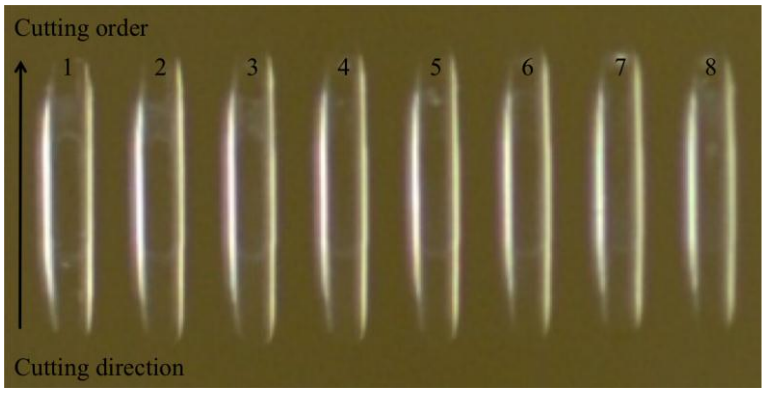

Figure 102 micrograph of the first eight grooves machined into silica at 40 krpm at 0.75 mm/min.

The entrance and exit of each groove were made with a linear gradient (see Figure 101) to a final depth of 17 µm. For each sample a new tungsten carbide, two flute, slot mill with chemical vapour deposition diamond coating (grit size ~0.5-3.5 µm) and a radius of 254 µm, was used as shown Figure 90. To ensure mill concentricity to the spindle, the mill was dressed in silicon carbide with a peck drilling routine to a depth of 20 µm, for five times as discussed in section 6.5.1. Each substrate surface

was probed to create a plane map to enable CNC to remove sample pitch, roll and yaw, as discussed in section 6.4. Sample probing was executed using a dressed tool where eight points on the surface were used to calculate the sample plane and four points on each side were used to calculate the sample's corner. A deionised water jet was used to provide tool and workpiece coolant and lubrication, at a rate of ~175 ml/min during every stage of machining and dressing.

The optimisation of spindle rotational and translational speeds have been discussed here. After the optimisation had been completed, the milled grooves were inspected and the surface metrology quantified. This is described in the next section.

6.6.2 Groove metrology

3D surface metrology data was collected of the first grooves milled, for each set of parameters, at the groove's centre point using a white light interferometry. A Zemetrics, ZeScope was used throughout this chapter as in previous chapters. Figure 103 shows a levelled image showing the variation in height of the milled groove, where the parameters used were 10 krpm for rotational speed and 1.5 mm/min for translational speed.

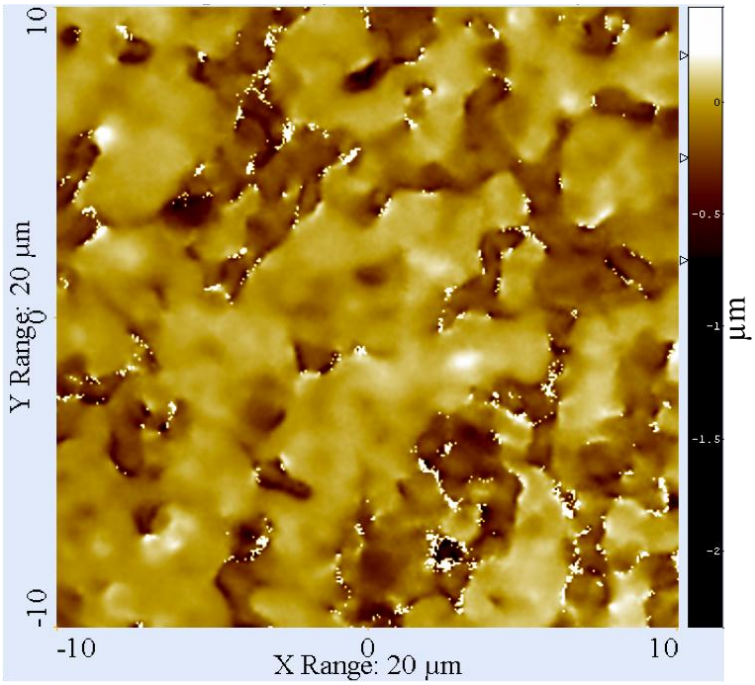

Figure 103 white light interferometer surface profile of the middle of the groove bottom, machined at 10 krpm and 1.5 mm/min, colour bar shows variations in height (µm). A rough surface has been generated with micron level pitting, making this machined in a brittle regime. This groove had a surface roughness (Sa) of 107.0 nm with a standard error of 16.7 nm.

Figure 103 shows the surface data of a groove milled with poor surface quality, which can be attributed to the silica being machined in a brittle mode. Many of the white pixels in Figure 103 are void pixels and are negated from any surface roughness calculations. These void pixel are caused by the scattering angle of the roughness being greater than acceptance angle of the objective [24]. Figure 103 has a surface roughness of 107.0 nm (Sa), with a standard error of 16.7 nm. Another groove was then milled with a different set of parameters of 60 krpm and 0.25 mm/min, resulting in ductile machining, as shown in the levelled data in Figure 104, a stark difference in roughness is clearly evident.

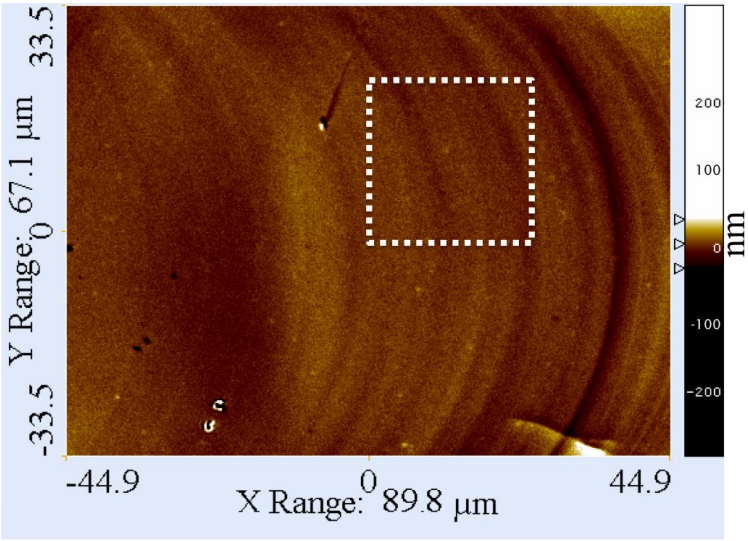

Figure 104 white light interferometer surface profile of the middle of the groove bottom, machined at 60 krpm and 0.25 mm/min, colour bar shows variations in height (nm). A smooth surface has been generated. This groove had a surface roughness (Sa) of 3.5 nm with a standard error of 0.75 nm. Notice dirt adhered to the surface by the presence of high points. White dotted square shows the approximate position of Figure 105.

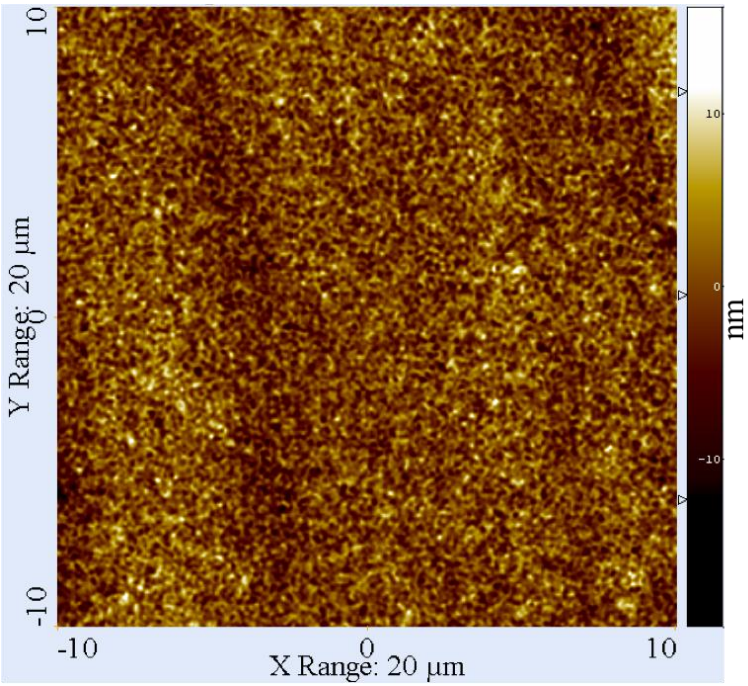

Figure 105 white light interferometer surface profile of the middle of the groove bottom, machined at 60 krpm and 0.25 mm/min, colour bar shows variations in height (nm). Taken from Figure 104.

Figure 104 and Figure 105 both show surface profile of the same groove, where Figure 105 is on a smaller scale. Figure 104 shows characteristic streaks left by the

diamonds within the diamond coating of the mill, which are the characteristic signs of a ductile machined surface. There is also no chipping present, again indicative of the ductile mode. However, there is a shallow scratch on the nanometre scale, shown in Figure 104. The high points present at the bottom of Figure 104, are pieces of debris adhered to the surface. Figure 104 has a surface roughness of 3.5 nm (Sa), with a standard error of 0.75 nm.

For further analysis of the groove samples, the feed rate is plotted against areal [25] average surface roughness (Sa), as is shown in Figure 106 and Figure 107. The feed rate is defined as the distance travelled by the mill in one revolution. Each Sa value was calculated by selecting ten, 10 µm by 10 µm square samples on each ~90 µm by ~70 µm scans in five columns and four rows. Square samples are used to stop the bias of surface texture, from the difference in lengths of the scan areas (*i.e.* ~90 µm by ~70 µm scans), effecting average surface roughness calculated. Appropriate polynomial levelling is then used before the areal average surface roughness (Sa) is taken; both applied using the commercially available software Image Metrology, SPIP. A mean was then taken over the twenty samples and the Sa plotted in Figure 106 and Figure 107.

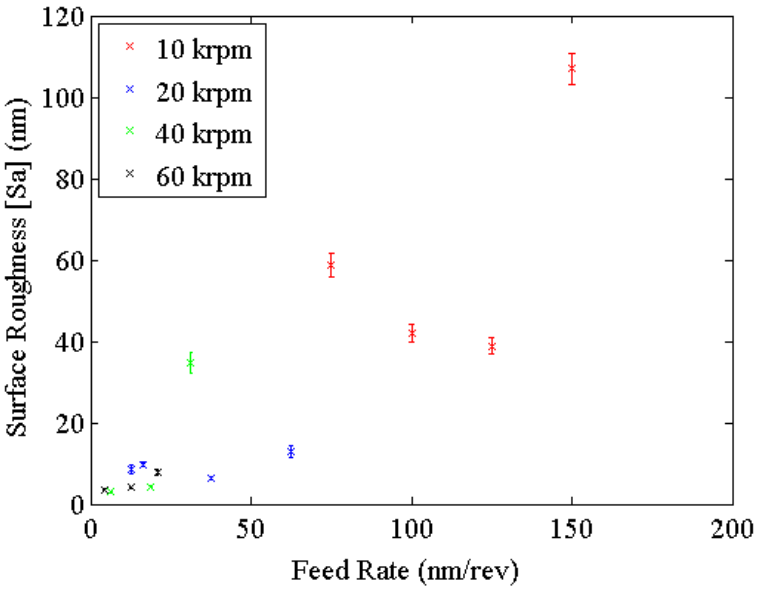

Figure 106 relationship between areal average surface roughness and feed rate with the standard error used for error bars.

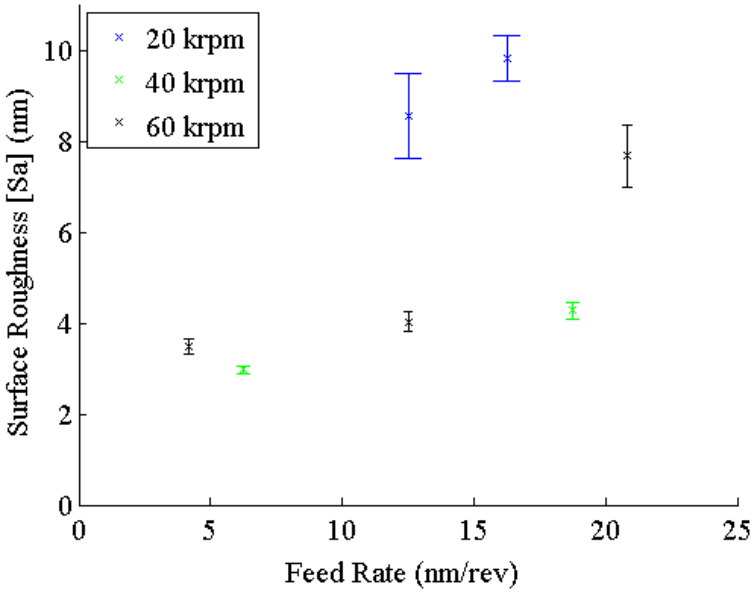

Figure 107 rescaled data from Figure 106 showing the relationship between areal average surface roughness and feed rate with the standard error used for error bars. The smoothest machining results occur at feed rates < 20.8 nm/rev.

Figure 106 and Figure 107 both show for feed rates <20.8 nm/rev that the surface roughness (Sa) becomes <10 nm with a small standard error, showing good consistency in surface roughness over the groove. For feed rates >20.8 nm/rev, a rougher surface finish (i.e. > 10 nm Sa) finish to the groove is seen, with larger variations in Sa over the groove, indicated by larger standard errors. As can be seen from Figure 107, the smallest surface roughness, is obtained at a rotational speed of 40 krpm or 60 krpm at a translation speed of 0.25 mm/min or 0.75 mm/min must be used.

Surface quality of the grooves is not only related to the surface roughness, thus visual inspection was also carried out via microscope inspection. Examples of chipping and other deflects are shown below in Figure 108.

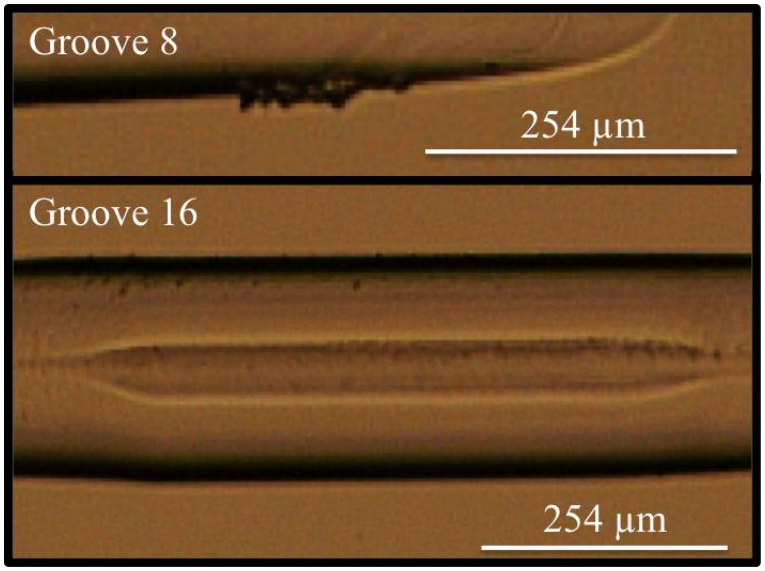

Figure 108 microscope image showing chips and a groove defect present in milled grooves at 40 krpm and 0.75 mm/min.

Figure 108 a) shows the chipping on the order of 125 µm, which would be an example of an unacceptable level of chipping. Figure 108 b) shows an example of a groove bottom defect. Both chipping and defects are visually searched for in each groove that was machined. Table 4, summaries the results from the microscope inspection of the sequentially machined grooves. As a metric the number of high quality grooves, *i.e.* those without chipping and defects, is given for each test set.

Table 4 quantity of machined grooves (see Figure 102) without chipping or groove defects for each machining parameter test, using microscope inspection.

Machining parameters		The quantity of machined grooves without chipping and defects
Rotational speed (krpm)	Translation speed (mm/min)	
10	0.750	1
10	1.000	1
10	1.250	3
10	1.500	2
20	0.250	3
20	0.325	3
20	0.750	5
20	1.250	4
40	0.250	2
40	0.750	6
40	1.250	1
60	0.250	1
60	0.750	1
60	1.250	1

As shown from Table 4 the groove that showed the smallest amounts of chipping and groove defects was milled at a rotational speed of 40 krpm and translational speed of 0.75 mm/min. It is apparent from Table 4 that all milled grooves suffered some defects. In the vast majority of the machine parameter runs, chipping occurred, similar to that shown in Figure 108. By combining the results of surface roughness from Figure 107 and visual inspection from Table 4 the parameters of a rotational speed of 40 krpm and translational speed of 0.75 mm/min were found to give the most favourable results. The groove had an average surface roughness of 3.0 nm (Sa), with a standard error of 0.34 nm and had the smallest amount of chipping and groove defects, from visual inspection. The optimum milling parameters have been found. In the next section the analysis of the subsequent grooves milled with the optimum machining conditions is included.

6.6.3 Continued analysis of optimised silica micromilling

The optimum machining conditions for silica micromilling have been discovered within the previous section. In order to understand the effects of prolonged machining, nineteen grooves were machined using the same machine parameter, allowing the effects on groove surface quality to be gathered. Figure 109 shows a micrograph of the second groove machined, where a smooth, unchipped profile is evident. A white light interferometer and AFM was used to analyse this groove, and the surface profiles are shown in Figure 110 and Figure 111.

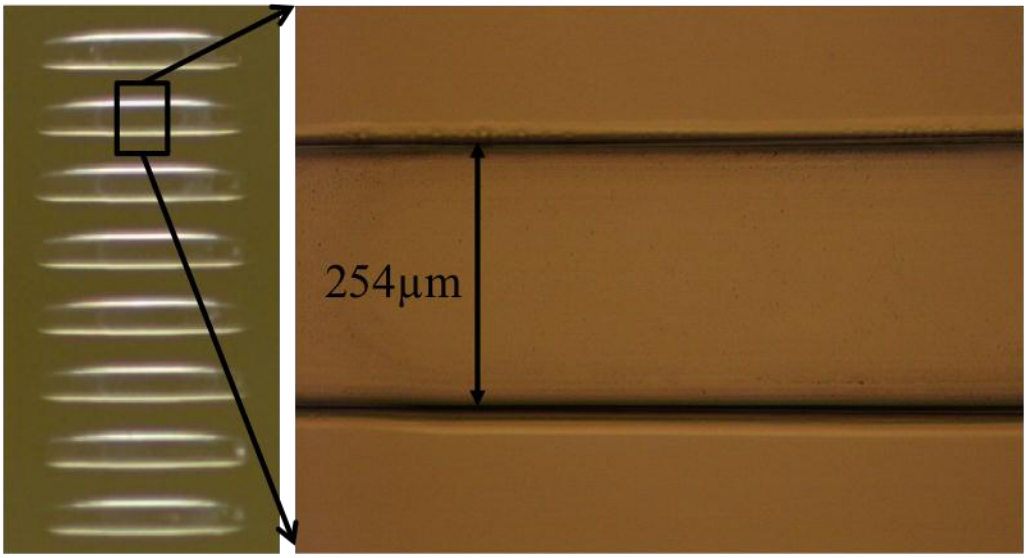

Figure 109 micrograph of second groove milled at 40 krpm and 0.75 mm/min.

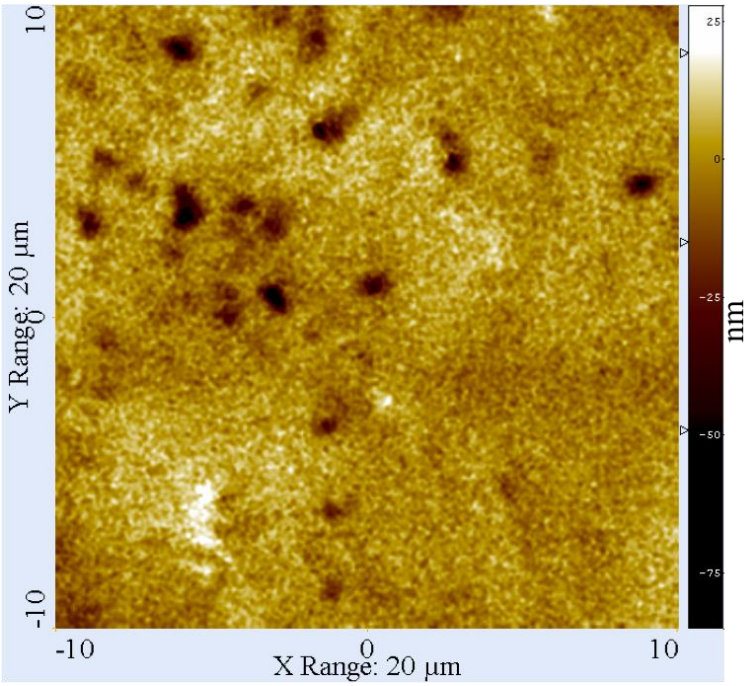

Figure 110 white light interferometer surface profile of the middle of the second groove bottom, machined at 40 krpm and 0.75 mm/min, colour bar shows variations in height (nm). The groove had an average surface roughness of 4.9 nm (Sa), with a standard error of 1.3 nm.

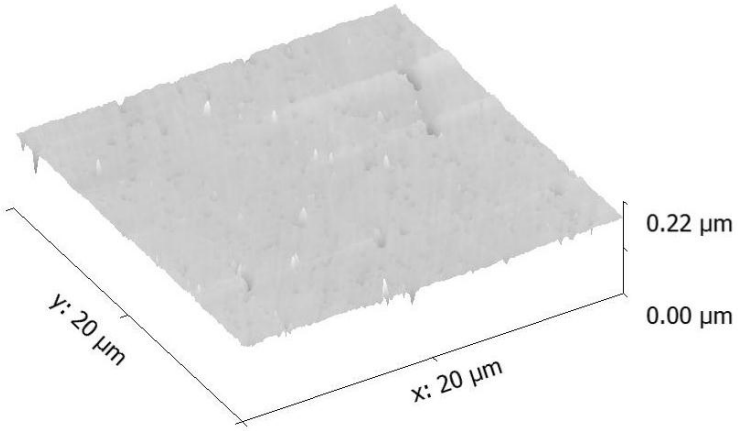

Figure 111 AFM surface profile of the middle of the second groove bottom, machined at 40 krpm and 0.75 mm/min. The groove had an average surface roughness of 2.7 nm (Sa).

Figure 110 shows a white light interferometer profile of the middle of the second groove bottom, machined at 40 krpm and 0.75 mm/min. The surface roughness for this sample is 4.9 nm (Sa), with a standard error of 1.3 nm and was measured in the same way as described in section 6.6.2. Figure 111 shows an AFM profile of the middle of the second groove bottom, machined at 40 krpm and 0.75 mm/min. The AFM scan was conducted on a Veeco, Caliber using tapping mode. The surface profile was analysed using Gwyddion (surface metrology software), where

polynomial levelling was implemented and the surface roughness calculated. Figure 111 shows that this second groove has a surface roughness of 2.7 nm (Sa). There are some signs of pitting in both Figure 110 and Figure 111 for this groove, but both profiles are free from chips and cracks. These profiles would be characterised as machined in a ductile regime as pitting is on such a small scale.

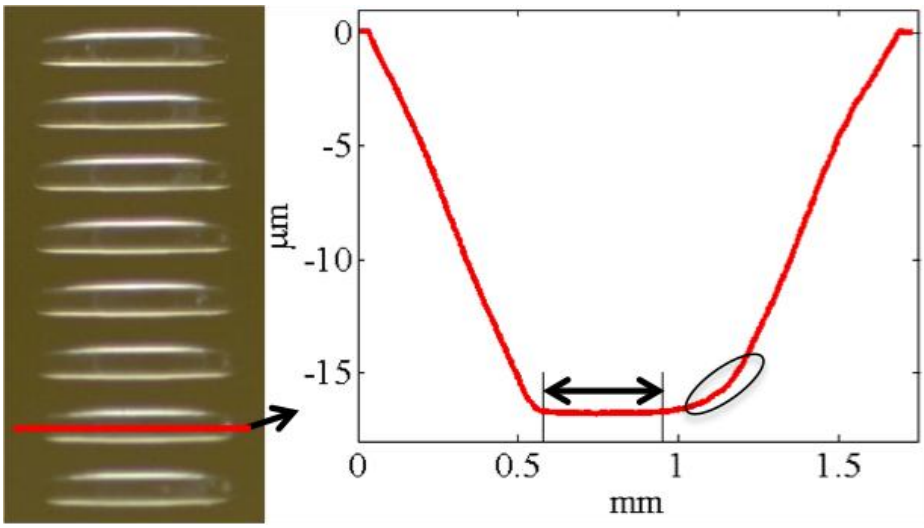

Figure 112 white light interferometer surface profile at 5x magnification of the seventh groove, machined at 40 krpm and 0.75 mm/min. Both the mean depth and deviation from flat is calculated between the black arrowheads. The black circle shows poor z axis performance.

Figure 112 shows a white light interferometer profile of the seventh groove milled and is typical for all eight grooves and shows the sloped entrance and exit. Figure 112 shows that good overall form is achieved, with the depth of cut staying constant along the groove bottom. The profile was taken with a 5x objective to increase the field of view when compared to the surface metrology data taken at 100x. The mean depth was calculated to be 16.8 µm, thus is 200 nm away from the programed depth of cut of 17 µm. The deviation from the flat of the groove bottom was measured by taking the standard deviation where it was calculated to be 19.4 nm. Thus, nanometre form has been achieved. The black circle shown in Figure 112 deviates from nanometre form and is probably caused by poor performance in the z axis lift stage, in either the force it can apply to the bed or in its feedback loop.

Within this section surface metrology is compared with white light interferometer and AFM data. In the next section mill wear is discussed and its relation to the grooves surface quality is given.

6.6.4 Mill wear

Mill wear becomes important when more than one groove is required from a single milling run. This is the main reason for milling nineteen grooves in succession to discover the effect of mill wear on groove quality. Figure 113 shows micrographs of a selection of the nineteen grooves, machined with the optimum parameter of 40 krpm and 0.75 mm/min.

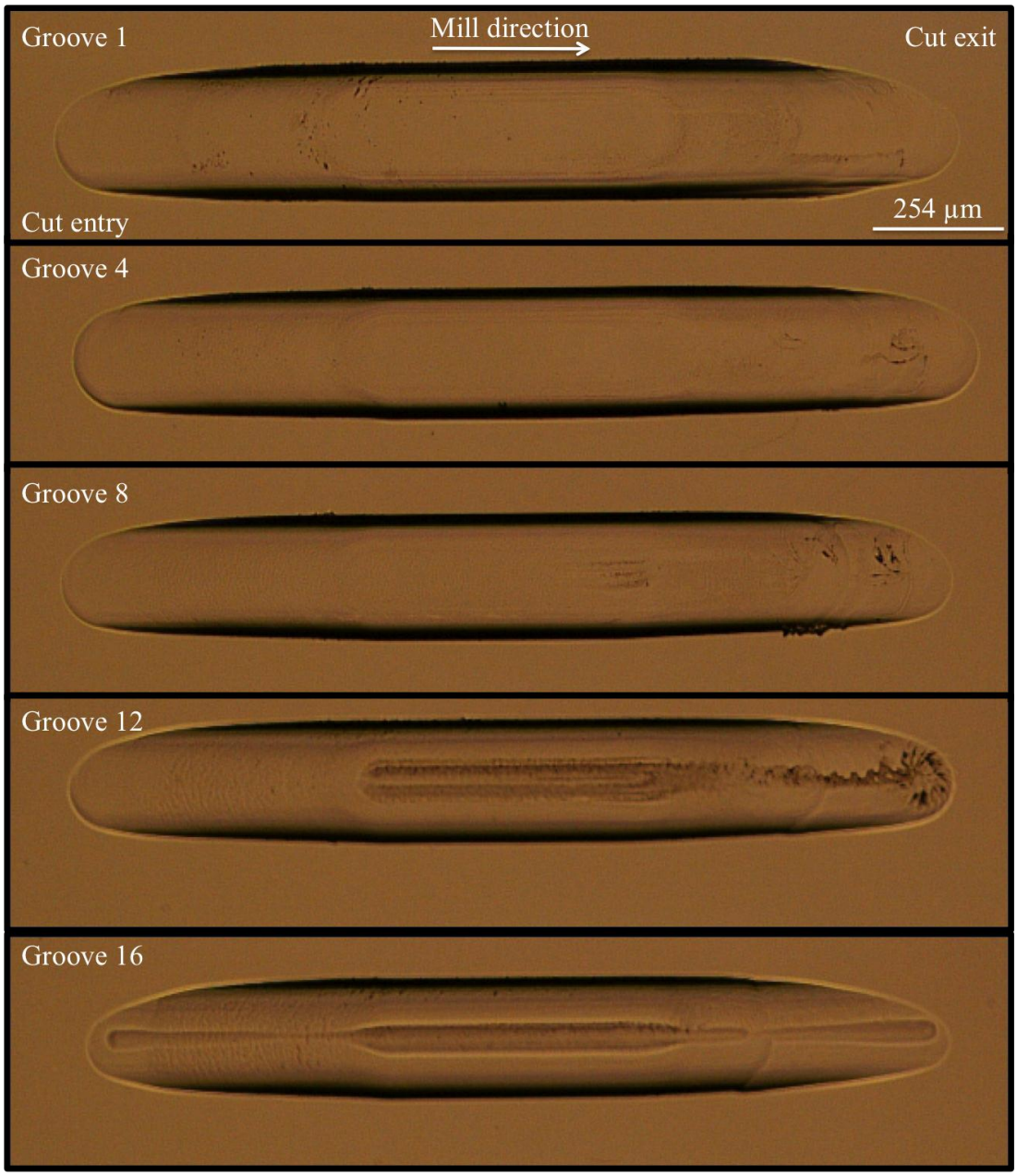

Figure 113 micrograph of grooves showing the progression of the groove defects caused by mill wear, machined at 40 krpm and 0.75 mm/min.

As shown in Figure 113, there is a gradual increase in groove bottom defects from groove numbers 8 to 16. This is thought to be caused by wear of the mill's diameter. There is also a noticeable change in roughness of the groove bottom, see Figure 114.

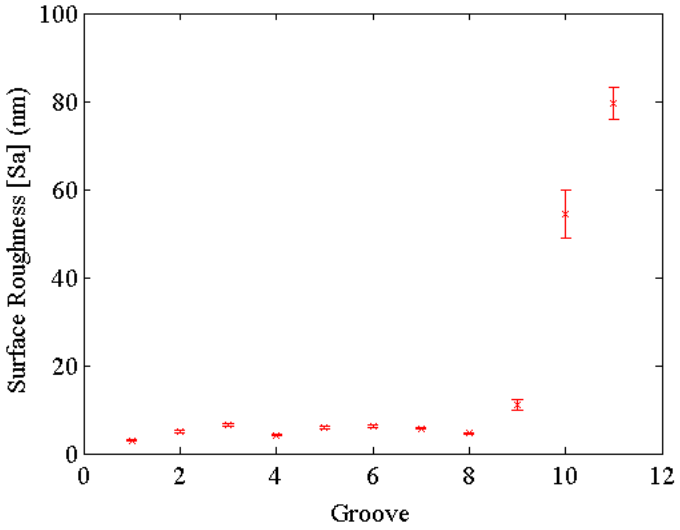

Figure 114 relationship between areal average surface roughness and the groove number (see Figure 102) with the standard error used for error bars. All grooves were machined at 40 krpm and 0.75 mm/min.

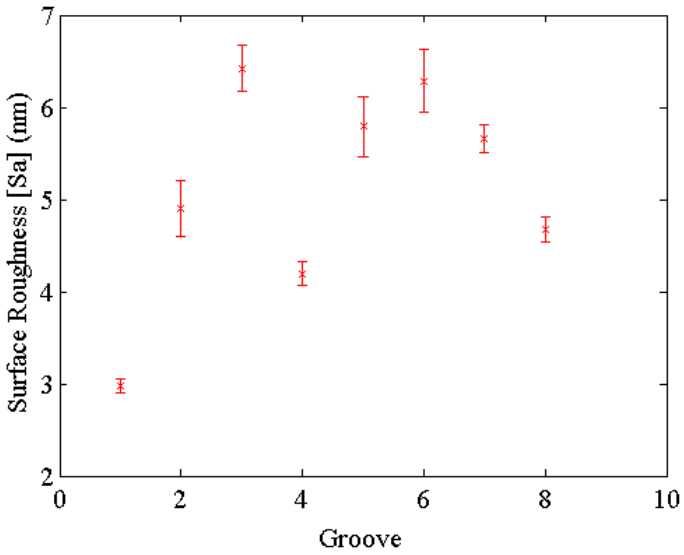

Figure 115 relationship between areal average surface roughness and the groove number (see Figure 102) with the standard error used for error bars. Machined at 40 krpm and 0.75 mm/min. Taken from Figure 114 for grooves number < 8. These eight grooves have a mean surface roughness (Sa) of 5.1 nm.

Figure 114 and Figure 115 shows for the first eight grooves there is relatively little deviation in surface roughness (Sa), until grooves 9 and 11. This change in surface

roughness is caused by the milling process changing from ductile removal of material to brittle, which is apparent in Figure 113, shown by the increase in groove bottom roughness. Figure 115 shows the variation in surface roughness (Sa) for the grooves 1 to 8, which were machined in a ductile mode. The mean surface roughness (Sa) of these values was calculated to be 5.1 nm, with a maximum surface roughness of 6.4 nm, as seen on groove 3. Using the Payne and Lacey theorem, as discussed in section 6.2.3, and the surface roughness (Sq) and a correlation length (L_C) values for groove 3, a propagation loss was calculated. A loss of 0.159 dB/cm is calculated for groove 3, which had an Sq = 10.4 nm and a L_C = 775 nm. Thus, the propagation loss (groove length = 1.5 mm) would be deemed small when compared to the propagation loss of 0.235 dB/cm [26] for the direct UV written waveguide (typical waveguide length = 2 cm).

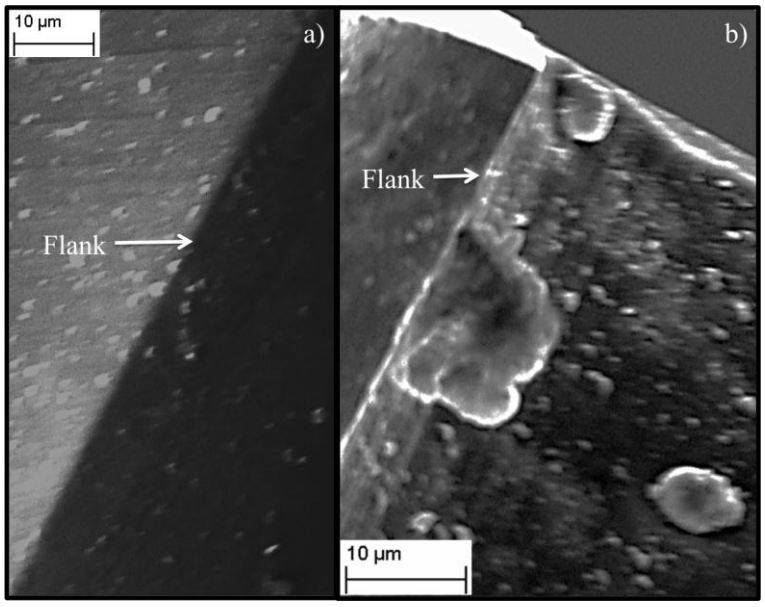

Figure 116 SEM micrograph of mill (see Figure 90) cutting flank. a) new fresh flank and b) worn flank after machining all nineteen grooves at 40 krpm and 0.75 mm/min.

Figure 116 shows SEM micrographs of mill cutting flanks. Figure 116 a) shows a micrograph of a new mill bit and Figure 116 b) shows a micrograph of a worn flank. Figure 116 b) clearly shows three large chips have been worn into the flank, ranging from 5 to 10 µm in size. This damage was caused after the machining of the nineteen grooves at the optimum parameters. This shows the precision milling process has a limiting number of grooves it can machine sequentially before mill wear effects groove quality, as seen in Figure 114.

Groove quality degradation via qualitative microscope inspection and quantitative surface metrology has been commented on in relation to mill wear. In the next section the micromilling technique for silica-on-silicon is compared to others in the literature.

6.7 Discussion

The ability shown here to physically micromachine silica with a 17 µm depth of cut and generate surfaces with an average Sa 5.1 nm over 8 grooves, is unprecedented. Previously work by Arif *et al.* demonstrated precision slot milled grooves in silica that were smooth, chip free, with a Sa of 23.8 nm but with a depth of cut of just 400 nm and a translation speed of 80 nm/rev [1]. Our method uses a depth of cut 40 times deeper, at 17 µm and is ~7 times smoother. Silica has also been machined with ball nosed cutters at 45° to the substrate by Foy *et al*. Again smooth, chip free surfaces were created with Sa of <60 nm at translation speeds of <16 nm/rev at a depth of cut of 17 µm [19]. However, we have created surfaces nearly ~12 times smoother at a similar feed rate (18.8 nm/rev) and are not limited by the ball nosed cutter geometry. Amin *et al.* have shown similar precision milling experiments in silicon, with depths of cut of 10 µm, feed rates of 125 nm/rev and showed Sa as large as 220 nm [27]. Our milling process with feed rates of 125 nm/rev, yielded surface roughness (Sa) of ~40 nm in silica. The most significant difference from previous works compared to the work shown here is that we have used an aerostatic bearing spindle [1] [19] [28] [27]. All the aforementioned works use ball bearing type spindles driven by either electrical or pneumatic means.

The differentiating factor between an aerostatic bearing spindles and ball bearing spindles is the amount of runout they possess. Spindle runout is the variation of the tool's rotational centre to the spindles rotational centre. Runout can be split into two types, static and dynamic runout. Static runout comes from the physical misaligned of the rotational centre of the tool and spindle and is caused by the imperfectness of the mechanical clamping of the tool. However, static runout can be reduced to negligible amounts by using precision collets and tools. Moreover, dressing of the

tool before machining in a hard material, can remove high points on the tool making it more concentric. To our knowledge no previously demonstrated precision milling process has included a dressing routine, which we have shown experimentally here. Dynamic runout is caused by random perturbations in the spindles rotation and is inherent to a spindle and can only be improved by balancing. It is believed that the static runout has been reduced to negligible levels via our dressing routine and the dynamic runout of our aerostatic bearing spindle is ~100 nm, as quoted by the manufacturer. In comparison the spindle runout figure supplied by Arif *et al.* and Foy *et al.* is ~1 µm [1] [19], an order of magnitude larger than the aerostatic spindle used here. Therefore we believe spindles with micron scale runout can cause the premature start of brittle type machining.

6.8 Fibre optic cladding removal

Silica optic fibres are far more abundant than silica-on-silicon devices, thus the machining of standard silica single mode fibre (SMF-28) to expose the core was attempted; preliminary results are shown in Figure 117. The precision milling technique is used in a similar way to that explained in section 6.6, where flat, smooth, chip free grooves are fabricated in planar silica with ductile micromilling. The fibres were mounted in standard aluminium v-grooves with UV curable glue. They were milled using the same optimised machining parameters for planar silica, which were a rotational speed of 40 krpm and a translational speed of 0.75 mm/min.

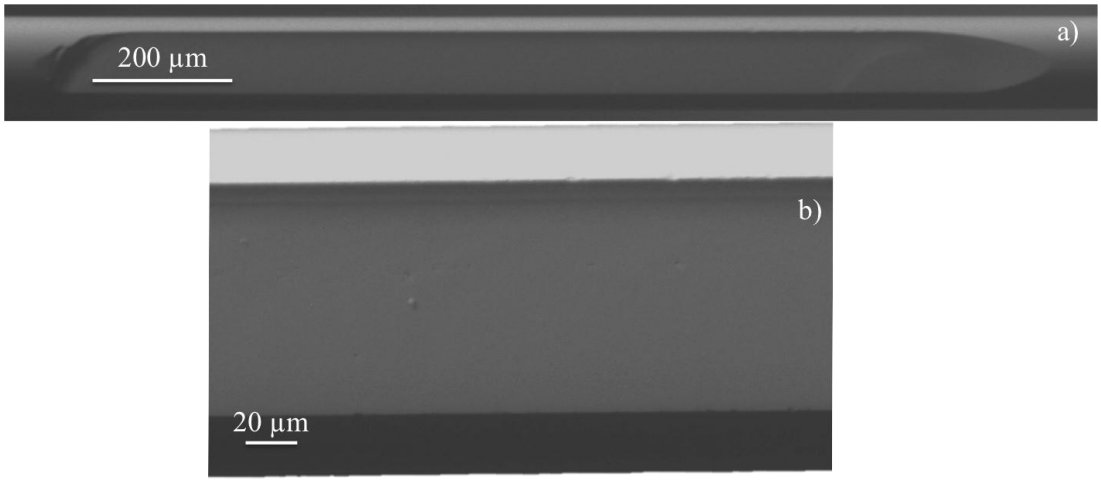

Figure 117 ductile regime milling of standard telecommunication optic fibre, used to remove the cladding and expose the core. a) and b) are both top view SEM micrographs.

Figure 117 shows SEM micrographs of fibres slot milled in a ductile regime where part of the silica cladding has been removed. Figure 117 a) shows the entire fibre, while Figure 117 b) shows an enlarged image of the machined area; notice the very smooth surface produced. For the fibre machined in Figure 117 a surface roughness was measured at ~5.0 nm (Sa). This is a revolutionary new way to machine/polish optic fibres, which are typically made with lapping and polishing in silica blocks [10]. The future research focus will be reaching the core of the fibre. The single cut, ductile, slot milling record was broken in this thesis, at a cut depth in silica of 17 µm, but in able to reach the core of a standard telecommunications optic fibre, 62.5 µm of material will be needed to be removed!

6.9 Conclusions

In this chapter it has been demonstrated that precision micromilling can produce grooves in a silica-on-silicon substrate, which are a smooth, chip free and with a mirror like finish. A precision micromill was constructed with high precision stages, high loop stiffness and good decoupling from the lab environment. The logic for sample setting with wax, cooling with deionised water and using diamond coated, tungsten carbide, slot micromills are stated. Sample mapping was discussed and an offset (systematic error) of 743 nm was found to exist between the programed axial

depth of cut and the actual depth of cut. The sampling mapping along with probing error and various averaging, had a random error of 277 nm. It was also shown that peck drill dressing in silicon carbide can be used to increase the groove surface quality. Mill cutter path is also critical in the groove surface quality achieved and it has been shown that a vertical plunge into a silica surface causes large amounts of cracking. A linear descent, however, in both the vertical and horizontal axes was found to remove this type of cracking entirely.

The micromill's machining parameters were optimised by monitoring average surface roughness and surface features, by means of a white light interferometer and microscope inspection. Via this approach it was found that optimum machining was obtained at a rotational speed of 40 krpm and a translational speed of 0.75 mm/min. Once machined, the grooves' average surface roughness (Sa) was measured and found to be 3.0 nm. The micromilling method uses a depth of cut 40 times deeper, at 17 µm and was ~7 times smoother than previously reported in the literature. The chapter also discusses the degradation of subsequent grooves milled with the optimum machining parameters and found good uniformity in the depth of each groove. The technique with a new mill could produce eight, 1.5 mm length grooves in the optical grade silica before mill wear affected groove surface quality. It is believed the large increases in depth of cut with no decrease in groove surface quality, compared to previous work, is related to the aerostatic spindle and preparatory dressing used in this work.

This chapter shows that precision milling is a strong candidate for the machining of silica. The method would be suitable for the removal of cladding layers, exposing the core of silica-on-silicon waveguides and thereby permitting access to the evanescent field of the mode. Thus, the technique may be suitable to the fabrication of planar waveguide sensors and other such devices.

References

1. M. Arif, M. Rahman, and W. Y. San, "Ultraprecision ductile mode machining of glass by micromilling process," Journal of Manufacturing Processes **13**, 50–59 (2011).

2. T. G. Bifano, T. Dow, and R. O. Scattergood, "Ductile-regime grinding: a new technology for machining brittle materials," Journal of Engineering for Industry (Transactions of the ASME) **113**, 184–189 (1991).

3. G. D. Quinn, P. Green, and K. Xu, "Cracking and the indentation size effect for Knoop hardness of glasses," Journal of the American Ceramic Society **86**, 441–448 (2003).

4. F. P. Payne and J. P. R. Lacey, "A theoretical analysis of scattering loss from planar optical waveguides," Optical and Quantum Electronics **26**, 977–986 (1994).

5. F. Grillot, L. Vivien, S. Laval, D. Pascal, and E. Cassan, "Size Influence on the Propagation Loss Induced by Sidewall Roughness in Ultrasmall SOI Waveguides," IEEE Photonics Technology Letters **16**, 1661–1663 (2004).

6. J. C. Stover, *Optical Scattering: Measurement and Analysis*, 2nd ed. (SPIE Press, 1995), pp. 20–53.

7. C. Holmes, "Thesis: Direct UV Written Planar Devices for Sensing and Telecommunication Applications," University of Southampton (2009).

8. "http://www.advaluephotonics.com/2-micron-fiber-laser-products.html," .

9. K. K. Lee, D. R. Lim, L. C. Kimerling, J. Shin, and F. Cerrina, "Fabrication of ultralow-loss Si/SiO2 waveguides by roughness reduction.," Optics letters **26**, 1888–1890 (2001).

10. A. Ghatak and K. Thyagarajan, *Introduction to Fiber Optics* (Cambridge University Press, 1998), pp. 97–383.

11. K. Okamoto, *Fundamentals of Optical Waveguides*, 2nd ed. (Elsevier Inc, 2006), p. 18.

12. K. Thyagarajan, Y. Bourbin, A. Enard, S. Vatoux, and M. Papuchon, "Experimental demonstration of TM mode-attenuation resonance in planar metal-clad optical waveguides," Optics Letters **10**, 288–290 (1985).

13. D. Kumar, V. K. Sharma, and K. N. Tripathi, "Design and fabrication of multilayer metal-clad dielectric surface plasmon waveguide polarizers," Optical Engineering **45**, 054601 (2006).

14. D. Huo, K. Cheng, and F. Wardle, "Design of a five-axis ultra-precision micro-milling machine—UltraMill. Part 1: holistic design approach, design considerations and specifications," The International Journal of Advanced Manufacturing Technology **47**, 867–877 (2009).

15. "http://www.aerotech.com/service-and-support/reference-library.aspx," .

16. T. J. Ko and H. S. Kim, "Micro-end-milling of single-crystal silicon," International Journal of Machine Tools and Manufacture **47**, 2111–2119 (2007).

17. C. J. Morgan, R. R. Vallance, and E. R. Marsh, "Micro machining glass with polycrystalline diamond tools shaped by micro electro discharge machining," Journal of Micromechanics and Microengineering **14**, 1687–1692 (2004).

18. C. J. Morgan, R. R. Vallance, and E. R. Marsh, "Micro-machining and micro-grinding with tools fabricated by micro electro-discharge machining," International Journal of Nanomanufacturing **1**, 242–258 (2006).

19. K. Foy, Z. Wei, T. Matsumura, and Y. Huang, "Effect of tilt angle on cutting regime transition in glass micromilling," International Journal of Machine Tools and Manufacture **49**, 315–324 (2009).

20. J. Gäbler and S. Pleger, "Precision and micro CVD diamond-coated grinding tools," International Journal of Machine Tools and Manufacture **50**, 420–424 (2010).

21. S. T. Smith and D. G. Chetwynd, *Foundations of Ultraprecision Mechanism Design* (CRC Press, Taylor & Francis Group, 1992), pp. 190–195.

22. E. Bartolome, "Signal conditioning for piezoelectric sensors," Analog Applications Journal High Performance Analog Products, Texas Instruments Incorporated 24–31 (2010).

23. MathsWorks, "Fitting an Orthogonal Regression Using Principal Components Analysis," (2012).

24. F. Gao, R. K. Leach, J. Petzing, and J. M. Coupland, "Surface measurement errors using commercial scanning white light interferometers," Measurement Science and Technology **19**, 015303 (2008).

25. D. J. Whitehouse, *Handbook of Surface and Nanometrology*, 2nd ed. (CRC Press, Taylor & Francis Group, 2011), p. 188.

26. H. L. Rogers, S. Ambran, C. Holmes, P. G. R. Smith, and J. C. Gates, "In situ loss measurement of direct UV-written waveguides using integrated Bragg gratings," Optics Letters **35**, 2849–2851 (2010).

27. A. K. M. N. Amin and M. D. Bin Musa, *High Speed End Milling of Single Crystal Silicon Wafer: An Economic Method of Machining of Silicon in Ductile Mode* (Lambert Academic Publishing, 2011), pp. 34–35.

28. K. T. J. Rusnaldy and H. S. Kim, "An experimental study on microcutting of silicon using a micromilling machine," The International Journal of Advanced Manufacturing Technology **39**, 85–91 (2007).

7 Conclusions

The conclusions drawn here summarise the experimental chapters 4, 5 and 6. In the summary of each chapter, the future directions for the work is also discussed.

7.1 Summary of precision dicing of silica

Chapter 4, precision dicing of silica, focuses on the optimisation of the dicing process used to create low loss input/output facets in the silica-on-silicon platform. It was demonstrated that dicing can produce facets in silica-on-silicon substrate with a smooth, mirror like finish. The dicing machining parameters were optimised by monitoring average surface roughness. It was found that pre-dressing and using a rotational speed of 20 krpm and a translational speed of 0.1 mms^{-1} gave the smoothest finish. Once machined, the facets areal average surface roughness (Sa) was measured and found to be 4.9 nm, a factor ~7.5 times improvement on previously seen roughnesses in optical grade silica. After finding the optimised machining parameters, these parameters were used to create a groove through a waveguides containing Bragg gratings. The grooved waveguide was used to determine the average interface loss per facet, caused by scattering as a consequence of facet surface roughness. A ratiometric loss technique was used to determine the total loss of the groove. An individual average interface loss of -0.63 dB for the TE polarisation and -0.76 dB for the TM polarisation was found, by subtracting losses from diffraction (longitudinal and transverse) and Fresnel losses caused by the light traversing the groove.

Speculating, other future work may include the dicing of waveguides in silica-on-silicon to determine the loss of a diced waveguide. To achieve this accurately and

precisely, Bragg gratings will be inscribed along the diced ridge to allow the grating based loss techniques to be used, as described in chapter 4. This work will also answer other questions about the limit of the approach, such as the minimum feasible ridge width.

Future work, in relation with the dicing of GGG ($Gd_3Ga_5O_{12}$, Gadolinium Gallium Garnet) waveguide lasers, where poor waveguides were produced in terms of both surface roughness and amount of chipping, would require a reduction in hardness of the deposited material. The poor groove quality was caused by the high level of hardness of GGG, which has similar mechanical properties to the commonly known garnet, YAG (Yttrium Aluminium Garnet), which has a Mohs hardness of 8.5 [1]. Thus, if an alternate crystal could be deposited, which has similar optical qualities as GGG for making lasers but was softer, this would aid diced waveguide production. Katherine A. Sloyan has recently deposited Sesquioxides, as a GGG alternative. These sesquioxides crystals are Ytterbium based and take the form YbO_3. This class of crystal has better laser host properties than GGG/YAG, particularly in terms of thermal management, and are also softer. Sesquioxides have Mohs hardesses ranging from 6.8-7 [1], approximately the same hardness as silica [2]. This should enable these crystals to be diced whilst obtaining similar surface roughnesses to that of silica. The smooth sidewalls of the channel waveguide should provide low loss propagation of the light, thus making efficient lasers.

7.2 Summary of photonic microcantilevers

In chapter 5, photonic microcantilevers, novel glass microcantilevers with integrated Bragg gratings and waveguides are demonstrated. Cantilever fabrication used a combination of direct UV writing, precision dicing and wet etching. Two cantilever interrogations methods have been shown; one utilising a single Bragg grating and the other using a pair of spectrally matched Bragg gratings to form a Fabry-Pérot interferometer. Both types of cantilever have been the subject of journal papers published by the author [3] [4]. Deflection theories for both interrogation techniques are also presented using appropriate bending theories. This allows the prediction of

central Bragg wavelength or optical phase shift to be calculated, for the single Bragg grating and Fabry-Pérot interrogation systems, respectively.

The cantilever device, with single Bragg grating interrogation, is then used with a lock-in technique to explore the change in its mechanical resonance characteristics, with changing external pressure. The cantilever device with single Bragg grating interrogation is oscillated to a mechanical resonance with a piezo. A phase sensitive technique is used to acquire amplitude and phase data on the mechanical resonance characteristics. The cantilever device is then subjected to changing external pressure within a vacuum system and has shown changes in the damping coefficient, due to the transition from molecular to viscous flow, at around 1 mbar, of the air. These changes in mechanical resonance for different air pressure agree with work carried out in optical fibre based cantilevers.

The second cantilever interrogation method, used a pair of spectrally matched gratings to form a Fabry-Pérot interferometer. A profilometer is used to deflect the Fabry-Pérot cantilever while reflection spectra is collected and coupled mode theory used to extract the optical phase. A phase shift of the Fabry-Pérot interferometer of 3.71 radians was measured for 491 μN of applied point force, 4.1 mm along the length of the cantilever. The actual Fabry-Pérot cantilever showed a greater phase shift than the predicted results, and was attributed to nonlinear bending at larger deflections.

A comparison was made between the single Bragg grating and the Fabry-Pérot interrogation, in terms of their performance. The smallest resolvable force of the Fabry-Pérot interrogation system was found to be 264 nN, which is approximately a factor of four times [5] improvement on the single Bragg grating cantilever interrogation. The spectral sharpness of the Fabry-Pérot was compared with a single Bragg grating, yielding a factor of eleven times improvement in terms of intensity/wavelength gradient. The Fabry-Pérot interrogation system had a wavelength shift force sensitivity, or the dynamic range, of 330 nm/N, which is a reduction of ~27% [5] from the single Bragg grating cantilever interrogation.

An extension of this work has been started by Peter Cooper (Ph.D. Student) in the field of silica-on-silicon MOMS (Micro Optomechanical Systems). The work includes the development of new fabrication techniques to create bridge

structures [6], where both sides of the cantilever structure are fixed. These new fabrication techniques may include dicing, milling and/or wet etching. The micromechanical structure will have a higher mechanical resonant frequency than that of the cantilevers discussed in chapter 5 due to the clamping of both ends.

Other potential avenues of future cantilever research include optical actuation of the mechanical structure by thermal heating (bi-metallic effects). This will be achieved by depositing metal on the cantilever that will evanescently interact with the optical mode from the waveguide. Heat from a laser pulse will be absorbed in the cantilever, causing it to oscillate. This will allow the use of mechanical resonances of the cantilever to be excited but without the need of an attached piezo to the cantilever, as shown in chapter 5. This will enable a mechanically resonant system to be used in a remote, possibly flammable environment. However, the laser power needed for the mechanical actuation may become unsafe.

7.3 Summary of precision micromilling of silica

Chapter 6, precision micromilling of silica, the focus is on the optimisation of a milling process, to create smooth grooves in a silica-on-silicon platform to access the evanescent field by removal of cladding material. Precision micromilling is a complementary technique to precision dicing, where the dicing was used to create low loss input/output facets and microcantilever structures previously. However, while dicing is restricted to two-dimensions, milling allows three-dimensional machining whilst also working in the ductile cutting regime. The ductile cutting regime enables the machining of flat, smooth, chip free grooves to be fabricated in silica. Thus, a precision milling machine was constructed.

Within precision micromilling of silica, a basic theory of milling and in particular, ductile milling, is included along with a thorough account of equipment and procedures used. It was shown that to achieve the feed rate per tooth, to machine silica in the ductile regime, the mill needed high precision stages, high loop stiffness and good decoupling from the lab environment.

The chapter also includes an overview of dominant machining factors affecting milled groove quality in silica. These machining factors included: sample setting with wax, cooling with deionised water and using diamond coated, tungsten carbide, slot micromills. Sample mapping was discussed and an offset of 743 nm was found to exist between the programed axial depth of cut and the actual axial depth of cut. The sampling mapping along with probing error and various averaging, had a random error of 277 nm. It was also shown that peck drill dressing in silicon carbide could be used to increase the groove surface quality by removing mill high points. Mill cutter path is also critical in the groove surface quality achieved and it has been shown that a vertical plunge into a silica surface causes large amounts of cracking. A linear descent, in both the vertical and horizontal axes, however, was found to remove this type of cracking entirely.

The milling procedure optimisation is also included in this chapter, whereby surface roughness and chipping amounts have been monitored. It was found that optimum machining was obtained at a rotational speed of 40 krpm and a translational speed of 0.75 mm/min. Once machined, the grooves average surface roughness (Sa) was measured and was found to be 3.0 nm. The micromilling method uses a depth of cut 40 times deeper, at 17 µm and was ~7 times smoother [7] than stated in the literature. The chapter also discusses subsequent grooves milled with the optimum machining parameters and found good uniformity in the depth of each groove. The technique with a new mill could produce eight, 1.5 mm length grooves in the optical grade silica before mill wear affected groove surface quality. It is believed the large increases in depth of cut with no decrease in groove surface quality, compared to previous work, is related to the aerostatic spindle and preparatory dressing, used in the technique developed here. This chapter shows that precision milling is a strong candidate for the removal of cladding layers, exposing the core of silica-on-silicon substrates, allowing access to the evanescent field.

A potential avenue of future work in precision milling is the machining and dressing of mill bits in situ. The notion is to machine mills on the spindle with a technique called wire electrode discharge grinding. The mills will be made from an electrically conducting matrix containing diamonds and an electrical discharge will erode material from the mill. It has been shown by Morgan *et al.* that diameters of 50 µm can be achieved in polycrystalline diamond [8]. At these sizes the precision milling

technique becomes a viable route in the production of optofluidic devices [9]. The ability to machine mills on the spindle would also allow redressing of the mills throughout the machining process, reducing cost and maintaining workpiece surface quality (form and roughness).

References

1. V. Peters, "Thesis: Growth and Spectroscopy of Ytterbium Doped Sesquioxides," University of Hamburg (2001).

2. G. W. Fynn and W. J. A. Powell, *Cutting and Polishing Optical and Electronic Materials*, 2nd ed. (Institute of Physics Publishing Inc., 1988), pp. 2–3.

3. L. G. Carpenter, C. Holmes, H. L. Rogers, P. G. R. Smith, and J. C. Gates, "Integrated optic glass microcantilevers with Bragg grating interrogation," Optics Express **18**, 23296–23301 (2010).

4. L. G. Carpenter, C. Holmes, B. D. Snow, J. C. Gates, and P. G. R. Smith, "Photonic Microcantilevers With Interferometric Bragg Grating Interrogation," IEEE Photonics Journal **4**, 1387–1395 (2012).

5. C. Holmes, L. G. Carpenter, H. L. Rogers, J. C. Gates, and P. G. R. Smith, "Quantifying the optical sensitivity of planar Bragg gratings in glass micro-cantilevers to physical deflection," Journal of Micromechanics and Microengineering **21**, 035014 (2011).

6. P. A. Cooper, C. Holmes, L. G. Carpenter, C. Sima, P. L. Mennea, C. James, and P. G. R. Smith, "Silica Microbeams for Tunable Bragg Gratings," CLEO-Europe/IQEC 2013 Munich 12-16 May 2013 (2012).

7. M. Arif, M. Rahman, and W. Y. San, "Ultraprecision ductile mode machining of glass by micromilling process," Journal of Manufacturing Processes **13**, 50–59 (2011).

8. C. J. Morgan, R. R. Vallance, and E. R. Marsh, "Micro machining glass with polycrystalline diamond tools shaped by micro electro discharge machining," Journal of Micromechanics and Microengineering **14**, 1687–1692 (2004).

9. C. Monat, P. Domachuk, and B. J. Eggleton, "Integrated optofluidics: A new river of light," Nature Photonics **1**, 106–114 (2007).

Appendix A

7.4 Publication list

7.4.1 Journal Publications:

L. G. Carpenter, H. L. Rogers, Peter A. Cooper, C. Holmes, J. C. Gates and P. G. R. Smith, "Low optical-loss facet preparation for silica-on-silicon photonics using the ductile dicing regime," Journal of Physics D: Applied Physics, awaiting type setting.

L.G.Carpenter, C.Holmes, B.D.Snow, J.C.Gates, P.G.R.Smith
Photonic microcantilevers with interferometric Bragg grating interrogation
IEEE Photonics Journal 2012 Vol.4(5) pp.1387-1395

L.G.Carpenter, C.Holmes, H.Rogers, P.G.R.Smith, J.C.Gates
Integrated optic glass microcantilevers with Bragg grating interrogation
Optics Express 2010 Vol.18(22) pp.23296-23301

C.Holmes, **L.G.Carpenter**, H.L.Rogers, I.J.G.Sparrow, J.C.Gates, P.G.R.Smith
Planar waveguide tilted Bragg grating refractometer fabricated through physical micromachining and direct UV writing
Optics Express 2011 Vol.19(13) pp.12462-12468

C.Holmes, **L.G.Carpenter**, H.L.Rogers, J.C.Gates, P.G.R.Smith
Physical sensitivity of silica micro-cantilevers fabricated using direct UV writing and micromachining
Journal of Laser Micro/Nanoengineering 2011 Vol.6(1) pp.26-30

C.Holmes, **L.G.Carpenter**, J.C.Gates, P.G.R.Smith
Miniaturisation of Bragg-multiplexed membrane transducers
Journal of Micromechanics and Microengineering 2012 Vol.22 pp.025017

C.Holmes, **L.G.Carpenter**, H.L.Rogers, J.C.Gates, P.G.R.Smith
Quantifying the optical sensitivity of planar Bragg gratings in glass micro-cantilevers to physical deflection
Journal of Micromechanics and Microengineering 2011 Vol.21 pp.035014

S.Ambran, C.Holmes, J.C.Gates, A.S.Webb, **L.G.Carpenter**, F.R.M.Adikan, P.G.R.Smith, J.K.Sahu
Fabrication of a multimode interference device in a low-loss flat-fiber platform using physical micromachining technique
Journal of Lightwave Technology 2012 Vol.30(17)

7.4.2 Coference Publications:

L.G.Carpenter, H.L.Rogers, C.Holmes, J.C.Gates, P.G.Smith
Facet Machining of Silica Waveguides with Nanoscale Roughness without Polishing or Lapping
CLEO/Europe-EQEC Munich 12-16 May 2013 (Poster)

L.G.Carpenter, H.L.Rogers, C.Holmes, J.C.Gates, P.G.Smith
Polish like facet preparation via dicing for silica integrated optics
Photonics West San Francisco 2-7 February 2013 (Oral)

L.G.Carpenter, H.L.Rogers, C.Holmes, J.C.Gates, P.G.Smith
MOMS accelerometers utilizing resonant microcantilevers with interrogated single mode waveguides and Bragg gratings
Photonics West San Francisco 2-7 February 2013 (Oral)

L.G.Carpenter, P.L.Mennea, H.L.Rogers, C.Holmes, J.C.Gates, P.G.R.Smith
Integrated corner mirrors as a platform for miniaturized planar strain sensing
European Conference on Integrated Optics (ECIO) Sitges Barcelona 18-20 April 2012 (Poster)

L.G.Carpenter, H.L.Rogers, C.Holmes, J.C.Gates, P.G.R.Smith
Integrated corner mirrors physically micromachined in silica-on-silica
IONS-9 Salamanca Spain 7-9 Apr 2011 (Oral)

L.G.Carpenter, H.L.Rogers, C.Holmes, J.C.Gates, P.G.Smith
Physically micromachined silica-on-silicon integrated corner mirrors
CLEO/Europe-EQEC Munich 22-26 May 2011 (Oral)

L.G.Carpenter, C.Holmes, P.G.R.Smith, J.C.Gates
Integrated optic glass microcantilever with Bragg gratings forming a Fabry-Perot interferometer for force sensing
CLEO/Europe-EQEC Munich 22-26 May 2011 (Oral)

L.G.Carpenter, C.Holmes, H.L.Rogers, J.C.Gates, P.G.R.Smith
Integrated optical glass microcantilevers for displacement and pressure sensing
IONS-8 Moscow 21-25 Jun 2010 (Oral)

L.G.Carpenter, C.Holmes, J.C.Gates, P.G.R.Smith
Planar micromachined glass cantilevers utilising integrated Bragg Fabry-Perot cavities
Photon 10 Southampton 23-26 Aug 2010 (Oral)

L.G.Carpenter, C.Holmes, H.L.Rogers, J.C.Gates, P.G.R.Smith

Appendix A

Investigating planar integrated glass cantilevers utilizing Bragg gratings and mechanical resonance in a vacuum
European Conference on Integrated Optics (ECIO) 2010 Cambridge 7-9 Apr 2010 (Oral)

C.Holmes, **L.G.Carpenter**, P.A.Cooper, H.L.Rogers, J.C.Gates, P.G.R.Smith
Micro-mechanical integrated optical structures
European Conference on Integrated Optics (ECIO) Sitges Barcelona 18-20 Apr 2012

H.L.Rogers, **L.G.Carpenter**, S.Ambran, C.Sima, D.J.Wales, R.M.Parker, C.Holmes, J.C.Gates, P.G.R.Smith
Direct grating writing: single-step Bragg grating and waveguide fabrication for telecommunications
IONS NA-3 Stanford USA 13-15 Oct 2011

H.L.Rogers, **L.G.Carpenter**, S.Ambran, C.Sima, B.D.Snow, R.M.Parker, C.Holmes, J.C.Gates, P.G.R.Smith
Direct grating writing: Single-step Bragg grating and waveguide fabrication for telecommunications and sensing applications
IONS-9 Salamanca Spain 7-9 Apr 2011

C.Holmes, **L.G.Carpenter**, J.C.Gates, I.J.G.Sparrow, P.G.R.Smith
Combining physical micro-machining and direct UV writing to fabricate novel planar tilted Bragg grating refractometers
CLEO/Europe-EQEC Munich 22-26 May 2011

C.Holmes, K.R.Daly, **L.G.Carpenter**, J.C.Gates, I.J.G.Sparrow, G.D.D'Alessandro, P.G.R.Smith
Enhancing chemical sensitivity of a tilted planar Bragg grating using a thin gold layer
CLEO/Europe-EQEC Munich 22-26 May 2011

K.A.Sloyan, **L.G.Carpenter**, T.C.May-Smith, C.Holmes, J.C.Gates, P.G.R.Smith, R.W.Eason
Fabrication of multilayer crystalline rib waveguides by a combined multi-step Pulsed Laser Deposition/precision machining technique
CLEO/Europe-EQEC Munich 22-26 May 2011

C.Holmes, **L.G.Carpenter**, H.L.Rogers, J.C.Gates, P.G.R.Smith
Physical sensitivity of silica micro-cantilevers fabricated using direct UV writing and micromachining
11th International Symposium on Laser Precision Microfabrication 7-11 Jun 2010
LPM2010 held in Stuttgart, Germany (A#198, ON-095)

C.Holmes, **L.G.Carpenter**, H.L.Rogers, J.C.Gates, P.G.R.Smith
Silica based micro-cantilevers fabricated using direct UV writing and micro machining for chemical and physical sensing applications
LPM 2010 Stuttgart 7-10 Jun 2010

C.Holmes, **L.G.Carpenter**, H.L.Rogers, J.C.Gates, P.G.R.Smith

Appendix A

Detection of first order phase transitions using direct UV written integrated optical planar Bragg gratings intrinsically defined within a silica micro-cantilever
CLEO/QELS 2010 San Jose 16-21 May 2010

C.Holmes, **L.G.Carpenter**, H.C.Hunt, J.C.Gates, P.G.R.Smith
Microfluidic multimode interference device
ECIO 2010 Cambridge 7-9 Apr 2010

C.Holmes, **L.G.Carpenter**, J.C.Gates, P.G.R.Smith
Micromachining of integrated optical circuits
SET for Britain House of Commons London 8 Mar 2010

Appendix B

If the direction of propagation of the light is parallel to the z axis, see Figure 119, and the refractive index is constant, then $n^2 = n^2(x, y)$. The solutions to the wave equations, take the form,

$$\boldsymbol{\mathcal{E}} = \boldsymbol{E}(x, y)e^{j(\omega t - \beta z)} \quad \textbf{Equation 98}$$

$$\boldsymbol{\mathcal{H}} = \boldsymbol{H}(x, y)e^{j(\omega t - \beta z)} \quad \textbf{Equation 99}$$

where β is the propagation constant of the mode and ω is the angular frequency. The propagation constant is related to the effective refractive index (n_{eff}) by $\beta = k_o n_{eff}$, where k_o is the free space wavenumber and $k_o = \frac{2\pi}{\lambda} = \frac{\omega}{c}$. The first term of the exponent in Equation 98 and Equation 99, is described as simple harmonic motion, as shown in Figure 118.

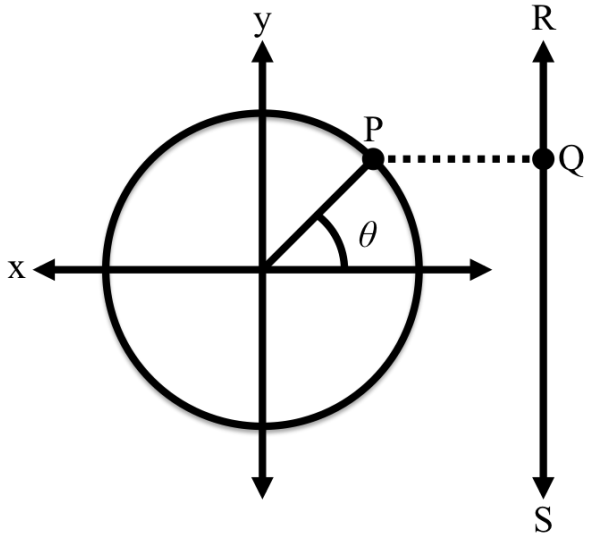

Figure 118 simple harmonic motion.

$$\theta = \omega t, y = A\sin\theta,\ y = A\sin\omega t,\ x = A\cos\omega t,$$

$$z = x + jy, z = A(cos\,\omega t + j\,sin\,\omega t) \therefore z = e^{j\omega t}$$

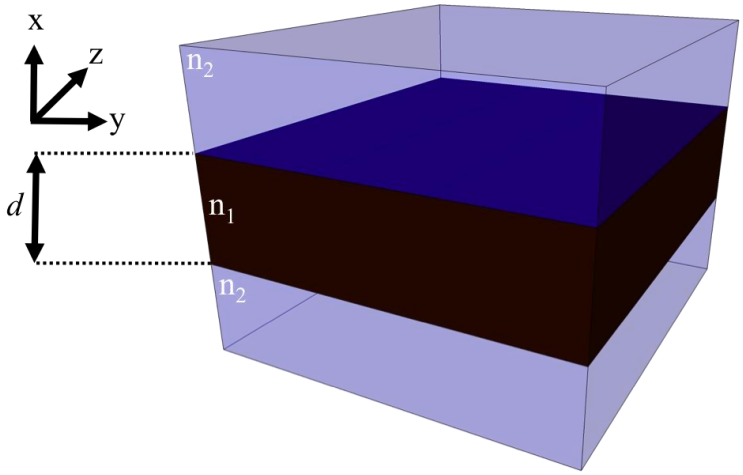

Figure 119 planar slab waveguide.

Equation 98 and Equation 99 describe the optical modes and their electromagnetic fields which are constant in x and y and propagate in the z direction. Further simplification of Equation 98 and Equation 99 can be achieved by referring back to Figure 119. As it can be seen, the refractive index is constant in two directions, both y and z, and only varies in x, thus $n^2 = n^2(x)$. This yields,

$$\mathcal{E}_j = E_j(x)e^{j(\omega t-\beta z)}, j = x, y, z \qquad \textbf{Equation 100}$$

$$\mathcal{H}_j = H_j(x)e^{j(\omega t-\beta z)}, j = x, y, z \qquad \textbf{Equation 101}$$

These are substituted back into Maxwell's equations,

$$\nabla \times \left(E_j(x)e^{j(\omega t-\beta z)}\right) = -\mu_o \frac{\partial}{\partial t}\left(H_j(x)e^{j(\omega t-\beta z)}\right) \qquad \textbf{Equation 102}$$

$$\nabla \times \left(H_j(x)e^{j(\omega t-\beta z)}\right) = n^2\varepsilon_o \frac{\partial}{\partial t}\left(E_j(x)e^{j(\omega t-\beta z)}\right) \qquad \textbf{Equation 103}$$

The curl of each is taken,

$$\nabla \times \boldsymbol{E} = \begin{vmatrix} \hat{\boldsymbol{x}} & \hat{\boldsymbol{y}} & \hat{\boldsymbol{z}} \\ \frac{\partial}{\partial x} & \frac{\partial}{\partial y} & \frac{\partial}{\partial z} \\ E_x(x)e^{j(\omega t-\beta z)} & E_y(x)e^{j(\omega t-\beta z)} & E_z(x)e^{j(\omega t-\beta z)} \end{vmatrix} \qquad \textbf{Equation 104}$$

$$\nabla \times \boldsymbol{E} = \hat{\boldsymbol{x}}\left(j\beta E_{\boldsymbol{y}} e^{j(\omega t-\beta z)}\right) - \hat{\boldsymbol{y}}\left(\frac{\partial \mathrm{E}_{\boldsymbol{z}}}{\partial x}\mathrm{e}^{\mathrm{j}(\omega \mathrm{t}-\beta \mathrm{z})} + j\beta \mathrm{E}_{\boldsymbol{x}}\mathrm{e}^{\mathrm{j}(\omega \mathrm{t}-\beta \mathrm{z})}\right) - \hat{\boldsymbol{z}}\left(\frac{\partial \mathrm{E}_{\boldsymbol{y}}}{\partial x}\mathrm{e}^{\mathrm{j}(\omega \mathrm{t}-\beta \mathrm{z})}\right) \quad \textbf{Equation 105}$$

$$\nabla \times \boldsymbol{H} = \begin{vmatrix} \hat{\boldsymbol{x}} & \hat{\boldsymbol{y}} & \hat{\boldsymbol{z}} \\ \frac{\partial}{\partial x} & \frac{\partial}{\partial y} & \frac{\partial}{\partial z} \\ H_x(x)e^{j(\omega t-\beta z)} & H_y(x)e^{j(\omega t-\beta z)} & H_z(x)e^{j(\omega t-\beta z)} \end{vmatrix} \quad \textbf{Equation 106}$$

$$\nabla \times \boldsymbol{H} = \hat{\boldsymbol{x}}\left(j\beta H_{\boldsymbol{y}} e^{j(\omega t-\beta z)}\right) - \hat{\boldsymbol{y}}\left(\frac{\partial \mathrm{H}_{\boldsymbol{z}}}{\partial x}\mathrm{e}^{\mathrm{j}(\omega \mathrm{t}-\beta \mathrm{z})} + j\beta \mathrm{H}_{\boldsymbol{x}}\mathrm{e}^{\mathrm{j}(\omega \mathrm{t}-\beta \mathrm{z})}\right) + \boldsymbol{k}\left(\frac{\partial H_{\boldsymbol{y}}}{\partial x} e^{j(\omega t-\beta z)}\right) \quad \textbf{Equation 107}$$

and substituted back into Equation 102 and Equation 103. Simplification yields,

$$j\beta \mathrm{E}_{\boldsymbol{y}} = -j\omega\mu_o \mathrm{H}_x \quad \textbf{Equation 108}$$

$$-\frac{\partial \mathrm{E}_{\boldsymbol{z}}}{\partial x} - j\beta \mathrm{E}_{\boldsymbol{x}} = -j\omega\mu_o \mathrm{H}_y \quad \textbf{Equation 109}$$

$$\frac{\partial \mathrm{E}_{\boldsymbol{y}}}{\partial x} = -j\omega\mu_o \mathrm{H}_z \quad \textbf{Equation 110}$$

$$j\beta \mathrm{H}_{\boldsymbol{y}} = j\omega\varepsilon_o n^2(x)\mathrm{E}_x \quad \textbf{Equation 111}$$

$$-\frac{\partial \mathrm{H}_{\boldsymbol{z}}}{\partial x} - j\beta \mathrm{H}_{\boldsymbol{x}} = j\omega\varepsilon_o n^2(x)\mathrm{E}_y \quad \textbf{Equation 112}$$

$$\frac{\partial \mathrm{H}_{\boldsymbol{y}}}{\partial x} = j\omega\varepsilon_o n^2(x)\mathrm{E}_z. \quad \textbf{Equation 113}$$

Equation 108, Equation 110 and Equation 112 only involve $\mathrm{E}_{\boldsymbol{y}}$, H_x and H_z, while Equation 109, Equation 111 and Equation 113 only involve H_y, $\mathrm{E}_{\boldsymbol{x}}$ and E_z. This shows that, for a planar slab waveguide, Maxwell's equations reduces to two components. The non-vanishing values of $\mathrm{E}_{\boldsymbol{y}}$, H_x and H_z of Equation 108, Equation 110 and Equation 112 form what is known as the transverse electric mode or TE mode, which has its electric field oscillating in the y axis (see Figure 119). Conversely, the non-vanishing values of Equation 109, Equation 111 and Equation 113, H_y, $\mathrm{E}_{\boldsymbol{x}}$ and E_z, form what is known as the transverse magnetic mode or TM mode, which has its magnetic field oscillating in the y axis (see Figure 119). Both the TE and the TM mode can be described by an ordinary second order differential equation obtained from the solution to the wave equation, which is analyzed next.

The electric field of the TE can be expressed by substituting Equation 108 and Equation 110 into Equation 112,

$$\frac{j\beta^2}{\omega\mu_o}\mathrm{E}_{\boldsymbol{y}} + \frac{1}{j\omega\mu_o}\frac{\partial^2 \mathrm{E}_{\boldsymbol{y}}}{\partial x^2} = j\omega\varepsilon_o n^2(x)\mathrm{E}_{\boldsymbol{y}} \quad \textbf{Equation 114}$$

$$\frac{1}{j\omega\mu_o}\frac{\partial^2 \mathrm{E}_{\boldsymbol{y}}}{\partial x^2} = \left(j\omega\varepsilon_o n^2(x) - \frac{j\beta^2}{\omega\mu_o}\right)\mathrm{E}_{\boldsymbol{y}} \qquad \textbf{Equation 115}$$

$$\frac{\partial^2 \mathrm{E}_{\boldsymbol{y}}}{\partial x^2} = (j^2\omega^2\varepsilon_o\mu_o n^2(x) - j^2\beta^2)\mathrm{E}_{\boldsymbol{y}} \qquad \textbf{Equation 116}$$

$$\frac{d^2 \mathrm{E}_{\boldsymbol{y}}}{dx^2} + (k_o^2 n^2(x) - \beta^2)\mathrm{E}_{\boldsymbol{y}} = 0 \qquad \textbf{Equation 117}$$

where k_o, the free space wavenumber $k_o = \omega\sqrt{\varepsilon_o\mu_o}$, is used. Equation 114 can be solved by applying boundary conditions for a specific planar slab waveguide. These boundary conditions are; a core layer centred around x = 0, with a thickness d, with a refractive index n_1 and cladding layer refractive index of n_2 (see Figure 119). The electric field within the core and cladding can be described by the following equations,

$$\frac{d^2 \mathrm{E}_{\boldsymbol{y}}}{dx^2} + (k_o^2 n_1^2 - \beta^2)\mathrm{E}_{\boldsymbol{y}} = 0, |x| < {}^{d}/_{2} \qquad \textbf{Equation 118}$$

$$\frac{d^2 \mathrm{E}_{\boldsymbol{y}}}{dx^2} + (k_o^2 n_2^2 - \beta^2)\mathrm{E}_{\boldsymbol{y}} = 0, |x| > {}^{d}/_{2} \qquad \textbf{Equation 119}$$